Summer 1994

Flow Kinematics and Dynamics of the Gulf Stream From Composite Imagery

Caitlin Patrice Mullen
Old Dominion University

FLOW KINEMATICS AND DYNAMICS OF THE GULF STREAM FROM COMPOSITE IMAGERY

by

Caitlin Patrice Mullen
Bachelor of Science, May 1987
Dickinson College, Carlisle, PA, USA

A Dissertation submitted to the Faculty of
Old Dominion University in Partial Fulfillment of the
Requirement for the Degree of

DOCTOR OF PHILOSOPHY
OCEANOGRAPHY

OLD DOMINION UNIVERSITY
AUGUST 1994

Approved by:

A. D. Kirwan, Jr. (Director)

Larry P. Atkinson

Charles R. McClain

Abstract

FLOW KINEMATICS AND DYNAMICS OF THE
GULF STREAM FROM COMPOSITE IMAGERY

Caitlin Patrice Mullen
Old Dominion University, 1994
Director: Dr. A. D. Kirwan, Jr.

A unique set of contemporaneous satellite-tracked drifters and five-day composite satellite images of the North Atlantic is studied in order to infer the near-surface flow kinematics and dynamics of the Gulf Stream. Using fractal and spectral analyses, two kinematic models, and a potential vorticity model, detailed comparisons are made between these data sets.

Fractal and spectral analyses show that the data set is not fractal, there is no geographic variability, and there is not a strong fractal scaling link between the drifter trajectories and composite temperature fronts as had been postulated by several investigators. These results indicate considerably more work needs to be performed before fractal analysis can relate surface flow characteristics with geometric properties of images.

Kinematic analysis of the contemporaneous data set is used to infer kinematic properties of the flow field including flow along temperature fronts. This was achieved by using thermal field characteristics obtained from composite images

in conjunction with kinematic feature models. Of the two kinematic models used for this phase of the study, it was found that Bower (1991) presents a better feature model than Dutkiewicz et al. (1993).

A barotropic potential vorticity model was developed to incorporate some dynamics into the analysis of the meandering Gulf Stream. Results show that there is good correlation between the drifter data, composite images, and the model trajectories.

There are two central results that have emerged from this study. The first is that considerable caution should be used in inferring fractal properties of both trajectories and images. This is a potentially powerful analysis tool, but, contrary to the claims of other scientists, there is little, if any, scaling link between the flow and surface temperature fields. The other result is that composite imagery and a suitable feature model can be used to infer flow along temperature fronts. This should have major ramifications on the quantitative use of image data.

To my mother and father,
Virginia and George Mullen,
who were always there for me.

Acknowledgements

I express sincere thanks to my advisor, Dr. A. D. Kirwan, Jr., for his unfaltering guidance and support throughout the past years. It was his encouragement and enthusiasm which aided in the completion of this project. I especially thank him for giving me the opportunity to change my field of study from geological to physical oceanography. When I first entered this program, I constantly expressed my interest in becoming a physical oceanographer. Dr. A. D. Kirwan, Jr. was the only one who listened and helped me achieve that goal. For that, I am deeply grateful.

Many thanks also go to the other members of my dissertation committee, Drs. Larry P. Atkinson and Charles R. McClain, for their helpful comments and insight into this project.

I am deeply grateful to all my friends at CCPO and the oceanography department who aided in the completion of this degree. There are many people deserving of individual thanks and I greatly appreciate everyone's support and friendship throughout the years. Thanks especially go to the staff of CCPO, Carole Blett, Karal Gregory, Beverly Mitchell and Julie Morgan, for all their help.

A very special thanks to my running partners, Margaret M. Dekshenieks, Cathy M. Lascara, and John M. Klinck. It was the run with this group at 1130 sharp everyday that kept my sanity intact. The discussions and friendships formed from

these runs are greatly appreciated. I also thank Cathy for our thought provoking conversations and her expertise in computer programming.

I thank all my military and police friends who would not let me lose sight of reality and the "big picture", and who have made my years in Norfolk truly enjoyable. I also thank my close friends, Douglas, Laurie, Deanna, and Pauline for their continued support and lasting friendships.

To John J. Holdzkom II, I express my thanks for his mathematical assistance, timely discussions, and his great friendship. A special thanks and appreciation goes to Dr. Glen H. Wheless for his invaluable discussions regarding this research, uncanny sense of humor, enthusiastic encouragement, great friendship, and for always having the time to listen to my complaints, problems, and ideas. These friendships will always be treasured.

I send my heartfelt thanks and love to my best friend - for without whom this project would not have been completed - thanks for everything through the good and bad times.

Last, but not least, I express my love and gratitude to my very dear family - George, Virginia, Siobhan, Brigid, Michael and Deirdre - for their unconditional love, understanding and support throughout the years.

"Nothing in the world can take the place of PERSISTENCE. Talent will not; nothing is more common than unsuccessful men with talent. Genius will not; unrewarded genius is almost a proverb. Education will not; the world is full of educated derelicts PERSISTENCE and DETERMINATION alone are OMNIPOTENT."

Calvin Coolidge

Contents

List of Tables

List of Figures

1 Introduction

It seemed to me a superlative thing
to know the explanation of everything,
why it comes to be, why it perishes,
why it is.
Socrates

This study analyzes a contemporaneous data set of satellite-tracked drifters and composite satellite imagery in order to infer the near-surface flow velocity of the Gulf Stream. The general goals of this study are to characterize the kinematic properties of the Gulf Stream, quantify the similarities and differences of the kinematic fields of the infrared imagery and drifters and ultimately relate dynamically the drifter velocities and thermal fields of the satellite images. The kinematics and dynamics of the Gulf Stream are investigated by applying spectral and fractal analyses methods to the data set. A model based on the exact non-linear potential vorticity equation was developed to study the dynamics of the Gulf Stream. Comparisons of the results of this dynamic model with those of the kinematic model of Bower (1991) and Dutkiewicz et al. (1993) were undertaken.

1.1 General Gulf Stream Information

The predominant kinematic feature within the North Atlantic is the Gulf Stream (Figure 1). The average width of the Gulf Stream is approximately 100 *km*, with a length that varies around 3000 *km* (Shaw and Rossby, 1984). Tempera-

Figure 1: Diagram illustrating the flow of the Gulf Stream along the eastern coast of the United States. It also shows circulation of water in the North Atlantic (from Iselin, 1936).

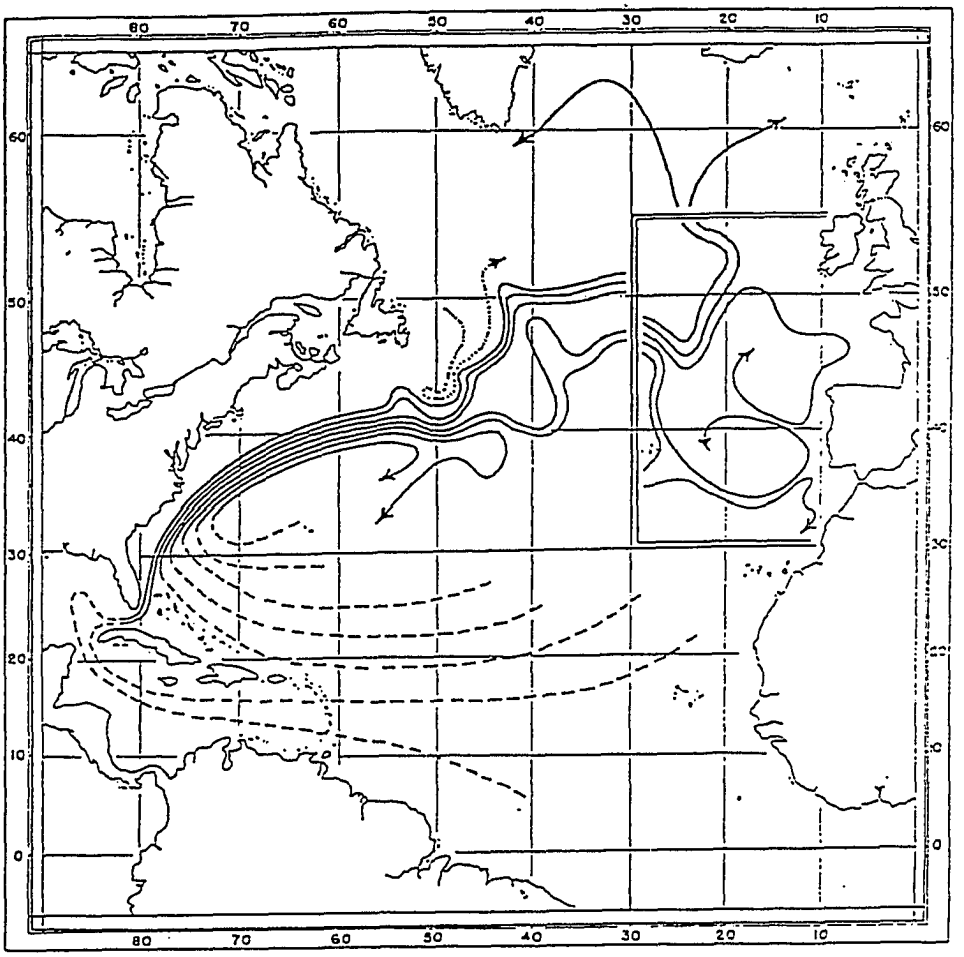

ture of the Stream ranges from 22-28°C, while the salinity at the surface of the Gulf Stream varies from 36.0 - 36.4 *psu*. It can attain salinity values of 36.7-36.8 *psu* at 100 m depth. In some instances the salinity value of the Gulf Stream can be as low as 35.4 *psu*. The cross-stream sea surface slope is on the order of 10^{-5}, sloping down to the west (Pond and and Pickard, 1983). The along-stream sea surface slope is on the order of -10^{-7} (Sturges, 1974).

According to the definition proposed by Iselin (1936), the Gulf Stream System is composed of three sections; the Florida Current, the Gulf Stream Proper and the North Atlantic Current (Figure 2). This system flows from the Florida Straits northward to Cape Hatteras, then north-eastward to the Grand Banks of Newfoundland. The Florida Current emerges from the Florida Straits and flows northward along the U.S. continental margin to Cape Hatteras. In this region, the Gulf Stream System is over water depths of 500 - 800 m where its course is guided by the topography of the continental slope. However, north of Cape Hatteras the Gulf Stream stops following the shelf break and flows north-eastward in the deep ocean, where the depths are greater than 4000 m. This region comprises the Gulf Stream Proper. The flow continues eastward as the North Atlantic Current. To the north of the Gulf Stream, there is a wedge of southward flowing slope water. The Stream is also flanked to the south by the westward flow of oceanic waters (Ingmanson, 1989), (Figure 3). Once the Gulf Stream begins to flow eastward, its strength weakens and meandering occurs, probably due to the loss of the slope constraints. The meanders increase dramatically downstream of Hatteras, causing the Stream to lose its structure. The focus here will be on the portion of the Gulf Stream ranging from the Straits of Florida to just south of the Grand Banks of Newfoundland, which will be termed the Gulf Stream.

Meanders are the "lateral shifts of the entire baroclinic structure associated

Figure 2: Figure displaying the three sections of the Gulf stream: A) the Florida Current, B) the Gulf Stream Proper and C) the North Atlantic. Several cold-core and warm-core rings are illustrated. (from Richardson, 1983b).

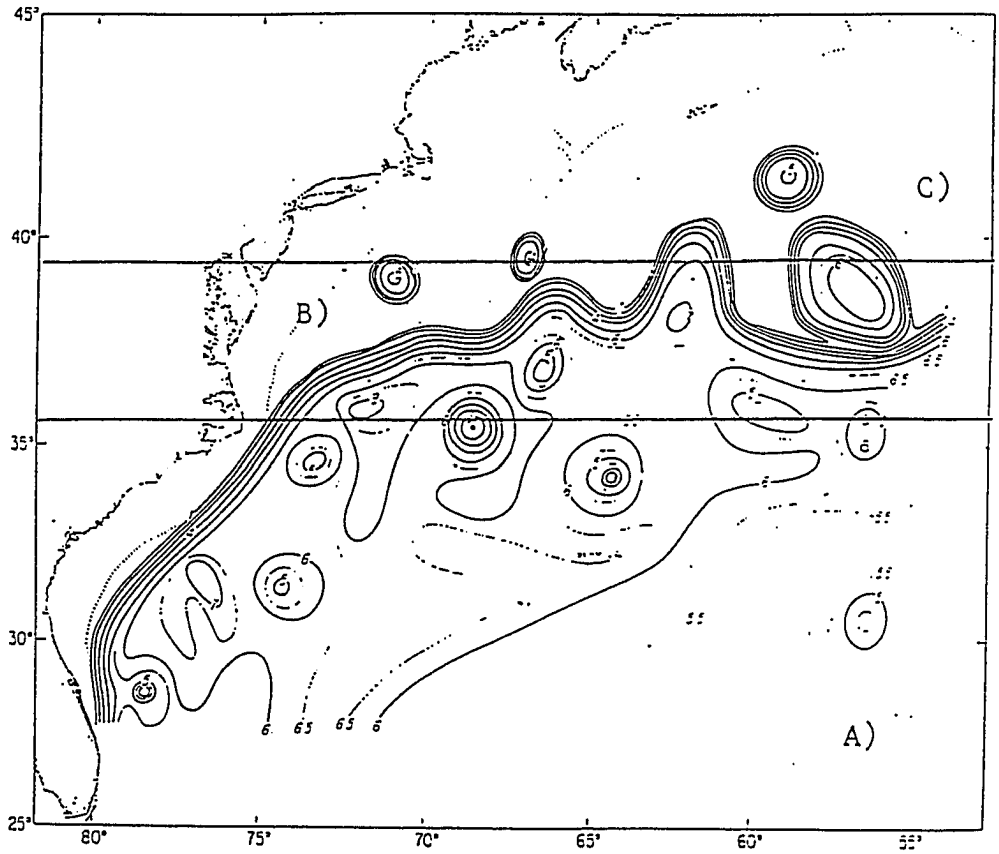

Figure 3: Diagram showing the westward flow of water north and south of the Gulf Stream. The numbers represent flow in sverdrups (from Ingmanson, 1989).

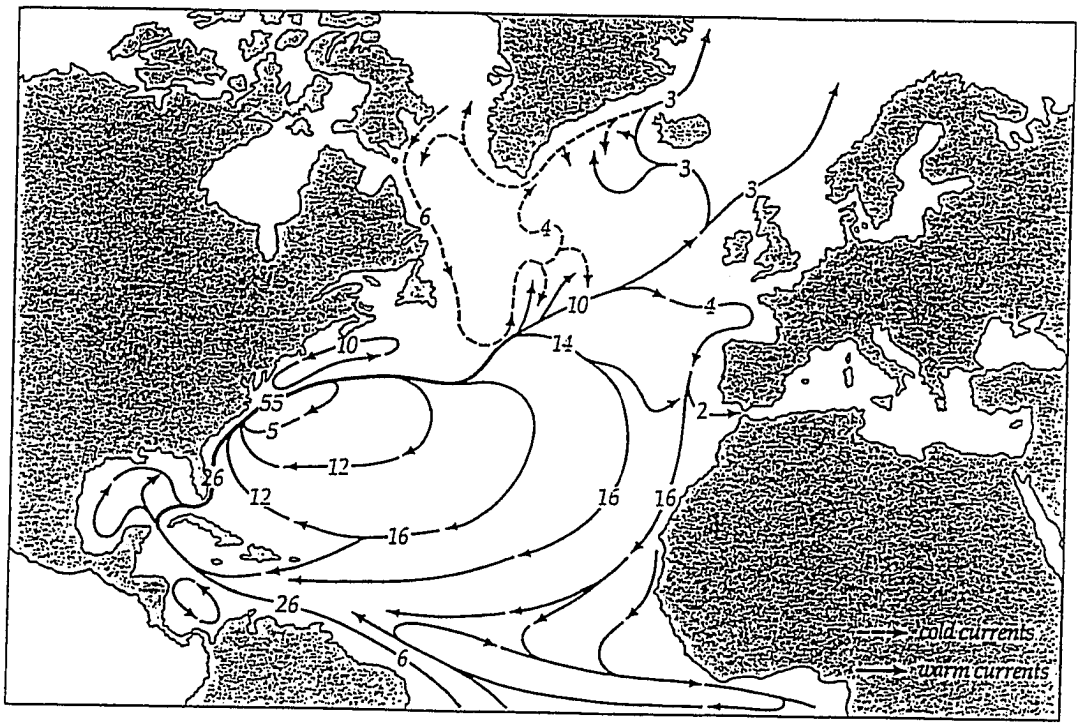

with the Gulf Stream" (Watts, 1983). The alongstream wavelengths of the meanders vary from 300 to 500 *km*. Table 1 taken from Watts (1983) displays the periodicities, wavelengths, propagation speeds and the amplitude root mean square (r.m.s.) of the Gulf Stream's variability along its path. Within the Florida Straits, the amplitude r.m.s. ranges from 5-10 *km* with wavelengths of approximately 150-170 *km*. At Cape Hatteras, the meanders propagate downstream at speeds up to 36 $km\ day^{-1}$, where their wavelengths reach a maximum 600 *km*. Around 65 - 70°W, the wavelength of the meanders decrease as the amplitude increases. The periodicity of the meanders is around 60 days with propagation speeds to the east of up to 10 $km\ day^{-1}$ (Watts, 1983). At 65°W, the meander amplitudes reach approximately 80 km. As the Gulf Stream continues along its path past Cape Hatteras out into the abyssal Atlantic, the wavelength and amplitude of the meanders increase. The width of the meandering region increases to about 300-400 *km* (Watts, 1983).

The swiftest portion in most parts of the Gulf Stream is to the west of the Stream's main axis, making the velocity profile asymmetric (von Arx, 1974, Figure 4). The main axis of the Gulf Stream is calculated from numerous experiments where the position of the Stream is determined relative to the coast. Thus, the main axis is the mean location of the Gulf Stream from these experiments. South of Cape Hatteras the location of the main axis is positioned over the 200 *m* isobath line. Von Arx (1974) has shown that the shear on the left hand side of the maximum velocity zone is greater than or equal to the Coriolis parameter. In contrast, the anticyclonic shear is less than or equal to the Coriolis parameter (von Arx, 1974). The cyclonic shear region is much narrower than the anticyclonic side. The velocity of the Gulf Stream decreases with depth, with the greatest velocities at or near the surface.

The spatial variability of the Gulf Stream spans a range of tens to thousands

Table 1: Path variability of the Gulf Stream. Letters represent previous studies which are cited in Watts, 1983.

	Florida Straits	Carolina Capes	Cape Hatteras 73°–75° W	~65°–70° W
Periodicities (days)	9–12 (d) 10–13 (k) 7–14 (c)	3– 8 (b) 4– 7 (m) 30–36 (i)	2– 60 (l)	50–60 (f) 45 (i) {20– 80 and ~ 12} (j)
Wavelengths (km)	170 (k) 1000 (c)	200–250 (b) 90–260 (h)	150–600 (l)	320–360 (f) {350–1000 and ~ 250} (j) 200– 400 (g)
Propagation speeds (km day^{-1})	17S (k) 100S (c)	30–45N (b) 40N (h)	18–36NE (l)	6– 7E (f) {5– 8E and ~20E} (j) 5–10E (g) ~17E (e)
Amplitude r.m.s. (km)	5 (a)	10–25 (a) 10 (m)	15–30 (l)	50–80 (f)
Growth and decay characteristics	Slow growth compared to advective time scale (a)	Perturbation at "Charleston Bump" and decay downstream (a, h)	Rapid growth, doubling variance each 50 km (l)	Moderate growth, doubling variance in ~400 km (f)
Comments	Seasonal variation in transport	—	—	Wavelength decreases as amplitude increases downstream (f) Interannual shifts >50 km (f)

Figure 4: Transverse profile of simultaneous electromagnetic velocity measurements in the Gulf Stream at the surface and 100 m depth. (from von Arx, 1974)

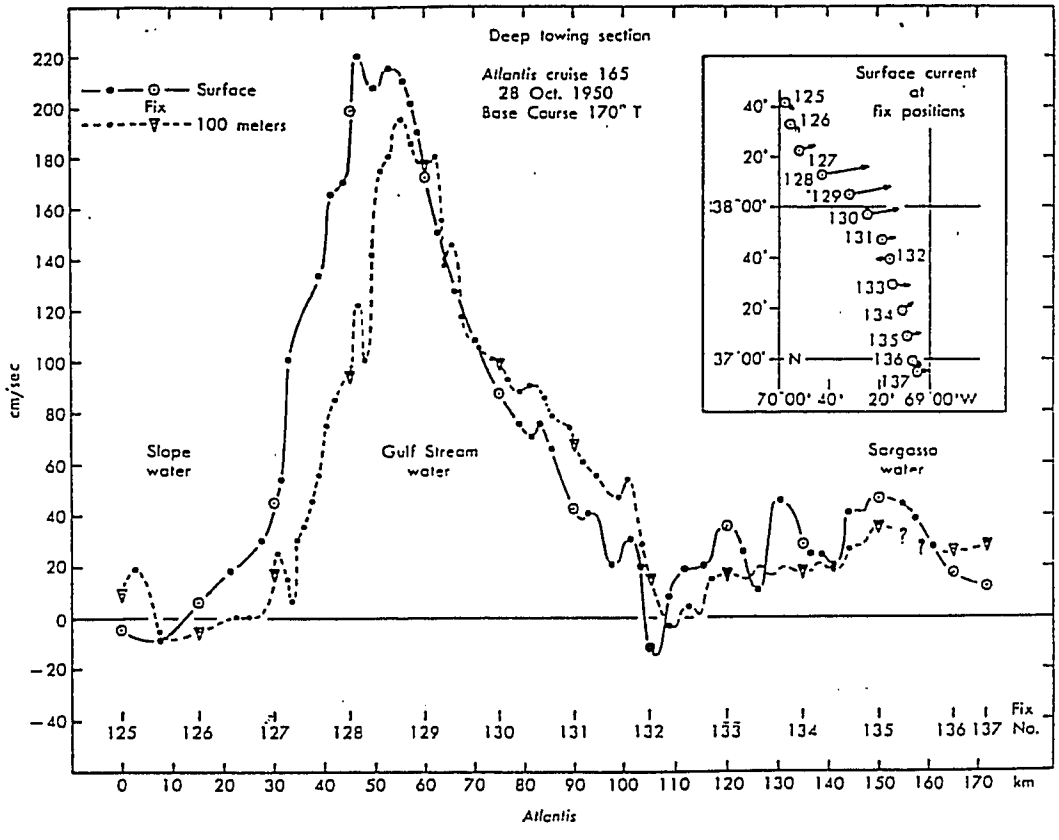

of kilometers. Robinson et al. (1974) has done extensive research on the variability of the Gulf Stream. He determined that the major decay scale is on the order of thousands of kilometers which approximates the length of the Gulf Stream. In addition to the large-scale variability he showed that ring vortex-shedding constituted intermediate-scale variation. Small-scale Gulf Stream variations are on the order of 20-30 *km*, essentially the width of the Stream. The time scales associated with the spatial variability also span a fairly large range. He showed that the time scale values for secular change, large-scale changes and small-scale variations were approximately 13 days, 1 day and 3 days, respectively. Finally, Robinson et al. (1974) noted that much longer time periods would be needed to determine the statistical nature of Gulf Stream dynamics. Other studies also show the large spatial and temporal variability of the Gulf Stream. Richardson (1983a) showed this in a synopsis of several different Lagrangian studies which consisted of SOFAR floats and surface drifters. The large range in spatial and temporal variability has posed problems in the theoretical understanding and interpretation of the nature of the Gulf Stream. Thus, it is important to obtain a clearer understanding of this characteristic in order to study the Gulf Stream.

The Gulf Stream has been the topic of a large number of research projects for the past several decades. These studies have ranged from quantitative analyses of the kinematics and dynamics of the Stream to a more qualitative description of the hydrography. The former is one of the objectives of this research proposal. In the past, only surface drifters or sequential satellite images were used to determine the surface flow of the Gulf Stream (Mullen and Kirwan, 1994). Presently, the information contained in the satellite imagery has very limited use in quantitative analyses and dynamical studies because of the ambiguity in what kinematic surface flow features the images represent.

This research effort will attempt to link drifter and temperature image data to infer near-surface flow kinematics and dynamics. Such an effort is based on the assumption that the surface temperature field is a reasonable surrogate for the flow field streamfunction. Of course, the surface temperature pattern is the result of many processes other than the horizontal flow. These include air-sea sensible and latent heat exchanges, upwelling or downwelling and diffusion. In local regions characterized by strong horizontal flow these other factors may be negligible and so gradients of the surface temperature may be a reliable indicator of the gradients of the streamfunction.

The basic approach will compare the sea surface temperature features from satellite composites with contemporaneous drifter trajectories in order to determine if there is correlation between the two data sets. The geometric properties of the composite thermal features will be used to determine the kinematics and surface flow structure of the Gulf Stream. If this method of analysis of an oceanographic phenomenon proves to be feasible, then the kinematic and dynamic information from the composite images would increase the use of remote sensing in ocean dynamical studies.

Within the past twenty years, oceanographic studies have been enhanced by the use of remote sensing techniques. The satellite sea surface images generated contain enormous amounts of information about oceanic processes. The images have been used to calculate surface flow velocities (La Violette, 1984; Vastano and Borders, 1984 and Svejkovsky, 1988). Unfortunately, such studies have mostly focused on obtaining flow kinematic information by tracking small-scale features in sequential satellite images. The purpose here is to recover flow kinematics and dynamics from a contemporaneous data set of composite images and satellite-tracked drifters to answer the question of what do composite images tell us about surface and sub-

surface flow.

1.2 Background

Most prior studies have employed one of two analyses methods for inferring flow kinematics from satellite imagery. Unlike the focus here, past work concentrated on extracting surface flow information from small-scale features in sequential images. The two methods developed to compute sea surface velocities from sequential images are feature tracking and maximum cross-correlation methods.

Feature tracking is an operator-dependent process in which a small-scale surface feature is isolated and subjectively tracked through a sequence of images. Sea surface velocities are then calculated from the image to image displacement of the feature and the time elapsed between the images. The idea behind this approach is that the feature is passive and merely advected by the flow. La Violette (1984) estimated surface velocities around the Alboran Sea gyre by tracking features in sequential Advanced Very High Resolution Radiometer (AVHRR) and Coastal Zone Color Scanner (CZCS) imagery. Vastano and Borders (1984) used this method with an interactive algorithm to track submesoscale features in the western North Pacific. A verification study of this procedure was undertaken along the California coast by Svejkovsky (1988). By using CZCS, AVHRR and calculated surface velocities from the images differed by a rms of 0.06 $m\ s^{-1}$ from the drifter velocities (Svejkovsky, 1988).

Although feature tracking has provided important contributions there are several problems with this procedure. The variability in cloud cover and thermal contrasts between images sometimes prevents the tracking of the most prominent and interesting surface feature (Mullen and Kirwan, 1994). Many features are surface

expressions of evolving energetic dynamical processes. Thus, evolutionary processes within the feature can hinder the selection, tracking and interpretation of surface patterns. Another difficulty with this approach is that only velocity values for small-scale features can be calculated. Thus, only a small portion of the entire data set available is used. Yet another major weakness is that the selection and tracking of a surface feature is subjective. This can cause operator induced variations in tracking and velocity calculations for a specific feature. Also, movement along temperature fronts is undetectable.

To overcome operator subjectivity, an objective approach for inferring flow was developed, the maximum cross-correlation method (MCC). This uses successive pairs of images. The MCC method selects a template box in the first image and a study area in the second image for the analyses. Once the template box and the point of interest (x,y) have been determined, then two-dimensional cross-correlation coefficients between this point and all points within the search area of the second image can be computed (Kamachi, 1989). The maximum value shows where the feature has moved from image one to image two. The velocity of the surface feature can then be calculated from the location of the maximum cross-correlation coefficient and the time elapsed between the successive images. Emery et al. (1986) first applied the technique to follow oceanographic surface features in sequential satellite images. They compared the calculated MCC velocity data with the surface current of the British Columbian coastal ocean. The determined velocities proved to be qualitatively consistent with the drifter data. Very short time intervals yielded the best results for the velocity field. It was also shown that as the separation between the images increased, the accuracy of the velocity field calculations diminished. Tokmakian et al. (1990) used the MCC method to estimate sea surface velocities along the Northern California coast from sequential AVHRR and CZCS imagery. Their research showed that the MCC method was successful in determining the

velocity field in some cases, but not in others. The most successful results were obtained through averaging several AVHRR velocity fields.

Although it is objective, there are several problems with the MCC method. The process uses a statistical-based feature recognition package to track a surface pattern, resulting in the question of whether the feature tracked is unique and identifiable. Non-advective processes cause the MCC method to break down. Deformational and rotational changes of surface features, which constantly occur in the oceans, can not be detected by the MCC method. Other evolutionary changes cause a deterioration in the correlation. As pointed out when using the feature tracking method, movement along temperature fronts also is undetectable here. Finally, the size of the search areas is small, which limits the amount of available data to be used.

1.3 Approach

Surface feature tracking and the MCC method have proven to be useful and important in obtaining near surface velocities for oceanographic phenomenon. However, due to the many problems encountered using these two methods, an alternate approach for inferring surface flow kinematics and dynamics from satellite imagery may be in order. One such approach would be to utilize satellite composite images in conjunction with feature models to obtain near-surface and surface flow information.

A composite is a weighted average of a sequence of images. Compositing of images produces a higher quality picture and decreases the number of images to be analyzed. Unlike small-scale feature tracking, composite images utilize a large portion of available data. Despite the advantages of composite imagery, there are some possible disadvantages in its utilization.

One drawback in the use of composite images to observe sea-surface temperature patterns is the possibility that image artifacts may be produced during the processing. The compositing can create surface spatial structures which may not otherwise be found within a certain oceanographic region. Because of this possibility, care must be taken in interpreting SST patterns. The focus here is to determine whether or not the problems encountered are as extensive and numerous as those encountered in the MCC and feature tracking methods. If problems encountered are minimal, then the use of composite images could be a very important contributor in the study of surface flow kinematics and ocean dynamics.

Apparently very little, if any, research has been done to test the applicability of composite imagery to oceanography. This study is the first to do so with contemporaneous surface flow data. Specifically, the sea surface temperature features and the contemporaneous drifter trajectories will be compared in order to determine the correlation between the two data sets. The comparisons would be made over similar geographic and temporal scales. The approach here is to determine how well large-scale composite features are correlated with oceanic surface flow. Once the time scales that show the best agreement between the drifter and composite data have been determined, spectral and fractal analyses will be carried out.

Fractal analysis will be used to determine the geometric properties of the drifter paths and composite temperature fronts. The geometric property calculated for this research will be the fractal dimension, which is the measure of the fractality of a geometric object. Fractal dimensions have been used to explain ocean mixing and diffusivity (Sanderson and Booth, 1991). Moreover, there is a close relationship between the fractal character of a signal and its power spectrum. The fractal dimension of a space curve implies a power-law dependence of its power spectrum. In contrast, the power-law dependence does not necessarily imply fractal behavior.

However, it can be used as an indicator of possible fractal behavior.

Spectral analysis techniques will be applied to this contemporaneous Gulf Stream data set. This analysis method will determine the dynamical implications of calculating spectral properties of the Gulf Stream path variability. It will be the technique used to quantify the variability of the Gulf Stream.

One goal of this research is to try to relate some quantifiable features of observations to oceanic dynamical processes by also quantifying these two approaches. In pursuit of this goal, these methods will be used to determine whether the two data sets display the same geometric properties. If the composite images and drifter trajectories do display similar geometric properties, then is there merit in just researching composite images to infer near-surface and sub-subsurface flow phenomenon? Will the drifter trajectories prove to be an important indicator of the thermal features of the composites? The geometric properties of the composite thermal features will be used to determine the kinematics and surface flow structure of the Gulf Stream. If this method of analysis of an oceanographic phenomenon proves to be feasible, then the kinematic and dynamic information from the composite images could be an important quantitative tool for ocean dynamical studies. Moreover, the approach could be applied to other regions where satellite imagery is available.

1.4 Research Questions

The following is a list of the questions which will be addressed in this study.

- Is it possible to relate quantifiable features of composite images to oceanic processes?
- Can the spectral and geometric properties of the contemporaneous data set be used to quantify the variability of the Gulf Stream?

- Are the calculated geometric (fractal) properties of large-scale composite features and corresponding time and space scales sufficient enough to infer near-surface flow?

A brief overview of the available data and methods utilized is described in Chapter 2. Descriptions of the kinematic and dynamic models implemented in this study are discussed in Chapter 3. A summary of the results obtained from the analyses is addressed in Chapter 4. The observations made and kinematic analysis of the data are explained in Chapter 5. Chapter 6 focuses on the results of the kinematic model and the dynamic model results can be found in Chapter 7. Some conclusions and future questions are discussed in Chapter 8.

2 Methods

Aristotle taught me to fix my judgement on that which is grounded upon reason, and not on the bare authority of the master.
Galileo Galilei

This chapter first describes the contemporaneous data set of drifters and satellite imagery. Following this description, the two analyses methods used to study this unique data set are discussed. These methods are fractal and statistical analyses. Fractal analysis will be used to determine the geometric properties of the drifter paths and composite temperature fronts. Statistical analysis will look at the power spectra of the data.

2.1 Composite Satellite Image Data

The infrared satellite imagery was collected by the advanced very high resolution radiometer (AVHRR) aboard the NOAA-9 satellite. This polar-orbiting satellite flies over the east coast of the United States twice a day. Because the NOAA-9 AVHRR system has three infrared channels, one short and two long, sea surface temperatures (SST) can be determined for both the night and day passes. The AVHRR data from NOAA-9 overlaps a set of drifter data by one year: 1985-1986.

The AVHRR data was received and processed by Dr. Otis Brown's group at the Rosenstiel School of Marine and Atmospheric Science (RSMAS) of the University

of Miami. Many steps were undertaken to process the data. The images were subsampled so that every fourth pixel in every fourth array was kept, giving a spatial resolution of about 4 *km*. The SST was determined by measuring the infrared radiation from the ocean, with corrections for atmospheric effects. Since the view from the satellite changes with each orbit, the images were remapped to an area between 85-62°W longitude and 22-42°N latitude. Also, cloud screening was applied to the remapped SST images to reduce the amount of cloud cover.

The next major processing step was to produce 5-day composites from a set of sequential images. A composite is a weighted average of a sequence of images. For each pixel of the five sequential images, the warmest SST was kept, thus decreasing the cloud cover. It is reasonable to create SST composite images because the surface temperature does not change that drastically within five days for the oceanographic space scales researched (Mullen and Kirwan, 1994). After the composites were formed, they were subjected to a second cloud screening. Finally, the SST fields were smoothed for each composite by applying a 3-by-3 pixel median filter. The final spatial resolution produced from processing the image data is 4 *km*. A more detailed description of the image data processing is discussed in Brown (1989).

The result of this is a slightly smoothed five day composited data set of the AVHRR images. For this AVHRR data set, five days is the minimum composite period. For periods less than five days, cloud cover combined with at most two images per day during the composite period inferior images tend to be produced.

The question arises as to whether a longer composite period is more appropriate. This was investigated early in the study. Ten, fifteen and thirty day composites were compared with appropriate drifter trajectories. Generally, these comparisons were not encouraging. With the longer composite periods the drifter typically traveled more than 10^3 *km* and thus, sampled a large portion of the Gulf Stream posi-

tion. This tended to obscure the local dynamical connections which were the focus of this study. All in all for this study, the five day composite period appears to be a reasonable compromise of competing effects.

2.2 FACTS Drifter Data

The surface drifters used in this study were deployed in 1984 as part of the Florida Atlantic Coast Transport Study (FACTS). The drifters consisted of a PVC pipe approximately 3 m in length and 10 cm in diameter with a dampener at the bottom. A 50 cm protrusion above the sea surface enabled the drifters to be easily tracked by Service ARGOS using the TIROS/NOAA random access receivers. Because the surface area of the drifter above the sea surface is very small, the wind effect on the drifter is negligible. Therefore, windage is not considered a problem in the analysis of the drifter data. A detailed description of the satellite-tracked buoys is discussed in Maul (1985). Complete discussion of the FACTS surface drifter paths can be found in FACTS study (1986).

All drifters were deployed 70 nm southeast of Cape Canaveral at 28°N latitude and 80°W longitude. They were positioned at the 75 m isobath. A single undrogued buoy was released each month from April 1984 to March 1985. This drifter data set generally coincides with that of the infrared satellite images.

The drifter and composite image data only overlap by one year. Considerable effort was made to obtain 1984 AVHRR imagery of the North Atlantic from NOAA/NESDIS. However, all attempts to retrieve this data were unsuccessful. Therefore, analyses were undertaken for only the data set described above.

2.3 Fractal Analysis: Yardstick Method

A fractal is any "geometric object whose shape is irregular and/or fragmented at all scales" (Osborne et al., 1989). In other words, the object is self-similar at different length scales. Self-similarity is a quality of a structure where the geometry on one length scale corresponds to the geometry at another (Moon, 1987).

The fractal dimension is the measure of the dimension of the fractal, which can be a non-integer. A fractal curve is irregular at all length scales, exhibiting small or large scale wiggles at any length (Osborne et al., 1989). Thus, one can determine the fractal dimension of any fractal curve. The data available for this research represents spatial curves which are most probably fractal curves. Therefore, their geometric properties may be determined from any fractal analyses method.

Fractal analysis is an analysis tool of the Dynamical Systems Theory. It is one of several tools used to study dynamical systems. There are also several different methods used in fractal analysis. One such method calculates the scaling exponent of a data set. This method determines the scaling properties and fractal dimension of a monofractal curve. Grassberger and Procaccia's (1983) method to calculate the correlation function of a time series can be applied to a monofractal space curve. The dimension calculated for a fractal curve by this procedure is called the correlation dimension (Osborne et al., 1989). It is obtained by determining the slope of a log-log plot of the correlation function. Both the yardstick and correlation dimension methods give spatial information about the space curve, while the scaling exponent method provides temporal information (Osborne et al., 1989). These three methods generally produce the same value for the fractal dimension for any monofractal space curve.

For this particular study the yardstick method was deemed to be the best

approach in finding the fractal dimension of a self-similar fractal curve (Mullen and Kirwan, 1994). The yardstick method gets its name from the length of the division, "yardstick", used to follow the space curve (see Mandelbrot, 1967, 1977, 1982). The approximate length of the space curve is determined by the relationship

$$L(\Delta) \approx \lim_{\Delta \to 0} \Delta^{(1-D)}, \tag{2.3.1}$$

where Δ is the yardstick length and D is the fractal dimension.

A certain length, delta, is used to walk along the space curve. As the delta is stepped along the curve, each new step starts where the previous one left off. Eventually by stepping the delta length along the curve, the number of delta steps will reach the end of the trajectory. Thus, the approximate length of the curve can be determined by multiplying the delta length by the number of steps made along the curve. For each delta value there is one corresponding approximate length. It is known that as the length of the yardstick decreases the approximate length of the curve increases without limit. But, with this type of data set the length of the curve can never be greater than the "true" length of the trajectory. In other words, it does not increase without limit and the approximate delta lengths will not obtain enormous values.

There are two limiting cases for the value of the fractal dimension, D. When D=0, the length of the curve is proportional to the yardstick length. This occurs for a continuous smooth curve, such as a sin or cos wave. The other limiting case is where D=1. In this case the length of the space curve is proportional to Δ^0. The length is thus independent of Δ. This is an example of the case of a random walk.

Different values can be chosen for the delta length. When a small delta value is chosen, the approximate length of the curve approaches the limiting value that is the true distance of the path. On the other hand, when a very large delta value is

chosen, the measurement process becomes meaningless for a finite trajectory. This is true because the delta length chosen eventually will exceed the span of the path.

By making log/log plots of the yardstick length versus the approximate length of the trajectory, the fractal dimension of the space curve can be calculated. Once the slope of the log/log plot is determined, the following equation is used to calculate the fractal dimension:

$$D = 1 - slope. \tag{2.3.2}$$

as shown by Osborne et al., (1989). Two FORTRAN programs were written to calculate the fractal dimension of any space curve. The first program will be explained below. The second program is exactly the same as the first with only one addition. The addition being that it determines the distance from the last delta step to last point on the original trajectory. This distance will only be a fraction of the chosen delta value. But, it will still be used to calculate the corresponding approximate length of the curve.

The space curves analyzed were the drifter trajectories and composite temperature information from the imagery. The temperature front gradient "line" on the coastal side of the Gulf Stream represents the space curve for the imagery (Mullen and Kirwan, 1994). As an example, the "line" outlining only this side of the 20°C water was labeled the 20°C temperature front. This was done for all temperature divisions for all five-day composite images. This data set is equally spaced in space.

The trajectory data used for this study is equally spaced in time, but not in space. In order to use the yardstick method the data needed to be equally spaced in space. Thus, a linear interpolation needed to be performed in order to achieve this. A delta value was picked to run through the FORTRAN program. After that the distance between the first two points on the original trajectory was calculated. If

this distance were greater than the chosen delta value, then the time, latitude and longitude were calculated for this delta position. Therefore, at every location the delta length was stepped along the curve, three values were recorded; time, latitude and longitude. As stated above, the approximate length was then calculated from the delta value and the number of steps it took along the curve.

A SUN SPARC station IPC was used to do all the data calculations. The FORTRAN program calculations were done in double precision.

The paths of the trajectories have many variations. Some of the paths are very long and curved, while others are very short and straight. Plots were made of the original trajectory with overlays of the calculated delta path. For very small delta values the path of the delta trajectory lies right on the original trajectory (Figure 5). But as the values for the yardstick length get increasingly larger the path of the delta latitude and longitude values fall farther and farther away from the original track (Figure 6). This phenomenon is expected, because as the delta value chosen increases the length of the delta path decreases.

When looking at the plots, Figures 5 and 6, one may expect that every delta point calculated should fall directly on the original trajectory. This is not the case because of the curvature of the path and the method in which the delta positions are calculated. In some instances the position of the delta point may lie on the original path, while in others it may be a small distance from the space curve. The offset of the delta point from the original path depends on the amount of curvature in the original path at that location. If there is a very large curve in the track, then the delta point will be at some distance off of the original track.

Lets take an instance where the next original trajectory point to be observed is located on the forward side of a large curve. The delta point calculated will be

Figure 5: Plot illustrating the "yardstick method" using a "small" delta value, 100 km, along a drifter trajectory. See text for discussion.

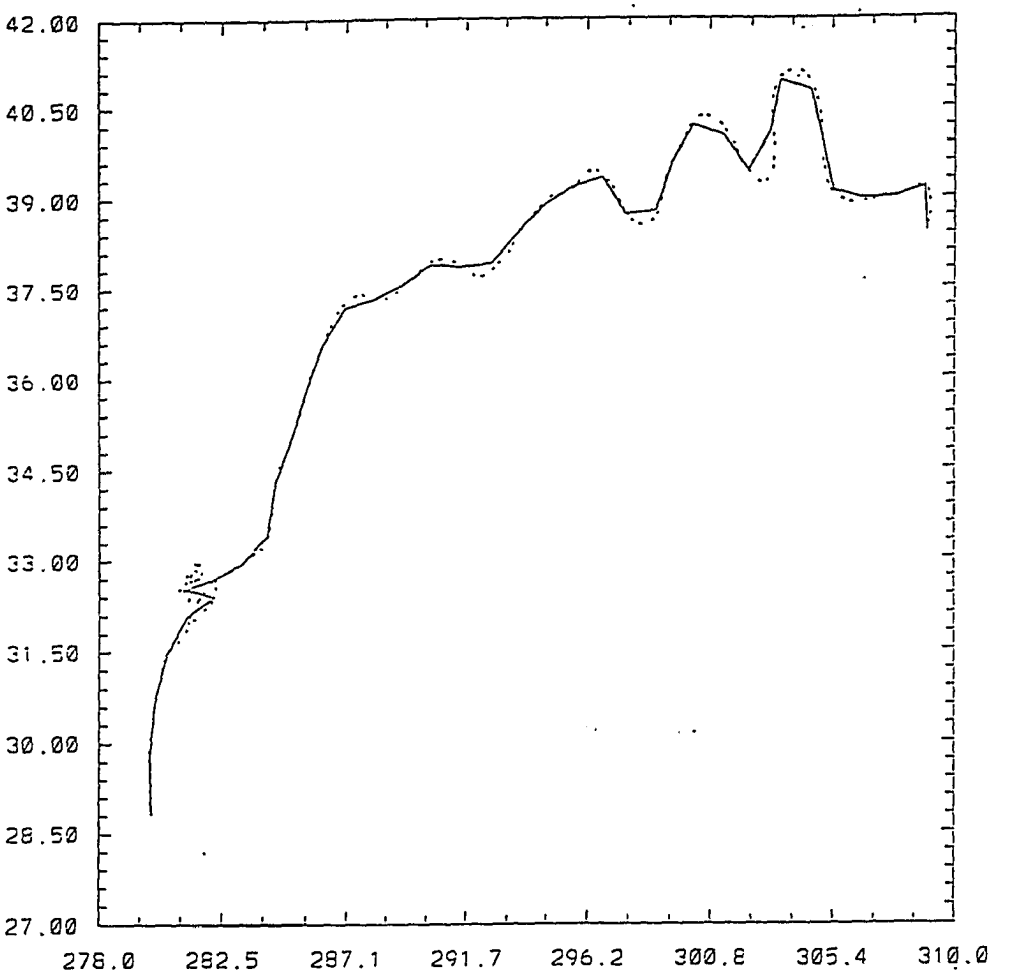

Figure 6: Plot illustrating the "yardstick method" using a "large" delta value, 500 km, along a drifter trajectory. See text for discussion.

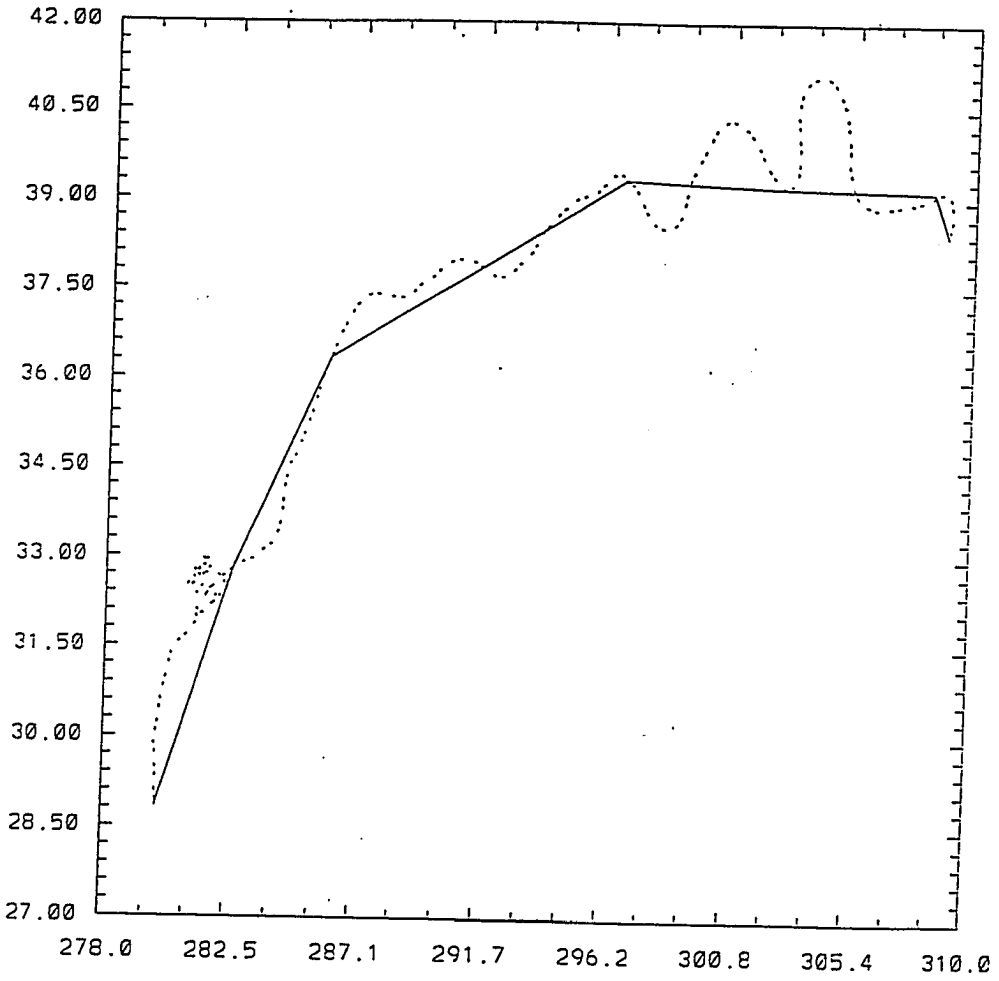

determined by doing a linear interpolation between the previous delta point and the corresponding point on the original curve. This original point is a delta distance away from the previous delta point. The calculations performed by the yardstick method would only involve these two points. Because of this, the remaining portion of the space curve will be neglected in this calculation. Consequently, the new delta point will fall somewhere on the straight line between the two points used for the linear interpolations and not on the original space curve. Therefore, in some cases the delta position calculated may fall next to the original path, but not directly on it.

2.4 Spectral Analysis: Power spectrum

Spectral analysis is the classical statistical technique used to estimate the power spectral density function of a data set. It is basically Fourier analysis with some modifications, so that it can be applied to stochastic functions of time (Chatfield, 1984). The power spectrum represents how the power is distributed with respect to the frequency. The variance of the process is represented by the total area under the curve of a power spectral plot. Peaks within the curve represent an important factor in the variance at that particular frequency or length scale. The Nyquist frequency is the upper bound of the frequency range where we can obtain important information. This value will be represented by $\omega_N = \pi/\Delta t$ because the data set are analyzed at equal intervals in time or space. A fast fourier transform (FFT) spectral analysis algorithm was utilized to calculate the spectra of the evenly spaced data sets. This program requires that there are no breaks in the data set and that the number of points is a multiple of two. Detrending was automatically performed and options were available for several types of smoothing. After some preliminary investigations, it was decided that the raw spectra were most appropriate for this

study. This is consistent with the analysis of Osborne et al. (1989).

There is a close relationship between the fractal character of a signal and its power spectrum, provided that the spectrum has a pure power law, $f^{-\alpha}$, and the Fourier phases are uniformly distributed random numbers (Mullen and Kirwan, 1994). Panchev (1971) shows that the spectral slopes of the latitude and longitude components of their data can be related to its fractal dimension by the following equation:

$$D = min\left[\frac{2}{\alpha - 1}, N\right], \tag{2.4.1}$$

where α is the slope of the spectrum and N is the space dimension. The fractal dimension of a space curve implies a power-law dependence of its power spectrum. In contrast, the power-law dependence does not necessarily imply fractal behavior because the spectrum may not be purely power law and the phases may not be perfectly random. However, it can be used as an indicator of possible fractal behavior. Perfect power-law spectra are not found in experimental data sets, but mathematical fractals do display a perfectly power-law relationship (Osborne et al., 1989).

Power spectral analysis will be applied to the two data sets. Passing the data through a filter can lead to biases in the spectral slope values. Therefore, the values obtained in this paper are from the unfiltered spectra. Power-law spectral plots will be graphed where the best fit line of the least squares fit method was used to determine the slope of the power-law spectrum. Slope values were obtained from the unfiltered spectra. Estimates of the spectral slope using (2.4.1) were also calculated. Henceforth, these spectral slope values will be called observed spectral slope and calculated spectral slope for the former and latter, respectively.

3 Model Descriptions

The sciences do not try to explain, they hardly even try to interpret, they mainly make models. By a model is meant a mathematical construct which, with the addition of certain verbal interpretations, describes observed phenomena. The justification of such a mathematical construct is solely and precisely that it is expected to work.

John von Neumann

This chapter describes the kinematic and dynamic models used in this study. The models are of barotropic meandering jets. The kinematic model was originally developed by Bower (1991) to study fluid exchange surrounding the Gulf Stream. Dutkiewicz et al. (1993) used a modified version of this model to study dispersion in the Gulf Stream region. Neither approach satisfies a reasonable potential vorticity balance, although, such a balance is widely believed to be important in the Gulf Stream. To address this deficiency a non-linear equivalent barotropic model was developed.

These models are quasi-geostrophic in that the velocity field is determined from a streamfunction. As indicated in the introduction, one premise of this study is that locally the surface temperature field is representative of the streamfunction. Thus, the streamfunctions described below are generally indicative of the surface temperature. Since the only data available for comparison is surface data, barotropic models are appropriate. A brief description of each model follows.

3.1 Kinematic Model Descriptions

Bower first introduced a simple two-dimensional kinematic model of a meandering jet in 1991. This model was developed to examine the kinematics of fluid exchange within the Gulf Stream region (Bower, 1991). She compared RAFOS float data with fluid paths in a meandering jet velocity field. This velocity field was represented by a uniform width jet which was deformed by an eastward propagating sinusoidal meander (Samelson, 1992). By analyzing the streamfunction field in a moving reference frame, Bower calculated the fluid trajectories relative to the wave pattern. Her model restricts the particles to move only along streamlines in the translating frame. The velocity fields illustrated in Bower (1991) represent an idealized scenario of a steadily propagating fixed wave pattern. However, the Gulf Stream is not a fixed wave pattern propagating in only one direction. It is constantly evolving over all time and space scales. Because of this fact, it is understandable why Bower's model fails to depict all aspects of the observed trajectories (Samelson, 1992). Moreover, this model has no dynamical aspects and thus, does not satisfy a potential vorticity balance for the Gulf Stream system.

Dutkiewicz et al. (1993) developed a kinematic model similar to Bower (1991) to examine turbulent mixing within the Gulf Stream. They note that Bower's kinematic model qualitatively displays the mixing processes of the Gulf Stream, but, lacks the necessary physics to explain the diffusion of particles across the jet. To overcome the limitations of Bower's model, Dutkiewicz et al. (1993) incorporated an additional velocity field which is represented by small-scale turbulence. This allows particles to cross streamlines in the translating frame. The portion of Dutkiewicz et al.'s model which will be addressed in this study represents only the deterministic velocity field of the meandering jet and does not include the turbulent velocity field. Again, it is important to note that this model also does not satisfy a potential

vorticity balance.

Both models are oriented on the x, y plane where x is positive eastward and y is positive northward. The meandering jet pattern propagates to the east. The two models have similar streamfunction representations. The similarities include a reference scale, Ψ_o, used to determine the maximum downstream velocity of 120 $cm\ sec^{-1}$. Both models prescribe center streamlines by $y_c = Asin(k_x(x - c_x t))$, where A is the amplitude, k_x is the wavenumber of the meanders and c is the phase speed. Here the quantities are fixed by observations. The particle trajectories $x(t)$ and $y(t)$ can be determined by the integration of

$$u = -\frac{\partial \Psi}{\partial y} = \frac{dx}{dt}$$

$$v = \frac{\partial \Psi}{\partial x} = \frac{dy}{dt}. \tag{3.1.1}$$

where u is the x component of the vector velocity $\mathbf{U}$, and v is the y component.

The streamfunction pattern used by Bower (1991) is represented by the following equation:

$$\Psi(x, y, t) = \Psi_o \left\{ 1 - tanh \left[\frac{y - y_c}{w/cos(\alpha)} \right] \right\}, \tag{3.1.2}$$

where $\alpha = tan^{-1}(Akcos(k(x - c_x t)))$ specifies the current direction and w is the scale width of the jet. The $cos(\alpha)$ term gives the meandering jet a uniform width throughout the field. For convenience Bower (1991) transformed the streamfunction field into a translating field in which the time dependence is implicit. However, here it is more convenient to use a fixed reference frame in which the streamfunction field and trajectory patterns evolve in time. Henceforth, this model will be referred to as BM91.

The streamfunction field for Dutkiewicz et al. (1993) kinematic model is

$$\Psi(x, y, t) = \Psi_o tanh \left(\left(\frac{\pi}{w} \right) (y - y_c) \right) + \zeta sin(k_y y), \tag{3.1.3}$$

where $k_y = 2\pi/4A$. Dutkiewicz et al. (1993) added the ζ term in order to model the recirculation which occurs within the meander bend region. By demanding that the maximum recirculation speed in the meander bend region be $1cm\ sec^{-1}$, the ζ term can be easily calculated. As with BM91, the *tanh* term provides the meandering jet shape of the Gulf Stream. Dutkiewicz et al. (1993) also utilized a translating streamfunction field, which as just stated, is not used here. The Dutkiewicz et al. (1993) model will be referred to as DM93.

As stated earlier there are some similarities between the two kinematic models, but there are also some distinct differences. The y_c parameter is the same. The π/w parameter in DM93 model corresponds to $1/w(cos(\alpha))$ in BM91. Recall that in BM91 the $cos(\alpha)$ term gives the jet uniform meander width. Since w is constant in DM93 that model has a variable jet meander width. Also with BM91, the Ψ_o term is constant. However, DM93 has an additional term of $\zeta sin(k_y y)$ which is a slowly varying function of y. As stated earlier this produces a weak recirculation in DM93.

Figure 7 illustrates some of the physical differences between the two models. As one can see, the meandering jet in DM93 shows spreading of the streamlines at the crests and troughs and thinning in the "straight" regions of the jet. This figure also illustrates a uniform width jet for BM91.

3.2 Dynamic Model Description

In order to incorporate some dynamics of the Gulf Stream region an equivalent barotropic PV model was developed. With the same coordinate system as BM91 and DM93, the governing equation is:

$$\frac{\partial q}{\partial t} + J(\Psi, q) = \sigma(x, y, t). \tag{3.2.1}$$

Figure 7: A diagram showing the physical differences between the two kinematic models. Dutkiewicz et al. (1993) is represented by the THICK streamlines and the streamlines for Bower (1991) are THIN.

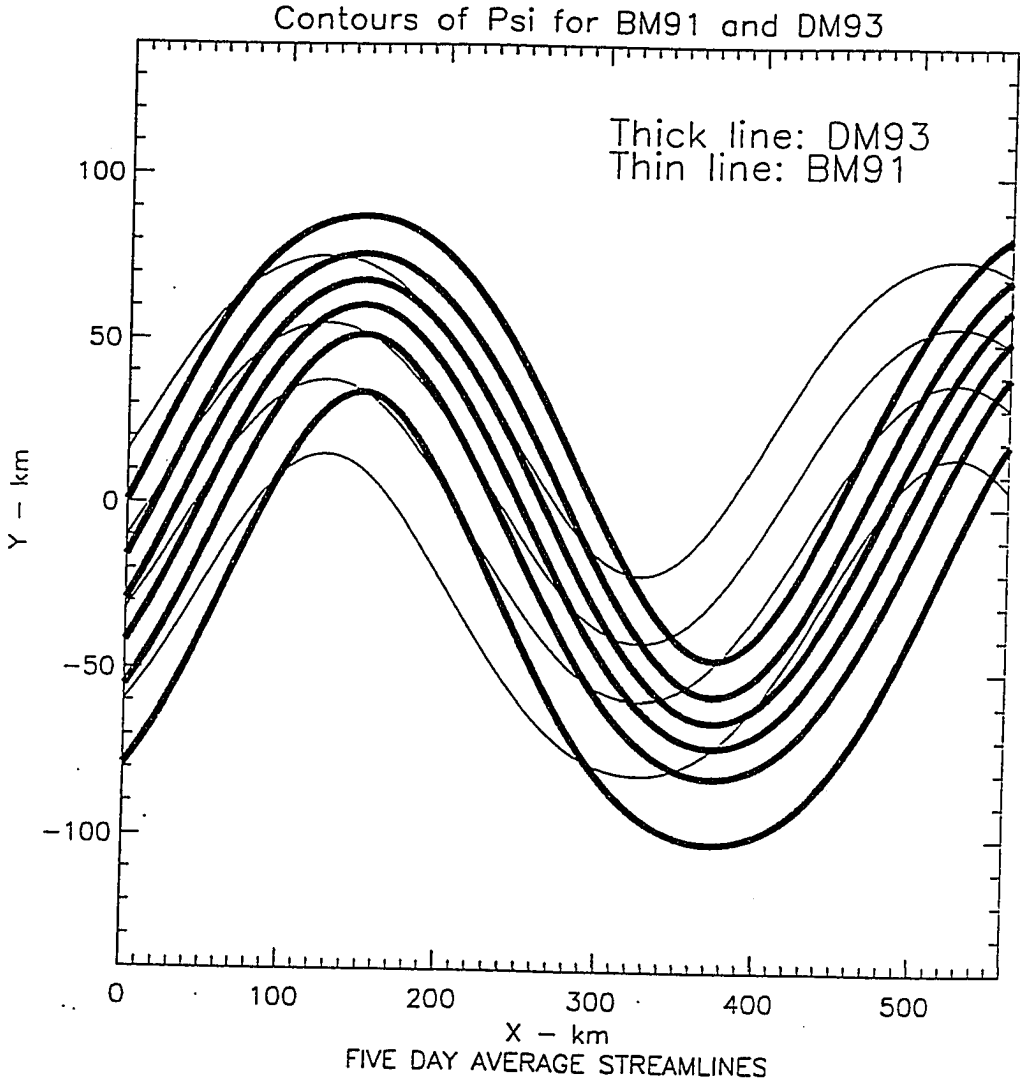

Here, q is the potential vorticity and is represented by

$$q = \nabla^2\Psi - \left(\frac{1}{r_d}\right)^2 \Psi + \beta y, \tag{3.2.2}$$

where and the streamfunction is Ψ. Also, r_d is the radius of deformation, f is the Coriolis parameter and $\beta = \partial f/\partial y$ represents the constant beta effect. Finally, σ is as yet an undetermined potential vorticity source.

Sources are unusual in potential vorticity models. The need for this term arise because the solutions developed here are discontinuous in potential vorticity. The source provides the jump in potential vorticity required as a particle transits the discontinuous potential vorticity regions. The source term has no effect on Ψ, since it and its first derivatives are continuous everywhere.

Solutions to (3.2.1) are to be obtained in the form

$$q(x, y, t) = q(x - ct, y),$$

$$\Psi(x, y, t) = \Psi(x - ct, y).$$

Substituting these forms into (3.2.1) the following relationship is produced

$$J(\Psi - cy, q) = \sigma(x, y, t). \tag{3.2.3}$$

Solutions to (3.2.3) will be developed for

$$q = \sum_{i=1}^{4} \Gamma_i(\Psi - cy) H_i(\gamma_i y + \beta_i) \tag{3.2.4}$$

where the Γ_i are analytic functions and H is the Heavyside step function

$$H(z) = \begin{cases} 1 & z > 0 \\ 0 & z < 0 \end{cases}$$

Here, $\alpha = \Psi - cy$. This form of the solution is consistent with an underlying premise of the study; namely that locally the temperature field represents the streamfunction. Eq (3.2.4) states that the relation between the temperature field and the streamfunction is different in different parts of the meandering Gulf Stream region.

Substitution of (3.2.4) into (3.2.3) gives

$$\sum_{i=1}^{4} J(\Psi - cy, \Gamma_i) H_i + \sum_{i=1}^{4} \Gamma_i J(\Psi - cy, H_i) = \sigma \tag{3.2.5}$$

Since

$$J(\Psi - cy, \Gamma_i) \equiv 0, \tag{3.2.6}$$

it is inferred that

$$\sum_{i=1}^{4} \Gamma_i J(\Psi - cy, H_i) = \sigma. \tag{3.2.7}$$

Note that (3.2.7) involves derivatives of the step function which are known to be the unit impulse or delta function. This means that the source function, σ, is composed of a sequence of delta functions.

To specify the Γ_i, solutions are sought for three separate regions. These include the Inner region, Outer: Upper region and the Outer: Lower region (see Figure 8). The Inner region is the portion of the model which pertains to the meandering jet, which is the main feature of the model. Both outer regions represent recirculation patterns. Clearly, the Outer: Upper region corresponds to the area north of the Gulf Stream, while the waters to the south (Sargasso Sea) are designated by the Outer: Lower region. Thus, take

$$\Gamma(\Psi - cy) = -\chi^2(\Psi - cy) + Q_i$$

in the Inner region $y \leq |A/2|$,

$$\Gamma(\Psi - cy) = Q_u$$

for the Outer: Upper region $y \geq A/2$, and

$$\Gamma(\Psi - cy) = Q_l$$

for Outer: Lower $y \leq -A/2$.

Figure 8: Diagram illustrating the three regions for the equivalent barotropic PV model. The regions are Inner, Outer Upper and Outer Lower.

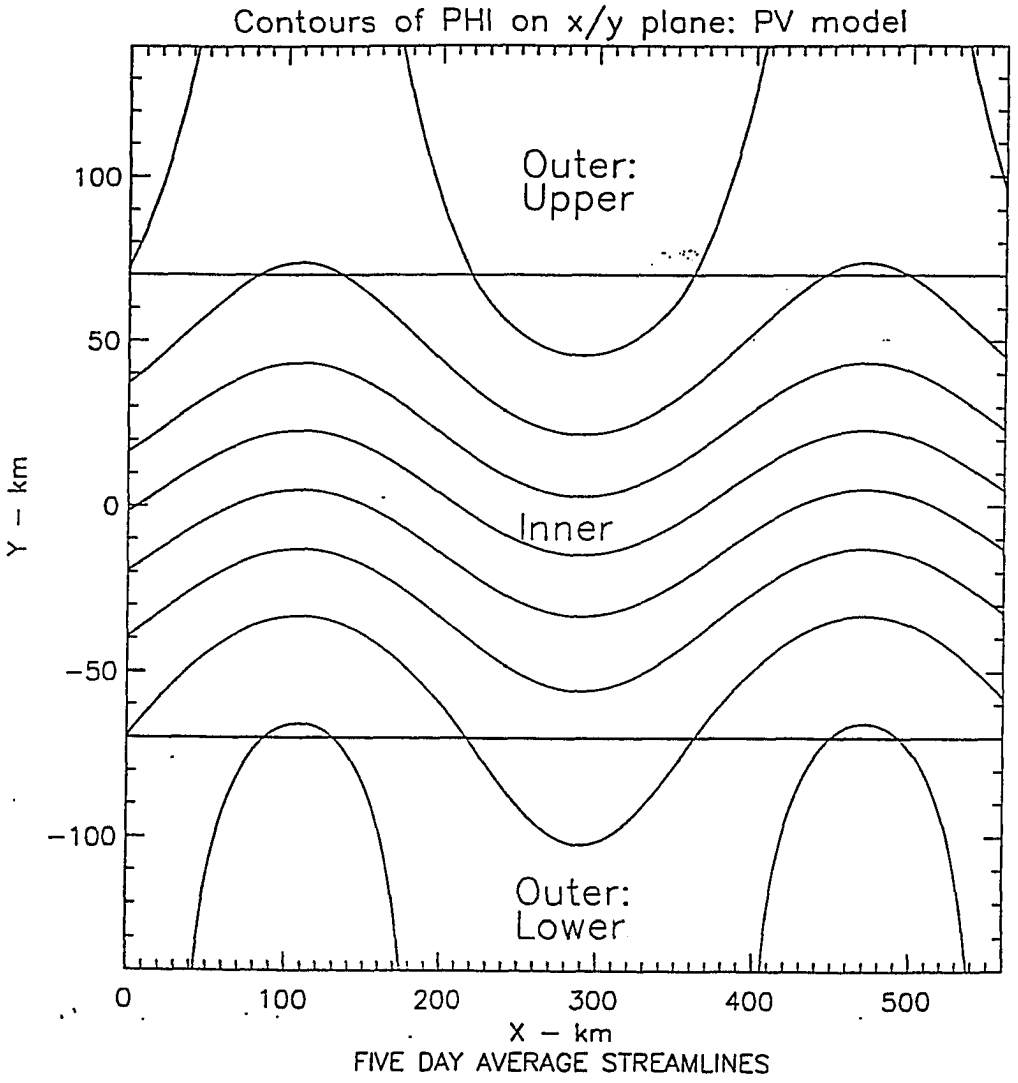

In view of the above, the compact representation of the potential vorticity, q, is

$$q(\alpha) = Q_l H\left(\frac{-A}{2} - y\right) + Q_u H\left(y - \frac{A}{2}\right) + (-\chi^2\alpha + Q_i)\left(H\left(y + \frac{A}{2}\right) - H\left(y - \frac{A}{2}\right)\right). \tag{3.2.8}$$

Substitution of (3.2.8) into (3.2.7) gives

$$\sigma(x - ct, y) = -\left[\frac{\partial\alpha}{\partial x}\Gamma(\alpha)\right]\left[-Q_l\delta\left(\frac{-A}{2} - y\right) + Q_u\delta\left(y - \frac{A}{2}\right) + \left(-\chi^2\alpha + Q_i\right)|_{y=-A/2}\delta\left(y + \frac{A}{2}\right) - \left(-\chi^2\alpha + Q_i\right)|_{y=A/2}\delta\left(y - \frac{A}{2}\right)\right]. \tag{3.2.9}$$

Here δ is the unit impulse generalized function; i.e.

$$\frac{dH(z)}{dz} = \delta(z).$$

An important consequence of this last equation is that potential vorticity is not conserved for particles that enter or leave the region given by $-A/2 \leq y \leq A/2$. Thus, if a particle originally in the Gulf Stream were to wander out into the Sargasso Sea, as it can in DM93, it would undergo a jump change in its potential vorticity appropriate for that region. Similarly if a particle in the Sargasso Sea were to be entrained by the Gulf Stream, then it also would undergo a jump change in its potential vorticity appropriate for the Stream.

Solutions in the form

$$\Psi(x, y, t) = Y(y) + \lambda G(y) S(k(x - ct)), \tag{3.2.10}$$

are sought. This form was motivated by the kinematic models and thus, has a simple physical interpretation. A steady background flow is represented by Y while λGS describes the meander perturbation. Also, S is a function to be specified shortly.

From (3.2.8)

$$\nabla^2\Psi = k^2G(y)S_{xx} + G_{yy}S + Y_{yy} \tag{3.2.11}$$

is obtained, where $k = 2\pi/L$ is the wavenumber with L as the wavelength. Using this result and (3.2.10) in (3.2.2) gives

$$q = k^2G(y)S_{xx} + [G_{yy} - \left(\frac{1}{r_d}\right)^2]S + Y_{yy} - \left(\frac{1}{r_d}\right)^2 Y + \beta y.$$

This can be reduced further by requiring $S_{xx} = -S$, or S is sinusoidal.

For the Inner region the equation to solve is

$$[G_{yy} + (\chi^2 - \left(\frac{1}{r_d}\right)^2 - k^2)G]S + Y_{yy} + [\chi^2 - \left(\frac{1}{r_d}\right)^2]Y -$$

$$(\chi^2 c - \beta)y - Q_i = 0. \tag{3.2.12}$$

The Lower region has an equation of the form

$$[G_{yy} - (k^2 + \left(\frac{1}{r_d}\right)^2)G]S + Y_{yy} - \left(\frac{1}{r_d}\right)^2 Y - Q_l = 0. \tag{3.2.13}$$

Finally, for the Outer: Upper region the following relationship exists

$$[G_{yy} - (k^2 + \left(\frac{1}{r_d}\right)^2)G]S + Y_{yy} - \left(\frac{1}{r_d}\right)^2)Y - Q_u = 0. \tag{3.2.14}$$

Note that in each region the equations are of the form

$$L_1(G)S + L_2(Y) = 0. \tag{3.2.15}$$

For the Inner region:

$$L_1 = \frac{d^2}{dy^2} + (\chi^2 - \left(\frac{1}{r_d}\right)^2 - k^2)$$

$$L_2 = \frac{d^2}{dy^2} - (\chi^2 - \left(\frac{1}{r_d}\right)^2)$$

and for the Outer regions:

$$L_1 = \frac{d^2}{dy^2} - (k^2 + \left(\frac{1}{r_d}\right)^2)$$

$$L_2 = \frac{d^2}{dy^2} - \left(\frac{1}{r_d}\right)^2.$$

Since S is a function of x and t, the only way for (3.2.12) to be satisfied is for $L_1(G) = L_2(Y) = 0$.

There are discontinuities in the three regions. Therefore, smoothness conditions are necessary. All coefficients are determined by requiring continuity of Ψ, $\partial\Psi/\partial x$ and $\partial\Psi/\partial y$ at the boundaries of the three regions. Continuity of $\partial\Psi/\partial x$ and $\partial\Psi/\partial y$ means that the velocities at the boundaries must be continuous. Since the derivatives of both the Y and G portions must be smooth at the upper and lower boundaries of the inner regions, "patches" are required at $y = -A/2$ and $y = A/2$.

The variables for the following equations are L, the wavelength of the meander; k, the wavenumber; c, the phase speed; r_d, the radius of deformation; A, the amplitude; M, the maximum distance of meander; β, the meridional gradient of the Coriolis parameter; U, the velocity ; and $\gamma = \pi/5A$.

Concentrating first on the Y portion of the Inner region, the solution to (3.2.9) is

$$Y_i = A_i sin(\alpha y) + B_i cos(\alpha y) + \frac{(\chi^2 c - \beta)y + Q_i}{\alpha^2}.$$

The coefficients A_i and B_i are obtained by focusing on the u velocity equations for the inner region. The velocity relationship for only the Y portion is $U_i = -dY_i/dy$. Here, U represents the u velocity for the Y portion only with the subscript representing the region of interest. Differentiation results in:

$$U_i = -\alpha\left[A_i cos\left(\alpha y\right) - B_i sin\left(\alpha y\right)\right] - \frac{\chi^2 c - \beta}{\alpha^2}. \qquad (3.2.16)$$

By solving this equation for the conditions at the upper and lower boundaries of the inner region yields

$$U_i\left(\frac{-A}{2}\right) = U = -\alpha A_i cos\left(\frac{\alpha A}{2}\right) - \alpha B_i sin\left(\frac{\alpha A}{2}\right) - \frac{\chi^2 c - \beta}{\alpha^2} \qquad (3.2.17)$$

and

$$U_i\left(\frac{A}{2}\right) = U - \delta = -\alpha A_i cos\left(\frac{\alpha A}{2}\right) + \alpha B_i sin\left(\frac{\alpha A}{2}\right) - \frac{\chi^2 c - \beta}{\alpha^2}. \qquad (3.2.18)$$

Subtracting (3.2.17) from (3.2.18), the coefficients obtained are

$$A_i = \frac{-U + \delta/2 - (\chi^2 c - \beta)/\alpha^2}{\alpha cos\left(\frac{\alpha A}{2}\right)}$$

and

$$B_i = -\frac{\delta}{2\alpha sin\left(\frac{\alpha A}{2}\right)},$$

where

$$\alpha = \sqrt{\chi^2 - \left(\frac{1}{r_d}\right)^2} > 0.$$

For G Inner, the relationship is defined in terms of cosines

$$G_i = cos(\gamma y),$$

where $\gamma = \pi/5A$.

The Y portion for the Upper and Lower regions are defined in terms of sinh and cosh. Y Upper is

$$A_u sinh\left(\frac{y}{r_d}\right) + B_u cosh\left(\frac{y}{r_d}\right) - Q_u r_d^2$$

while Y Lower is presented by

$$A_l sinh\left(\frac{y}{r_d}\right) + B_l cosh\left(\frac{y}{r_d}\right) - Q_l r_d^2.$$

Again the coefficients are obtained by solving the relationship $-dY/dy$. The velocity for the lower region is

$$U_l = U = -\frac{dY}{dy} = -\left(\frac{1}{r_d}\right)\left[A_l cosh\left(\frac{y}{r_d}\right) + B_l sinh\left(\frac{y}{r_d}\right)\right]. \qquad 3.2.19$$

To meet the required boundary conditions, (3.2.19) must match U_i at $y = -A/2$ and it must be equal to zero at $y = -M/2$. This will insure a recirculation pattern

in the lower region. By applying the above criteria to (3.2.19), the coefficients for the lower region become

$$B_l = \frac{-Ur_d}{cosh\left(\frac{A}{2r_d}\right) tanh\left(\frac{M}{2r_d}\right) - sinh\left(\frac{A}{2r_d}\right)},$$

and

$$A_l = B_l tanh\left(\frac{M}{2r_d}\right).$$

The U velocity equation to solve for the upper region is

$$U_u = U - \delta = \left(\frac{1}{r_d}\right)\left[A_u cosh\left(\frac{y}{r_d}\right) + B_u sinh\left(\frac{y}{r_d}\right)\right]. \qquad (3.2.20)$$

Similar conditions apply for determining the coefficients for the upper region, where (3.2.20) equals U_i at $y = A/2$ and zero at $y = M/2$. Thus, the coefficients for this region are

$$B_u = \frac{(U-\delta)r_d}{cosh\left(\frac{A}{2r_d}\right) tanh\left(\frac{M}{2r_d}\right) - sinh\left(\frac{A}{2r_d}\right)},$$

$$A_u = -B_u tanh\left(\frac{M}{2r_d}\right),$$

$$B_l = \frac{-Ur_d}{cosh\left(\frac{A}{2r_d}\right) tanh\left(\frac{M}{2r_d}\right) - sinh\left(\frac{A}{2r_d}\right)},$$

and

$$Al = B_l tanh\left(\frac{M}{2r_d}\right).$$

Finally, the G portions for the Upper and Lower are shown by the following equations and coefficients definitions. G Lower is defined by

$$A_{lg} sinh(\gamma y) + B_{lg} cosh(\gamma y)$$

and G Upper is

$$A_{ug} sinh(\gamma y) + B_{ug} cosh(\gamma y),$$

where

$$A_{lg} = \frac{sin\left(\gamma\frac{A}{2}\right) + cos\left(\gamma\frac{A}{2}\right) tanh\left(\gamma\frac{A}{2}\right)}{cosh\left(\gamma\frac{A}{2}\right) - sinh\left(\gamma\frac{A}{2}\right) tanh\left(\gamma\frac{A}{2}\right)},$$

$$B_{lg} = \frac{cos\left(\gamma\frac{A}{2}\right) + A_{lg}sinh\left(\gamma\frac{A}{2}\right)}{cosh\left(\gamma\frac{A}{2}\right)}$$

and

$$A_{ug} = \frac{sin\left(\gamma\frac{A}{2}\right) + tanh\left(\gamma\frac{A}{2}\right)cos\left(\gamma\frac{A}{2}\right)}{sinh\left(\gamma\frac{A}{2}\right)tanh\left(\gamma\frac{A}{2}\right) - cosh\left(\gamma\frac{A}{2}\right)},$$

$$B_{ug} = \frac{cos\left(\gamma\frac{A}{2}\right) - A_{ug}sinh\left(\gamma\frac{A}{2}\right)}{cosh\left(\gamma\frac{A}{2}\right)}.$$

The coefficients for the G portions were obtained by requiring that the following relationships are satisfied:

$$G_u\left(\frac{A}{2}\right) = G_i\left(\frac{A}{2}\right) \qquad G_l\left(\frac{-A}{2}\right) = G_i\left(\frac{-A}{2}\right)$$

and

$$G'_u\left(\frac{A}{2}\right) = G'_i\left(\frac{A}{2}\right) \qquad G'_l\left(\frac{-A}{2}\right) = G'_i\left(\frac{-A}{2}\right).$$

As stated earlier, the solutions to (3.2.15) for all three regions were obtained by requiring that continuity exists at the boundaries. This model gives a more realistic representation of the Gulf Stream meandering jet and will be termed PVM94 for the remainder of the paper.

4 Results of Analyses

Do you see O my
brothers and sisters?
It is not chaos or death–
it is form, union, plan–
it is eternal life–
it is Happiness.
Walt Whitman

In this chapter, the results obtained from the two analyses methods, fractal and spectral analyses, are presented. These analyses were performed on the contemporaneous data set of satellite-tracked drifters and satellite composite imagery. The first section discusses the fractal analysis results. It explores the relationship between the geometric properties of the drifter trajectories and those of the image temperature fronts. The results obtained from the spectral analyses method are detailed in the last section of this chapter.

4.1 Fractal Analysis

Some recent studies have concentrated on the use of multifractals to analyze different data sets (see, e.g. Schertzer and Lovejoy, 1987; Paladin and Vulpiani, 1987; Osborne et al., 1989). Multifractal properties display different fractal dimensions at different scales. As noted by Mullen and Kirwan (1994), reliable estimates of multifractal properties require large accurate data sets. This means that there is no opportunity, in the present case, to determine any geographic variability in scaling

properties, since it is not feasible to look at multifractal properties for subsets of this data base. Hence, the decision to focus on monofractal properties was made. Consequently, a different approach for analyzing this data was developed in which the Gulf Stream was divided into two distinct geographic regions.

Conventionally, Cape Hatteras is the division point in studying the different regions of the Gulf Stream. The Cape has become this delimiter because south of Hatteras the waters are affected by the topographical beta effect and the meanders are characterized by small amplitudes and wavelengths. To the east of Cape Hatteras, the flow is governed by the planetary beta effect and meanders possess substantially larger amplitudes and wavelengths as compared to the region south of Hatteras. For this study, 37°N and east of 74°W was chosen as the breakpoint between these two dynamically different regions because the focus of the study is to concentrate on the large-amplitude meanders of the Gulf Stream. The region located north of 37°N and east of 74°W will be called GT37 for the remainder of the paper, while south and west of the designated latitude and longitude division will be termed LT37. One of the goals of the research is to see if different dynamics would be reflected in different fractal scaling. This approach is used to answer the question: Is there geographic variability in the data set? Through this analysis it is possible to determine if fractal scaling in the contemporaneous data set shows geographic variability. Multifractal analysis would not make it possible to determine this independence or dependence on geographic location.

The drifter trajectories and temperature fronts are spatial curves which some believe to be fractal. As stated in Chapter 2, the yardstick method was used to determine the fractal nature and scaling ranges of the data sets. The fractal dimension from the yardstick method is calculated by using the power-law relation in (2.3.1) along with (2.3.2). As shown in (2.3.1) for fractal curves, the length of the

curve diverges as the delta length becomes smaller and smaller (Provenzale et al., 1989). Figures 9 and 10 display example plots of curve length versus delta length in kilometers for the drifter data. One can clearly see the divergence of trajectory lengths for small delta values. Within this region, the curves display the relationship shown in (2.3.1) (Provenzale et al., 1989).

By making log/log plots of the yardstick length versus the approximate length of the trajectory, the fractal dimension of the space curve can be calculated. Once the slope of the log/log plot is determined, (2.3.2) is used to calculate the fractal dimension. Figures 11 and 12 give example plots of log delta versus log length for the drifter trajectory data. The slope value used to calculate the fractal dimension of a space curve is determined from the least squares fit line drawn on Figures 11 and 12. The fractal dimension, error and corresponding scaling range are presented in Table 2. The average fractal dimension for all drifter trajectories is $D = 1.21 \pm 0.02$ over a scaling range of 83-343 *km*. All errors are obtained from the statistical errors of the least-squares fit line to the space curves.

The values of both the scaling range and fractal dimension for the drifter trajectories decrease substantially if only the paths which correspond to satellite imagery are observed. Here, the fractal dimension calculated is 1.17 ± 0.02 with a range of scales of 65 - 182 *km*. Table 2 shows that these values are much closer to those calculated for the temperature fronts of the satellite imagery. The fractal dimensions and scaling ranges for the temperature fronts will be discussed in more detail later in this section.

The average value for all drifter trajectories is generally consistent with previous studies (Mullen and Kirwan, 1994). Osborne et al. (1989) applied three different fractal analyses methods on three drifters deployed in the Kuroshio extension in

Figure 9: Delta length versus curve length for drifter trajectory 4480.

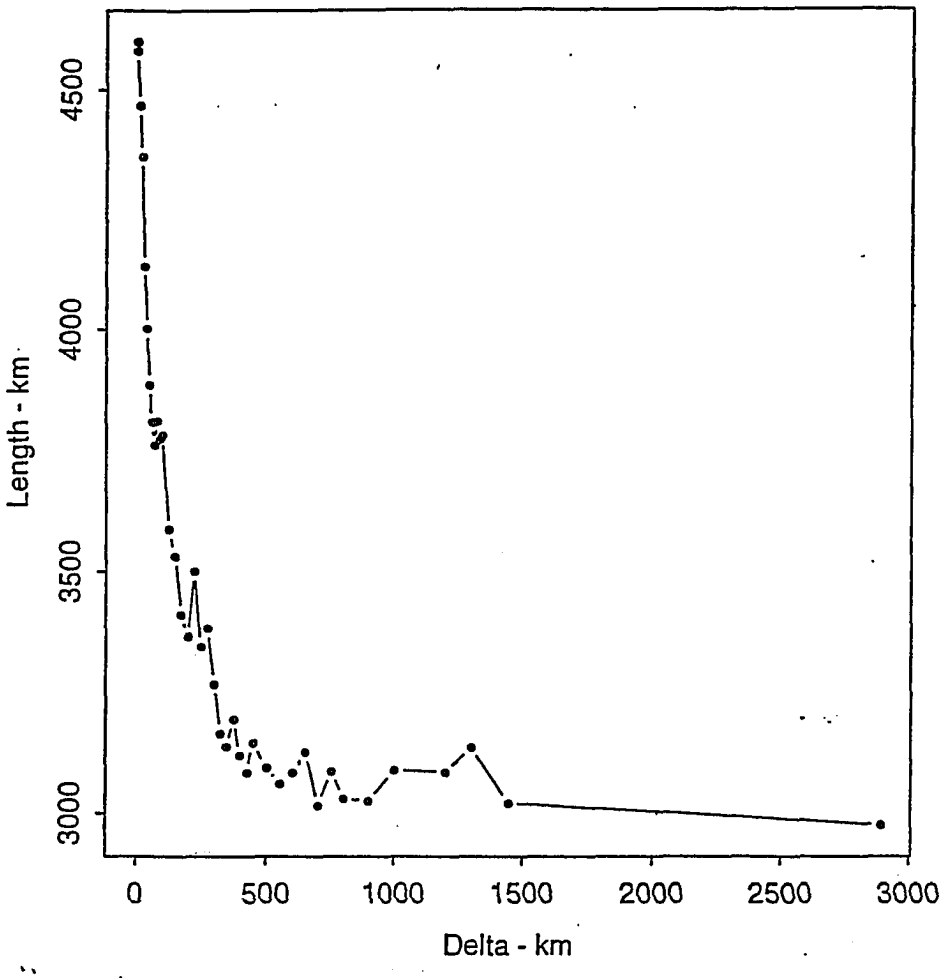

Figure 10: Delta length versus curve length for drifter trajectory 4481.

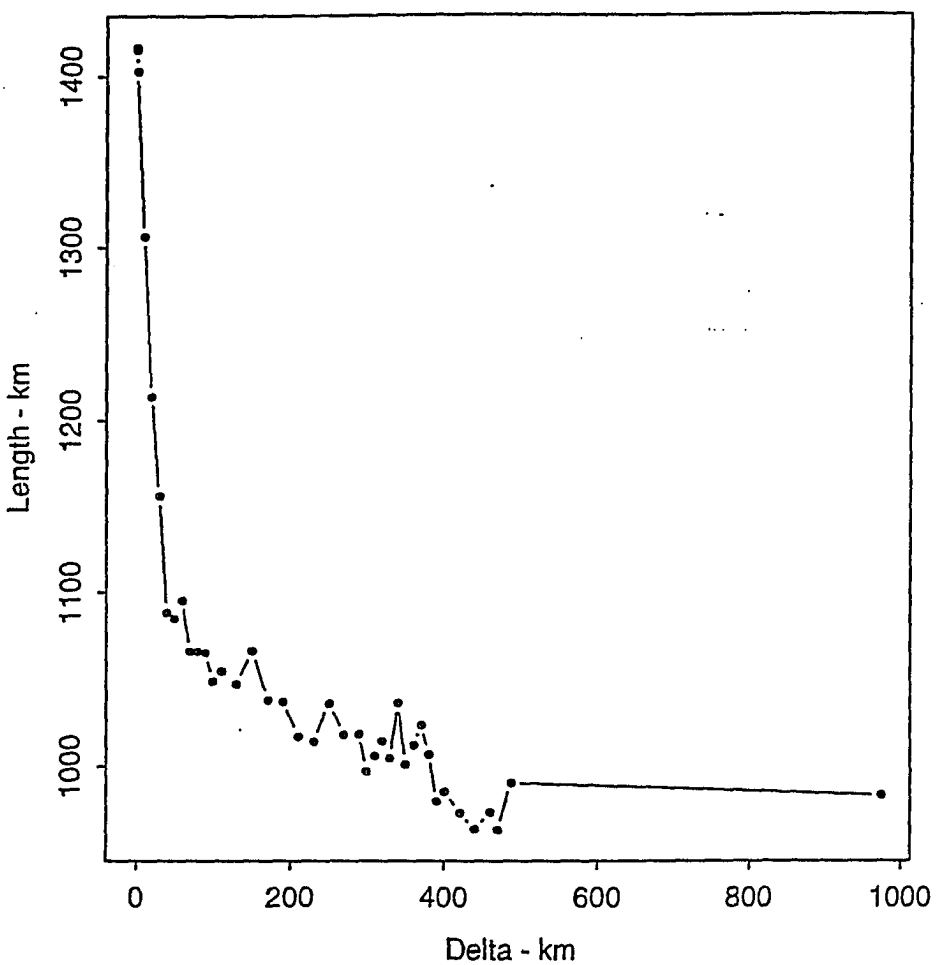

Figure 11: Log delta versus log length for drifter trajectory 4480. D = 1.108

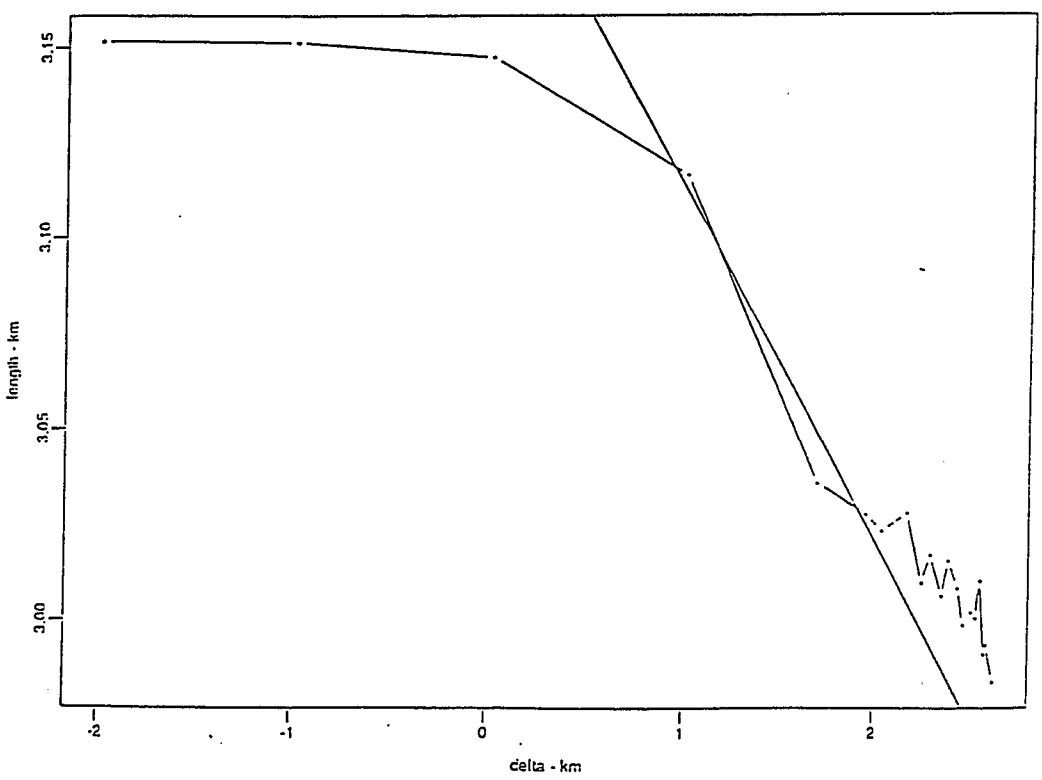

Figure 12: Log delta versus log length for drifter trajectory 4481. D = 1.090

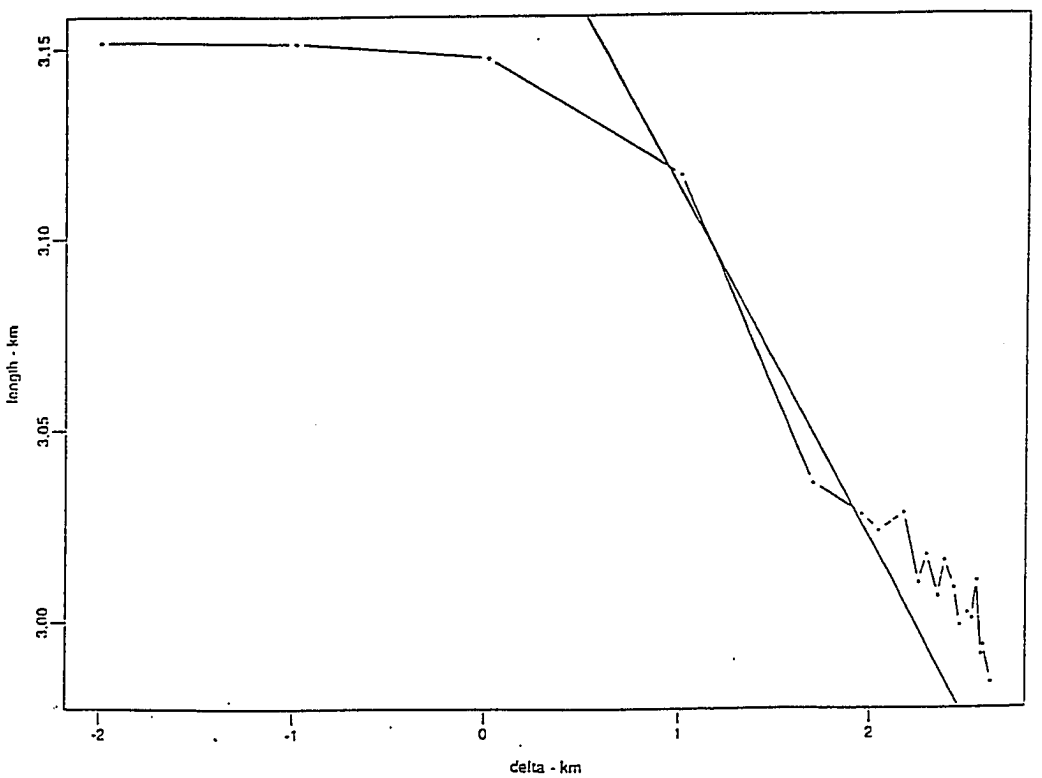

Fractal Dimension		
DATA	**D**	**RANGE**
Drifters	1.21 ± 0.02	83 - 343 km
Temp front: LT37	1.12 ± 0.01	4 - 41 km
Temp front: GT37	1.12 ± 0.01	4 - 34 km

Table 2: Fractal Dimension Values for Temperature Fronts and FACTS drifters

1977. The yardstick method was one of the methods used to determine the fractal dimension of the drifter trajectories. The average fractal dimension for the drifters was D = 1.23 ± 0.06 on the scaling range of 20 to 100 *km* (Osborne et al., 1989). Unlike this analysis, Osborne et al. (1989) removed the average drifter displacement from each trajectory by either removing the mean velocity or the linear least-squares fit trend. Osborne et al. (1989) discovered that without removing the mean drift current from the raw data the value of the fractal dimension was lower. Another thing to note about the yardstick method used in Osborne et al. (1989) is that they used by using an average delta value instead of the strict version of the method. They did this because their data was equally spaced in time, but not in space. As stated in Chapter 2, the data for this research is equally spaced in space. Thus, the strict version of the yardstick method was utilized.

Sanderson and Booth (1991) calculated the average fractal dimension of ten drifters released in the NE Atlantic over the Rockall Trough in 1983 by using the yardstick method algorithm implemented by Rapaport (1985). They also removed the mean drift current for each trajectory. They determined that D = 1.28 ± 0.08 over the space scale extending from 5 to 100 *km* (Sanderson and Booth, 1991). For calculating the fractal dimension, Sanderson and Booth (1991) restricted the delta value to be between five times the average distance between two consecutive points and 0.2 times the maximum distance between two points on the curve.

In an earlier study by Sanderson and Goulding (1990) analyzed clusters of

drifter data from Lake Erie, the Atlantic Equatorial Undercurrent and in the waters near Long Island to determine the fractal dimension of relative trajectories between drifter pairs. Again, the fractal dimension calculated was consistent with other studies, where the average value was $D = 1.3 \pm 0.1$ over a much smaller scaling range of 10 - 4000 m. Sanderson and Goulding (1990) did not remove the time averaged velocity. They also restricted the delta length value to fall within the range of the root mean square step length between consecutive points and one fifth the total displacement of the longest space curve (Sanderson and Goulding, 1990).

The FACTS drifter trajectories display an average fractal dimension of $D = 1.21 \pm 0.02$ over a scaling range of 83 - 343 km which is consistent with past studies. Osborne and Caponio (1990) state that for large and meso-scale oceanic processes Lagrangian fluid parcel trajectories are fractal space curves with a fractal dimension of approximately 1.3. The above studies all have a fractal dimension within the range of $D = 1.2$ to 1.3. These studies also show a consistent scaling range of approximately 12 - 100 km, except in Sanderson and Goulding (1990) where the scaling range is much smaller with a range from 10 - 4000 m. Previous studies and the present study show that drifter trajectories are fractal.

Recall that for this study the satellite imagery is divided into two regions, GT37 and LT37. Examples of the temperature front space curves for image 85 as described in Chapter 2 are illustrated in Figure 13 (Mullen and Kirwan, 1994). Once these temperature space curves were produced, fractal analysis was undertaken. Analysis of all the composite satellite images determined a fractal dimension of $D = 1.12 \pm 0.01$ for both GT37 and LT37. The scaling range for LT37 was 4 - 34 km and 4 - 41 km for GT37. Figure 14 illustrates the fractal dimension for the two geographic regions of the satellite images (Mullen and Kirwan, 1994). Comparisons between the two geographic sections show that there is no variability in the fractal

Figure 13: Temperature fronts greater than 37°N for image 85.

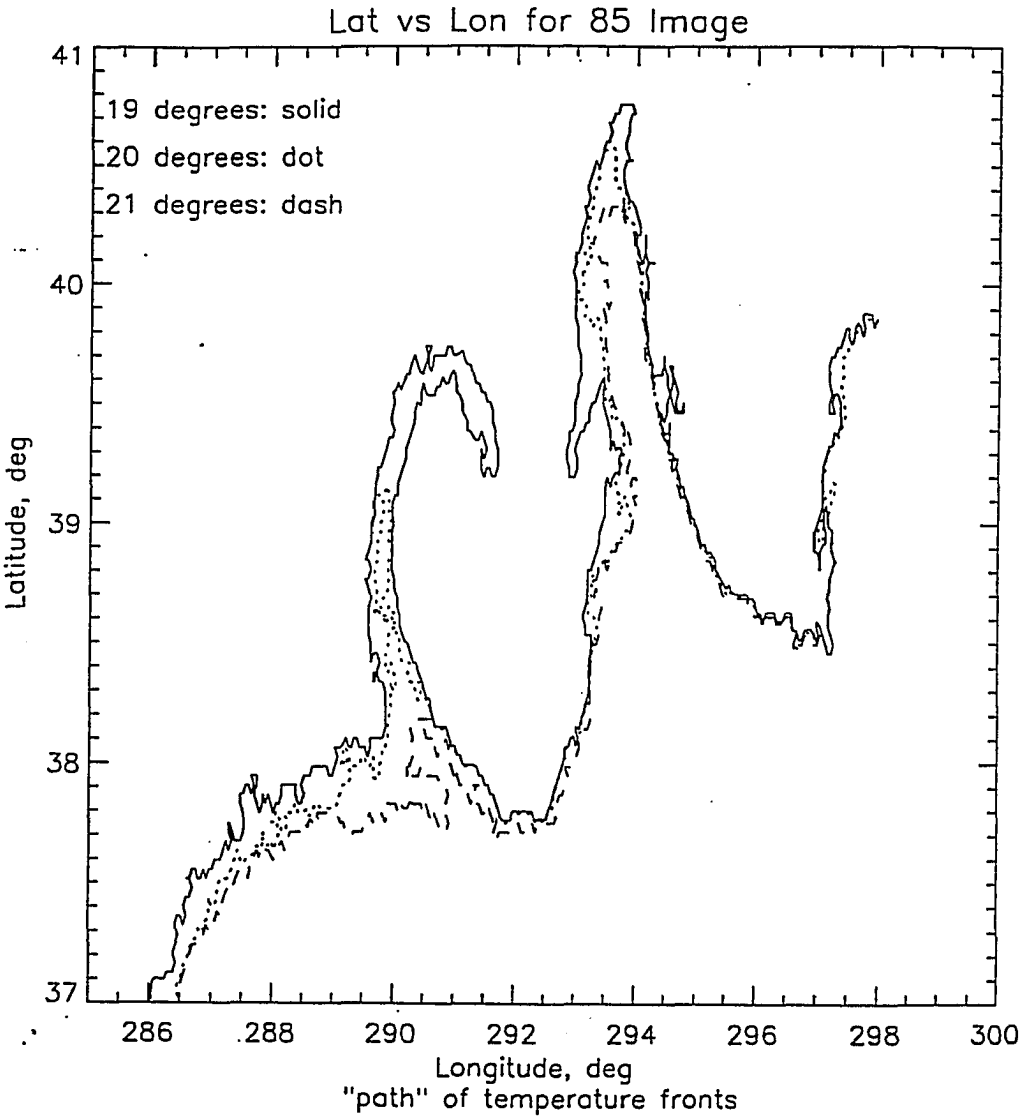

Figure 14: Graph displaying the value of the fractal dimension for the different geographic regions. LT 37: less than 37°N region, GT 37: greater than 37°N region.

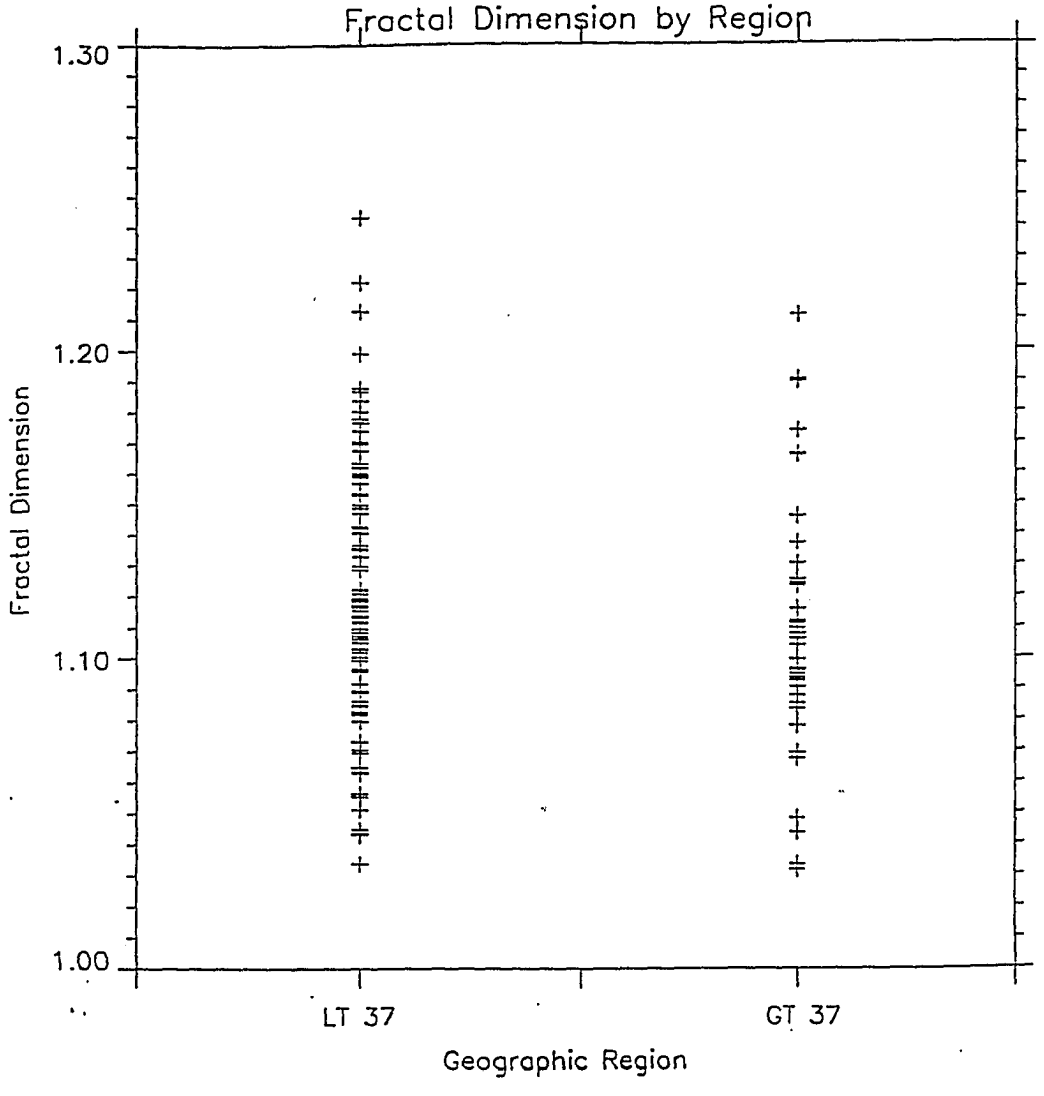

dimension. That is, there is no dependence on the location of the temperature front and its value of D (Mullen and Kirwan, 1994). Table 2 shows that the fractal dimension and scaling range are internally consistent for the image temperature fronts. The analysis suggests that the composite image data set is not fractal.

The fractal dimension for the temperature fronts is low compared to the past studies on spatial curves. The previous studies showed that the space curves were fractal and scaled over a wide range. Here, the temperature front space curves span a smaller scaling range and are most likely not fractal. Preliminary comparisons between the geometric properties for the drifter trajectories and composite image temperature fronts suggests that there is not a strong link between the two data sets.

4.2 Spectral Analysis

In Chapter 2 it was shown that there is a strong relationship between the fractal character of a self-similar space curve and the log slope of its power-law spectrum. Power spectral analysis was applied to both data sets of satellite-tracked drifter trajectories and the satellite composite temperature fronts. Figure 15 displays the power spectral plots for the latitude and longitude components of the drifter trajectories. Similar plots for the temperature fronts are represented in Figure 16. The power spectral slope for the data, which is termed the calculated slope, was determined by using (2.4.1). The lines on Figures 15 and 16 represent the calculated slope. Once the calculated slope was obtained and recorded for each space curve, it was used to determine the corresponding scaling ranges. The calculated slope lines were overlaid onto the spectral plots with the first point on the graphs being the starting point of the calculated slope lines. Thus, all scaling regions for the data sets begin on the low frequency end of the power spectra plots. It is important to

Figure 15: Power spectra plots of the latitude and longitude components for drifter 4480.

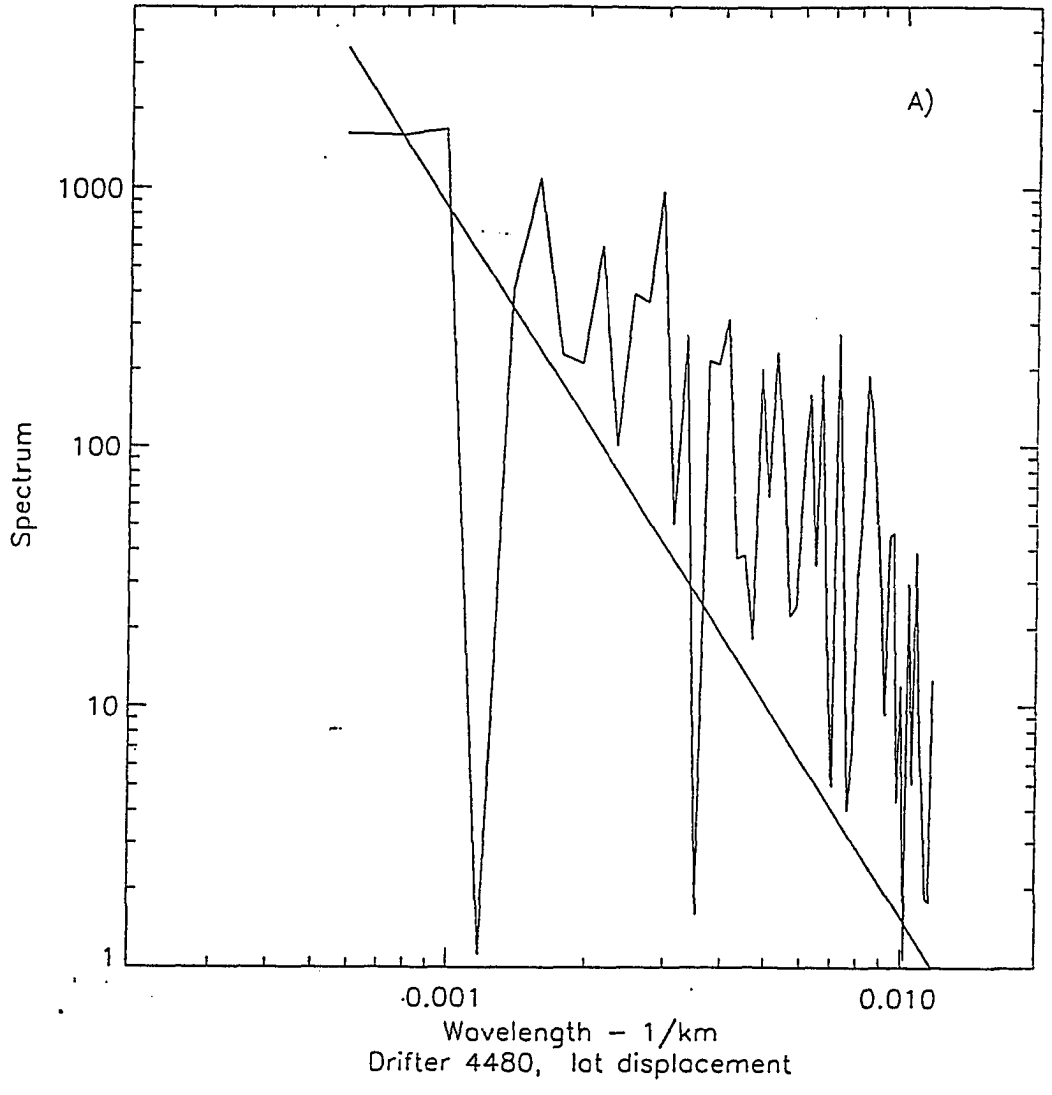

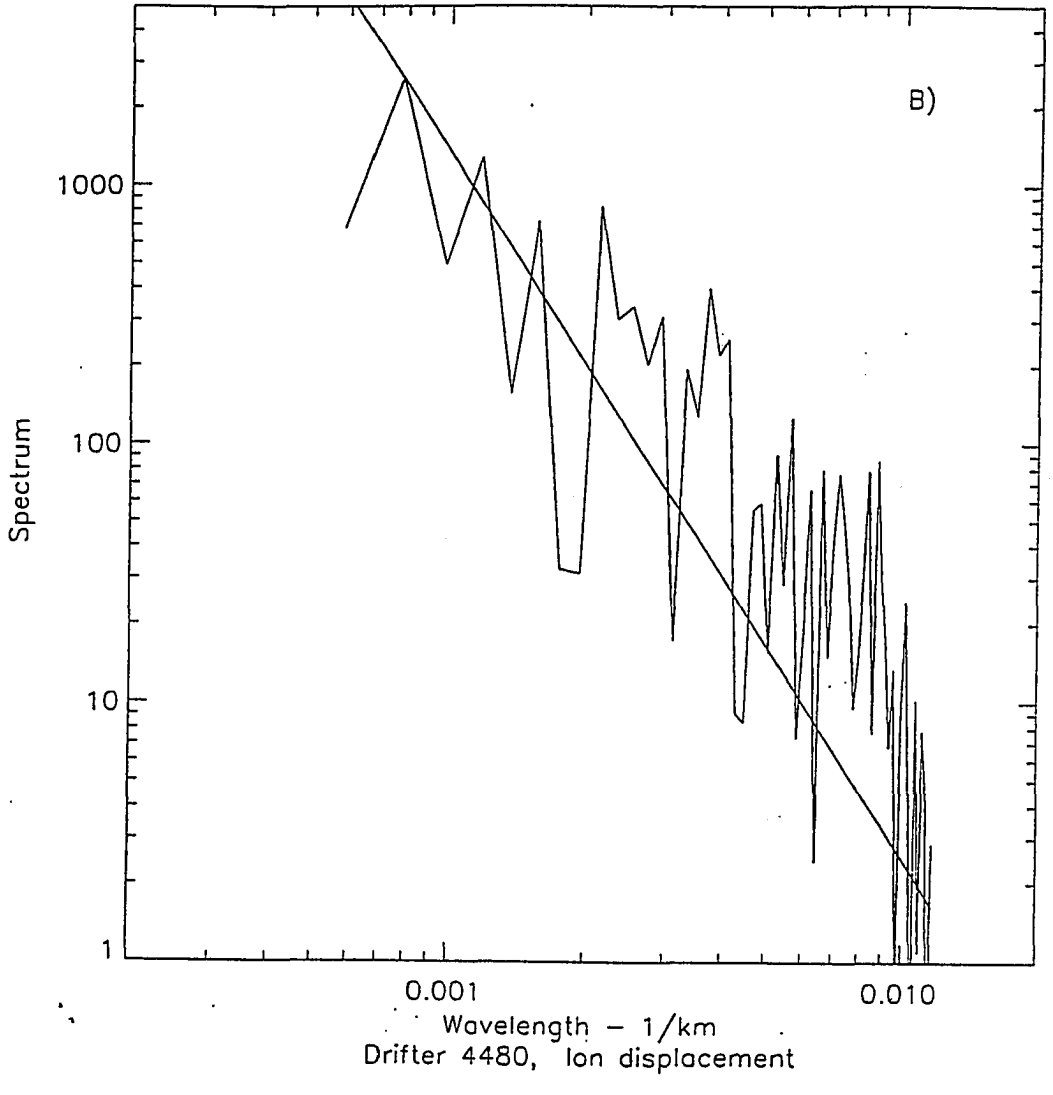

Figure 16: Power spectra plots of the latitude and longitude components for image 47, GT37, temperature front 21C.

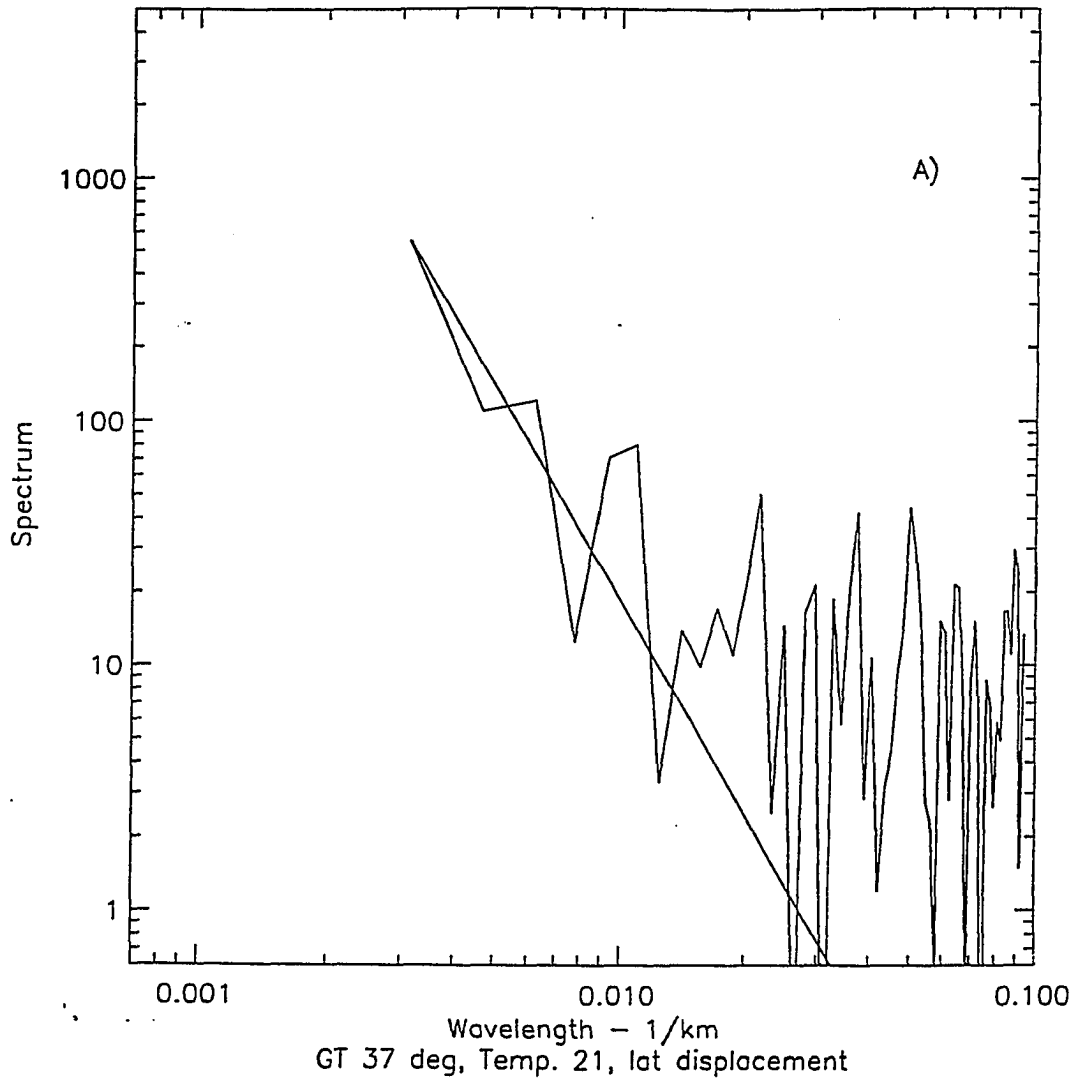

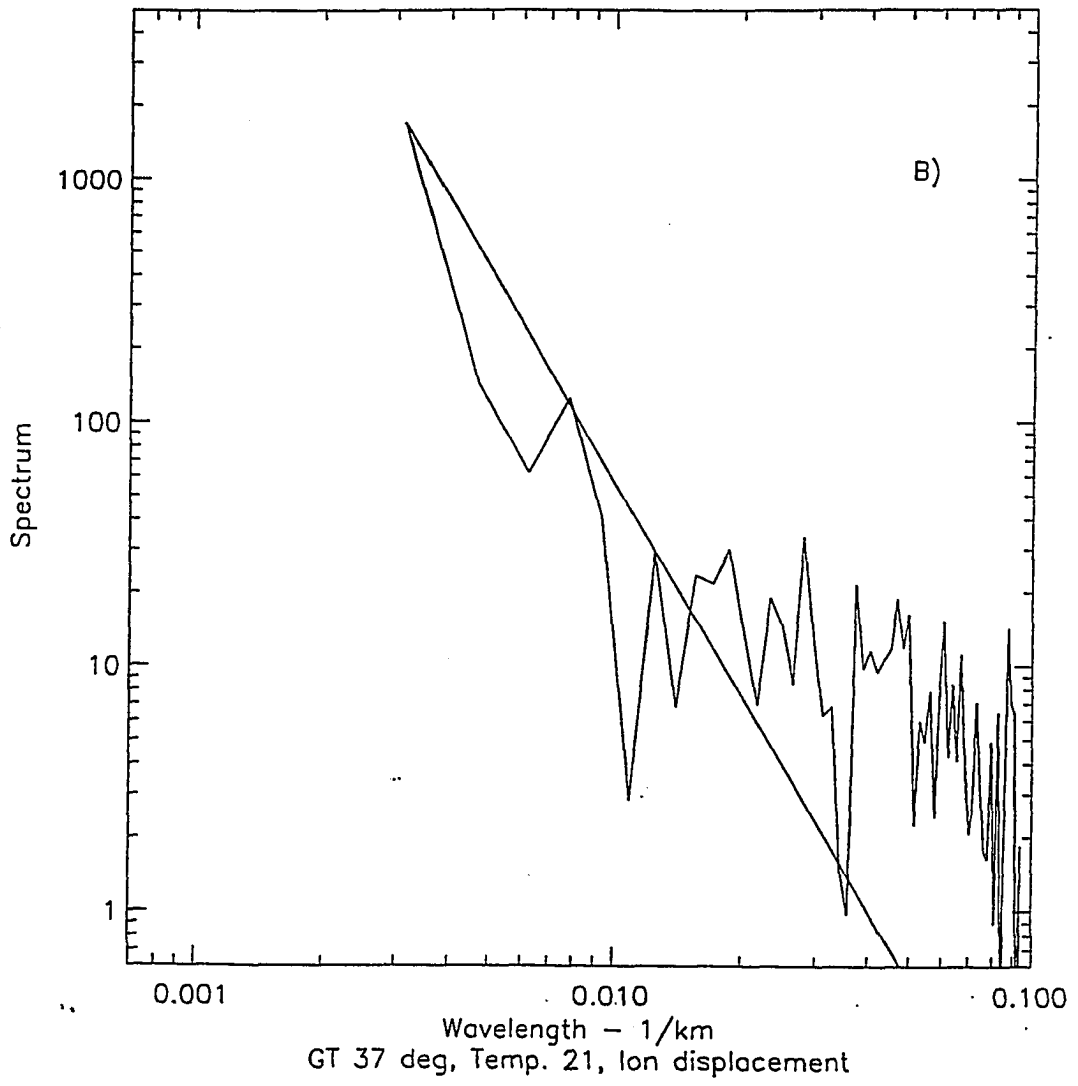

Scaling Range: Drifters		
IMAGE	SPECTRAL SLOPE	RANGE
2083	2.31 ± 0.01	1360 - 6250 km
4471	2.65 ± 0.01	496 - 1667 km
4472	2.55 ± 0.01	635 - 1667 km
4474	2.60 ± 0.01	250 - 625 km
4476	2.87 ± 0.01	247 - 769 km
4477	2.82 ± 0.01	551 - 2500 km
4478	2.55 ± 0.01	273 - 1334 km
4479	2.74 ± 0.01	1111 - 1667 km
4480	2.72 ± 0.01	1082 - 2084 km
4481	2.87 ± 0.01	156 - 588 km

Table 3: Spectral slope values and scaling ranges FACTS drifters

note that on some spectra plots the starting point for the calculated slope line ranged anywhere from the second to seventh point on the spectra. This did not greatly affect the overall scaling range of the data sets.

Spectral analysis of the drifter trajectories revealed spectra displaying a power-law dependence (Figure 15). Table 3 gives the calculated slope values and scaling ranges for the drifter data. The uncertainties in the values are from the statistical errors in determining the fractal dimension. The resultant average spectral slope and scaling range for the drifter paths are 2.67 ± 0.01 and 616 - 1915 km, respectively. This low calculated slope value is consistent with past spectral studies of drifter trajectories. Osborne et al. (1989) determined an average spectral slope of 2.63 ± 0.07 for the three buoys deployed in the Kuroshio Extension. They chose a range of 0.04 - 1.0 $rad\ dy^{-1}$ over which the least-squares method was used to fit the spectra.

Care must be taken in conducting spectral analysis and calculating the spectral slope values of a data set. The slope characteristics often are dependent upon the degree of spectral smoothing and the a-priori selected scaling range (Mullen and Kirwan, 1994). Since calculations of the power spectral slope is not always straightforward and may depend on the above stated criteria, a different approach

Scaling Range: LT37		
IMAGE	SPECTRAL SLOPE	RANGE
1	2.80 ± 0.01	291 - 1096 km
47	2.81 ± 0.01	137 - 599 km
52	2.74 ± 0.01	167 - 777 km
57	2.79 ± 0.01	166 - 665 km
60	2.81 ± 0.01	139 - 385 km
65	2.87 ± 0.01	159 - 623 km
85	2.81 ± 0.01	83 - 193 km
92	2.85 ± 0.01	169 - 713 km
96	2.75 ± 0.01	135 - 545 km
101	2.77 ± 0.01	225 - 908 km
116	2.78 ± 0.01	153 - 526 km

Table 4: Spectral slope values and scaling ranges for LT37

to determining the spectral slope and scaling ranges was employed. Instead of fitting the spectra to power-laws by the least squares fit method, as previous studies have elected to do, this study focuses on utilizing the calculated spectral slope to determine the scaling range. This approach was discussed earlier in this section.

Power spectral analysis was applied to the two sections of the Gulf Stream. Following the above procedure, the calculated slope values and the observed scaling ranges were determined. Table 4 and Table 5 give a few representative spectral slopes derived from the self-similar character of the space curves. The tables show that the calculated slope values and the scaling ranges are fairly consistent within and between the geographic regions. Both regions have similar average spectral slope values and scaling ranges. The average calculated slope for LT37 is 2.79 ± 0.01 over a scaling range of 139 - 434 *km*, while GT37 displays an average spectral slope value of 2.82 ± 0.01 with scales from 134 - 434 *km*. Overall, the spectra for both data sets display a power-law dependence. Despite the fact that this image data set displays power-law dependence, it does not mean that it is necessarily fractal.

Comparisons between the spectral slope values and scaling ranges of the drifters

Scaling Range: GT37		
IMAGE	SPECTRAL SLOPE	RANGE
1	2.83 ± 0.01	189 - 923 km
47	2.82 ± 0.01	104 -379 km
52	2.85 ± 0.01	57 - 205 km
57	2.84 ± 0.01	71 - 160 km
60	2.77 ± 0.01	112 - 342 km
65	2.84 ± 0.01	237 - 789 km
85	2.79 ± 0.01	140 - 485 km
92	2.81 ± 0.01	168 - 406 km
96	2.79 ± 0.01	95 - 279 km
101	2.85 ± 0.01	106 - 335 km
116	2.78 ± 0.01	196 - 476 km

Table 5: Spectral slope values and scaling ranges for GT37

with those of the temperature fronts reveal that drifter trajectories have a much lower average calculated slope. However, the average scaling range for the drifter paths is much larger. It is interesting to note that if the scaling ranges for the drifter data set are calculated for only those drifters which correspond to the composite imagery, the scaling range and spectral slope values are closer to that computed for the imagery. This was evidenced also in the calculations for the fractal dimension. In such a case, the average spectral slope value becomes 2.72 ± 0.01 over a scaling range of 656 - 1418 *km*.

In order to determine whether the location of the temperature front affects the values calculated for the spectral slope and fractal dimensions, the composite image data was divided into two regions: greater than 37°N and less than 37°N. Results show that the spectral slope and fractal dimension of the different regions, as well as the corresponding scaling range, are consistent between the regions (Mullen and Kirwan, 1994). The drifter trajectory data is also internally consistent, as well as similar to past studies. Thus, there is no geographic variability to the contemporaneous data set. Further analysis of the drifter trajectory and temperature front data

reveals that their spectral slope values and scaling ranges are drastically different. This suggests that there is not a strong link between the paths of the drifters and the composite image temperature fronts. The fractal dimension also suggests that the contemporaneous data set of drifters trajectories and composite images is not fractal, except in the case where all the drifter data is analyzed. In this case, the fractal character was consistent with past studies showing the drifter paths to be fractal.

5 Kinematic Analysis

There is nothing in the whole
world which is permanent
Everything flows onward;
all things are brought into
being with a changing nature;
The ages themselves glide by
in constant motion.
Ovid

Kinematics is the description of motion of material bodies without reference to the dynamics causing the motion. Nearly all oceanographic observations are kinematic. It is the responsibility of the dynamicist to infer dynamical processes from observations of kinematic properties. Pursuant to the above, this section provides a detailed kinematic analysis of the simultaneous data set. The results obtained from this analysis later are used to assess three models.

This chapter focuses on the kinematic analysis of the drifter trajectories and composite imagery of the Gulf Stream. One of the main objectives here is to determine whether the drifter patterns are important indicators of thermal features. Several different avenues are pursued. These include temperature transects across the Gulf Stream deduced from imagery and comparisons between the satellite composite temperature fronts and the drifter trajectories. This discussion will concentrate mainly on four drifter paths and simultaneous satellite imagery; i.e. drifter trajectories and composite satellite images that span the same time period. This is referred to as a contemporaneous data set. It is important to note that the phrase

"temperature front" is used to define the delineation between temperature fields on the five-day composite images.

5.1 Temperature Along Drifter Trajectories

In order to understand the relationship between the drifter trajectories and the temperature field of the composite imagery, temperature values for the trajectories need to be obtained. The temperature signatures for four Lagrangian drifter paths 4478, 4479, 4480 and 4481 were obtained by extracting the information from their contemporaneous satellite image. Table 6 gives a summary of the drifter data. The starting and ending dates for the composite imagery are shown in Table 7. The drifter paths were overlaid onto their corresponding composite satellite images, and then the temperature values were recorded using NASA SEAPAK software on a PC computer (McClain et al., 1992). Once these values were recorded, plots of the temperature versus the distance along the trajectory were generated. This was done to see how closely the path of the drifters correlated with the temperature fronts of the Gulf Stream.

The composite satellite imagery is defined by an image number from 1 to 116. This number, which is the starting date for the image, corresponds to the sequential day of 1985. The drifter trajectories are referred to by their drifter numbers which were assigned during the FACTS study.

Recall that a major focus of this study was to determine the geographic variability of the contemporaneous data set. Thus, the study area was divided into two regions, GT37 and LT37. GT37 region is characterized by large variability and dramatic meandering of the Gulf Stream. The following is a description of the drifter trajectories in relation to their contemporaneous composite images.

Table 6: A summary of all FACTS drifter data, including the latitude and longitude of the starting point.

Track	Start	Start Lat	Start Lon	End
2083	04/06/84	28.00 N	79.99 W	02/14/85
4471	06/12/84	28.00 N	80.00 W	04/29/85
4472	07/12/84	28.00 N	80.00 W	04/29/85
4474	09/13/84	28.00 N	79.99 W	04/29/85
4476	10/16/84	28.00 N	80.00 W	12/01/84
4477	11/15/84	28.00 N	80.00 W	04/30/85
4478	12/11/84	28.00 N	80.02 W	04/29/85
4479	01/25/85	28.00 N	80.02 W	04/30/85
4480	02/15/85	28.00 N	80.02 W	04/30/85
4481	03/16/85	28.00 N	80.02 W	04/30/85

Table 7: Starting and ending periods for the composite image data.

Image	Start	End
1	01/01/85	01/05/85
6	01/06/85	01/10/85
11	01/11/85	01/15/85
16	01/16/85	01/20/85
21	01/21/85	01/25/85
26	01/26/85	01/31/85
32	02/01/85	02/05/85
37	02/06/85	02/10/85
42	02/11/85	02/15/85
47	02/16/85	02/20/85
52	02/21/85	02/25/85
57	02/26/85	02/28/85
60	03/01/85	03/05/85
65	03/06/85	03/11/85
71	03/12/85	03/15/85
75	03/16/85	03/20/85
80	03/21/85	03/25/85
85	03/26/85	04/01/85
92	04/02/85	04/05/85
96	04/06/85	04/10/85
101	04/11/85	04/15/85
106	04/16/85	04/20/85
111	04/21/85	04/25/85
116	04/26/85	04/30/85
121	05/01/85	05/05/85

The first drifter trajectory described in this section is 4478. It was deployed in late 1984. Unfortunately, there was intense cloud cover during the time period in which 4478 corresponds to satellite imagery. Therefore, only two images, image 1 (see Appendix) and image 6 (Figure 17) can be analyzed for this drifter. The drifter trajectory of 4478 for image 6 spans several hundred kilometers over a period of five days. Figure 17 shows that drifter 4478 flows in the 22°C waters but, does not correspond directly to an image temperature front. A portion of the trajectory/temperature relationship is obscured by cloud cover. Once the drifter reaches latitudes above Cape Hatteras the temperature along the path increases and then decreases substantially as shown in Figure 18. This figure displays the temperature versus distance along the trajectory of 4478 corresponding to image 6. The constant values in this figure represent the cloud cover depicted in Figure 17.

Drifter 4479 was deployed on January 25, 1985 and remained active until April 30, 1985 (see Table 6). For images 26, 32, 37 and 42 the drifter appears to follow relatively closely the 22°C isotherm (Figures 19, 20, 21 and 22). Figure 19 shows drifter 4479 superposed on image 26. Here, the trajectory appears to flow along with the Gulf Stream following a constant temperature. This is also illustrated in Figure 23 which displays the temperature observed along the drifter trajectory. Figure 20 shows a much shorter trajectory for 4479 for the same time period. The drifter appears to have been caught in some circulation pattern. The last image for this drifter in LT37 is image 37 (Figure 21) which shows the drifter still flowing within the 22°C temperature region. Figure 22 shows that drifter 4479 flows along a temperature front of 21°C. Here, it has begun to flow into GT37. Clearly, Figure 23 shows that drifter 4479 corresponds quite well to a constant temperature region. As before, the constant temperature values around the 400 *km* mark in Figure 23d depict a region of cloud cover.

Figure 17: Image 6 of the Gulf Stream with drifter 4478 overlaid in black. The colorbar is in °C. (image courtesy of RSMAS)

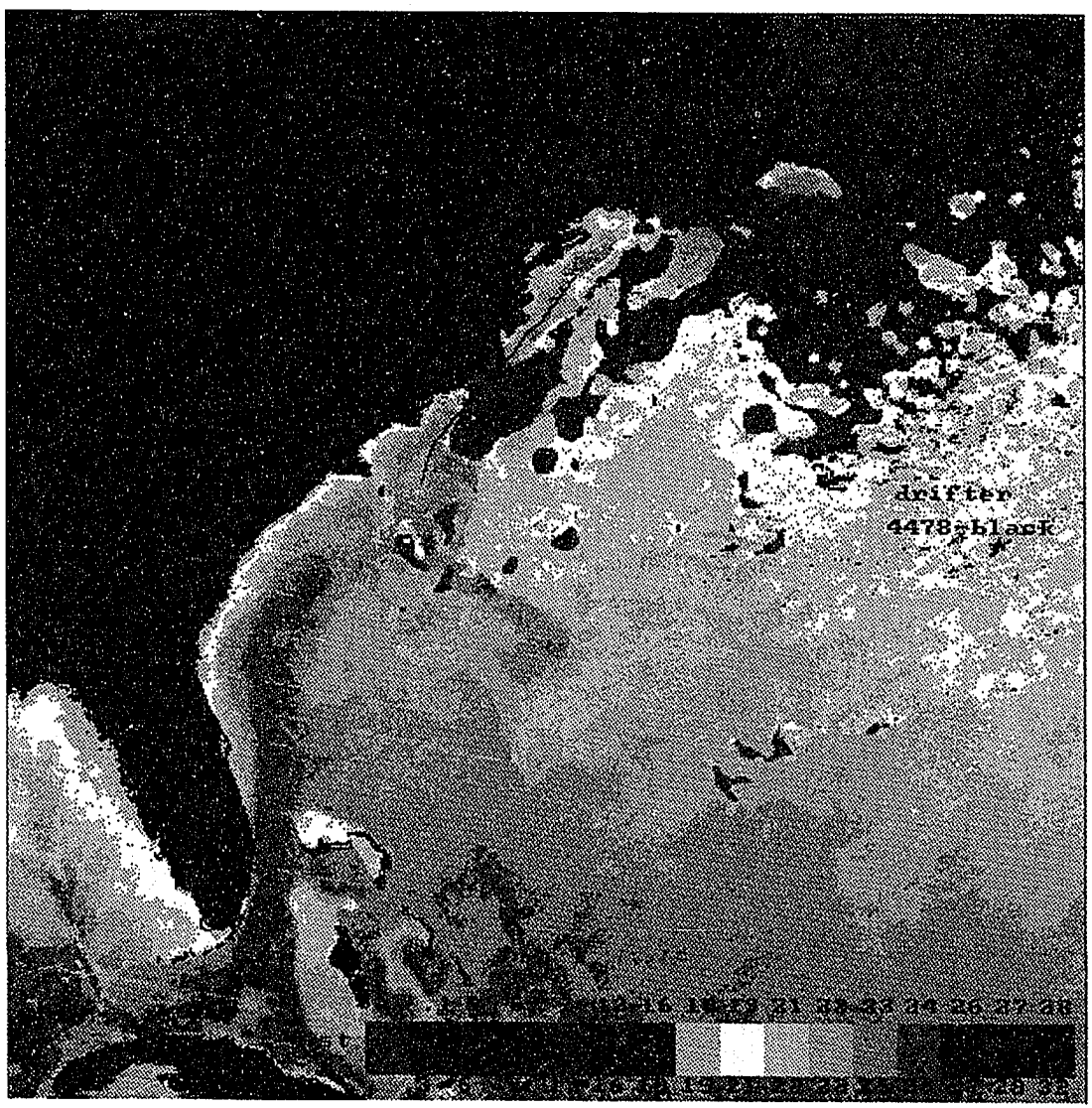

Figure 18: Plot depicting the temperature versus distance along the drifter trajectory of drifter 4478 for image 6.

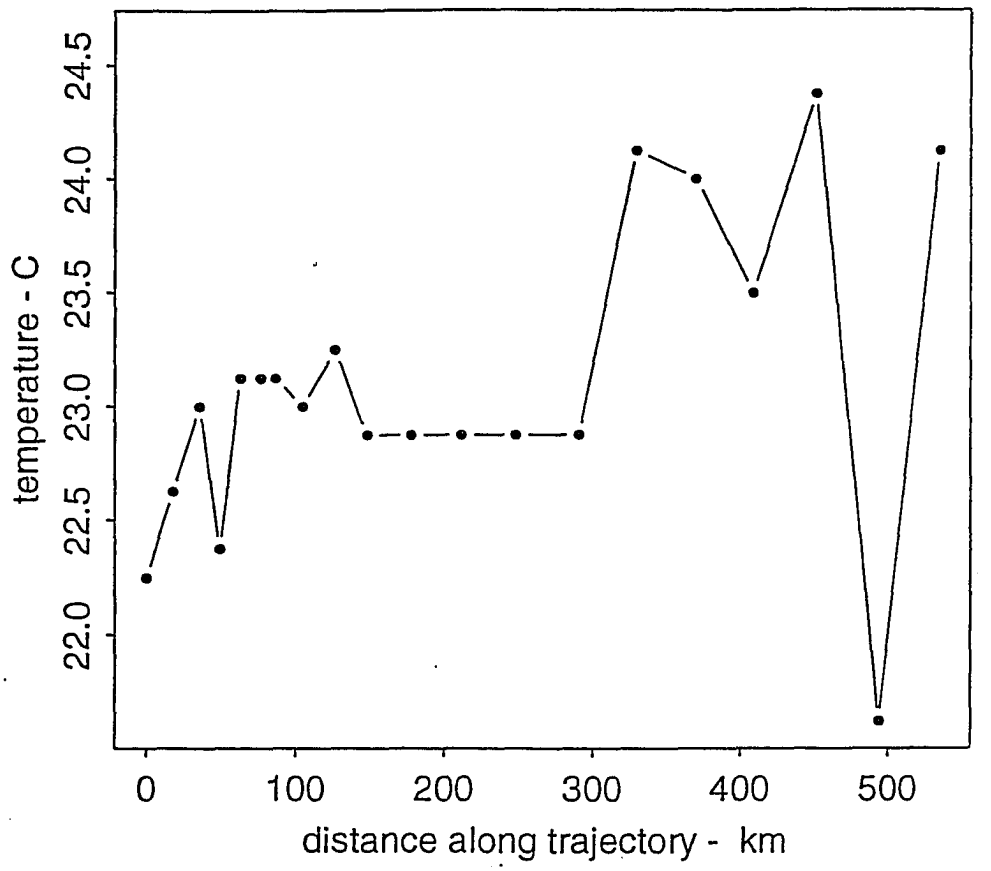

Figure 19: Image 26 of the Gulf Stream with drifter 4479 overlaid in black. (courtesy of RSMAS)

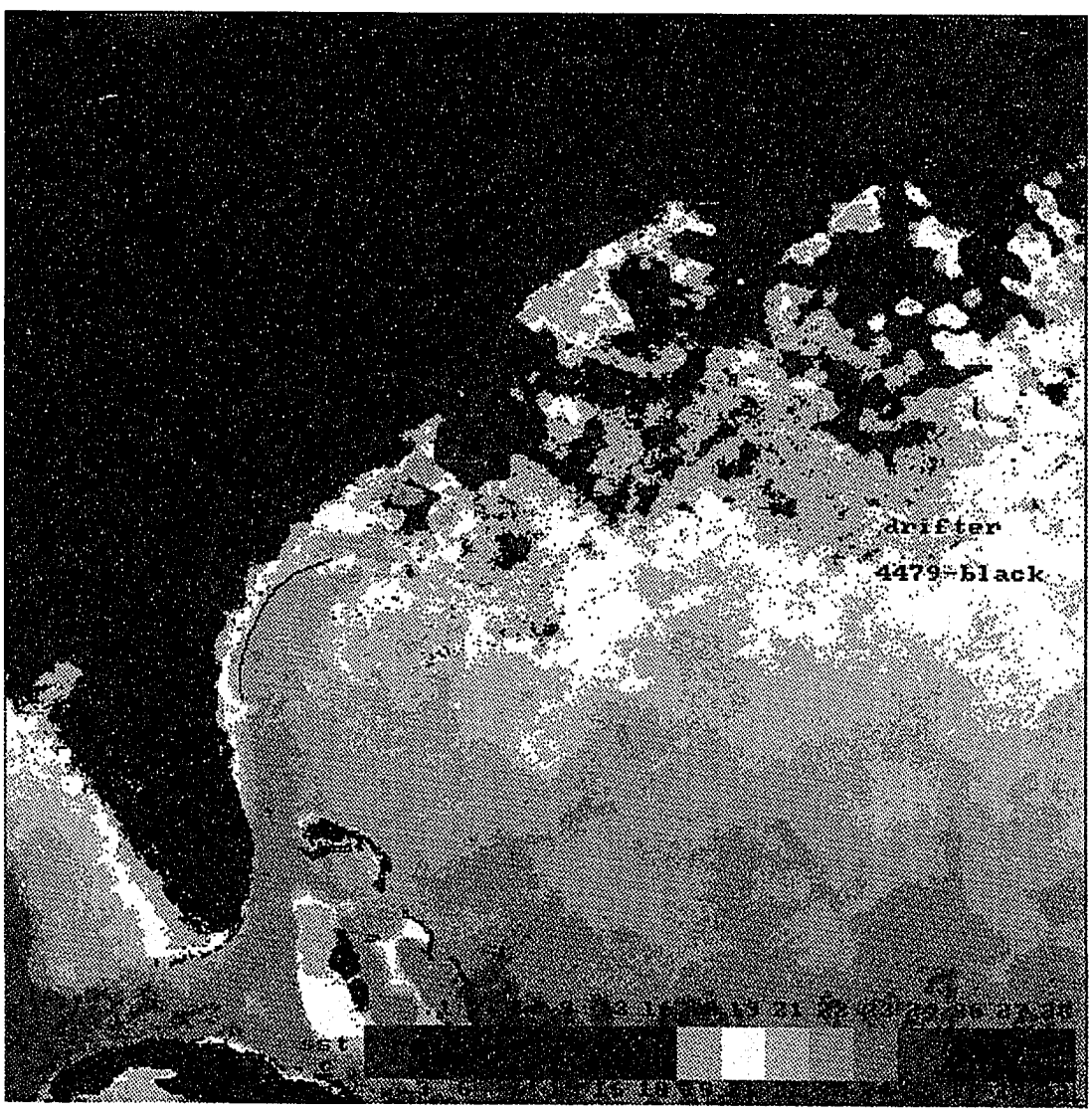

Figure 20: Image 32 of the Gulf Stream with drifter 4478 overlaid in black and drifter 4479 superposed in light blue. (courtesy of RSMAS)

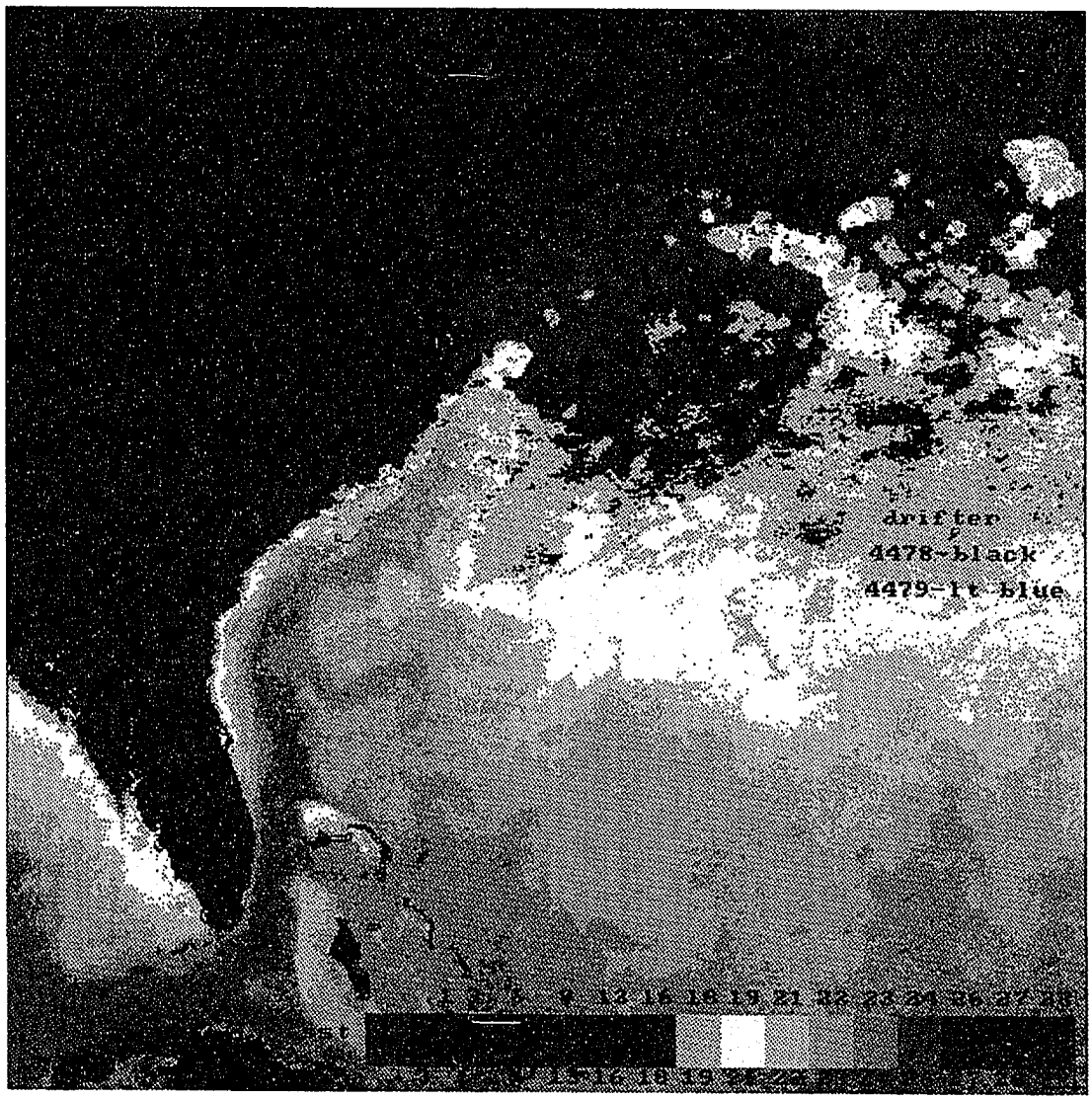

Figure 21: Image 37 of the Gulf Stream with drifter 4479 overlaid in black. The gray coloring in the upper right hand corner is cloud cover. (courtesy of RSMAS)

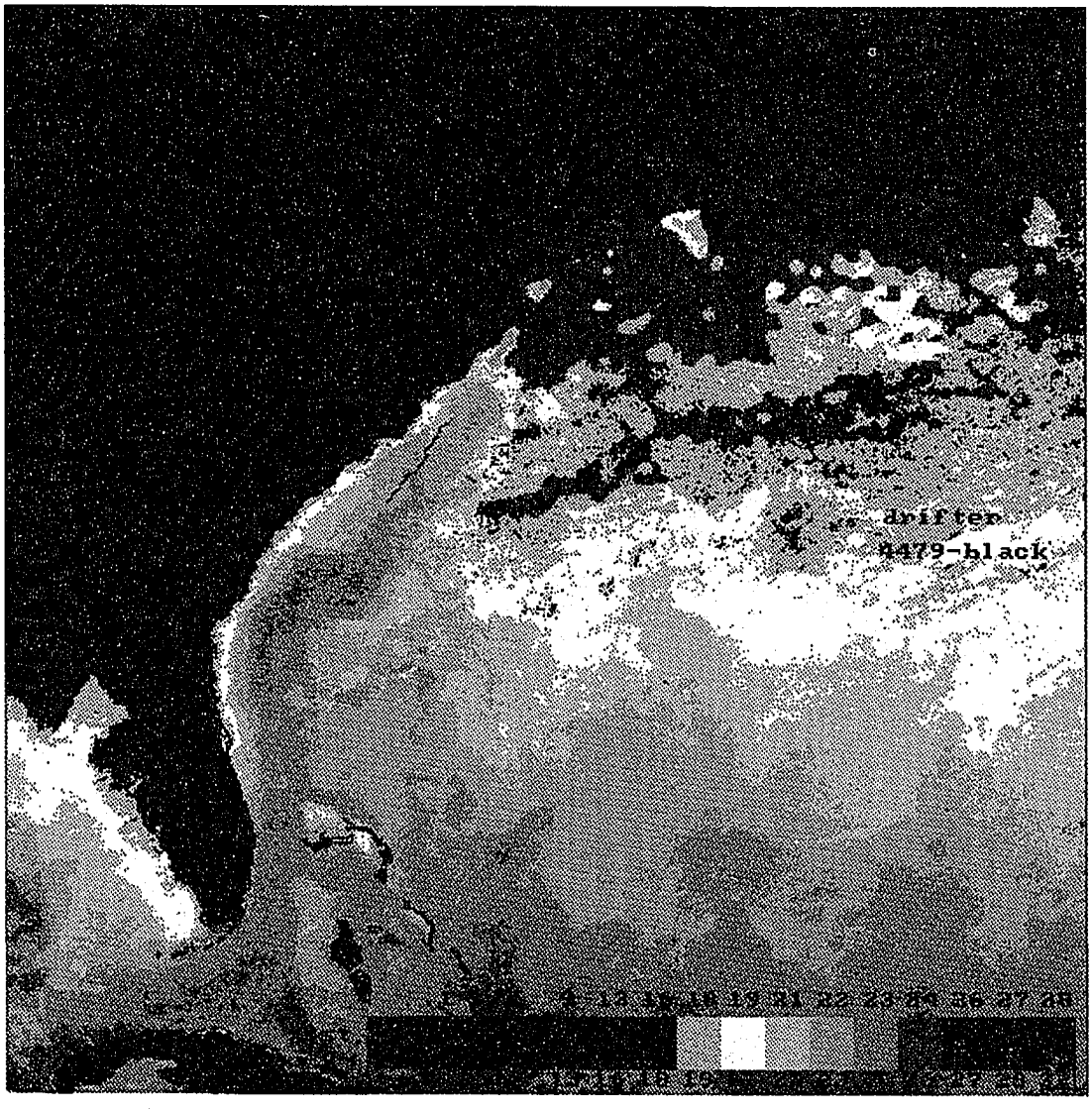

Figure 22: Image 42 of the Gulf Stream with drifter 4478 (red) and 4479 (black) overlaid. The gray coloring is cloud cover. (courtesy of RSMAS)

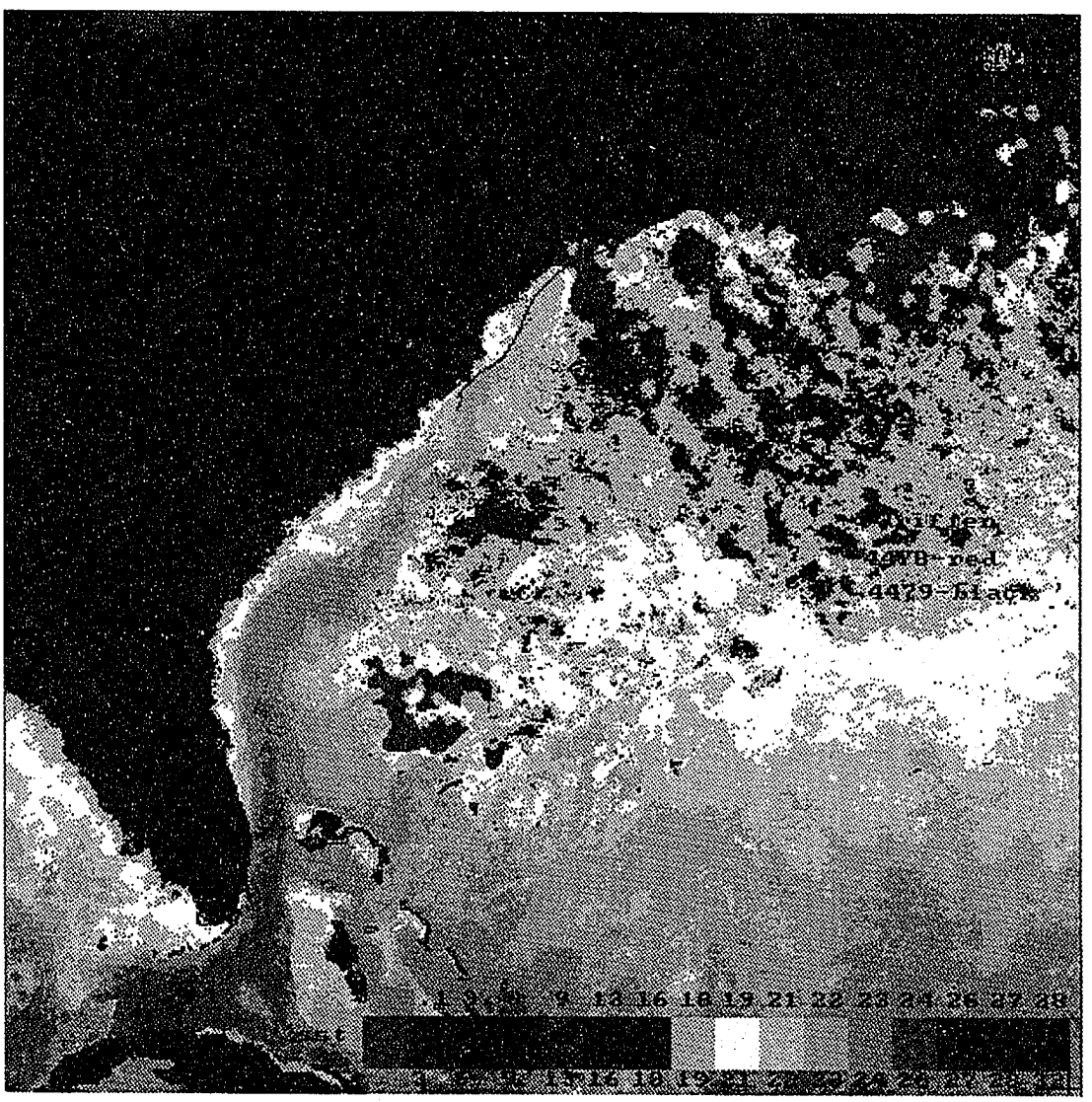

Figure 23: Plot displaying the temperature along drifter trajectory 4479. a) image 26, b) image 32, c) image 37 and d) image 42.

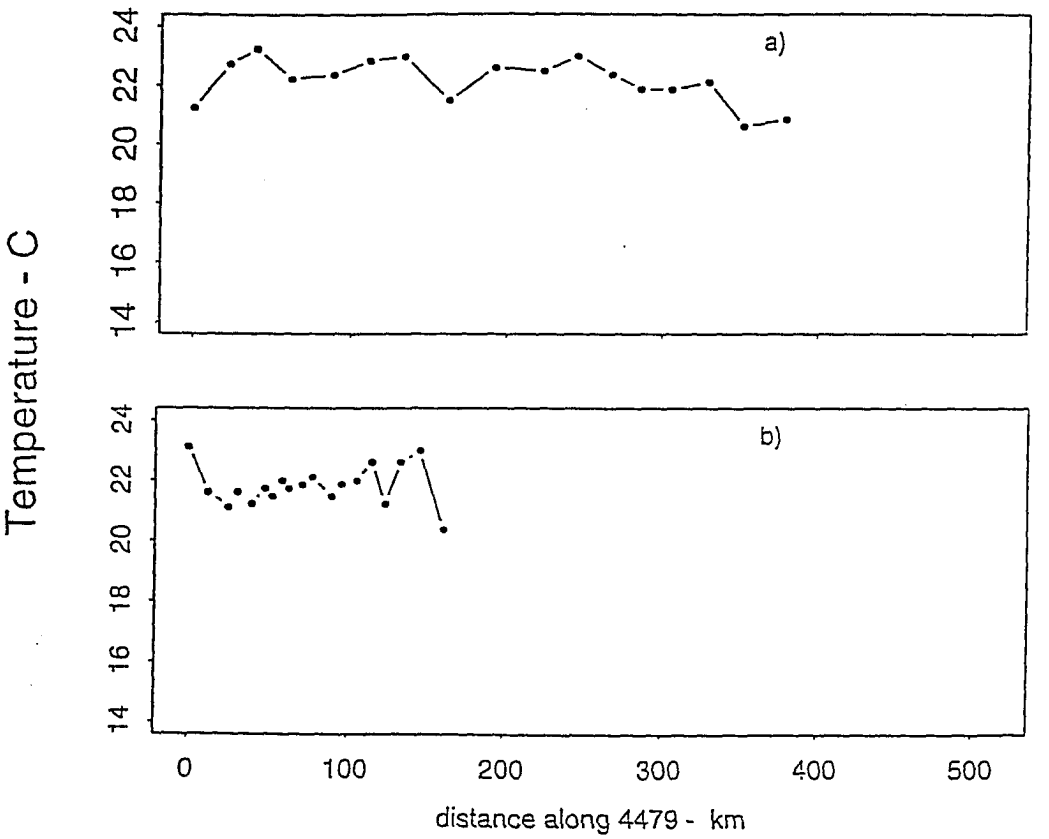

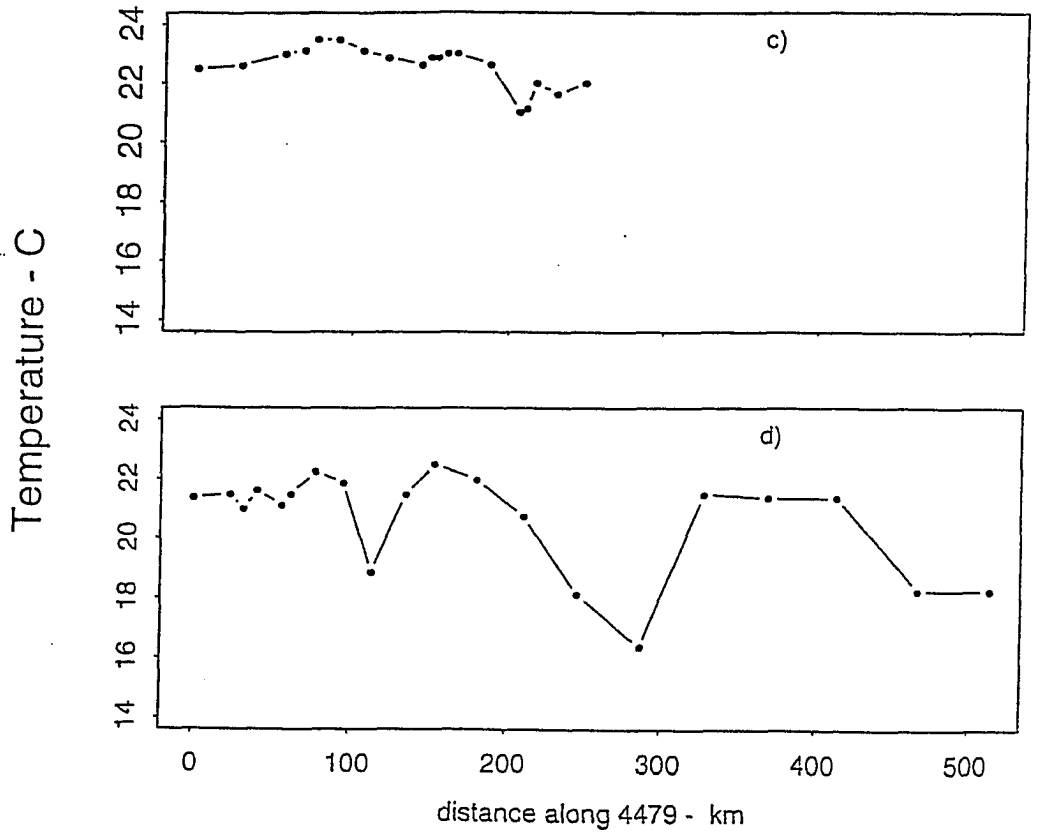

There is added importance to analyzing the drifter track in GT37, which has to do with the variability in location of the Gulf Stream. Here, observations are made regarding the relationship between the drifter trajectory location within the Gulf Stream and its corresponding temperature values.

Once 4479 nears the meandering region of the Gulf Stream, it too begins to "meander" and flow along the temperature front and then into different temperature regions. The drifter follows the meandering of the Gulf Stream and appears to flow along its Northern edge (Figure 24). Drifter 4479 extends over hundreds of kilometers during the five day period for image 47. Unfortunately, the "path" of the Gulf Stream is not continuous during this time period and it is difficult to quantify how closely the drifter follows the Gulf Stream. The temperature observed along the path for drifter 4479 is illustrated in Figure 25. As shown by this plot the temperature remains fairly constant around 18-20°C. The plot does show that the colder temperatures of 12-13°C do correspond to the troughs in the meanders and the crests have warmer waters. This can also be observed in image 47 (see Figure 24).

Drifter 4480 was deployed on February 15, 1985 and spent most of its lifetime within the contemporaneous time and space scales of this study. Figure 26 is a graphic representation of the drifter path for 4480 corresponding to these scales. The temperature values along the trajectory do not change drastically. The average change is only two degrees. The most variability in the drifter location in relation to a temperature front is found within LT37.

Figure 27 depicts drifter 4480 on image 47. This shows the drifter following the 23°C temperature field. The next five-day composite image shows that it continues to follow the 23°C temperature front and eventually works its way into 21°C waters (Figure 28). The next few images, 57, 60, 65 and 80, show that the trajectory for

Figure 24: Image 47 of the Gulf Stream with drifters 4478 (red), 4479 (black) and 4480 (light blue) overlaid. (courtesy of RSMAS)

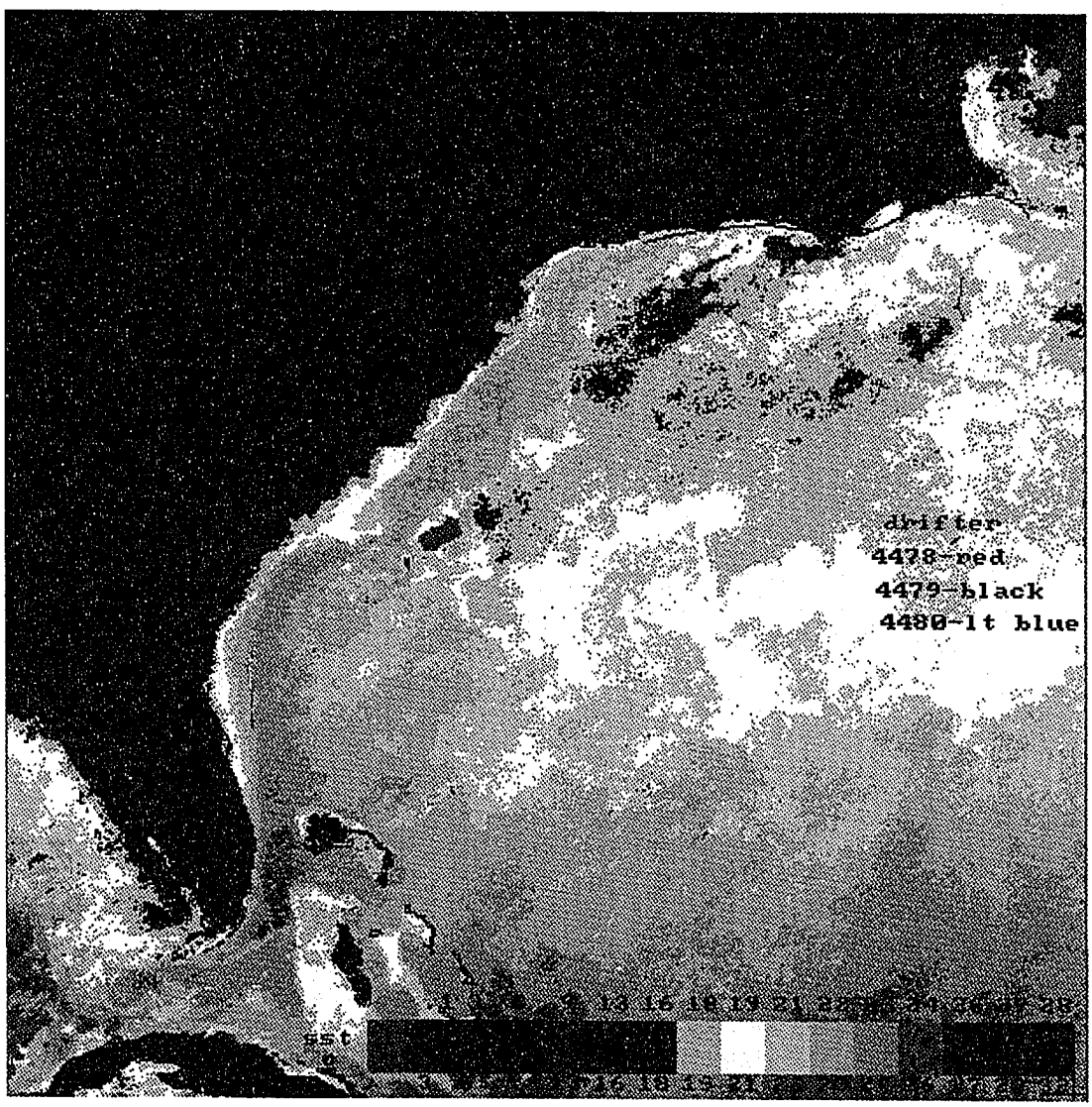

Figure 25: Temperature versus distance along drifter 4479 for image 47.

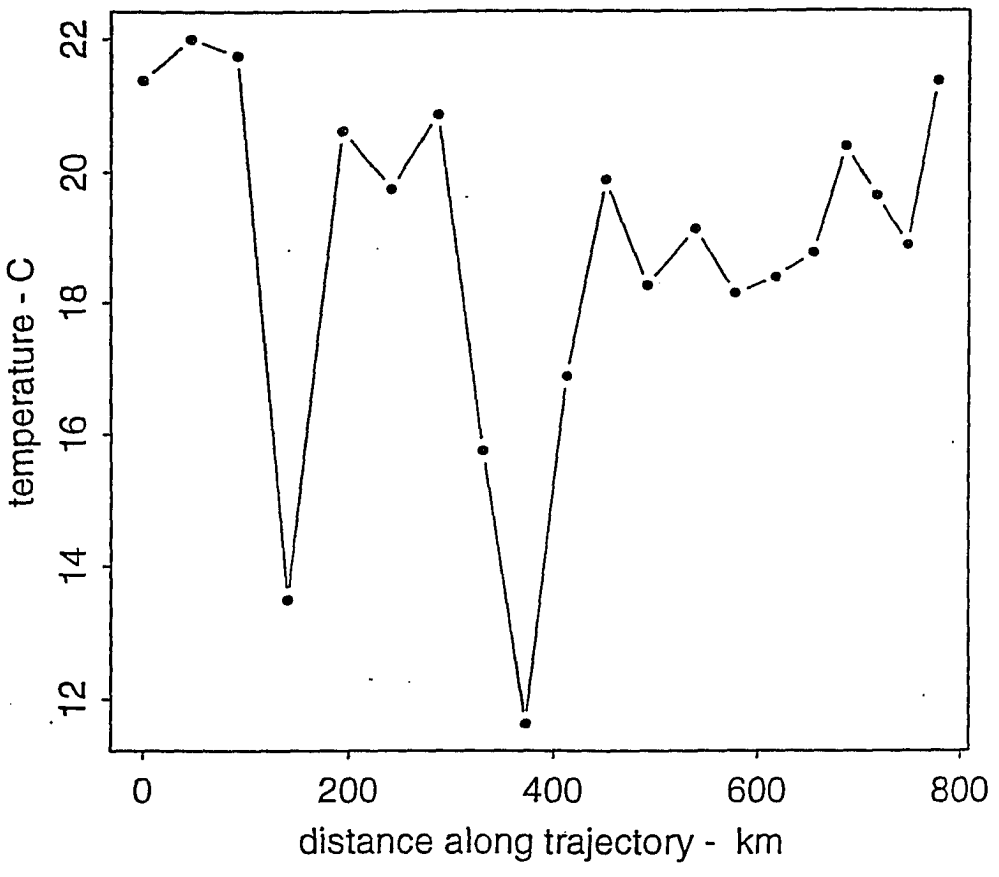

Figure 26: Plot displaying the trajectory for drifter 4480.

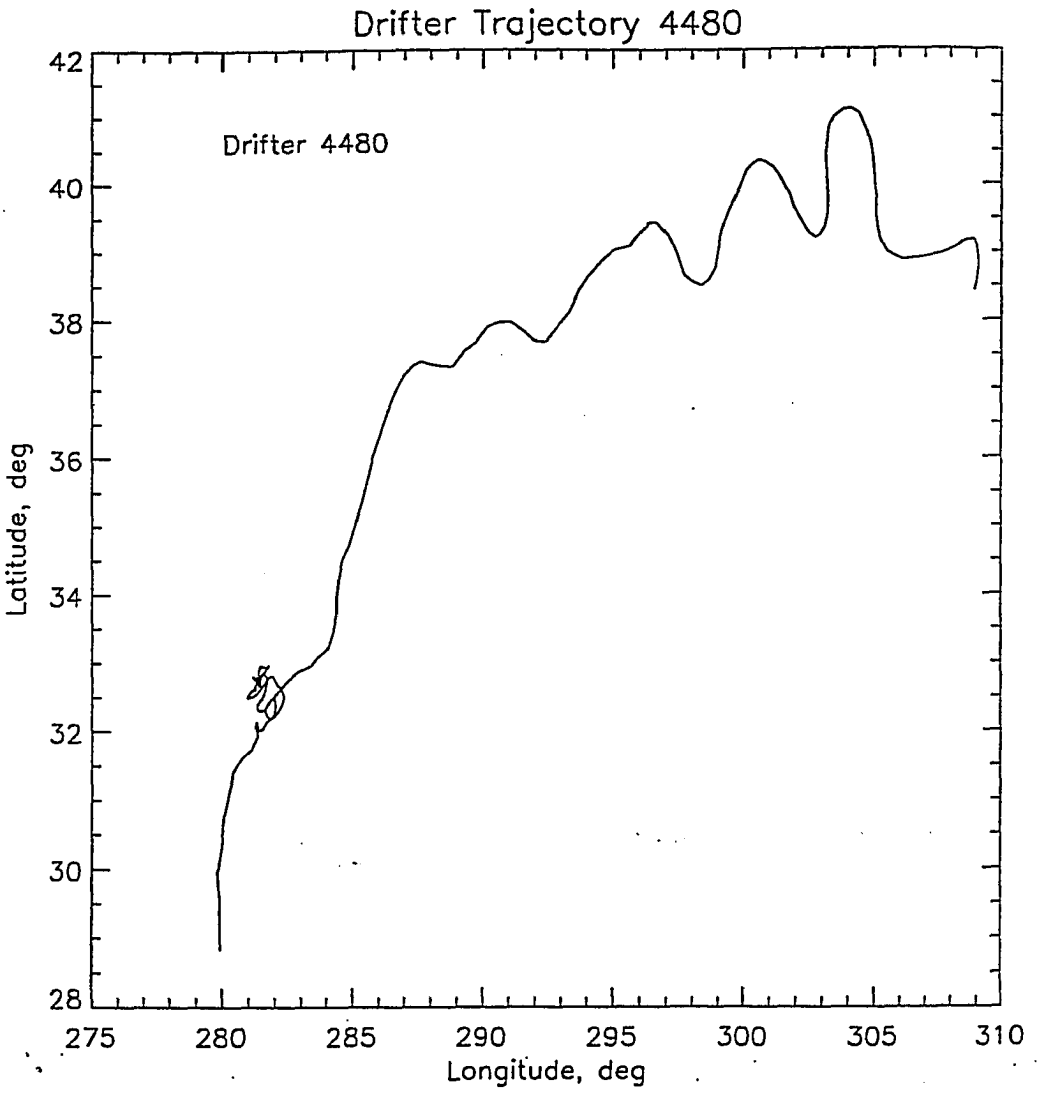

Figure 27: Image 47 of the Gulf Stream with drifter 4480 overlaid in black. (courtesy of RSMAS)

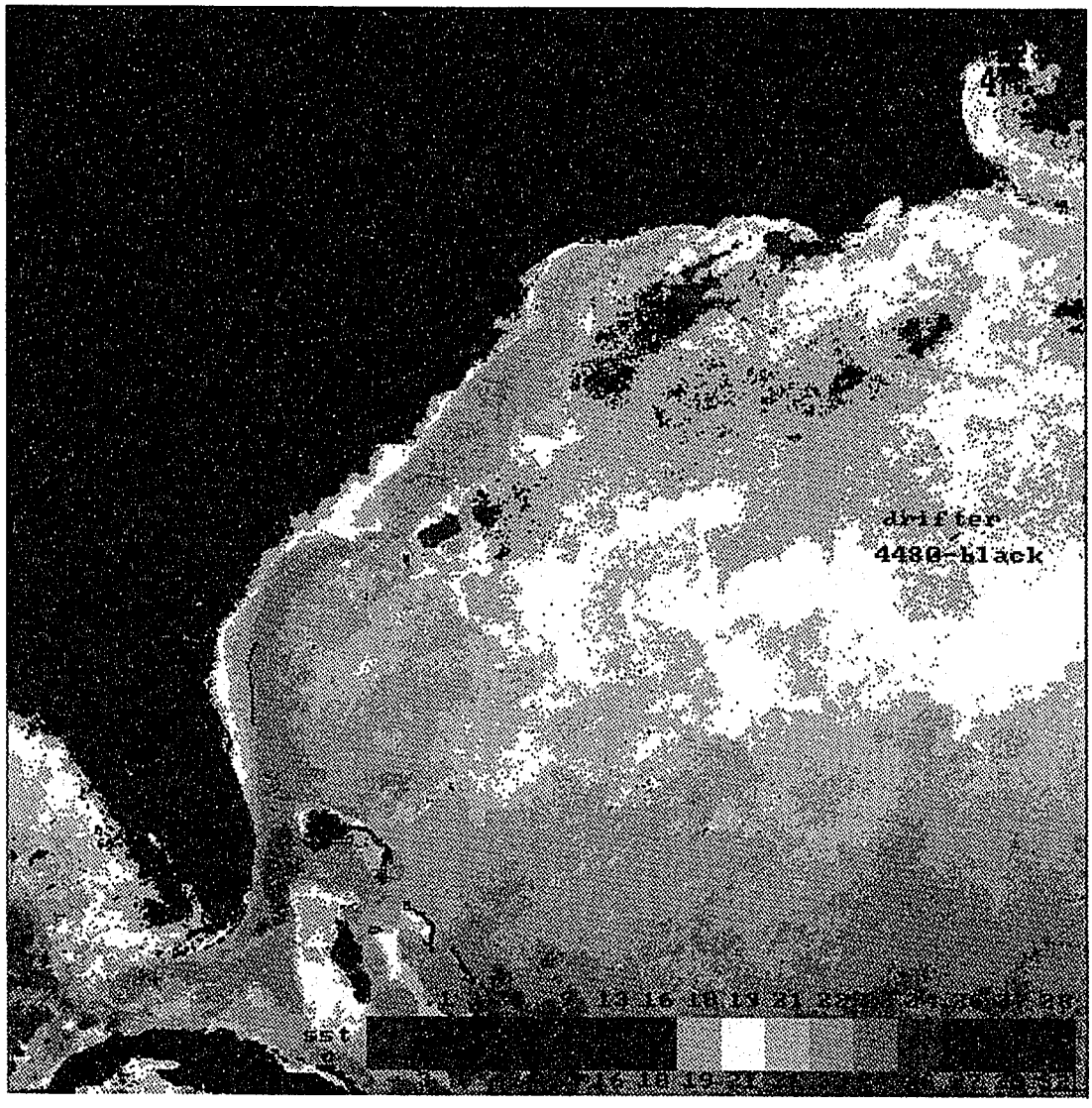

Figure 28: Image 52 of the Gulf Stream with drifter 4480 overlaid in black. (courtesy of RSMAS)

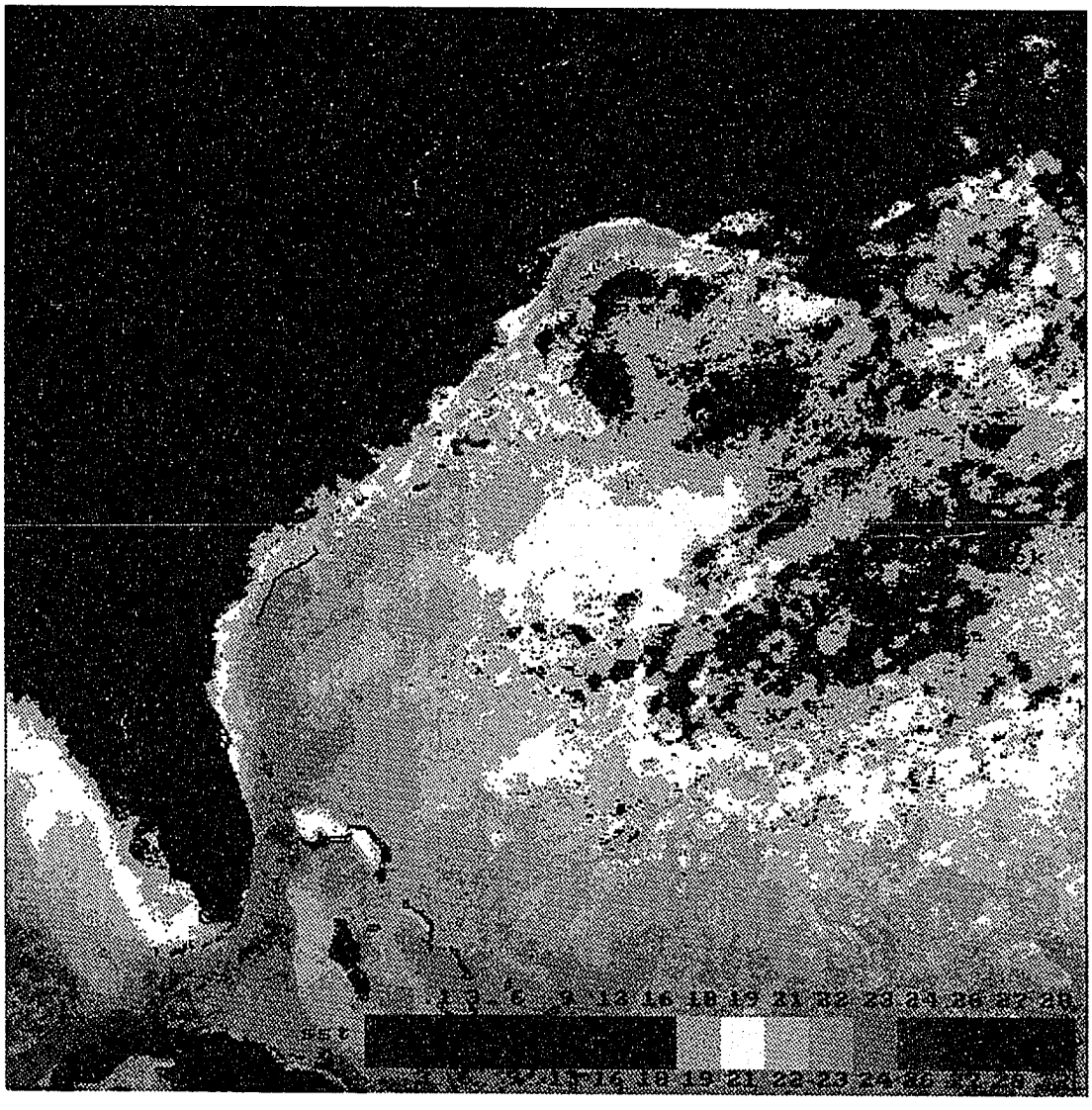

4480 does not follow any particular temperature front and it has a very short path for the same length of time as the other images (see Appendix). Figure 29 shows the exact temperature values followed by drifter 4480 over images 47 and 52.

Image 85 shows that drifter 4480 does closely correlate with the 23°C temperature front (Figure 30). This image is a seven-day composite. Figure 31, the plot depicting the temperature along the drifter trajectory for 4480 on image 85, shows this close correlation. Perhaps, this is because the drifter has traveled a longer distance over a longer time period. Figure 32 shows a histogram of the temperature values seen by drifter 4480 in image 85. The average temperature seen by 4480 in image 85 is approximately 23°C. The narrow character of the histogram confirms the fact that drifter 4480 does follow very closely the 23°C temperature front.

In GT37, the drifter trajectory for 4480 seems to follow closely the temperature front in some instances and not in others. The corresponding images to the region for drifter 4480 and 4481 are image 92, 96 and 101 (Figures 33, 34 and 35). These images display the drifter trajectories for 4480 and 4481 over the corresponding time periods. Figure 33 shows 4480, black colored trajectory, flowing along the Gulf Stream in the 23°C temperature region. It does not follow the temperatures front exactly, but does mimic its shape. Over time 4480 finally is located in GT37 where it follows the Gulf Stream meandering shape displaying crests and troughs. In Figure 35, image 101 shows drifter 4480 still following the Gulf Stream but, now within a much lower temperature region than found in Figure 33. Figure 36 illustrates the temperature values seen by drifter 4480 as it flows along the Gulf Stream. It shows the increase and decrease in temperatures along the drifter path. In Figure 36a, the small amount of variability in the temperature along the path is illustrated; part b shows the variance in temperatures at the crest and troughs; and part c shows how little the temperature varies along drifter 4480 in image 101.

Figure 29: Plot showing the temperature values of drifter 4480 along its path through images a) 47, b) 52, c) 57 and d) 60. (courtesy of RSMAS)

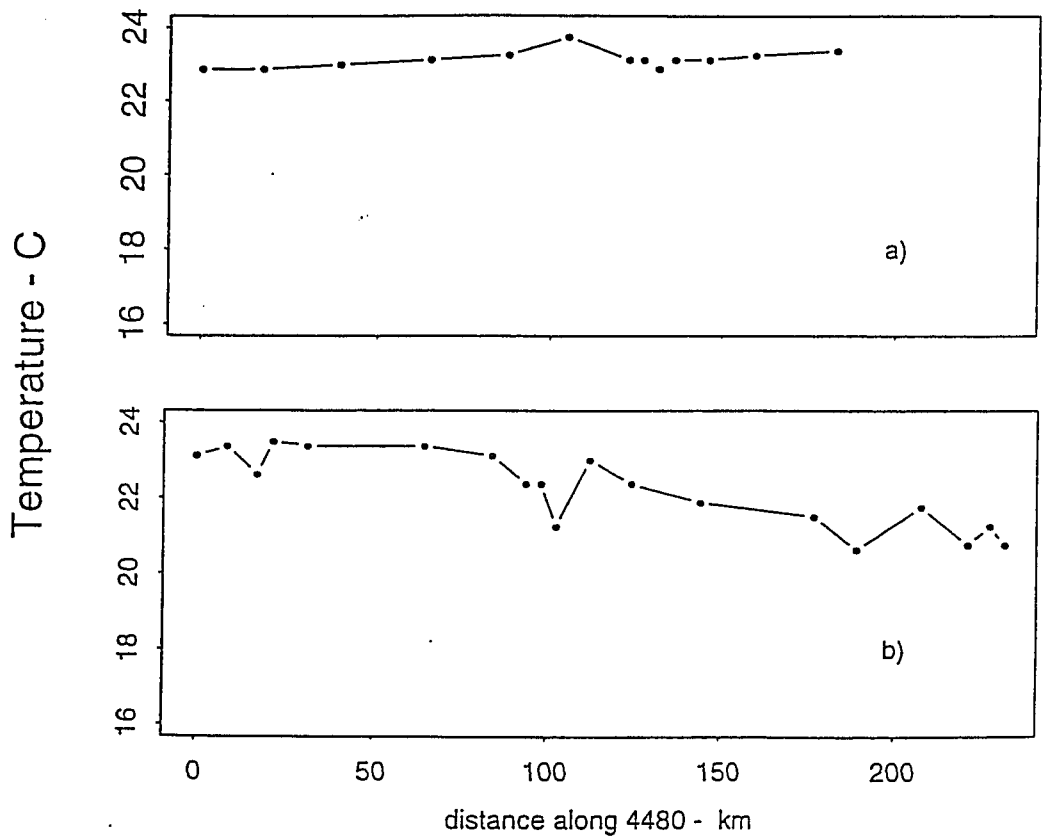

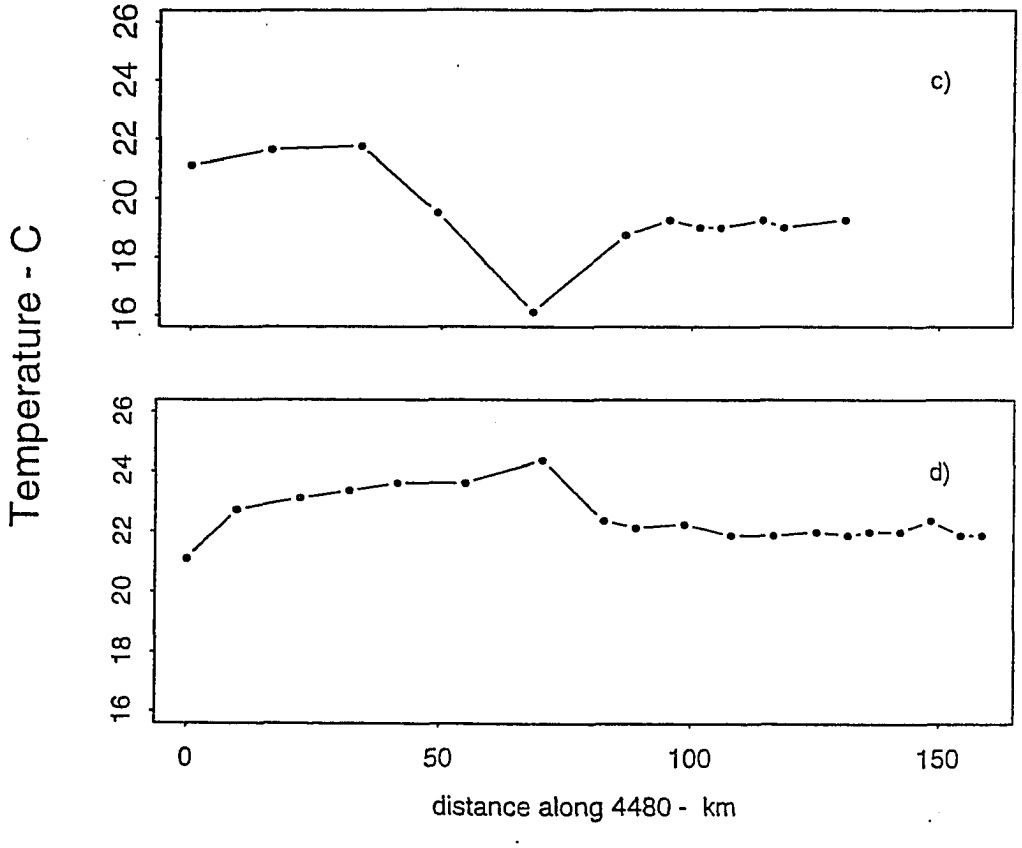

Figure 30: Image 85 of the Gulf Stream with drifter 4480 and 4481 superposed in black and light blue, respectively. (courtesy of RSMAS)

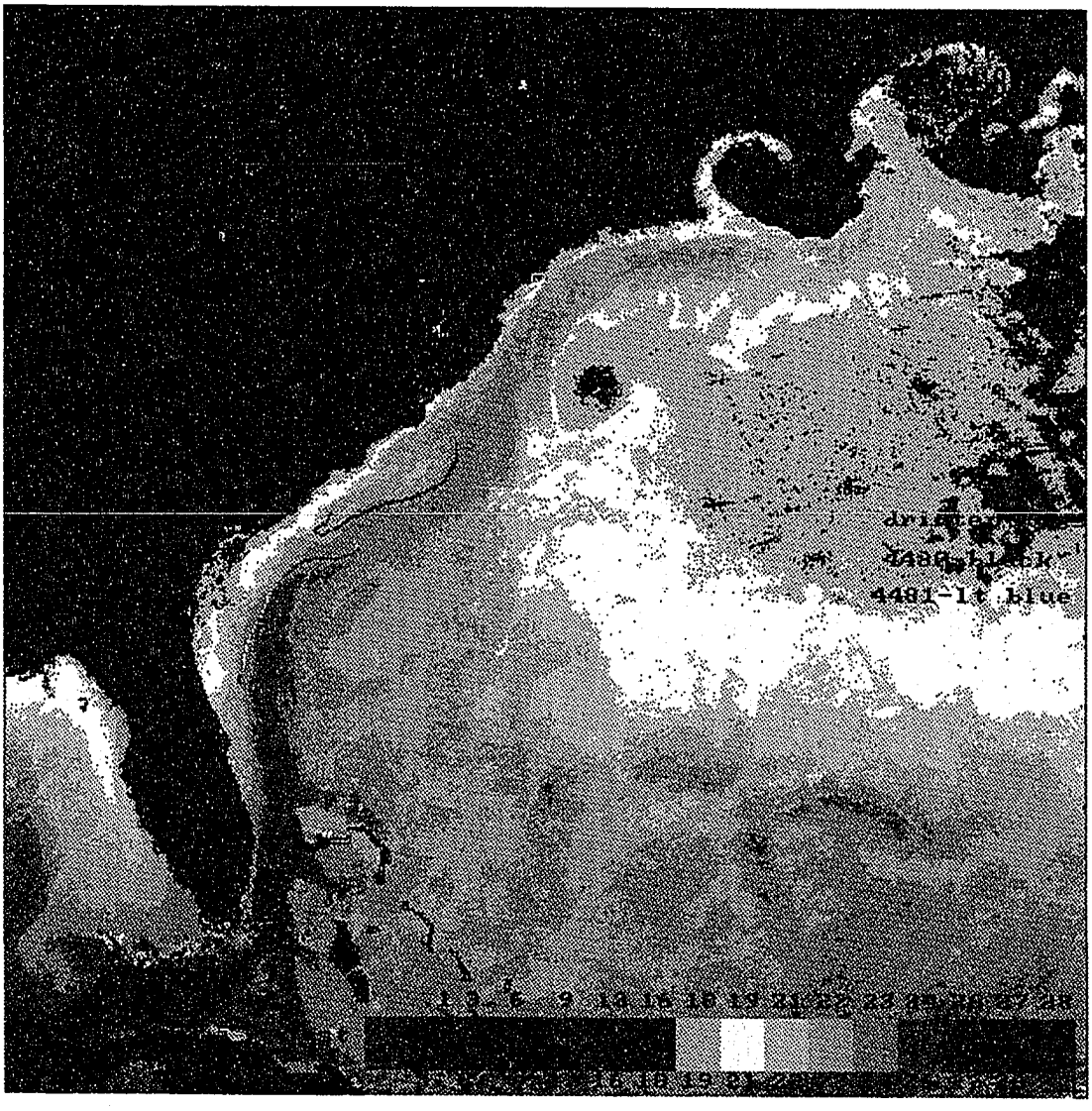

Figure 31: Temperature versus distance along drifter 4480 for image 85.

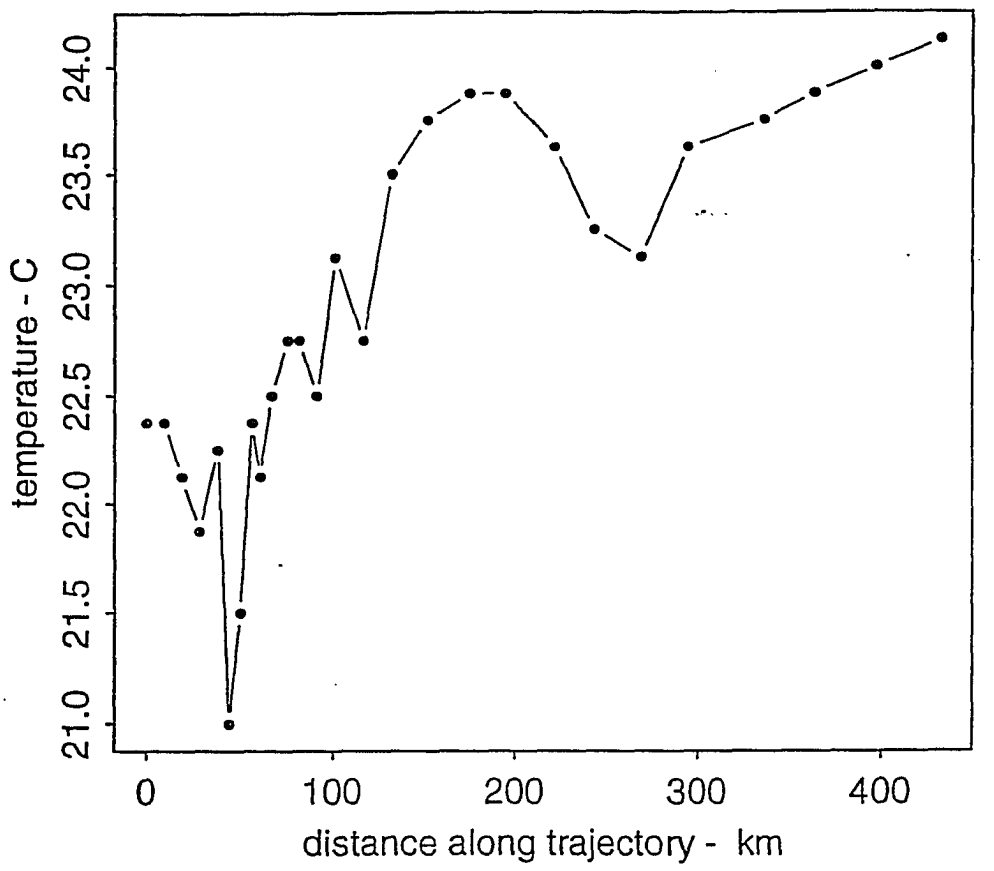

Figure 32: Histogram representing the temperature values observed by drifter 4480 on image 85 with a mean temperature value of 23.274°C.

Mean: 23.274 deg C.

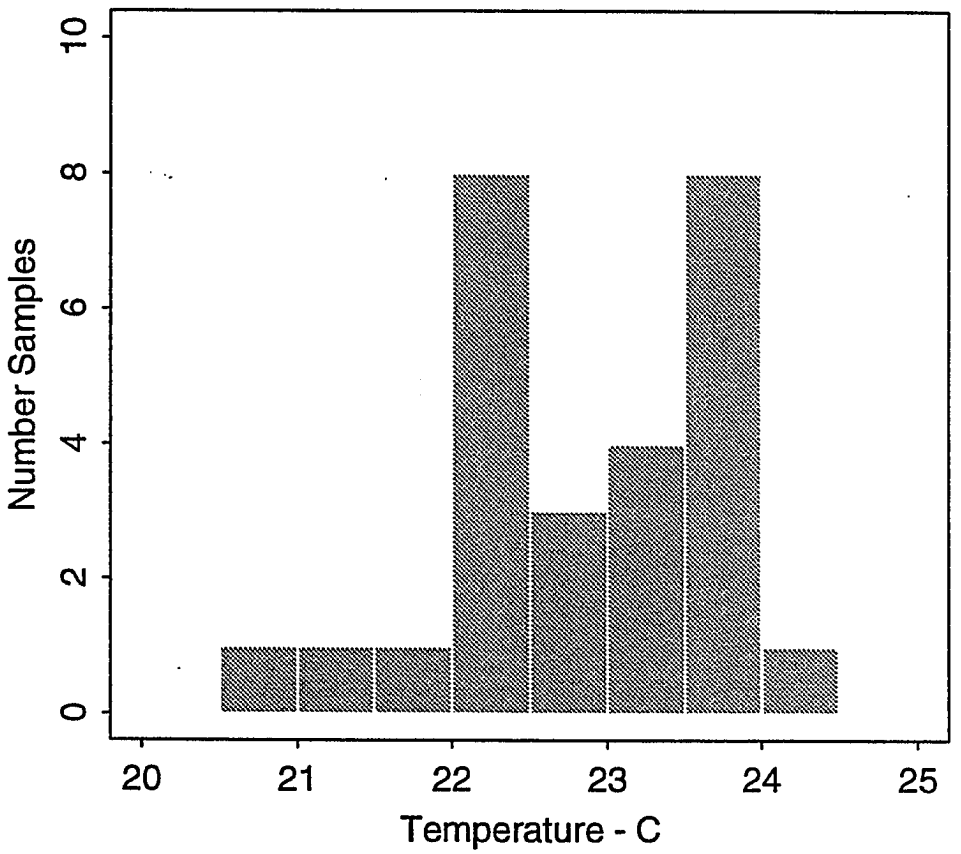

Figure 33: Image 92 of the Gulf Stream with two drifters superposed. Drifter 4480 - black, Drifter 4481- light blue, (courtesy of RSMAS)

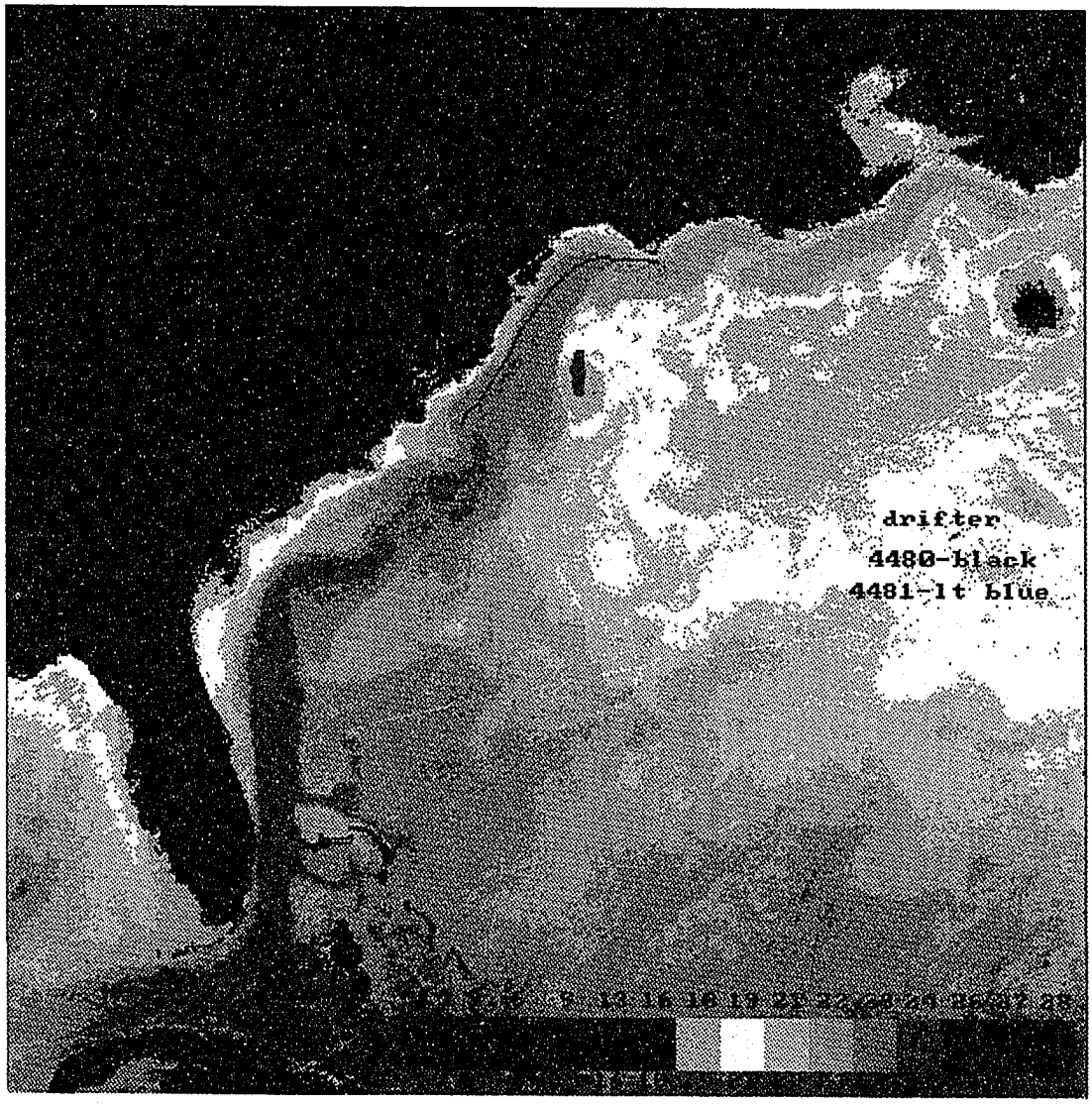

Figure 34: Image 96 of the Gulf Stream with two drifters superposed. Drifter 4480 - black, Drifter 4481- light blue, (courtesy of RSMAS)

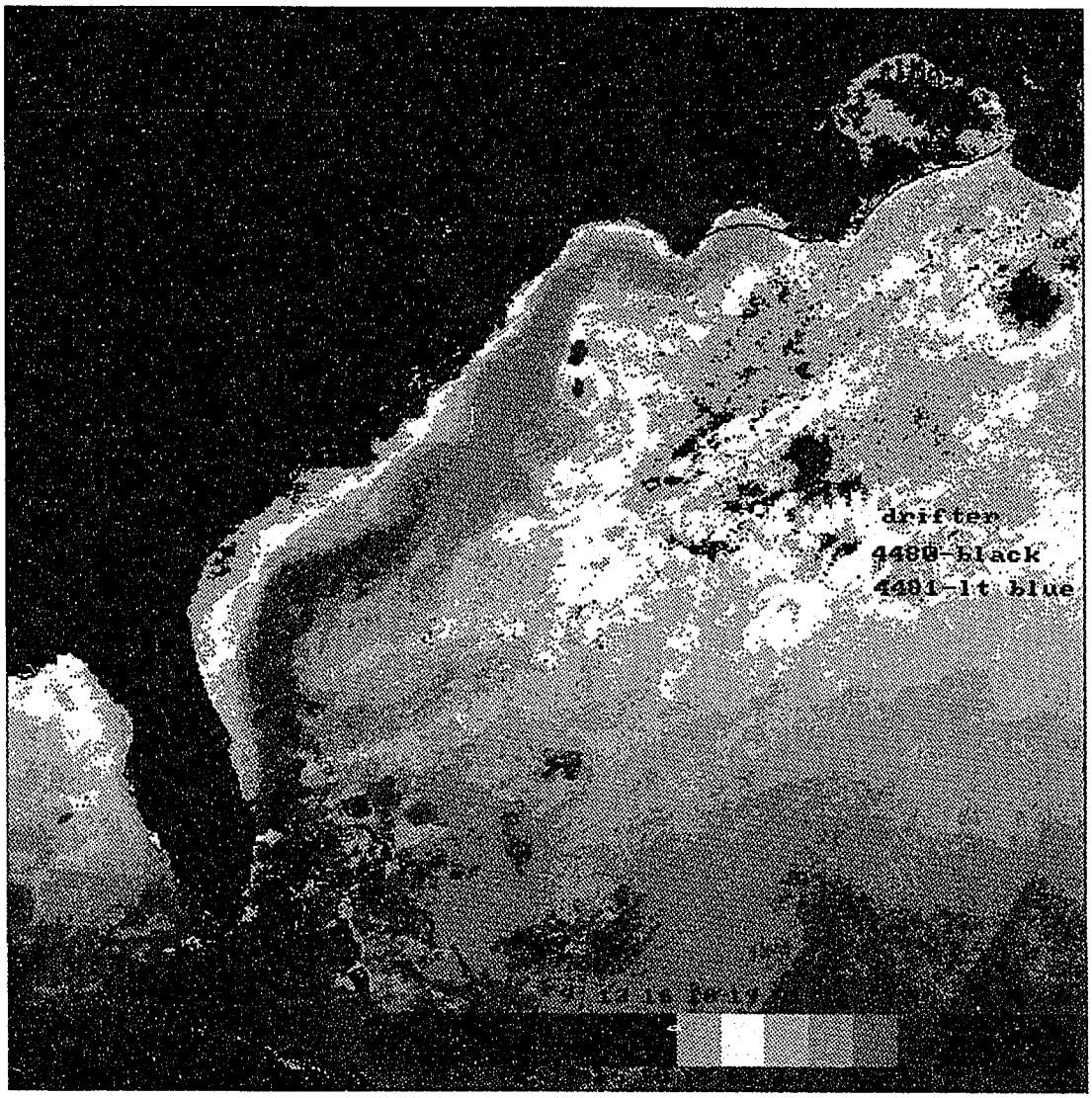

Figure 35: Image 101 of the Gulf Stream with two drifters superposed. Drifter 4480 - black, Drifter 4481- red, (courtesy of RSMAS)

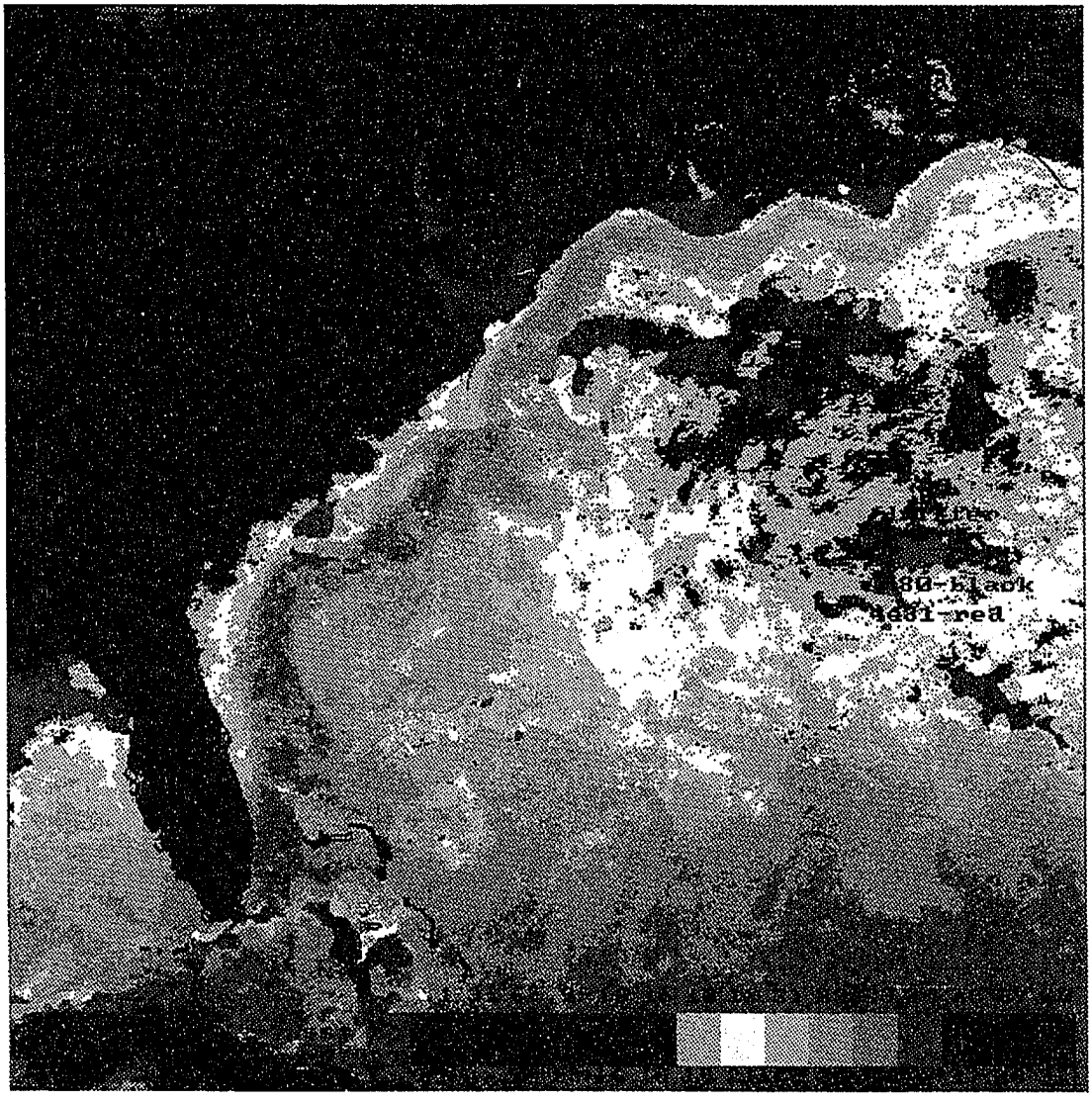

Figure 36: Plot depicting the temperature values for drifter 4480 in images a) 92, b) 96 and c) 101.

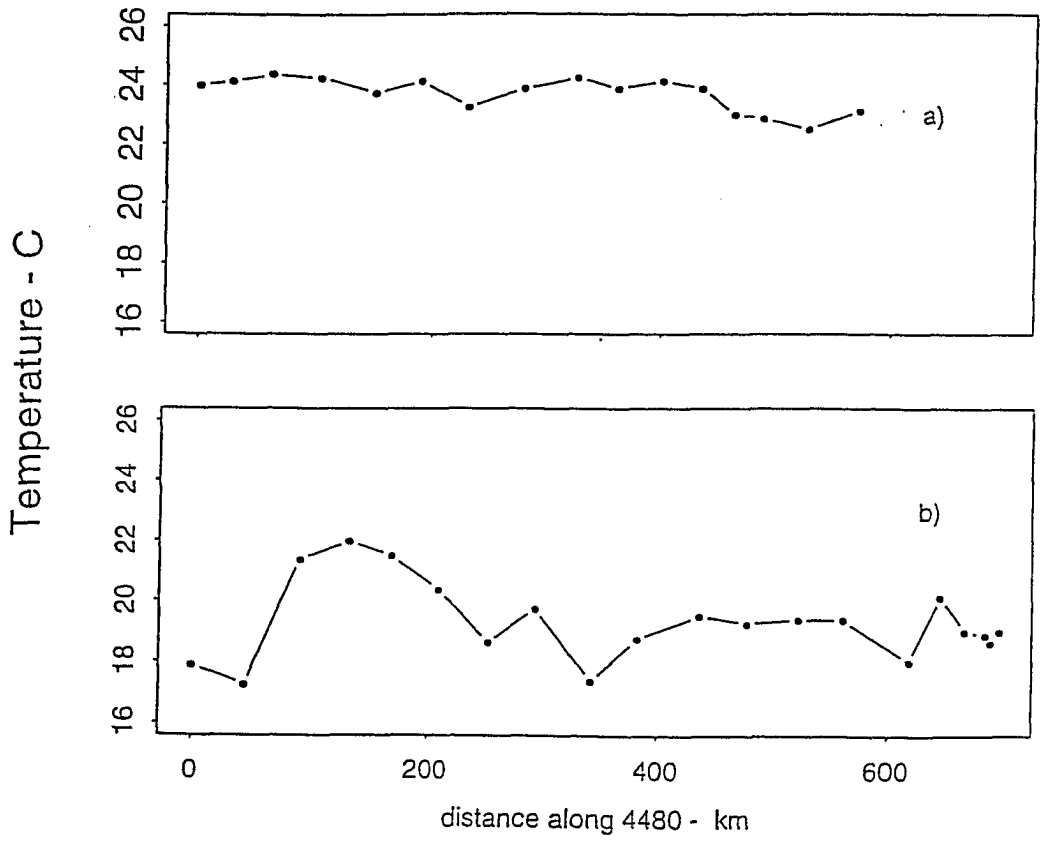

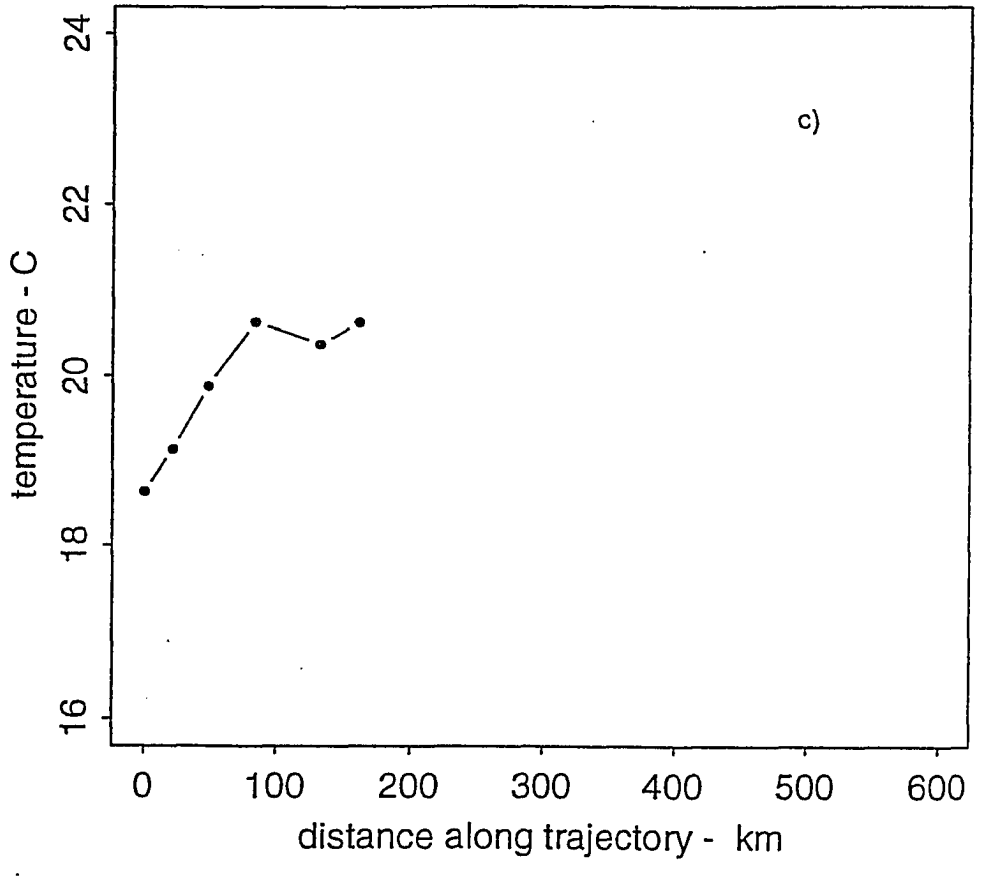

Drifter 4481 was deployed on March 16, 1985, and recorded data only until April 30, 1985. Thus, the drifter remained in LT37 for its entire lifespan as seen in Figure 32. This drifter closely follows the 25°C temperature front of the Gulf Stream in image 92 (see Figure 33). It clearly mimics the shape of the Stream in this area. Image 96 shows that 4481 moves along with the Gulf Stream but, once again not exactly along a temperature front (see Figure 34). However, it does remain in the 23°C temperature range, the dark orange color band. The path of 4481 on image 101 is relatively short compared to the previous trajectories on other images (see Figure 35). This is caused by the decrease in drifter speed. The path starts in warmer water and flows into cooler waters where it closely follows the 20°C temperature front (see Figure 35). The decrease in temperature is surprising because all images are representative of the same month, with image 101 being the latest in that month. Perhaps, the decrease is due to the fact that the Gulf Stream has lost most of its structure and is not as coherent as in previous images.

Figures 37 and 38 show that the drifter 4481 does follows a relatively constant temperature front within the 23-25°C range. Drifter 4481 exhibits little variability in its temperature values until its path corresponds to image 101. Here, the value drastically decreases to 20°C (see Figure 38). This was discussed earlier in reference to the imagery (see Figure 35). A histogram of the temperature observed by drifter 4481 was generated (Figure 39). Its mean value of 23.72°C with its low standard deviation is consistent with the description stated above. The trajectory path of 4481 for images 80, 106, 111, and 116 are extremely short and thus, at present warrant little explanation (see Appendix). In summary, regardless of whether observations were made in GT37 or LT37, most drifter trajectories for a given time period did not exactly follow a specific temperature front. However, overall the drifter trajectory usually did fall within a certain temperature range (a specific color band).

Figure 37: Temperature versus distance along drifter trajectory 4481 for images a) 85 and b) 92.

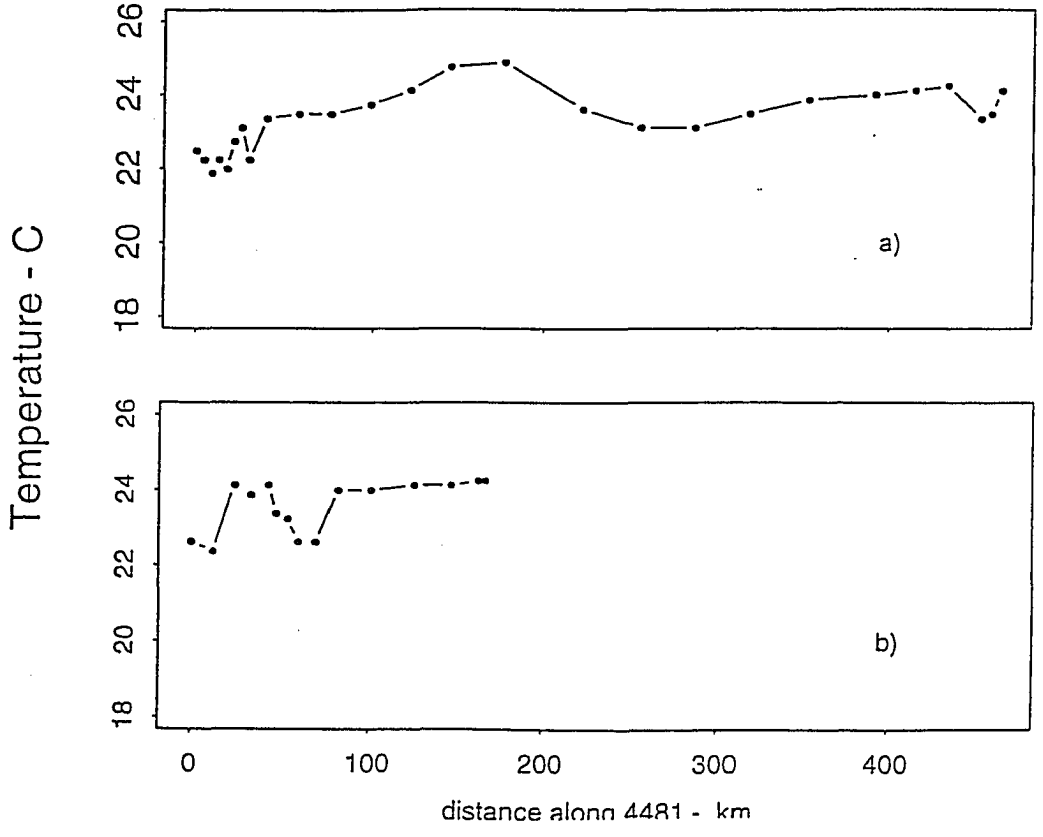

Figure 38: Temperature versus distance along drifter trajectory 4481 for images a) 96 and b) 101.

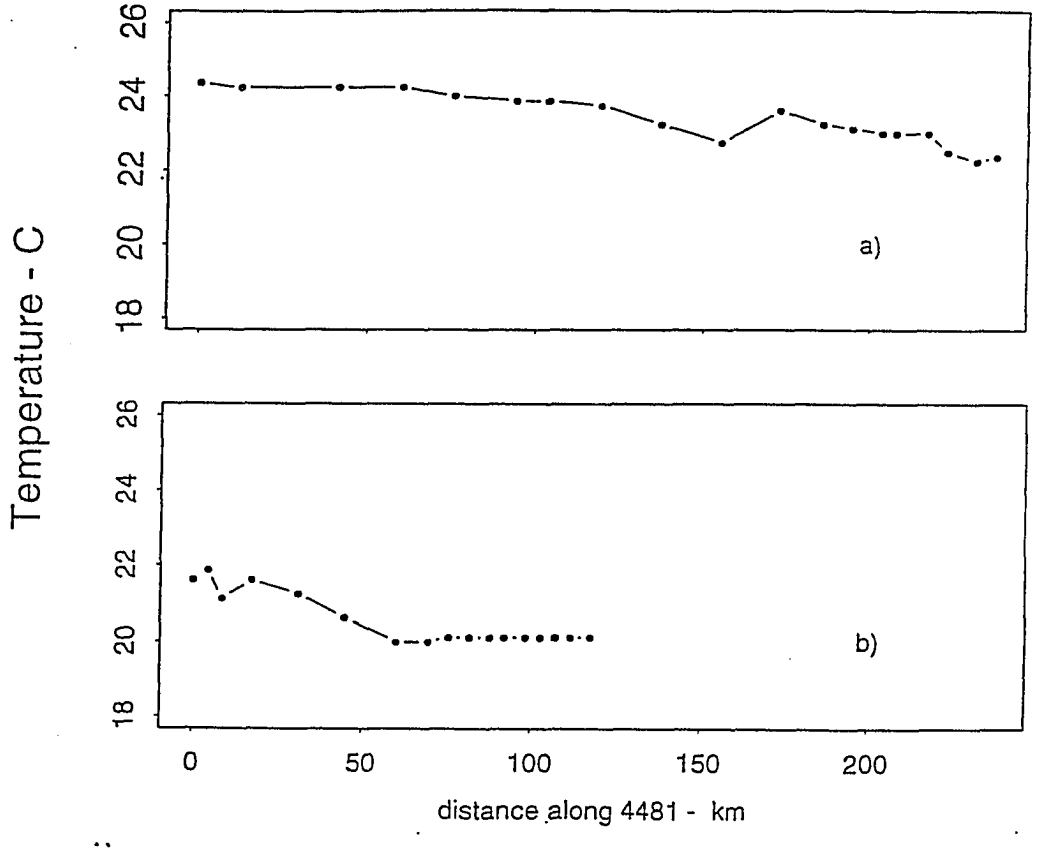

Figure 39: Histogram of the temperature along the path of 4481 on image 85. mean temperature = 23.724°C.

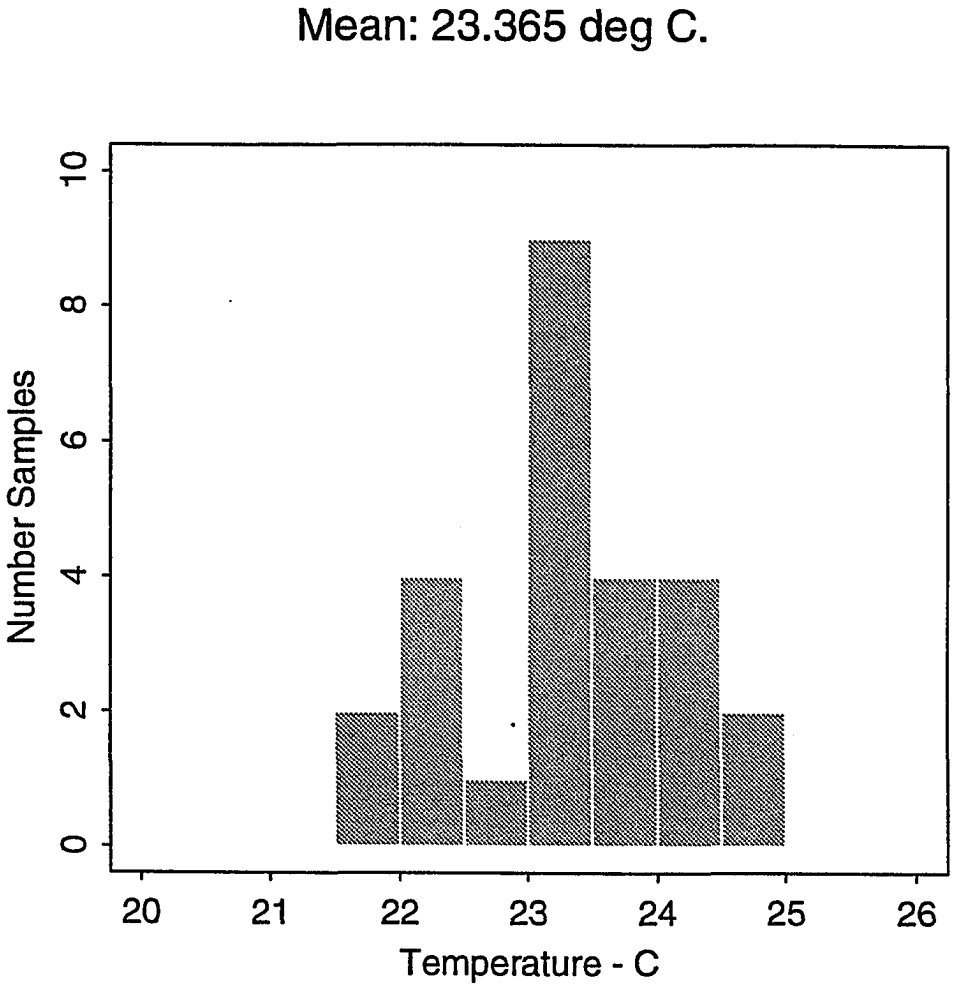

5.2 Temperature at Meander Crests and Troughs

The point addressed here is the relationship between the position on the Gulf Stream meander and the temperature field. Image 96 is a composite satellite image of the Gulf Stream for the time period April 6 - 10, 1985 (see Figure 34). This figure shows that the drifter 4480 closely follows the meandering jet of the Gulf Stream. Figure 40 illustrates the position of the Gulf Stream crest and trough in relation to the drifter trajectory. As pointed out in both panels of Figure 40, the warmer temperature along the path for drifter 4480 is located in the meander crests and the lowest temperatures are found in the meander troughs (Mullen and Kirwan, 1994). This is also depicted for image 92 in the first plot, but the change in temperature is not as dramatic. By analyzing temperature versus distance along the drifter trajectory plots for GT37, it becomes clear that there is a relationship between the warmer temperature of the drifter path and the crests of the meanders. This should help determine whether there is a correlation between the temperature field and velocity field of the Gulf Stream. Analysis of drifter 4480 on image 92 shows that the temperature at the crest is warmer than at the trough. The same holds true on image 96. However there is an exception to this observation as shown in image 101. Within this image, the drifter encounters warmer temperatures, but only by 0.3°C, at a meander trough (see Figure 35).

Analyses of four GT37 images, 47, 92, 96 and 101, shows that overall the temperature in the crests is warmer than in the meander troughs. This is depicted in Figure 40. For image 92, drifter 4480 has a temperature of 24.0°C at its crests and 23.4°C at the troughs. Looking at image 96 and drifter 4480, the temperature in the first trough (farthest east) is 17.8°C, the corresponding crest has a value of 22°C. The next trough/crest sequence has values of 17.8°C for the trough and 20.3°C for the crest. Again, this shows that the temperature at the crest is slightly warmer

Figure 40: Plot displaying temperature versus distance along trajectory 4480 on image a) 92 and b) image 96. C = crest region of Gulf Stream, T = trough region of Gulf Stream.

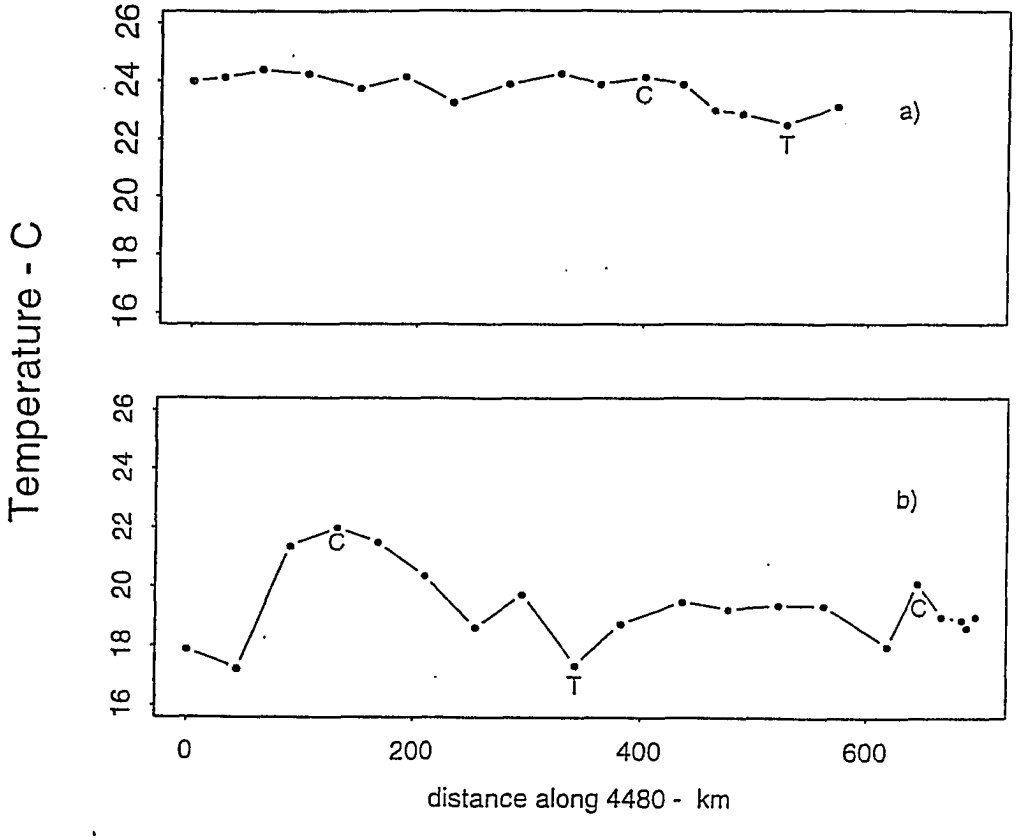

at the crest is slightly warmer than at the troughs. The temperature values for drifter 4480 at the crests and troughs for image 101 are the same, approximately 19°C. Finally, image 47 displays drifter 4479 in GT37. However, the "path" of the Gulf Stream is not continuous. Because of this the temperature values at the crest and troughs were difficult to determine. The crest farthest to the east displays a temperature of 20.6°C while the corresponding trough has a value of 11.9°C. The next crest has a temperature value of 20.5°C. Overall, this analyses shows that meander crests do correspond to warmer temperature values, while the troughs are correlated with colder values.

5.3 Meander Amplitudes and Wavelengths

Meander wavelengths and amplitudes are important parameters to calculate through the kinematic analysis of this contemporaneous data set. The sequential set of composite images, 92, 96 and 101 (see Figures 33, 34 and 35), are analyzed in order to obtain their meander amplitudes and wavelengths. In image 92, the wavelength from crest one (farthest to the west) to crest two (middle region) is approximately 262 *km*, while from crest two to crest three (farthest to the east) it is much greater at 436 *km*. The amplitudes corresponding to these three crests are 30 *km*, 26 *km* and 28.16 *km*, respectively. Similar results for image 96 are observed (see Figure 34). The wavelength from crest one to crest two is 255 *km*; and from crest two to crest three it is 485 *km*. It is interesting to note that the meander amplitudes are larger than in image 92. These amplitudes range from 37 - 41 *km*. Image 101 has wavelength values of 322 - 396 *km*. Here, the amplitudes are similar to those calculated for image 92. The amplitudes calculated are 28 *km*, 30 *km* and 26 *km* for crest one, crest two and crest three, respectively.

Analysis of these three images reveals an average wavelength of 360 *km* and

an average amplitude of 32 *km*. These values are consistent with past studies of waters east of 70°W, where the wavelengths have been recorded between 200 - 400 *km* (Halliwell and Mooers, 1983; Tracey and Watts, 1986). Furthermore, it is interesting to note that overall the meander wavelengths decrease as the amplitudes increase (Halliwell and Mooers, 1983).

5.4 Meander Phase Speeds

GT37 is dominated by the high degree of Gulf Stream meandering. These meanders can have different phase speeds and can propagate east or westward. A representative case for determining the meander phase speed is discussed below. This example is depicted by images 92, 96 and 101 with drifters 4480 and 4481 superposed on the images (Figures 33, 34 and 35). In order to determine the phase speeds of each meander, the direction of the meanders needed to be calculated. This was done by marking the crest of a meander on image 92 and then marking the corresponding crest on the following image. If the displacement between the two image meander crests is to the right, then the Gulf Stream meander is propagating to the east. The time elapsed for each image is known. Once the distance between the meander crests for the two composite images is calculated, the phase velocity can be obtained.

Three separate sets of meander crests can be delineated in composite images 92, 96 and 101. The number of days elapsed between images 92 and 96 is five. Calculations show that the phase speeds for the crest displacement between image 92 and 96 are for crest one (farthest to the west): 9 $km\ dy^{-1}$, crest two: 9 $km\ dy^{-1}$ and crest three: 18 $km\ dy^{-1}$. This value is two times as large as the others because of the dramatic increase in distance traversed from meander to meander. The following are the meander phase speeds for image 96 and 101; crest one: 9 $km\ dy^{-1}$,

crest two: 22 $km\ dy^{-1}$ and 5 $km\ dy^{-1}$ for crest three. The average speed for the GT37 is 12 $km\ dy^{-1}$. Past observational studies have recorded average phase speeds of approximately 10.0 $km\ dy^{-1}$, 10.0 $km\ dy^{-1}$ and 10.8 $km\ dy^{-1}$ (Hansen (1970); Gillman (1988); Pratt (1988), respectively). Vazquez and Watts (1985) also obtained similar values. Phase speed values used in model studies of a meandering jet range from 10.0 $km\ dy^{-1}$ to 14.0 $km\ dy^{-1}$ (Bower (1991); Cushman-Roisin (1993); Dutkiewicz et al. (1993)). Here, the observed values will be used as the meander phase speed in the kinematic and dynamic models of the Gulf Stream. The main conclusion to draw from this analysis is that the meanders are propagating eastward at an average phase speed of 12 $km\ dy^{-1}$.

5.5 Speeds at Meander Crests and Troughs

The speed of the drifter at the meander crests and troughs is also an important factor needed in the analysis of the correlation between the composite imagery and drifter trajectories. Four images and corresponding drifters for GT37 are analyzed in order to calculate the speed at specific locations along the Gulf Stream (see Figures 24, 33, 34 and 35). Image 47 (see Figure 24) shows drifter 4479 flowing along the meandering Gulf Stream. There are three crests and two troughs on the image. Crest one corresponds to the meander crest farthest to the west. It has a drifter speed of 184 $km\ dy^{-1}$. The next crest has a drifter speed of 182 $km\ dy^{-1}$. Finally, the speed of 182 $km\ dy^{-1}$ is calculated for the drifter on the third crest. The speeds at the troughs are lower than those observed at the crests of the meanders. The first trough has a value of 177 $km\ dy^{-1}$ while the second one has a value of 163 $km\ dy^{-1}$.

In the sequence of composite satellite images (see Figures 33, 34 and 35), the speed at the crests and troughs can be calculated. For image 92 (see Figure 33), the drifter speed at the crest is 158 $km\ dy^{-1}$ and at the trough it is 157 $km\ dy^{-1}$.

Figure 34 shows image 96 with drifter 4480 in GT37. Drifter 4480 clearly flows along the Gulf Stream following its meander pattern. Speed values of drifter 4480 were calculated at each crest and trough along the trajectory. The first trough region has a drifter speed of 87 $km\ dy^{-1}$, while its corresponding crest has a much higher value of 148 $km\ dy^{-1}$ As the drifter flows into the next trough its speed increases to 152 $km\ dy^{-1}$. Finally at the last crest, the drifter speed has increased to 165 $km\ dy^{-1}$. The last composite in this sequence of images is image 101 (see Figure 35). The drifter speed is slightly lower at the crest than the trough. It has a value of 120 $km\ dy^{-1}$ at the crest and 135 $km\ dy^{-1}$ at the trough. Overall, it appears as if the drifter speeds are slightly higher at the meander crests than at the troughs and that the speeds are high in the GT37 region of the Gulf Stream.

The speed of drifter 4480 also increases substantially after the drifter begins to flow eastward away from the coast and the effects of topography. Here, it obtains values of up to 180 $km\ day^{-1}$ (FACTS, 1986). The speed for drifter 4480 increase within image 96 (see Figure 34) and then decrease slightly in image 101 (see figure 35). Studies on these drifters shows that the speeds are quite high in GT37 region of the Gulf Stream. Overall, the analysis here demonstrates that the drifters move faster at the meander crests than they do at the troughs.

5.6 Transects Across the Gulf Stream

In order to determine whether the gradients of the composite temperature field have a direct relationship with the drifter trajectories and velocities, the entire temperature field of the Gulf Stream must be understood. In addition to the analysis of the temperature values along the drifter path, temperature values across the Gulf Stream must be obtained. Therefore, several "transects" were made across the Gulf Stream. The term "transect" is used here to define the perpendicular line cutting

across the Gulf Stream where temperature values were extracted from the satellite imagery. These transects also cut through the corresponding drifter on the image. Once the data is extracted from the satellite imagery, temperature and speed values were calculated at the drifter/transect intersection. This information can be used to help determine whether there is a relationship between the surface velocities and temperature field. Note that analysis will be performed on LT37 and GT37, with the emphasis concentrating on the speed and temperature values obtained for the drifters in the meandering portion of the Gulf Stream.

Several transects were made across the Gulf Stream in LT37. Here, the flow is governed by the bottom topography. Figure 41 shows three transects across drifter 4479 for the time period corresponding to image 42. The transect farthest to the north along the drifter path has a speed of 79 $km\ dy^{-1}$ and a temperature value of 21.50°C. Values of 70 $km\ dy^{-1}$ and 21.63°C are evident for the middle transect across drifter 4479 in image 42. The last transect has a speed of 60 $km\ dy^{-1}$ with a temperature of 22.50°C at the drifter transect intersection.

Drifter 4480 in image 47 closely follows the 23°C temperature front. Within this image (Figure 42) the drifter trajectory is just off the coast of Florida. Three transects were made across this path to obtain the speed for this drifter. Starting at the northern transect the speeds are 55 $km\ dy^{-1}$, 83 $km\ dy^{-1}$ and 74 $km\ dy^{-1}$. The corresponding temperatures for the three transects are 23.38°C, 23.50°C and 23.00°C. Drifter 4481 has speeds which range from $150-180\ km\ dy^{-1}$. These speeds are much greater than those experienced by drifter 4480. For image 52, three more transects were made across the drifter path (Figure 43). Drifter 4480 continues to flow along the temperature front as in image 47. The temperature values are within the 23°C temperature range.

Drifters 4480 and 4481 are both located in the LT37 in image 85 (Figure 44).

Figure 41: Image 42 of the Gulf Stream with two drifters superposed. Drifter 4478 - red, Drifter 4479 - black. Drifter 4479 has three transects across it. (courtesy of RSMAS)

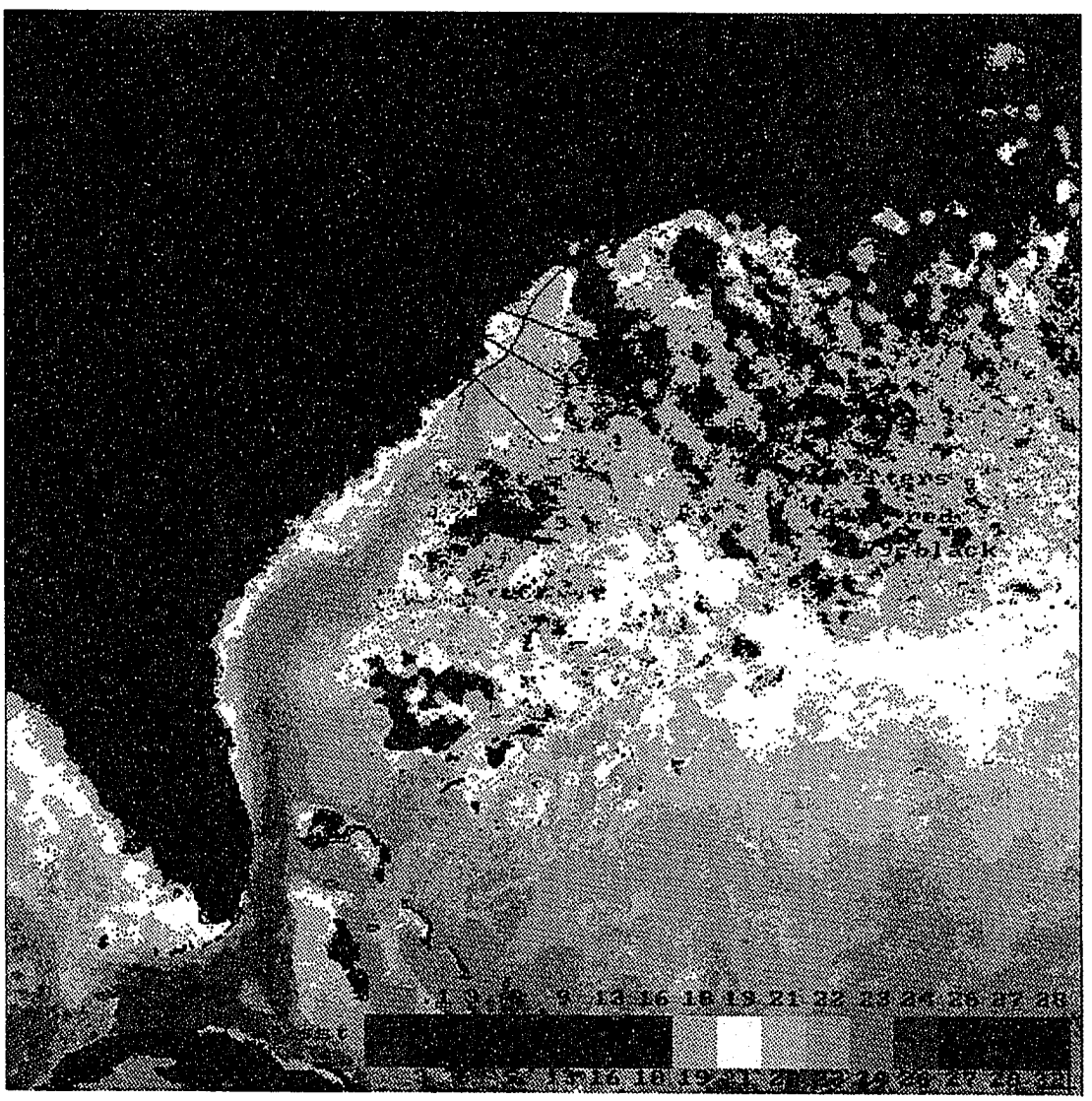

Figure 42: Image 47 of the Gulf Stream with three drifters superposed. Drifter 4478 - red, Drifter 4479 - black with six transects, Drifter 4480 - light blue with three transects. (courtesy of RSMAS)

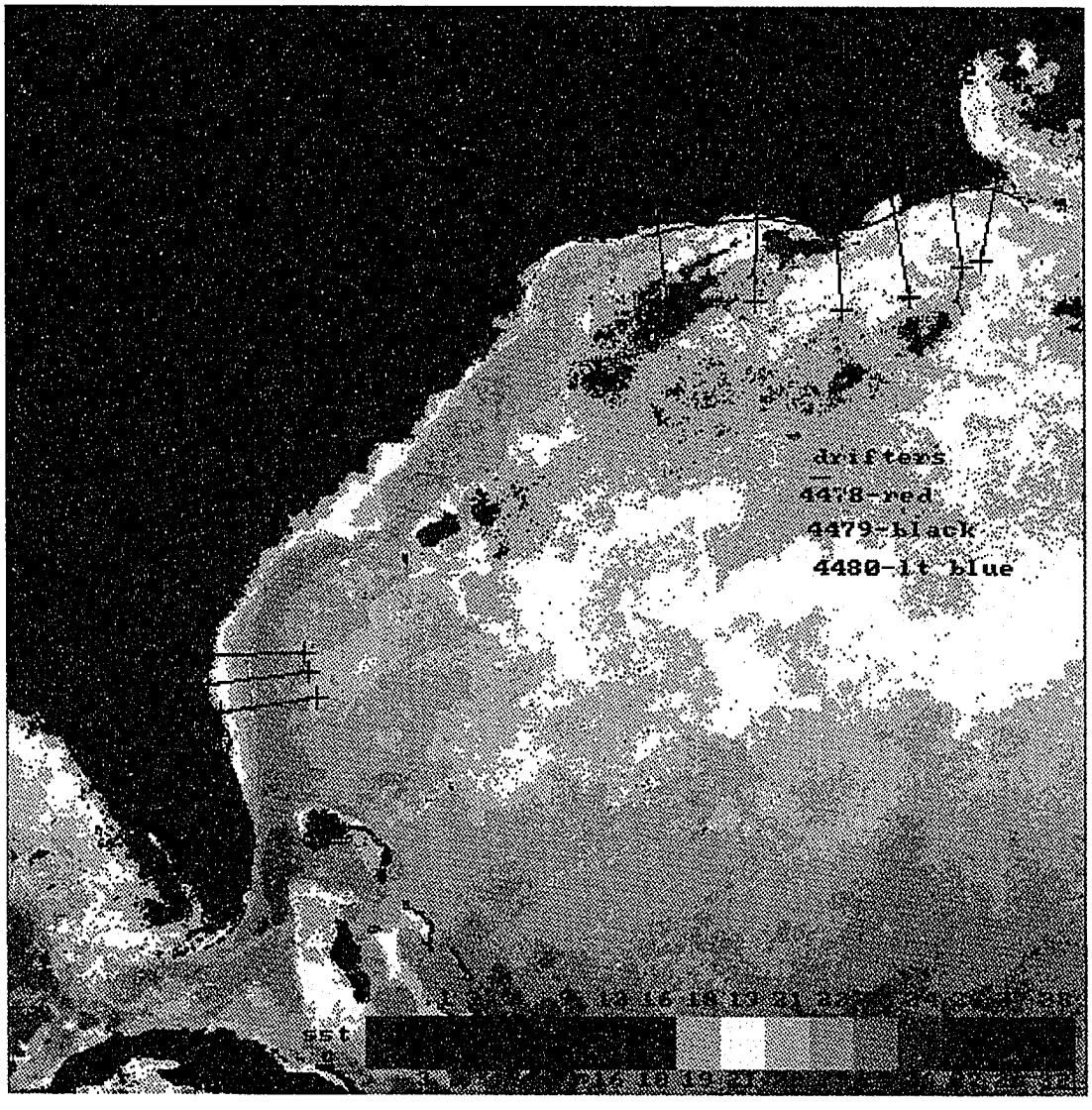

Figure 43: Image 52 of the Gulf Stream with two drifters superposed. Drifter 4479 - red, Drifter 4480 - black withe three transects. (courtesy of RSMAS)

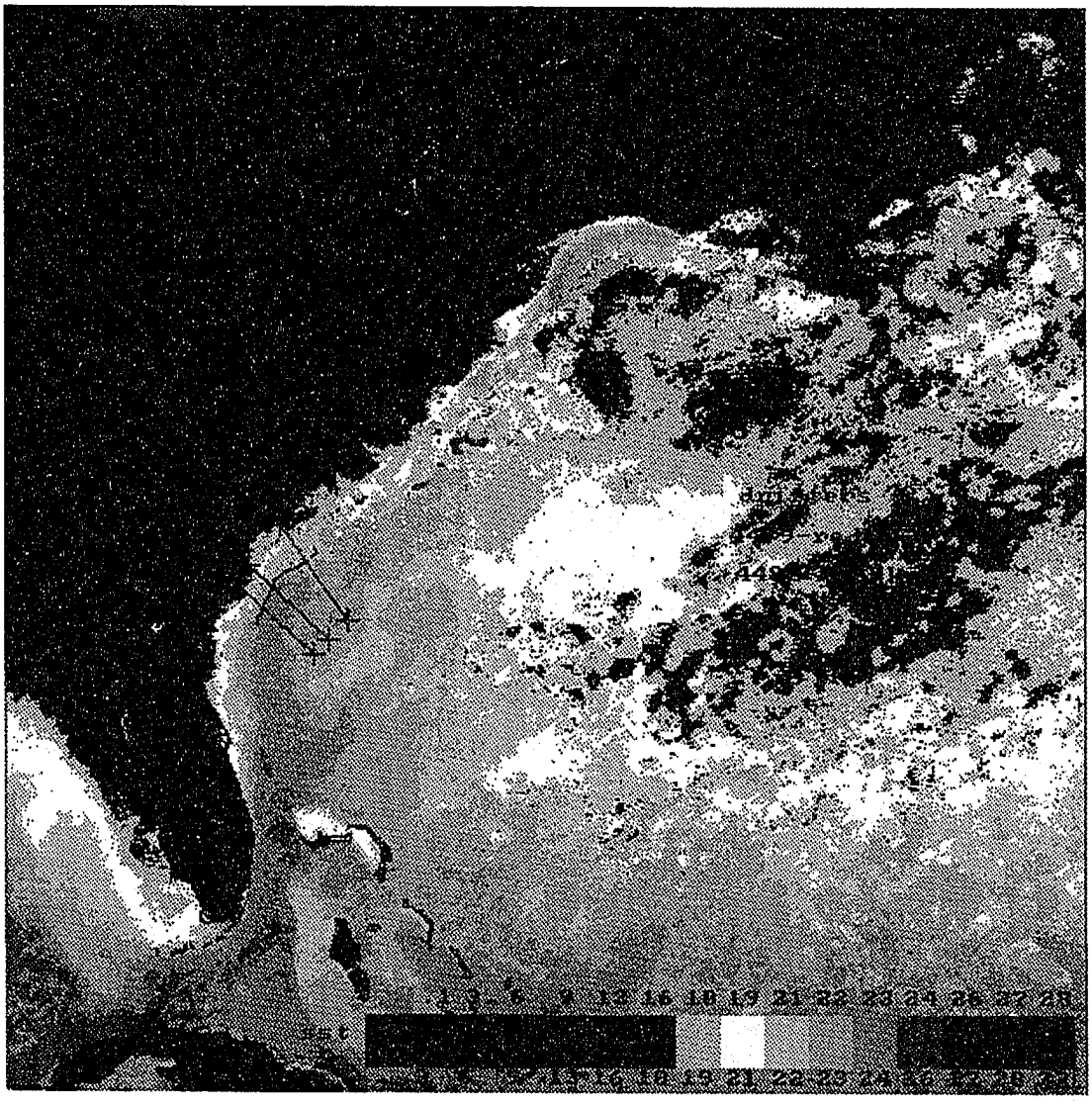

Figure 44: Image 85 of the Gulf Stream with two drifters superposed. Drifter 4480 - black with three transects, Drifter 4481- light blue with three transects. (courtesy of RSMAS)

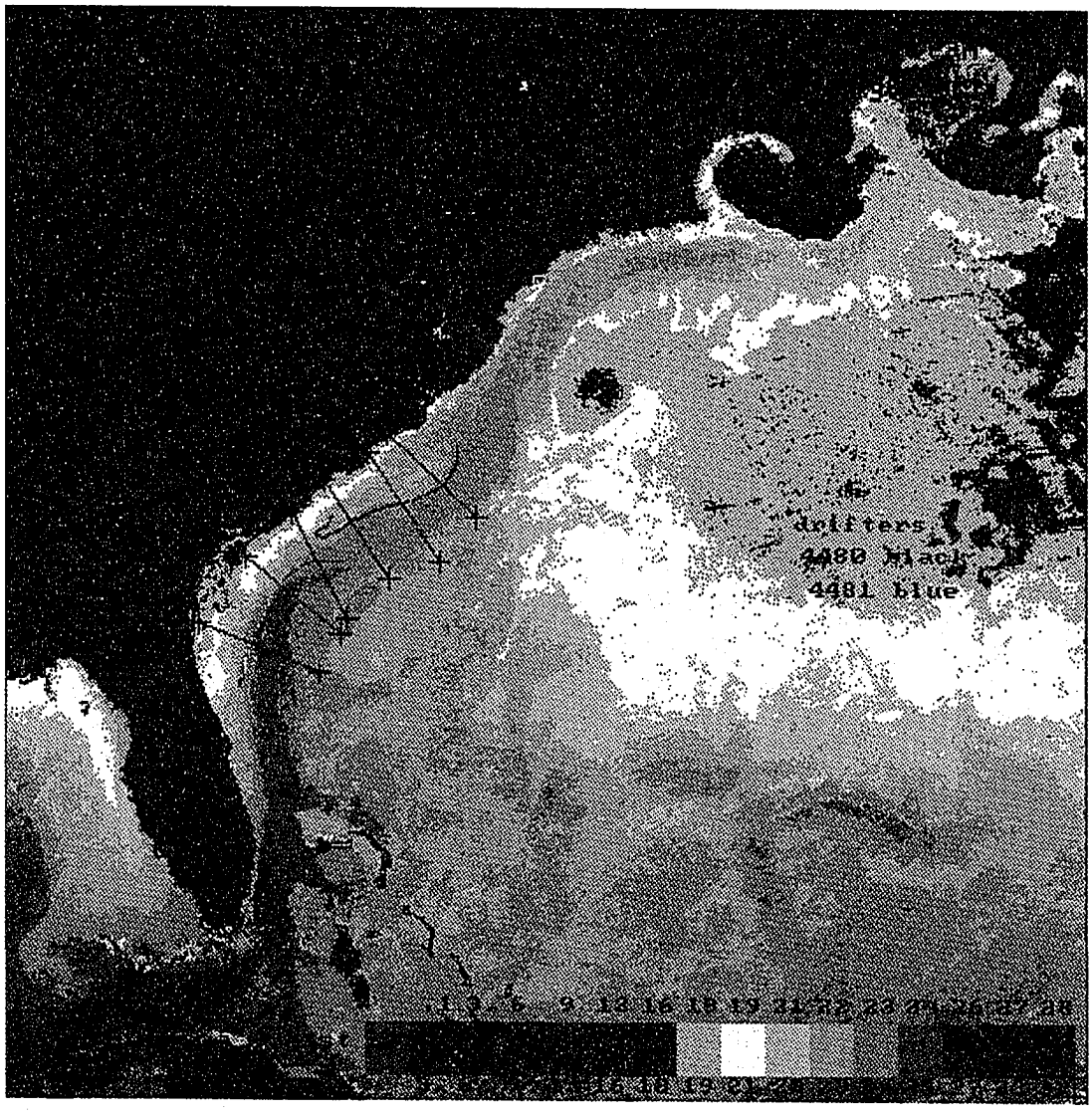

Three transects were made across each drifter, but perpendicular to the Gulf Stream. Transect 1 for drifter 4480 is the line farthest to the North. A temperature value of 22.875°C and a speed of 63 $km\ dy^{-1}$ were determined at this drifter location. The middle transect revealed a speed of 46 $km\ dy^{-1}$ and a temperature of 22.85°C. Finally for this image and drifter 4480, the third location of the drifter has a speed of 33 $km\ dy^{-1}$ and a temperature of 23.50°C. For drifter 4481, the temperature and speed are 23.13°C and 67 $km\ dy^{-1}$, 23.42°C and 57 $km\ dy^{-1}$ and 24.13°C and 35 33 $km\ dy^{-1}$ for transect 1, transect 2 and transect 3, respectively.

Figure 45 depicts image 92 and two drifters superposed. The temperature values for the drifter 4480/transect intersection range from 23.38 - 24.63°C, while the velocities with a range from $136 - 158\ km\ dy^{-1}$ are much higher than those calculated for image 85. The high values are most likely due the fact that the drifter has started flowing eastward away from the constraints of the bottom topography. Drifter 4481, which is still located in the LT37, has significantly lower speed on the order of $35 - 48\ km\ dy^{-1}$ with consistent temperature values of 23.0 - 24.0°C at the intersection.

Finally, the sequence of composite images that portrays transects cutting across the Gulf Stream is image 96 (Figure 46). Because the drifter trajectory for 4480 is relatively long, five transects were undertaken. This drifter is confined to GT37 and follows the Gulf Stream closely, however its north-south excursion is somewhat less than the meander pattern as depicted by the composite image 96.

This phenomena is also seen in other images as well and deserves some comment. There are several possible explanations. One is that the compositing shows meandering growth in a region that the drifter has already transited. Another possibility is that the surface temperature is not always a reliable surrogate for the flow field streamfunction. Resolution of this question will require further analysis.

Figure 45: Image 92 of the Gulf Stream with two drifters superposed. Drifter 4480 - black with three transects, Drifter 4481 - light blue with three transects. (courtesy of RSMAS)

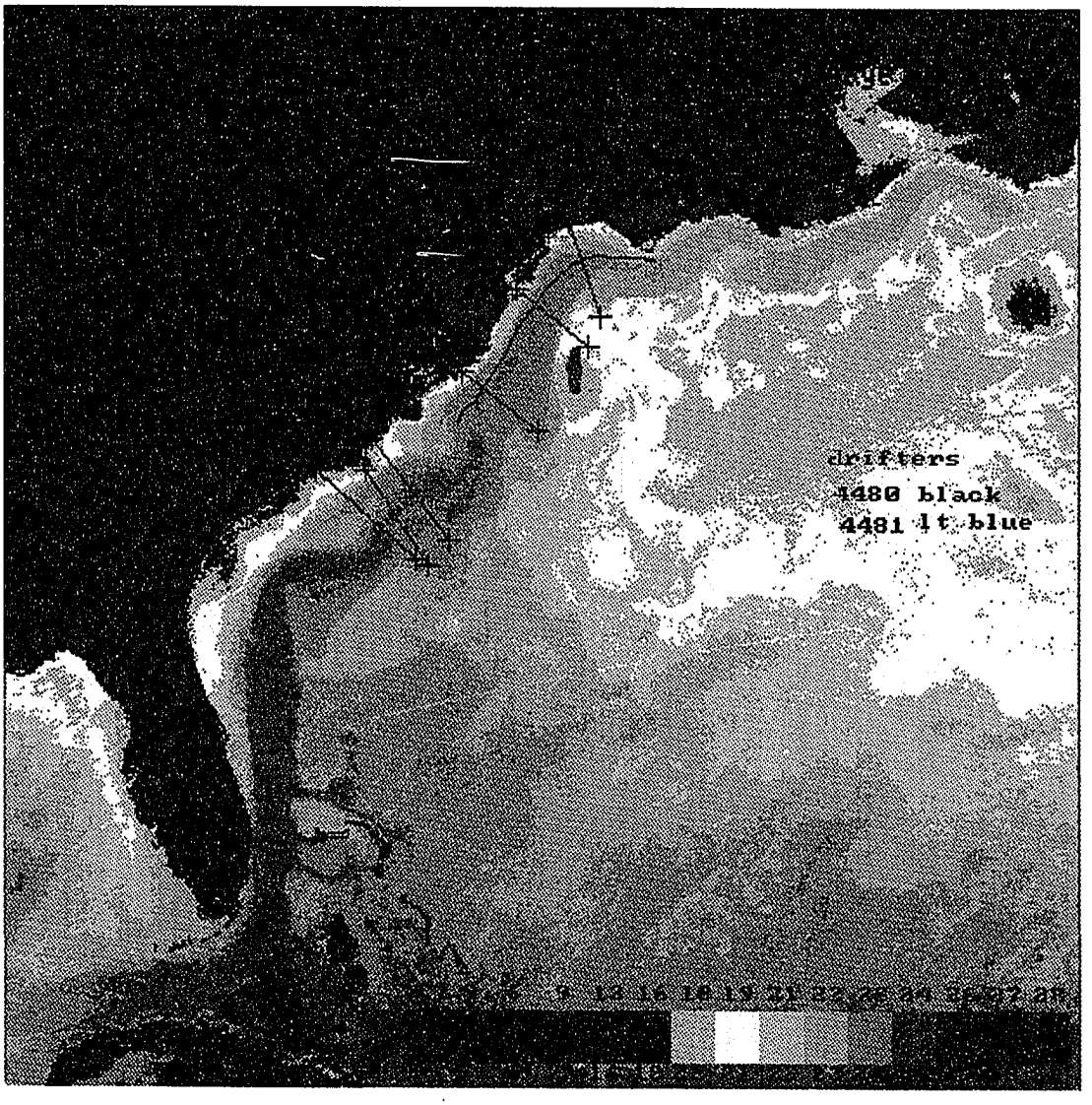

Figure 46: Image 96 of the Gulf Stream with two drifters superposed. Drifter 4480 - black with five transects, Drifter 4481 - light blue with three transects. (courtesy of RSMAS)

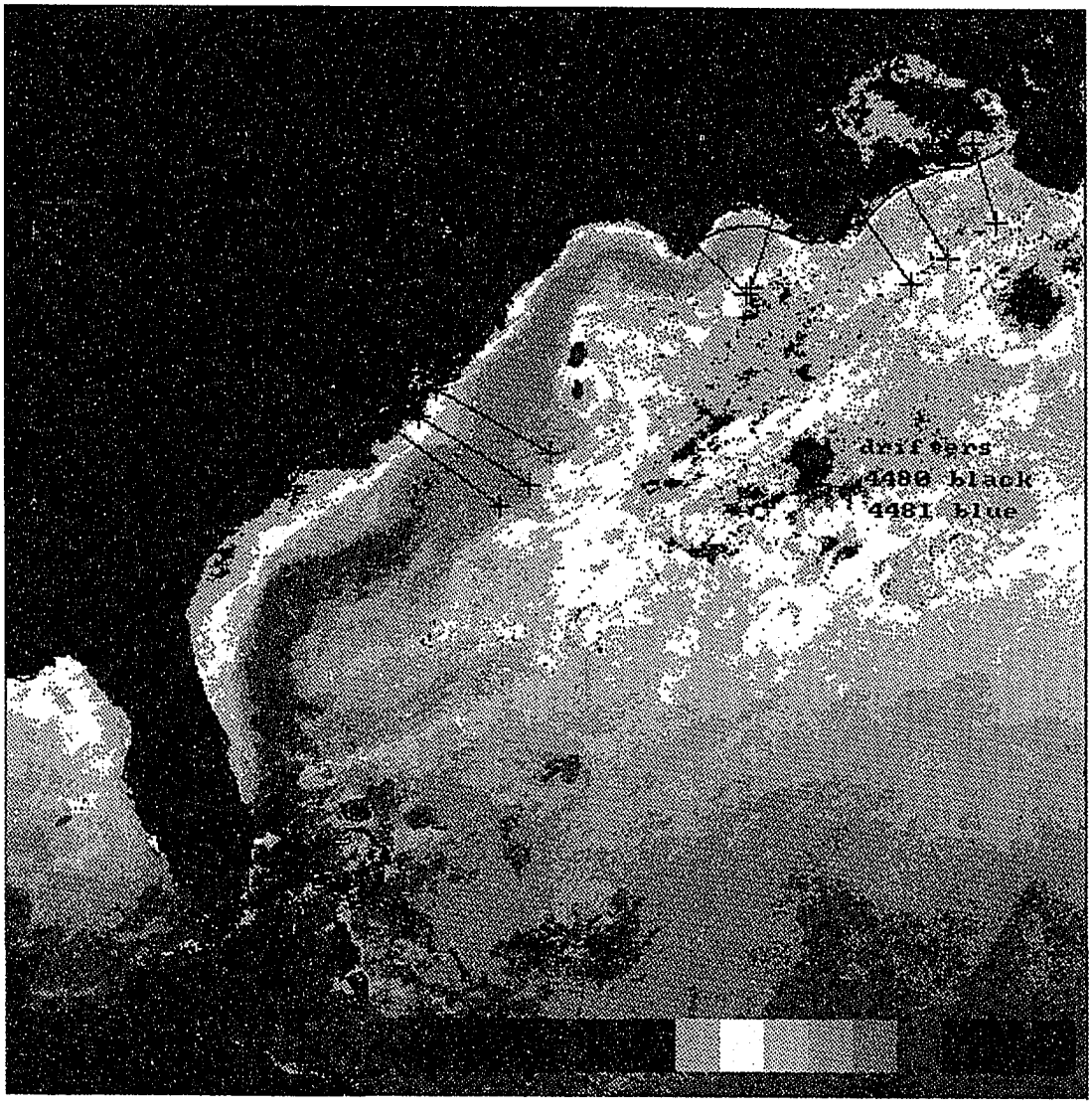

As shown by the yellow and green coloring at the transect/drifter intersection, it is evident that the temperatures are much colder than the two previous images. These values are centered around 19.5°C. In this region, the drifter has reached speeds of up to 175 $km\ dy^{-1}$. These speeds are considerably higher than those observed in LT37. Drifter 4481 remained in the LT37 region. Its speeds at the drifter/transect intersections are much lower than those for drifter 4480. The average value is approximately 67 $km\ dy^{-1}$. However, the orange color surrounding the drifter 4481 shows that the temperature at this intersection is warmer, approximately 23.5°C.

Drifter 4480 is located on the edge of image 101 (Figure 47). As seen here the Gulf Stream has become "patchy" in this region. Nevertheless, three transects were taken across the Gulf Stream. The transect farthest to the west registered a speed of 130 $km\ dy^{-1}$ with a temperature of 19.9°C for drifter 4480. The next two transects show a speed of 95 $km\ dy^{-1}$ and 20.4°C, and 84 $km\ dy^{-1}$ and 19.9°C for transect two and transect three, respectively. The drifter/transect intersection for drifter 4481 displays a speed of 38 $km\ dy^{-1}$.

The above analysis shows that within GT37 the drifter speeds are very large, reaching values up to 200 $km\ dy^{-1}$ in some instances. These high surface speeds are consistent with past observations (Richardson, (1981); Halkin and Rossby, 1985). Values of approximately $120 - 200\ km\ dy^{-1}$ also have been used for model studies (BM91 and DM93). LT37 depicts values which are much smaller than those recorded for GT37. Speeds in this region are on the average $40 - 60\ km\ dy^{-1}$.

Profiles of the temperature across the Gulf Stream were generated from the transect data. Several figures will be described which depict the temperature versus distance along the transect. The majority of the profiles show a sharp temperature gradient on the coastal side of the Gulf Stream. The sharp gradient occurs within

Figure 47: Image 101 of the Gulf Stream with two drifters superposed. Drifter 4480 - red with three transects, Drifter 4481 - black with one transect. (courtesy of RSMAS)

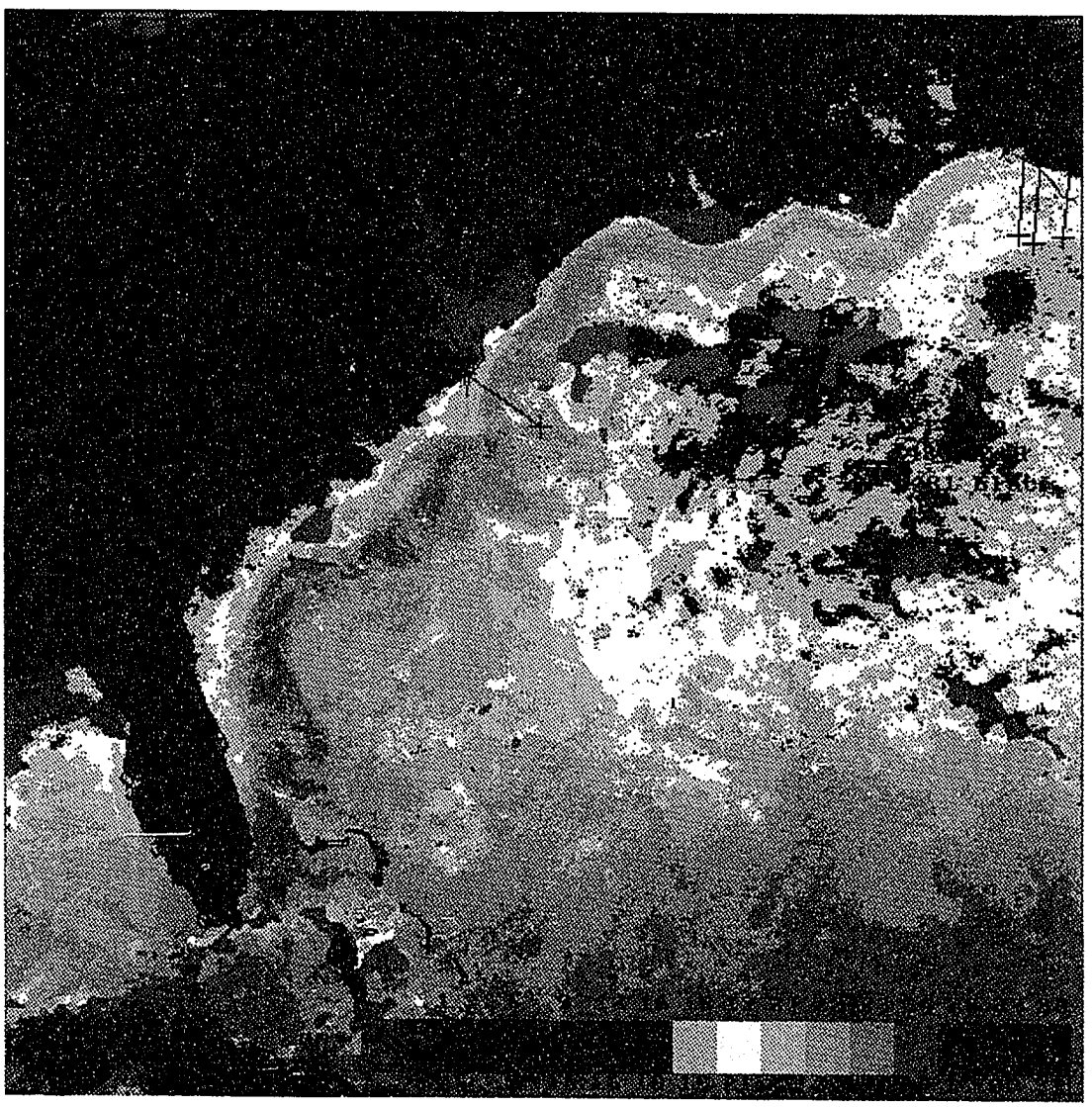

the first 70 km along the profile. Figure 48 shows the temperature profiles across the Gulf Stream for image 47 with the location of drifter 4479 marked by an "x". These transects across the Gulf Stream clearly display the sharp gradient on the coastal side of the Gulf Stream. Note that the left hand side of the graph represents the coastal side of the Gulf Stream, thus the reader is looking upstream when viewing these plots. This figure displays information for GT37. One thing to note is that the location of the drifter is always trapped within the sharp gradient region or just at the tip of it where the temperature starts to become relatively constant. This seems to be a general characteristic of surface drifters. Kirwan and Cresswell (1982) and McNally et al. (1983) attribute this to surface convergence in the strong gradient regions.

Image 96 with its corresponding contemporaneous drifter 4480 has a temperature profile across the Gulf Stream similar to image 47. This is illustrated in Figure 49. Again, the sharp gradient on the coastal side of the Gulf Stream is observed. As one travels along the transect towards the open ocean, the temperature values progressively increase within the 50-70 *km* range. Outside this distance, the temperatures reach a maximum and level off. They retain a constant temperature for hundreds of kilometers, then there is a gradual decrease in temperature. These profiles for image 47 and 96 are representative for other images and their contemporaneous drifter trajectories within GT37. However, in some instances the temperature profile across the Gulf Stream does not display this steep gradient on the western side of the Stream.

The conclusion drawn from these figures is that in most cases the temperature profile across the Gulf Stream is similar to the velocity profile across the Stream (von Arx, 1974, see Figure 4). However, as explained above, some temperature profiles do not exhibit profiles similar to the velocity profile. These different cases

Figure 48: Temperature along transect across 4479 and image 47. Transect two is farthest to the west (a). The "X" marks the location of 4479 on the transect. The line represents the delineation of the sharp gradient in temperature values.

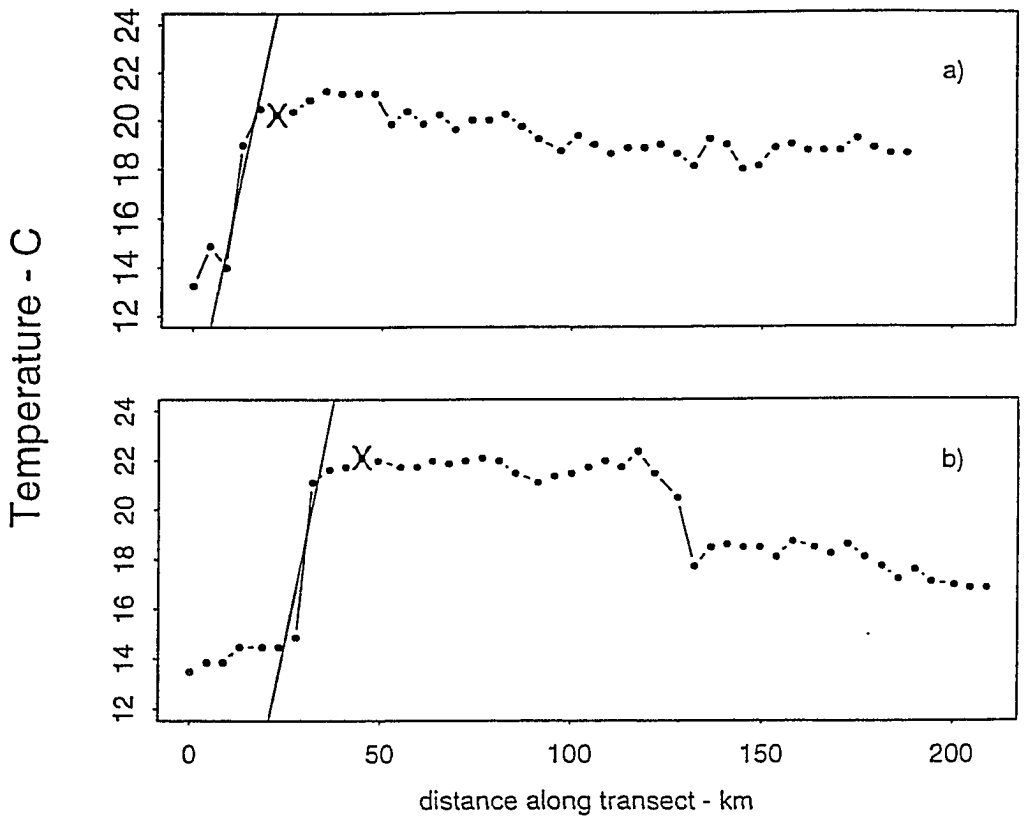

Figure 49: Temperature along transect across 4480 and image 96. Transect two is farthest to the east (a). The "X" marks the location of 4479 on the transect. The line represents the delineation of the sharp gradient in temperature values.

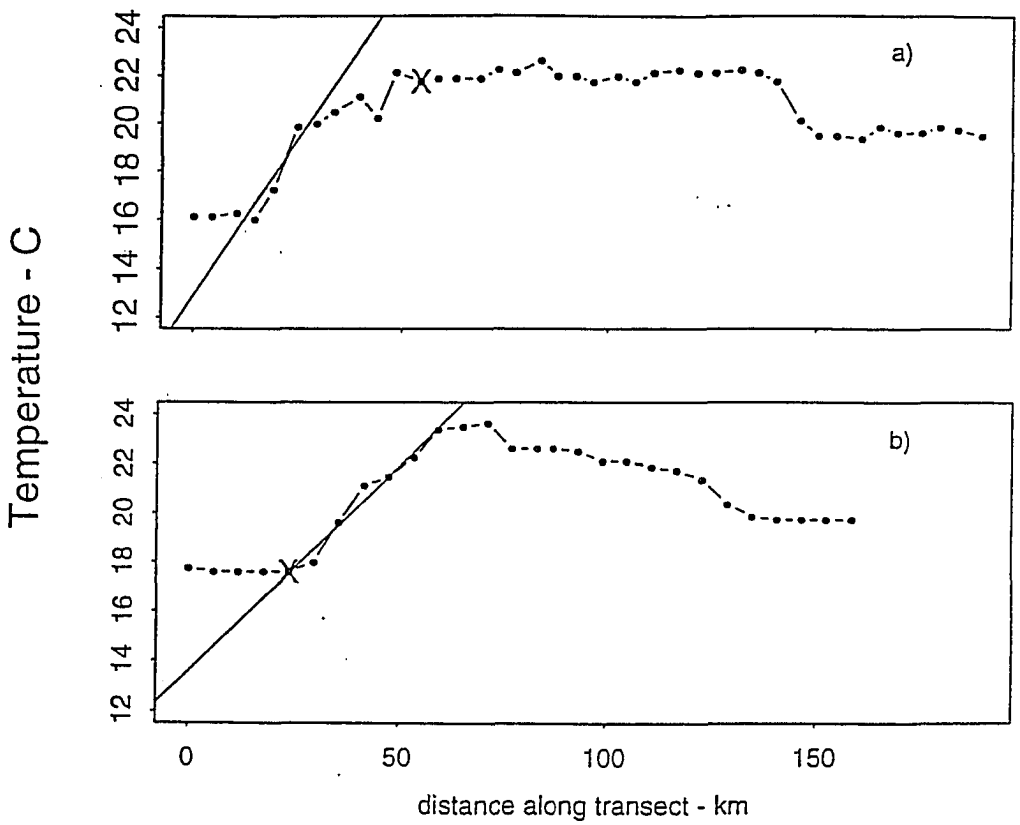

show that the relationship between the two fields is not straight forward. Despite this finding, perhaps with further analysis of the data a direct relationship between the velocity and temperature fields of the Gulf Stream can be established.

It is these profiles and the temperature along the drifter trajectory that prompts one to ask whether it is possible to infer the near-surface speed of the Gulf Stream from the temperature field of the composite imagery. Because of the close correlation between the drifter locations and given temperature fronts, as well as the good correlation between the drifter location and composite surface features, it appears that it is possible to infer the near surface velocity field from analyzing the composite temperature field. To test this, the three models of the meandering Gulf Stream GT37 discussed in Chapter 3 were used . The first two are kinematic models of a meandering jet developed by Bower (1991) and Dutkiewicz et al. (1993). The other a equivalent barotropic potential vorticity model of the Gulf Stream. The analyses of the two contemporaneous data sets by utilizing these models is discussed in subsequent chapters.

5.7 Standardization Parameters

After completing the kinematic analysis on the contemporaneous data set, kinematic analysis also was made on the rest of the composite images. These were analyzed to determine the "standard" values for amplitude, wavelength and phase speed. The median values from these calculations were used to conduct the "standardization tests" for the two kinematic models and dynamic models. The "standardization tests" were undertaken to determine whether the values obtained in the previous six sections were representative for all images. The sample sizes for each of these calculations were different. The sample size for the amplitude calculations was 41 samples. Twenty-five samples were utilized to determine the median wavelength. A

slightly larger sample size of 28 was used for determining the phase speed.

A histogram displaying the recorded amplitudes for all composite image meander crests is shown as Figure 50. The median amplitude value is 38 *km*. This value was used in the kinematic and dynamic models for the "standardization tests" of the data sets. Close inspection of this figure shows that the observed amplitude values calculated in Section 5.3 fall within the peak region of the histogram.

Figure 51 shows a median wavelength of 363 *km* for the "standardization test". The histogram shows the observed values from Section 5.3 concentrated in the 350 - 450 *km* region, a region with a high number of samples. The median phase speed for the "standardization test" is $7km\ dy^{-1}$ (Figure 52). Unlike the amplitudes, the observed values of wavelength are scattered throughout the histogram.

Overall, the "standardization tests" reveal a larger amplitude, larger wavelength and a lower phase speed than the observed parameters obtained from the contemporaneous data set. These values will be used in the "standardization tests" for the kinematic and dynamic models. For the remainder of the paper, the "standardization tests" and parameters will be referred to as STD. If STD is not specified, then the parameters used in the models will be the observed values discussed in the previous six sections of this chapter.

5.8 Summary

Several conclusions can be drawn from the kinematic analysis of the contemporaneous data set.

- Most drifter trajectories do not follow exactly a specific temperature front. However, the drifters do remain within a temperature band.

Figure 50: Histogram of the amplitudes from the "standardization tests" of the composite imagery. Median amplitude = 39 *km*.

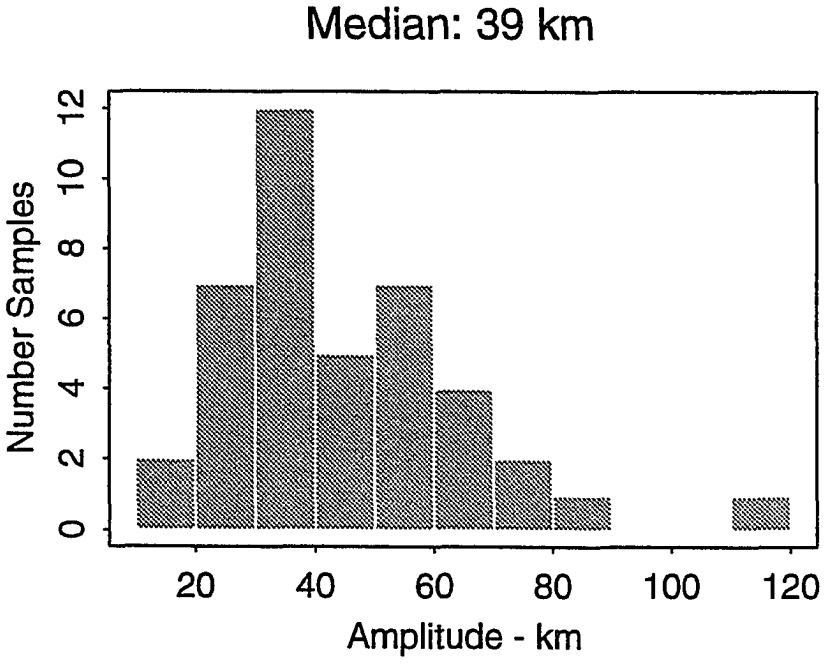

Figure 51: Histogram of the wavelengths from the "standardization tests" of the composite imagery. Median wavelength = 363 *km*.

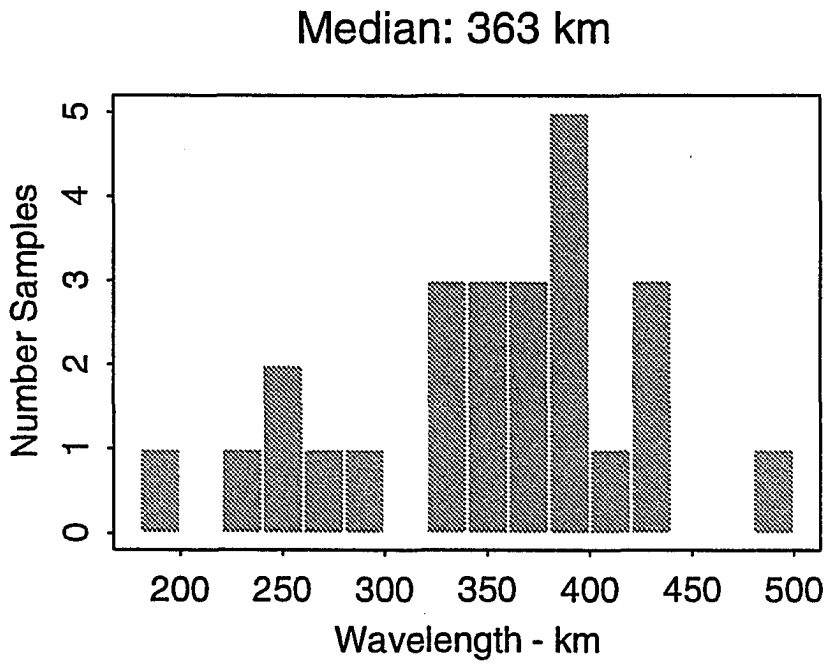

Figure 52: Histogram of the phase speeds from the "standardization tests" of the composite imagery. Median phase speed = 7 $km\ dy^{-1}$.

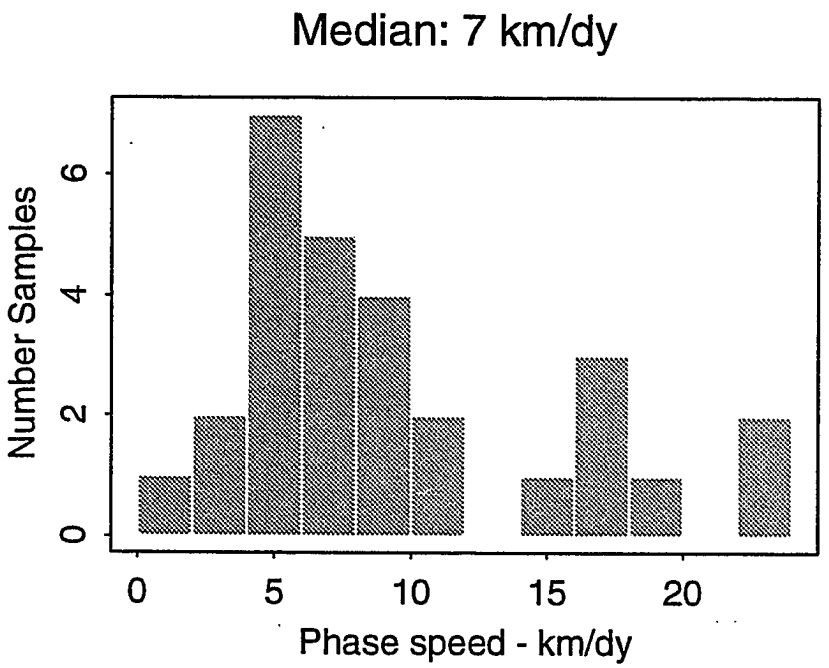

- Meander crests correspond to warm temperatures, whereas the troughs revealed colder temperatures.
- In GT37, the average meander amplitude and wavelength are 32 km and 360 km, respectively.
- Meanders propagate eastward with an average phase speed of 12 $km\ dy^{-1}$.
- Drifters move faster at meander crests than they do at the troughs.
- Drifter speeds within GT37 are very large ranging up to 200 $km\ dy^{-1}$. In LT37 the speeds are much lower and range from $40 - 60\ km\ dy^{-1}$.
- In most cases, the temperature profile across the Gulf Stream is similar to the velocity profile across the Gulf Stream.
- The STD values for the composite imagery are amplitude = 39 km, wavelength = 363 km and phase speed = 7 $km\ dy^{-1}$.

6 Kinematic Model Results

All our knowledge has its
origin in our perceptions.
Leonardo da Vinci

This chapter focuses on the results obtained from the kinematic models, BM91 and DM93. Three different experiments are performed with each of the models. A comparison between the two kinematic models utilizing the model parameters for DM93 constitutes the first experiment. The second experiment, termed the standardization experiment, involves the use of the STD parameters. The final experiment, which will be referred to as the observation experiment, uses the observed data values for the contemporaneous data set which are obtained in Chapter 5.

Section 6.1 compares the results obtained from DM93 and BM91. In this analyses, identical parameters are used in each model in order to determine the similarities and differences between the models. The set of parameter values utilized are the same as those used by Dutkiewicz et al. (1993) for their study of a meanering jet. This provides a direct comparison between the two models.

The standardization experiments are addressed in Section 6.2. Here, the STD parameters are used in both models. Five different case studies are pursued in order to determine the extent that geographic placement of the particles within the jet influence the resultant particle trajectories.

In Section 6.3, the observation experiments are detailed. As in Section 6.2, the experiments are run for each kinematic model, DM93 and BM91. Because of the lack of suitable data, only three cases are undertaken. These experiments are pursued in order to determine how closely the results model the true drifter trajectories observed in the composite imagery.

The u and v velocity components and speed for each particle trajectory generated in Sections 6.2 and 6.3 are discussed in Section 6.4. The purpose here is to determine the utility of these two kinematic models for inferring the near-surface velocity field from composite satellite imagery. The speeds calculated from the observed experiments and the drifter speeds also are compared in this section. Finally, Section 6.5 provides a detailed summary of Chapter 6.

6.1 Comparison of BM91 and DM93

The purpose of this experiment was to compare the behavior of the two models utilizing the original DM93 parameters. This comparison is made with the same initial conditions and parameters for both models. The values used are from DM93 where the amplitude = 70 km, wavelength = 450 km, width = 70 km, and phase speed = 14 $km\ dy^{-1}$. The scale factor Ψ_0 is calculated by requiring that the maximum current speed be 120 $km\ dy^{-1}$. A maximum recirculation speed of 1 $km\ dy^{-1}$ is used to calculate β. By using these parameters, a five-day composite streamfunction field is generated for the two models.

Figures 53 and 54 display the streamfunction fields for DM93 and BM91, respectively, along with three particle trajectories. The trajectories are generated by releasing three particles simultaneously into the streamfunction field. The line of particles is oriented perpendicular to the streamlines. The starting position of these

particles was chosen so that the "box" particle was released from the position (0,0) and the other two particles were in a line normal to the axis of the meandering jet. Each trajectory spans the five-day composite time period. The time interval between symbols along the trajectory is approximately 0.2 days in Figure 53 and 0.1 days in Figure 54.

Inspection of Figures 53 and 54 clearly shows that the trajectories generated by the two models are significantly different. In figure 53, the "box" particle starts at the initial position of (0,0) and travels within the meandering jet pattern crossing the streamlines. The crossing is expected, since the streamfunction is time dependent. At the crest the particle flows from warm to cool water as it moves away from the peak of the crest. As the particle approaches the jet trough it converges towards the center of the stream and eventually flows from warm to cold water in the trough region. The middle trajectory ("star") seems to be constrained between two streamlines and thus follows a nearly constant temperature at the crest. As it leaves the crest it converges towards the center streamline. The "plus" trajectory is much shorter than the others, since its velocity is considerably less. The particle enters the crest moving from cold to warm water. It crosses the other trajectories, as well as the streamlines.

The streamfunction field for BM91 is illustrated in Figure 54. The three trajectories superposed on this field correspond to the same trajectories displayed in Figure 53 for DM93. The "box" particle trajectory is characteristically similar to the one in Figure 53. Just as in Figure 53, this particle moves from warm water in the crest to cool water in the trough, as it flows from the crest to trough. It also converges towards the center of the stream field. In the trough it continues to move from warm to cold water. The BM91 "star" trajectory is significantly different from the DM93 "star" trajectory. Within the crest of the meandering jet, the "star" par-

Figure 53: Diagram illustrating the five-day average streamfunction field for DM93. The "box", "star" and "plus" lines represent particle trajectories. The time interval elapsed between each symbol along the trajectory is 0.2 days. Water north of the Gulf Stream meandering jet region represents the cold water of the North Atlantic. South of the meandering jet region is the warm water of the Sargasso Sea.

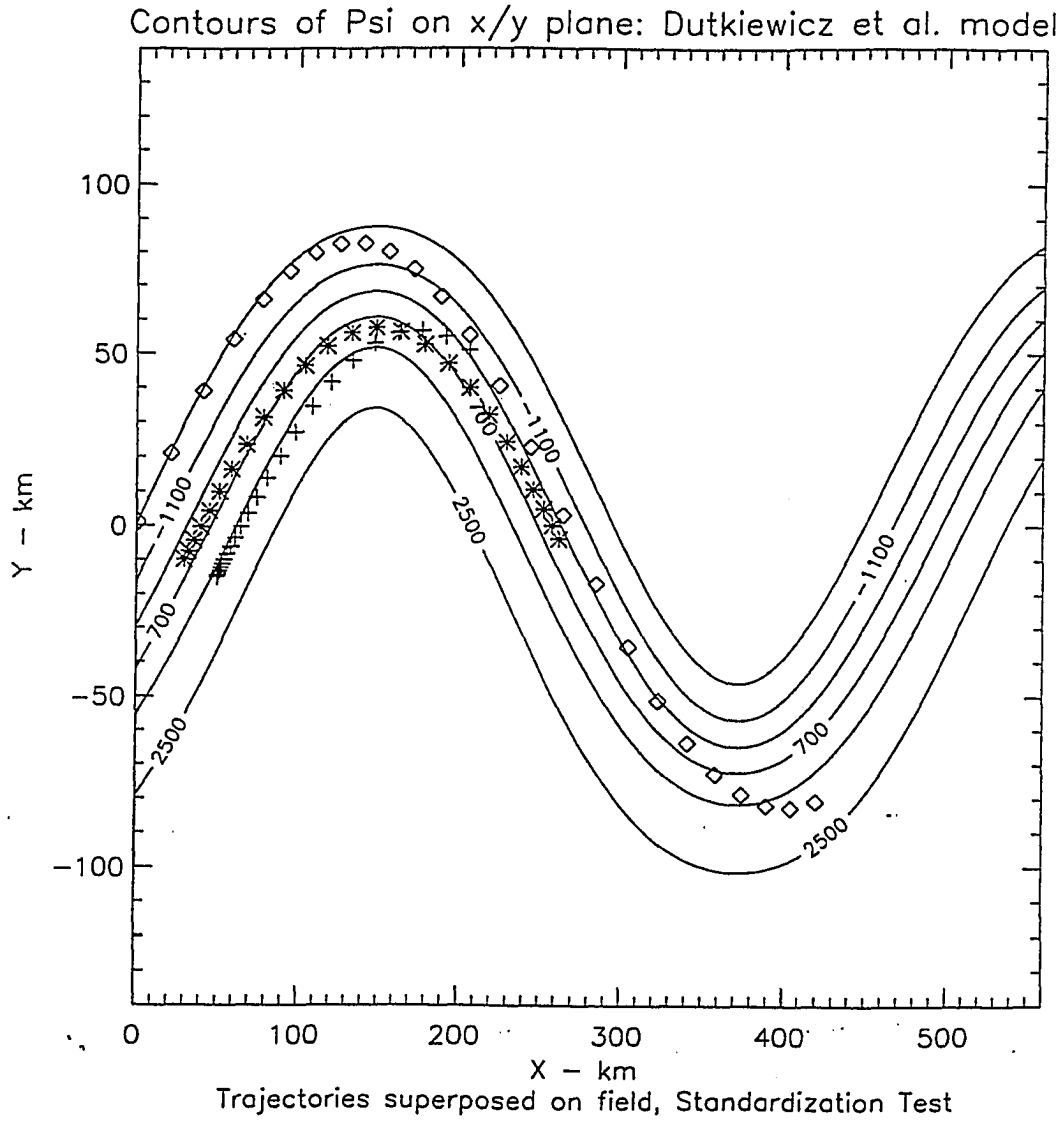

Figure 54: Diagram illustrating the five-day average streamfunction field for BM91. The "box", "star" and "plus" lines represent particle trajectories. The time interval between symbols is 0.1 days.

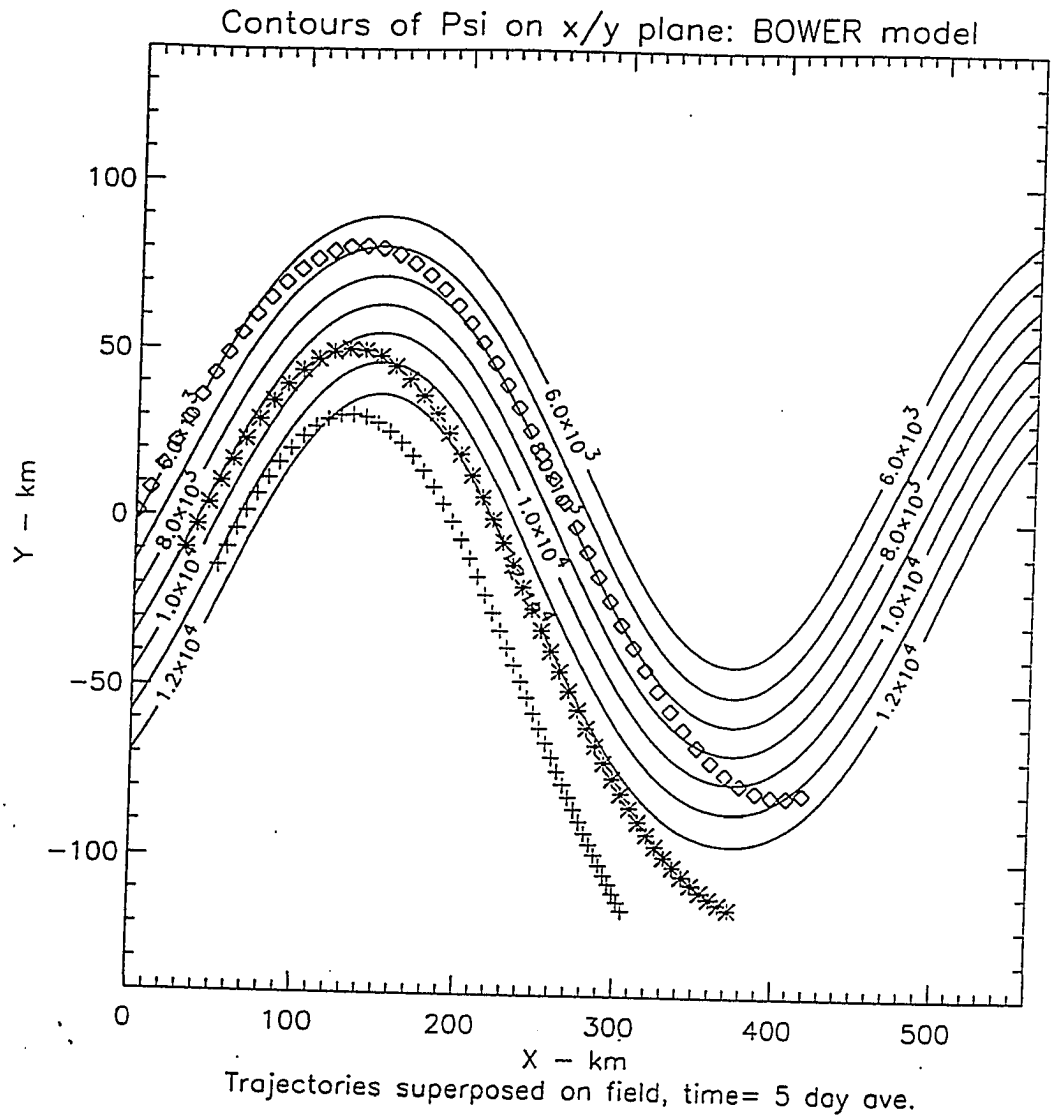

ticle flows from warm to cold water. As it flows away from the crest it diverges from the center of the streamfunction field and the meandering jet pattern. The length of this trajectory is much longer in BM91 than the "star" particle trajectory illustrated in Figure 53. Clearly, the "plus" path is also different from the DM93 "plus" path. The BM91 "plus" trajectory remains in cold water and never enters the meadering jet of the streamfunction field. This path is also much longer than its counterpart in Figure 53. Another curious difference between these two models is that the DM93 trajectories cross each other, but the BM91 trajectories do not.

These model results are unexpectedly different. The scaling width is most likely the cause for the significant difference between the two kinematic model results. The addition of the β term in DM93 also plays a factor. This term models the recirculation in the meander bends. It is a slowly varying function of y, thus it effects the geometry of the trajectories produced. Because of this dissimilarity, the analysis of the STD and observed data sets using both these models is important to pursue.

6.2 Standardization Experiments

Several experiments were undertaken using the standardized parameters in each model. These parameters were discussed in Section 5.7. Recall that the STD values are amplitude = 39 km, wavelength = 363 km, phase speed = 7 $km\ dy^{-1}$, width = 50 km and the Ψ_o and β scale factors are determined by their maximum speeds for their respective regions. The model runs are performed on different regions of the meandering jet.

The focus of the experiments was to determine the role that geographic placement of the particles within the stream play in the geometry of the trajectories. The

geographic locations consist of the following cases: A) initial position of (0,0) for the northernmost particle, B) the western flank of the crest, C) the peak of the crest, D) the eastern flank of the crest and E) the low of the trough. Four of these starting positions were chosen because they represent four distinct regions of a meandering jet, the crest, trough and the eastern and western flanks of the crest. The fifth was chosen for its initial position of (0,0). Note that three particles are initially aligned normal to the stream axis at these locations and released instantaneously. The time interval elapsed between symbols along the trajectory is approximately 0.2 days.

In case A for DM93 (Figure 55), the "box" particle closely follows the meandering jet pattern and remains restricted to the axis of the Stream. The particle moves from warm to cold water at the crest. Once it reaches the trough it moves from cold back into warm water. At the second crest, it moves from cold to warm water. The entire trajectory for this five-day period is actually longer than shown on this plot. The true x distance of the "box" trajectory extends 781 km over five days.

The "star" parcel trajectory has a much shorter length. At the crest, this particle flows from warm to cold water. It diverges from the center streamline as it flows towards the trough. The third path ("plus") is extremely short and appears to flow from cold to warm water.

The next scenario, case B (Figure 56), also depicts two relatively short trajectories and one extremely long trajectory for the five-day composite period. Note that the total distance in the x direction covered by the "star" trajectory is 751 km. This particle, just like the one that had the longer path in Figure 55, is concentrated in the region directly surrounding the center streamline, the area of maximum velocity. Flowing from crest to trough, the "star" parcel moves from warm to cool water.

Figure 55: Plot depicting three trajectories superposed on the five-day average streamfunction field for DM93. The "box", "star" and "plus" lines represent particle trajectories produced from STD parameters. The symbols are equally spaced in time with an interval of 0.2 days.

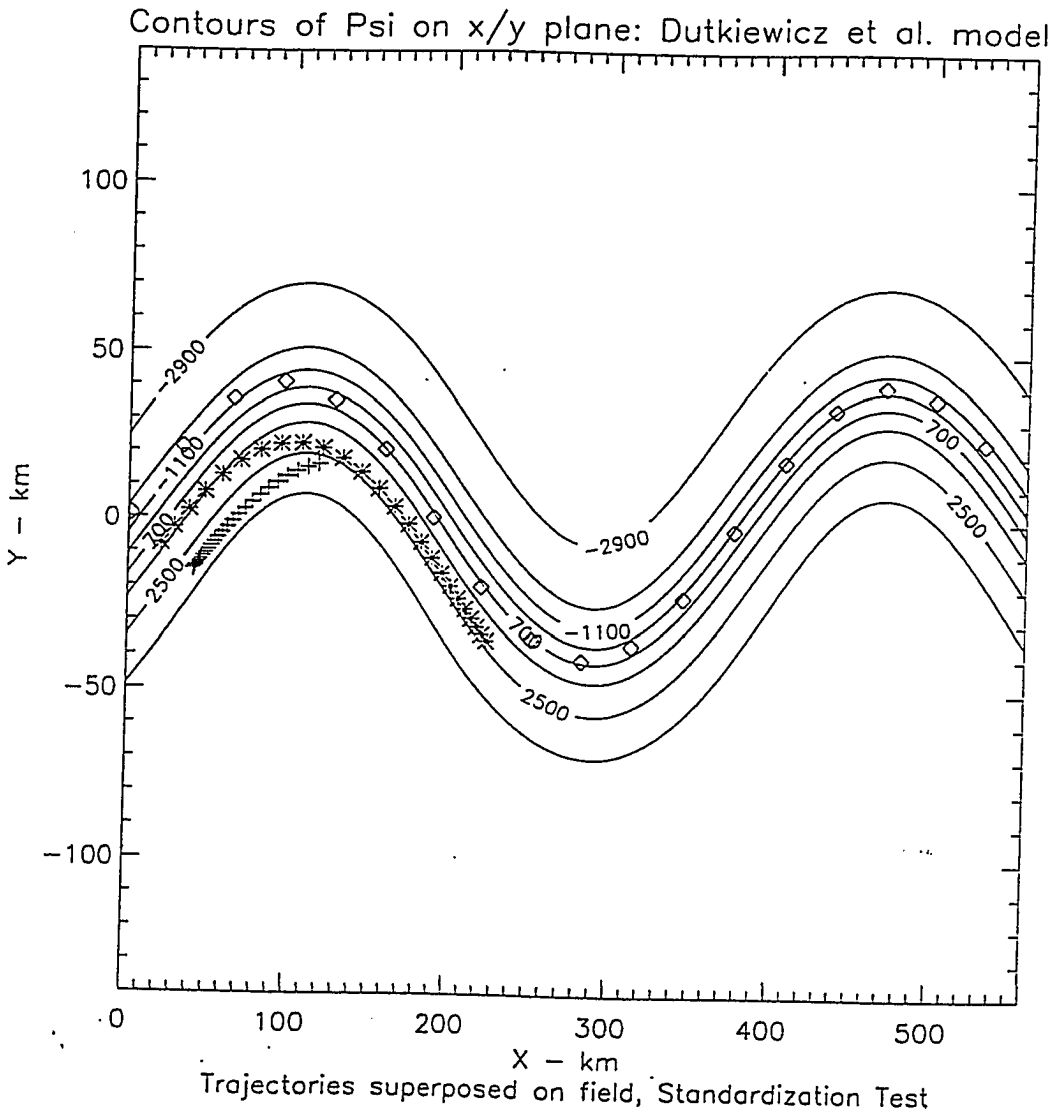

Figure 56: Same as Figure 55, but the starting position is different.

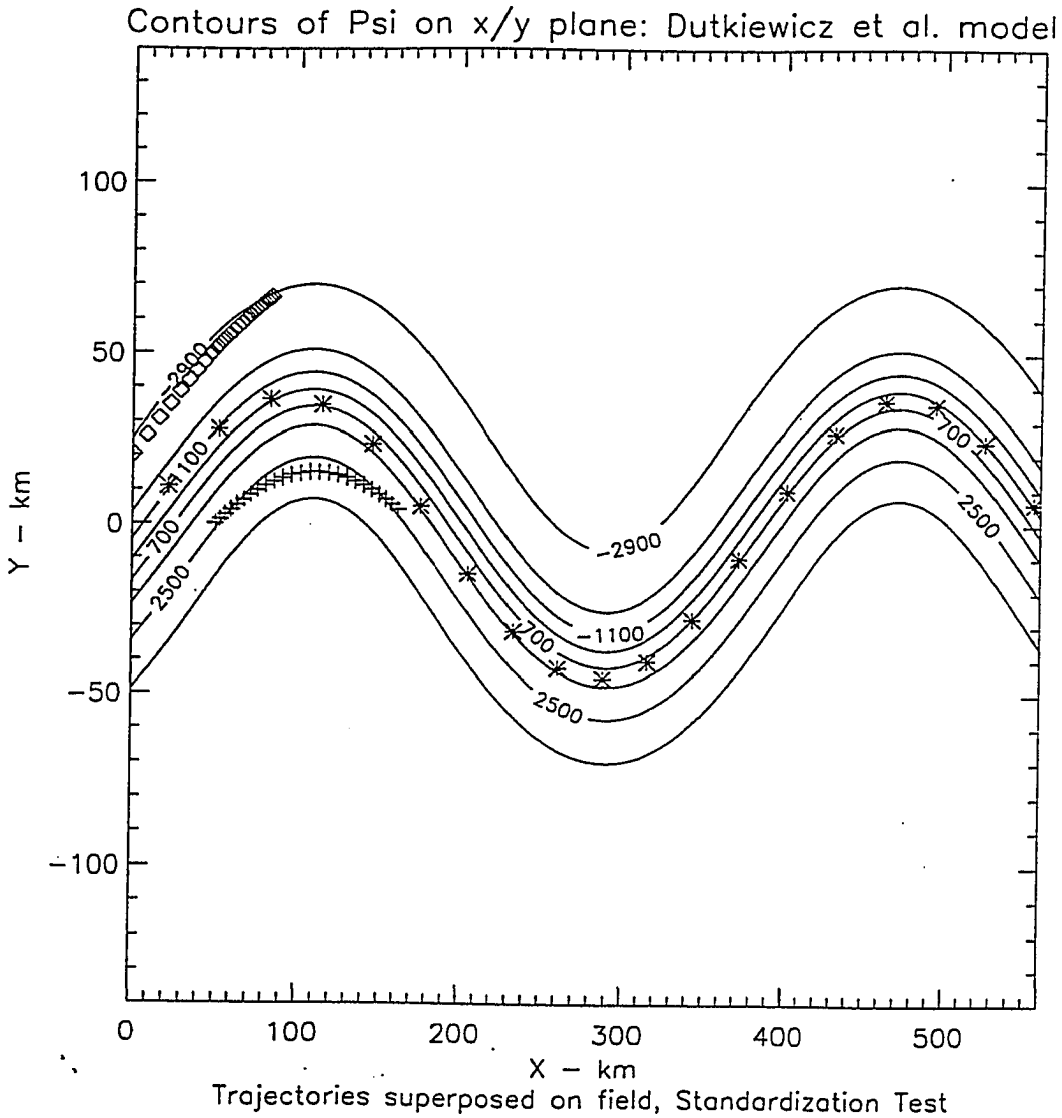

As is leaves the crest it diverges only slightly from the center, but later converges back towards the center as it moves up the western flank of the second crest. The "box" trajectory diverges from the center streamline towards the warm water of the crest peak. The "plus" trajectory is extremely short and appears to follow a fairly constant temperature.

Case C is shown in Figure 57. Here, the three particles are released at the peak of the first crest. As in the other cases, one particle was started north of the center streamline, one south of that streamline and the last one is positioned near the center streamline. The northernmost trajectory ("box") begins in warm water and flows towards cold water as it converges to the centerline. At the crest, it continues to flow from warm to cold water. The "star" parcel which is started at the center streamline again closely follows the meandering jet. It too moves from warm water at the crest into cold water. As this "star" particle moves towards the trough it diverges from the centerline slightly. In doing so, it moves into cold water. At the trough, it then flows from cold back into the warm water, thus converging back towards the center streamline of the jet. On the western flank of the second crest the "star" and "box" parcel trajectories cross each other. The maximum length x distance reached is 886 km for the five-day period. Once again the "plus" particle trajectory is significantly shorter in length compared to the other two and flow away from the center of the jet.

Figure 58 depicts the three trajectories with their initial positions on the eastern flank of the first crest of the meandering jet system. The "plus" particle moves towards the center from warm to cold water. The middle particle ("star") flows towards the trough moving from cold to warm water as it continues its path to the second crest. The "box" trajectory is similar in length to the other trajectories. Once it reaches the trough it appears to maintain a fairly constant temperature,

Figure 57: Same as Figure 55, but the starting position is different.

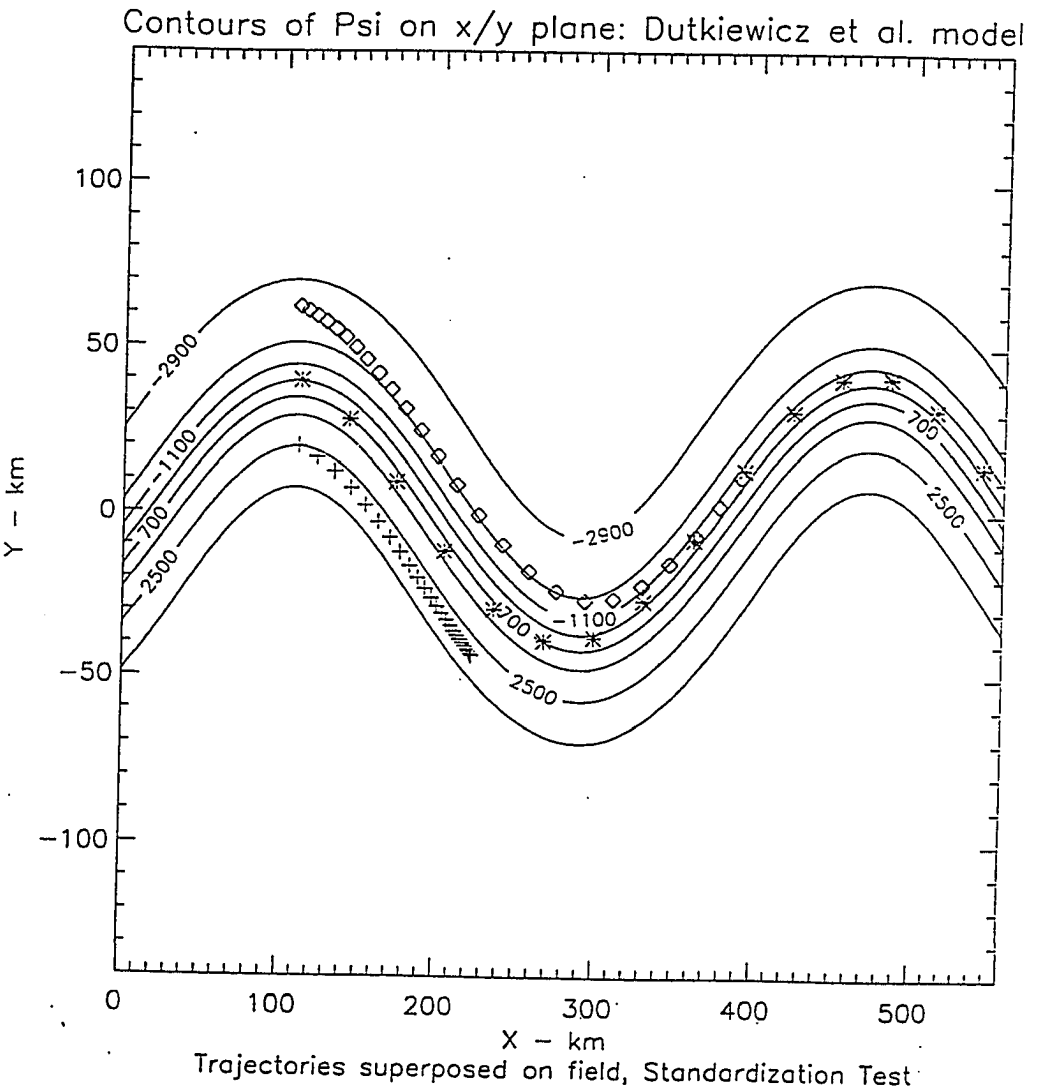

Figure 58: Same as Figure 55, but the starting position is different.

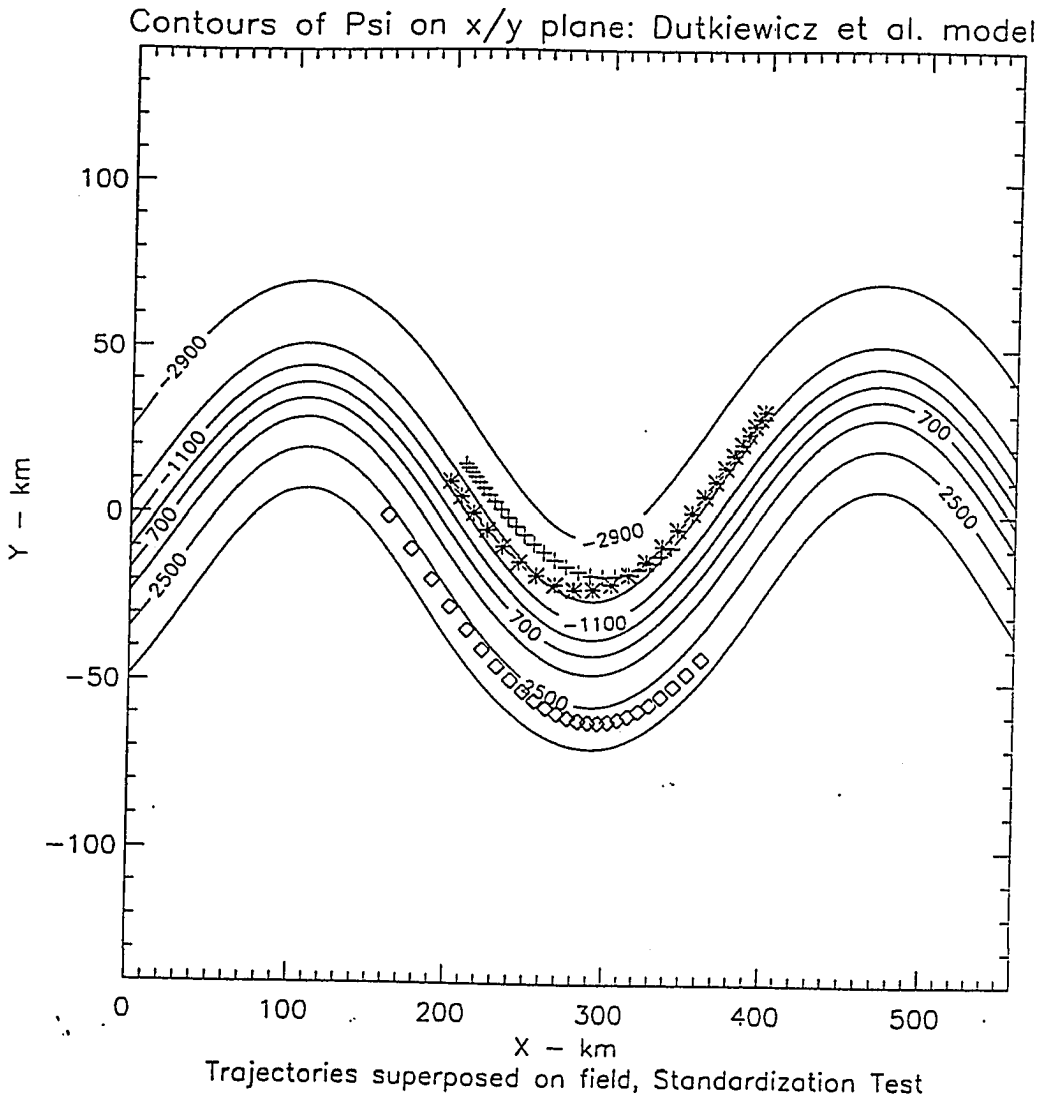

Trajectories superposed on field, Standardization Test

which is much colder than the other two particles.

In the last case, the particles are released from the trough and continue to flow towards the second crest (Figure 59). The northernmost trajectory ("plus") flows into warm water of the crest and away from the center streamline. The "star" particle moves from the cold water of the trough into the warm water of the crest. But, as it flows down the eastern flank of the crest, it moves back towards cool water. This particle reaches a distance in x of 986 *km*. Once again the "box" trajectory crosses the "star" trajectory. It too flows from the cold water in the trough to the warm water at the crest. However, at the crest it moves towards warm water and converges to the center, unlike the "star" particle which diverges away from the center streamline.

There are several conclusions that can be drawn from DM93. All particles released nearest the center streamline best follow the meandering jet pattern and have the longest trajectories. Particles cross each other, as well as the streamlines. Particles at the crest move from warm to cold water, and vice versa at the trough. However, there are some exceptions where the particles travel from cold to warm water in the crest and warm to cold in the trough. On the northern side of the upstream flanks of the crests, the particle trajectories always diverge from the centerline. In contrast on the southern side, the particles converge toward the center streamline. On the downstream side of the crests, the particles on the northern side converge towards the center streamline. However, the parcels diverge from the streamline of maximum velocity when they are on the southern side.

The same five cases were analyzed for BM91 (see Figures 60, 61, 62, 63 and 64). Figure 60 is a depiction of case A for BM91. Here the initial position is (0,0). Once the "box" particle reaches the crest, it moves from warm to cold water; however at

Figure 59: Same as Figure 55, but the starting position is different.

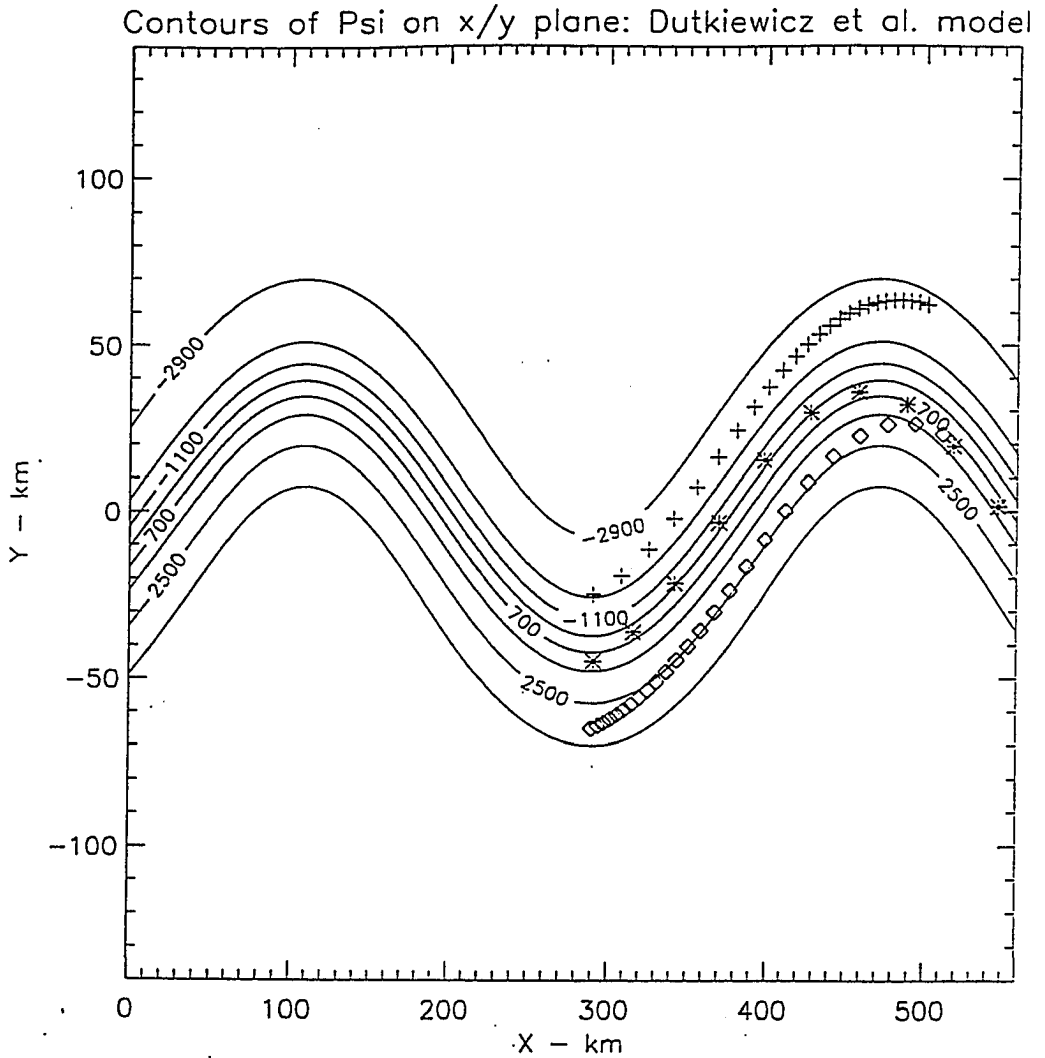

Trajectories superposed on field, Standardization Test

Figure 60: Plot depicting three trajectories superposed on the five-day average streamfunction field for BM91. The "box", "star" and "plus" lines represent particle trajectories produced from STD parameters. The time elapsed between symbols is 0.1 days

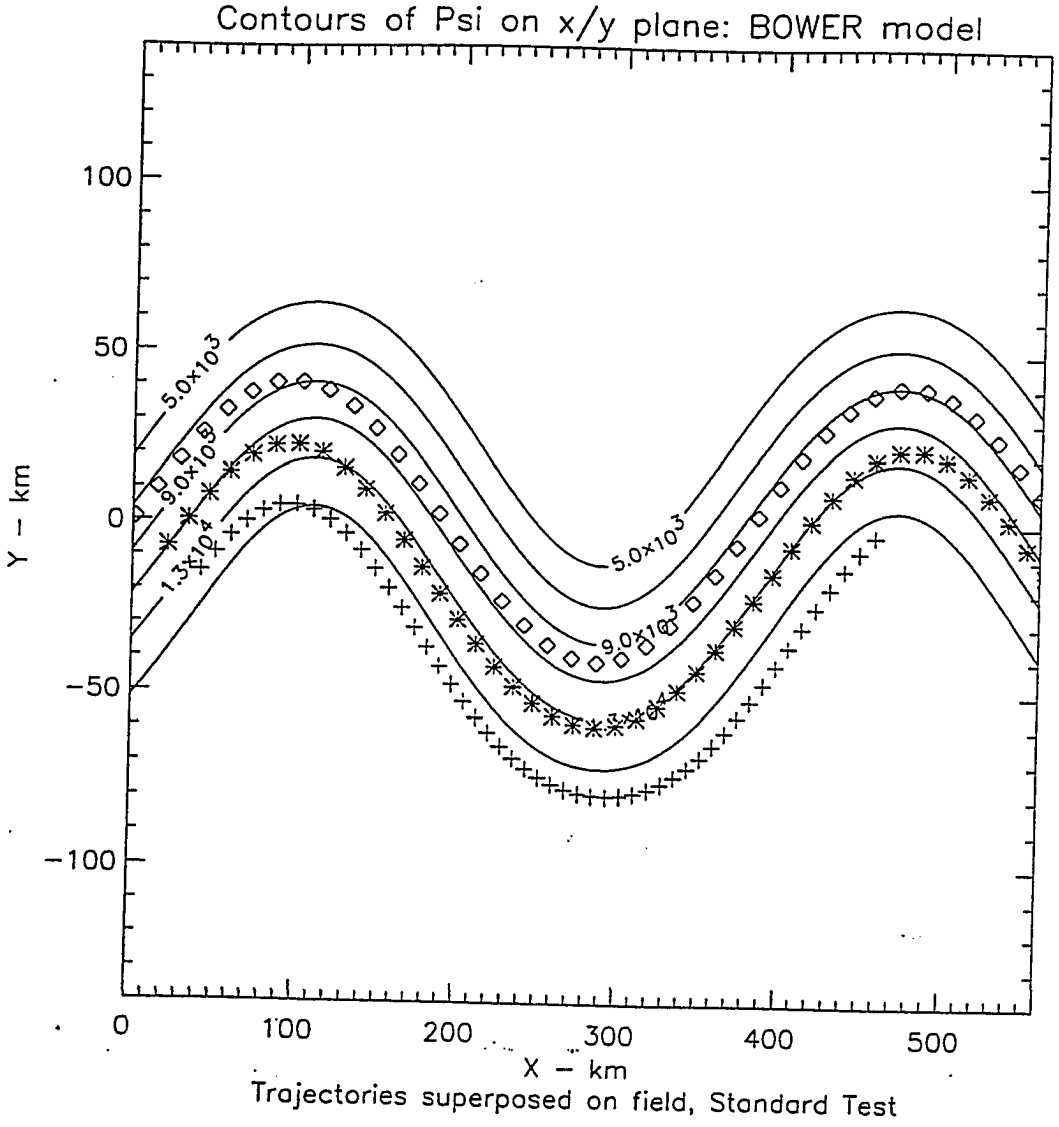

Trajectories superposed on field, Standard Test

the trough, it flows from cold to warm water. This trajectory spans an x distance of 716 *km*. The "star" particle also flows from warm to cold water at the crest and from cold to warm at the trough. The x distance traversed by this particle reaches a maximum of 644 *km*. The "plus" trajectory flows from warm to cold water at the crest. It continues to follow the jet pattern as it flows over the five day period. For BM91, the time interval between the symbols along the trajectories is about 0.1 days.

Case B (Figure 61) also displays three trajectories that closely follow the five-day composite shape of the meandering jet. All three particles move from warm to cold water at the crests. At the troughs the opposite situation prevails, each trajectory moves from cold to warm water. As the three particles flow into the second crest they move from cool into warm water. As seen in Figure 61, these trajectories appear to remain evenly spaced throughout their five-day period. The three particles travel x distances which are 635 *km*, 734 *km* and 573 it km for the "box", "star" and "plus" particles, respectively. This is an interesting contrast to the same case displayed by DM93 (see Figure 56). In DM93, two of the trajectories are extremely short and their paths do not remain evenly spaced.

The particles released at the peak of the crest are depicted in Figure 62. Again, the trajectories remain evenly spaced and travel farther than shown in the plot. The particles reach x distances of 699 *km*, 818 *km* and 731 *km* from the northernmost trajectory southward. At the trough the three trajectories move from cold to warm water.

Figure 63 represents the scenario where the particles are released at the eastern flank of the first crest of the meandering jet. The three trajectories exhibit a similar pattern. These particles also move from cold to warm water in the trough. They

Figure 61: Same as Figure 60, but the starting position is different.

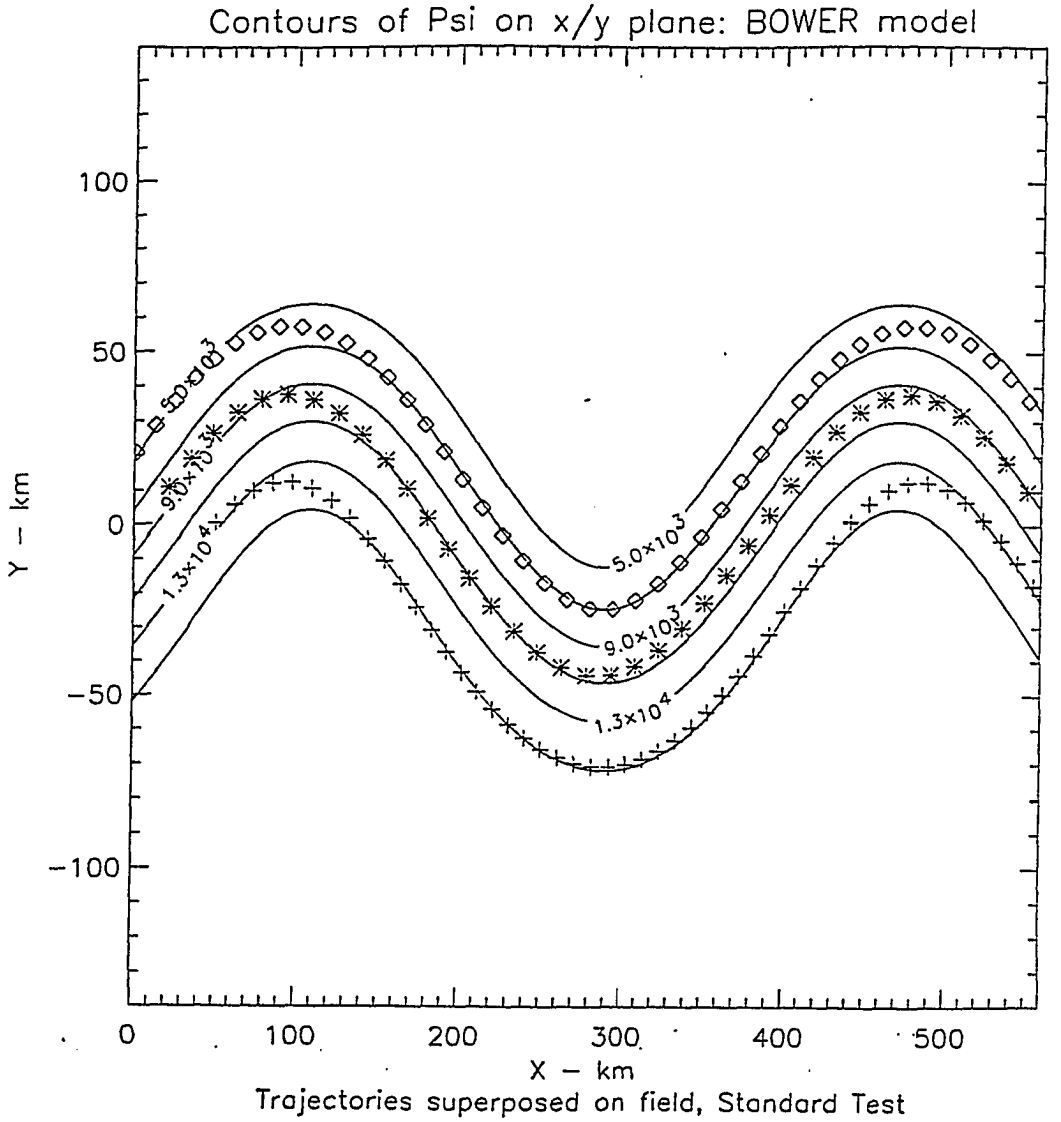

Trajectories superposed on field, Standard Test

Figure 62: Same as Figure 60, but the starting position is different.

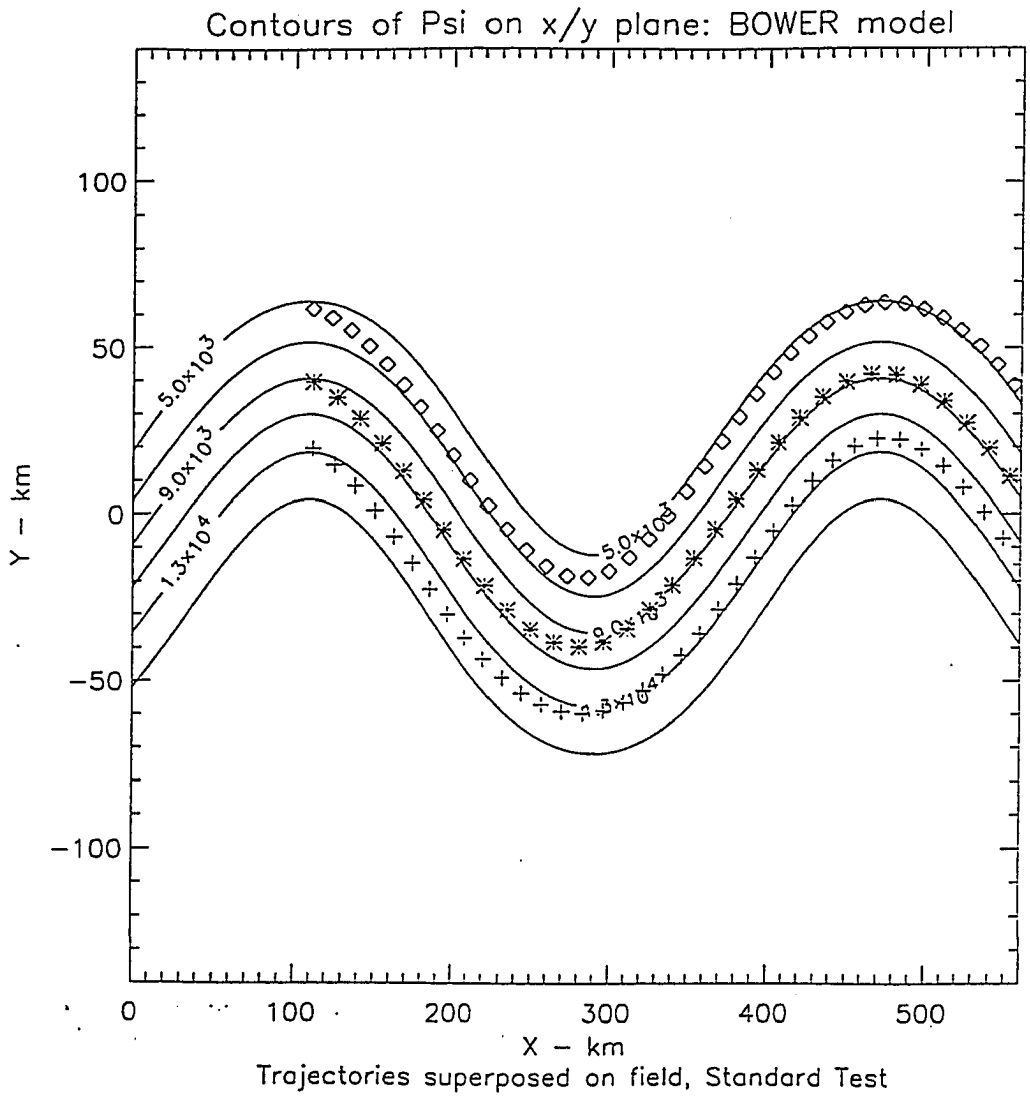

Figure 63: Same as Figure 60, but the starting position is different.

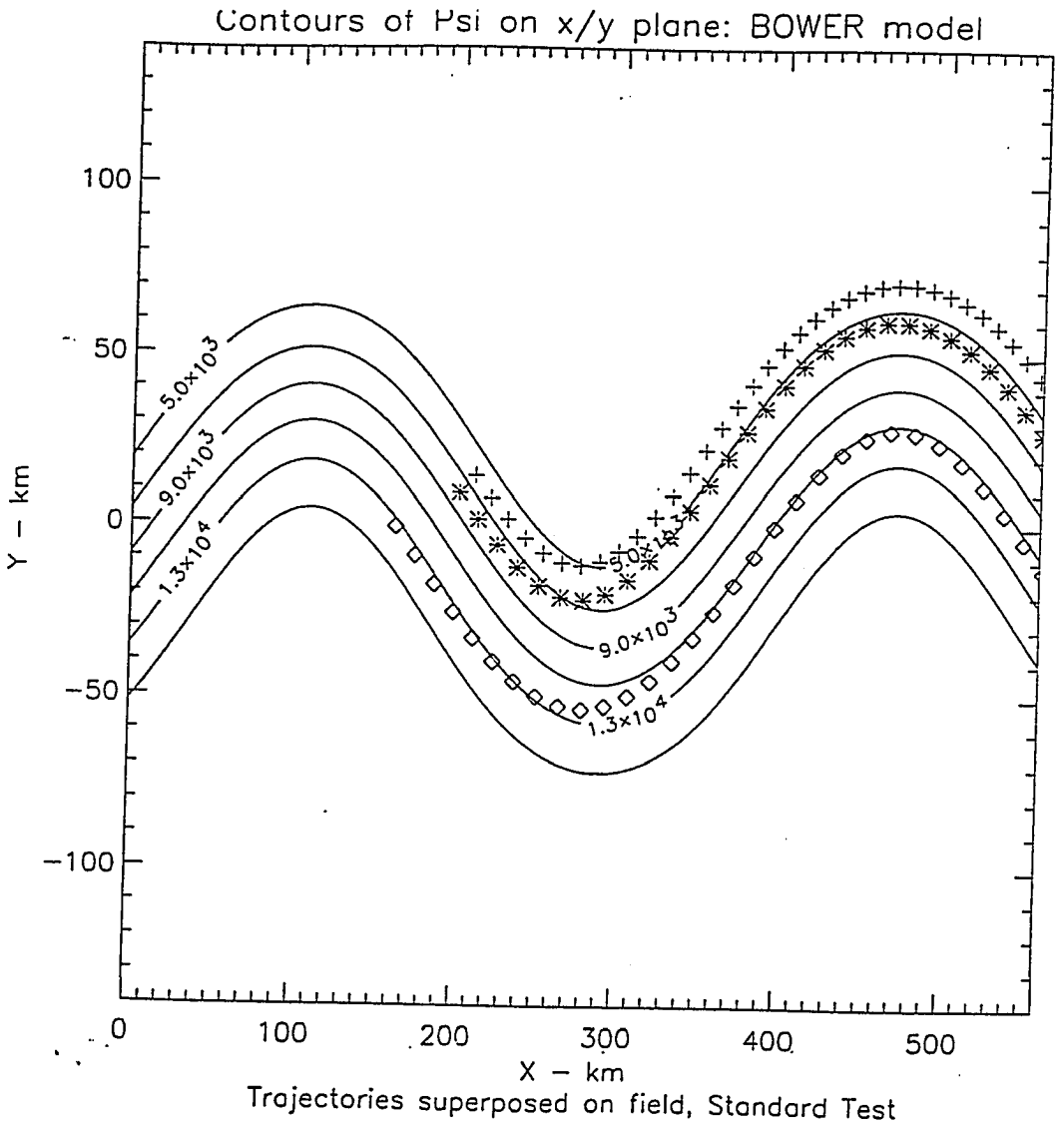

also reach x distances much greater than their counterparts when this case is run in DM93 (see Figure 58). Their distances are at least twice as long as those in DM93.

In the final case for this experiment, case E (Figure 64), the particles flow from the trough into the second crest. All three trajectories move from warm to cold water at the crest. Again, the trajectories are evenly spaced throughout the five-day time period. The trajectory x distances are longer than the ones observed in DM93 for the same run (see Figure 63). The "plus" trajectory reaches a maximum of 974 *km*, the "star" trajectory has a distance of 989 *km* and the x distance for the "box" trajectory is 784 *km*.

There are several conclusions which can be drawn from the above analyses of the STD data. Some similarities between the two model results can be seen, as well as their differences. Particles at the crest tend to flow from warm water into cold water just as seen in DM93. However, DM93 also showed instances where the particles traveled from cold to warm water in the crest. Both models also produced trajectories that move from cold to warm water in the troughs. A major difference between the two models is the maximum distance in x that was obtained. In BM91 the particles reach distances at least twice as long as their counterparts in DM93. The particles appear to remain relatively evenly spaced as they flow along the meandering jet pattern. A significant difference between the two models is the fact that the particles in BM91 do not cross each other as they do in DM93.

6.3 Observation Experiments

Three observation experiments were run for each model. These cases are related to the data obtained from the set of sequential composite images with their corresponding drifter trajectories superposed (see Figures 33, 34 and 35). This set

Figure 64: Same as Figure 60, but the starting position is different.

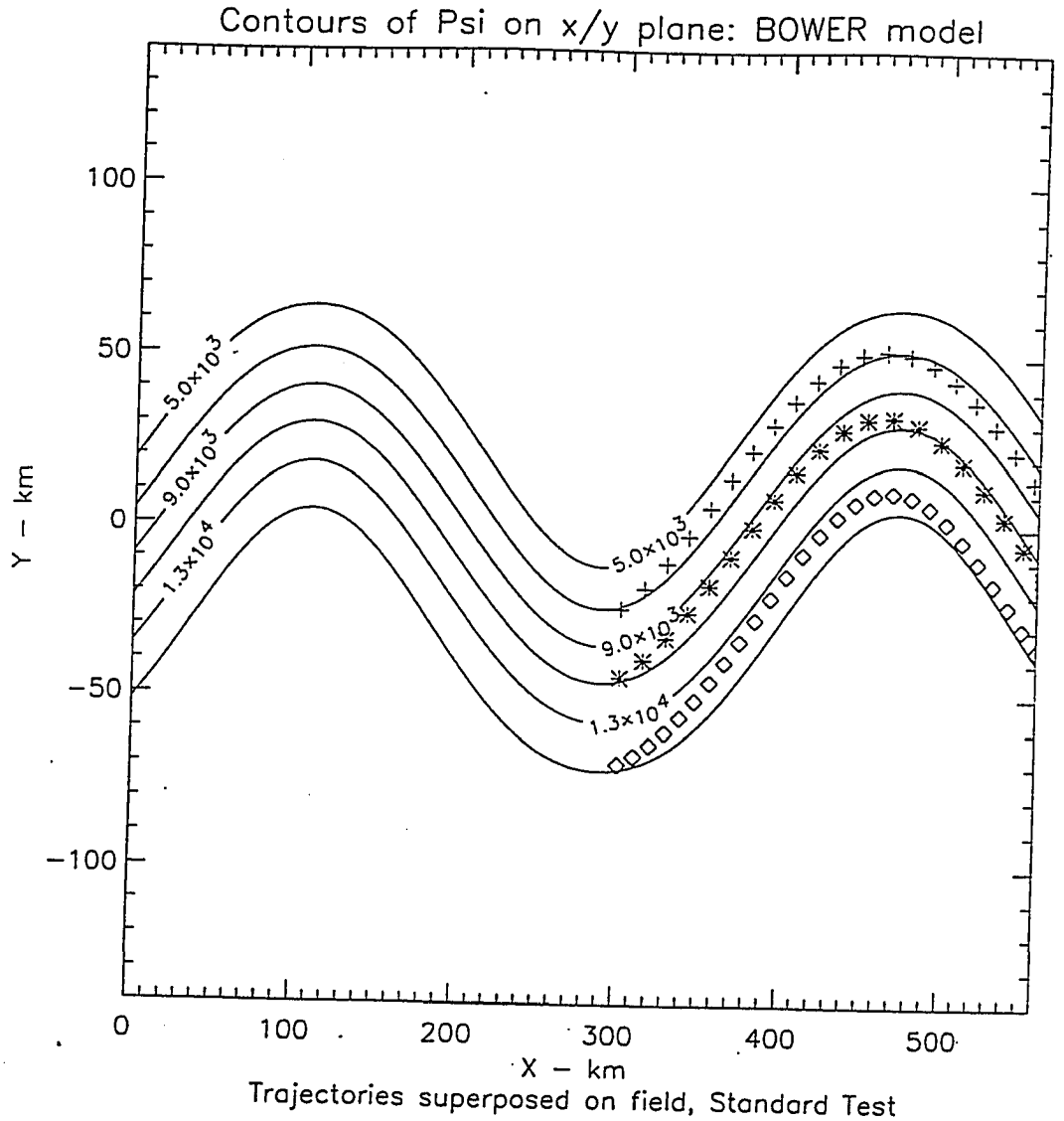

of contemporaneous drifters and images depict the meandering jet portion of the data set. The following is a list of the cases undertaken for the observation experiments: case 1) drifter 4480 on image 92, case 2) drifter 4480 on image 96 and case 3) drifter 4480 on image 101. In each case one particle is released from the exact position of the starting point for a particular drifter from the contemporaneous data set. The observation experiments for DM93 are reported first. A maximum speed of 158 $km\ dy^{-1}$ is utilized to determine the Ψ_o scale factor. The β scale factor is calculated by requiring that the maximum recirculation speed is 1 $km\ dy^{-1}$. A width of 50 km was chosen for all observation experiments. This value is larger than the original value used in BM91, but is smaller than that used in DM93. This value was chosen because it best represents the observed data of the meandering Gulf Stream.

Results of the first case are shown in Figure 65. The spacing between the symbols represents a time period of 0.1 days. Here, the amplitude = 26 km, wavelength = 262 km, phase speed = 9 $km\ dy^{-1}$ and width = 50 km. In image 92 (see Figure 33), only a portion of drifter trajectory 4480 is in GT37. Drifter 4480 is located near the middle of the stream. For DM93, the particle is released close to the same location on the meandering jet as drifter 4480 is on the image meandering jet. The model trajectory travels along the streamfunction field meandering with the jet (see Figure 65). The trajectory moves from warm water in the crest to cold water. In the trough it then moves from cold to warm water. In the next crest/trough region, the particle moves in the opposite direction. It is difficult to make a true comparison between the model results and the drifter trajectory because 4480 is only in GT37 for a short period of time for image 92.

Case 2, Figure 66, uses an amplitude = 37 km, wavelength = 255 km, phase speed = 9 $km\ dy^{-1}$ and width = 50 km. After creating a five-day average composite streamfunction field for this case, a particle is released within the model meandering

Figure 65: Diagram showing a particle trajectory superposed on the five-day average streamfunction field for DM93. The "box" line represents the particle trajectory produced from case 1 of the observation experiments. The spacing between symbols is 0.1 days. See the text for further discussion.

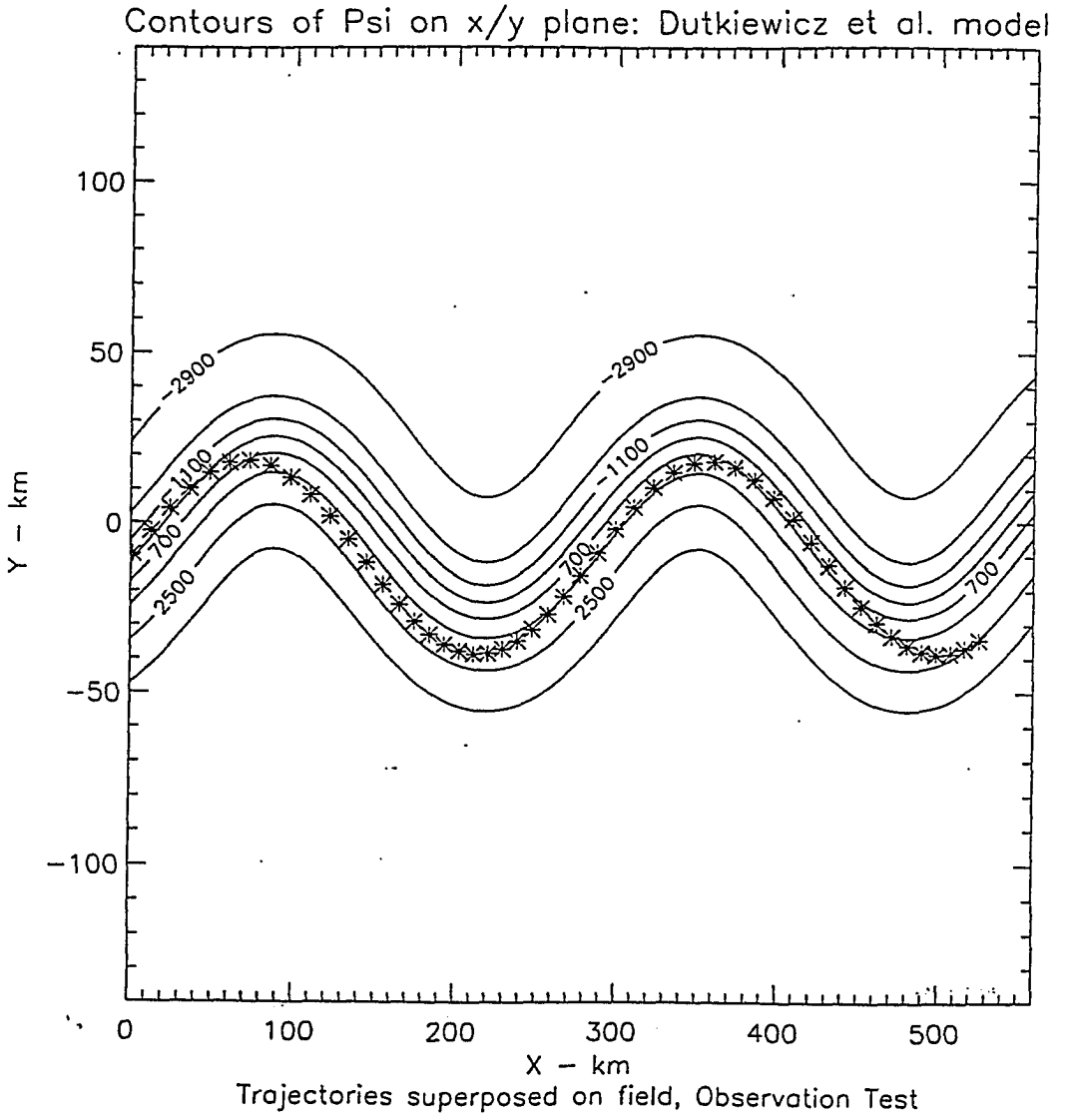

Figure 66: Same as Figure 65, but this is for case 2 of the observation experiments. The time interval is 0.5 days.

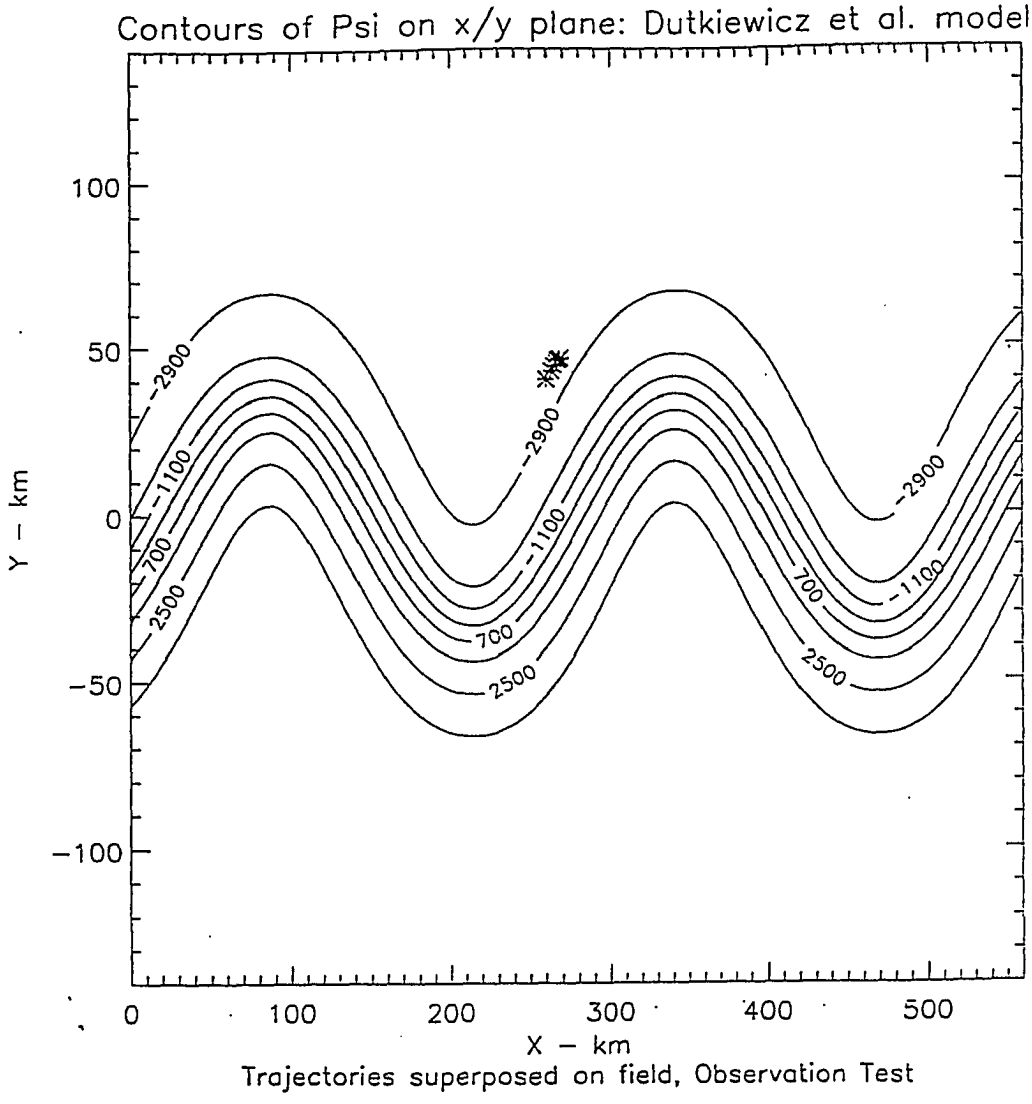

Trajectories superposed on field, Observation Test

jet at the same location as drifter 4480 on image 96. Figure 66 shows that the particle has an initial position on the western side of the crest within the recirculation region of the streamfunction field. Because of this, the trajectory does not follow the meandering jet pattern. In contrast to this the drifter trajectory, which is positioned at this same location on image 96 (see Figure 34), travels a great distance and closely follows the meandering jet pattern. In this case, the time interval between symbols is 0.5 days which is much greater than in the first.

Figure 67 shows a particle which is released at the crest of the meandering jet. Here, a time interval of 0.5 days is also used because of the length of the trajectory produced. For this case, the amplitude = 26 km, wavelength = 396 km, phase speed = 5 $km\ dy^{-1}$ and the width remains constant at 50 km. This trajectory appears to closely follow the streamlines of the meandering jet and travel a short distance as depicted by the drifter trajectory in image 101 (see Figure 35).

The same experiments were carried out for BM91. The results are again different from those obtained in DM93. All figures depicting this experiment have a time interval of 0.1 days between symbols along the trajectories. Case 1 is depicted in Figure 68. This case is difficult to analyze for the same reasons as stated for DM93. Here, the trajectory also follows the meandering jet pattern. But, just as in DM93, the model trajectory is quite different from the drifter trajectory superposed on image 92. The BM91 particle travels from warm water to cold water in the crest. In the trough it goes from cold to warm water. water. The model trajectory reveals a path quite similar to the drifter trajectory in image 96.

Figure 69 shows the five-day average streamfunction field for case 2. The particle is started at the same location as drifter 4480 on image 96 (see Figure 34). It follows the meandering jet pattern. At the crest it moves from warm to cold

Figure 67: Same as Figure 65, but this is for case 3.

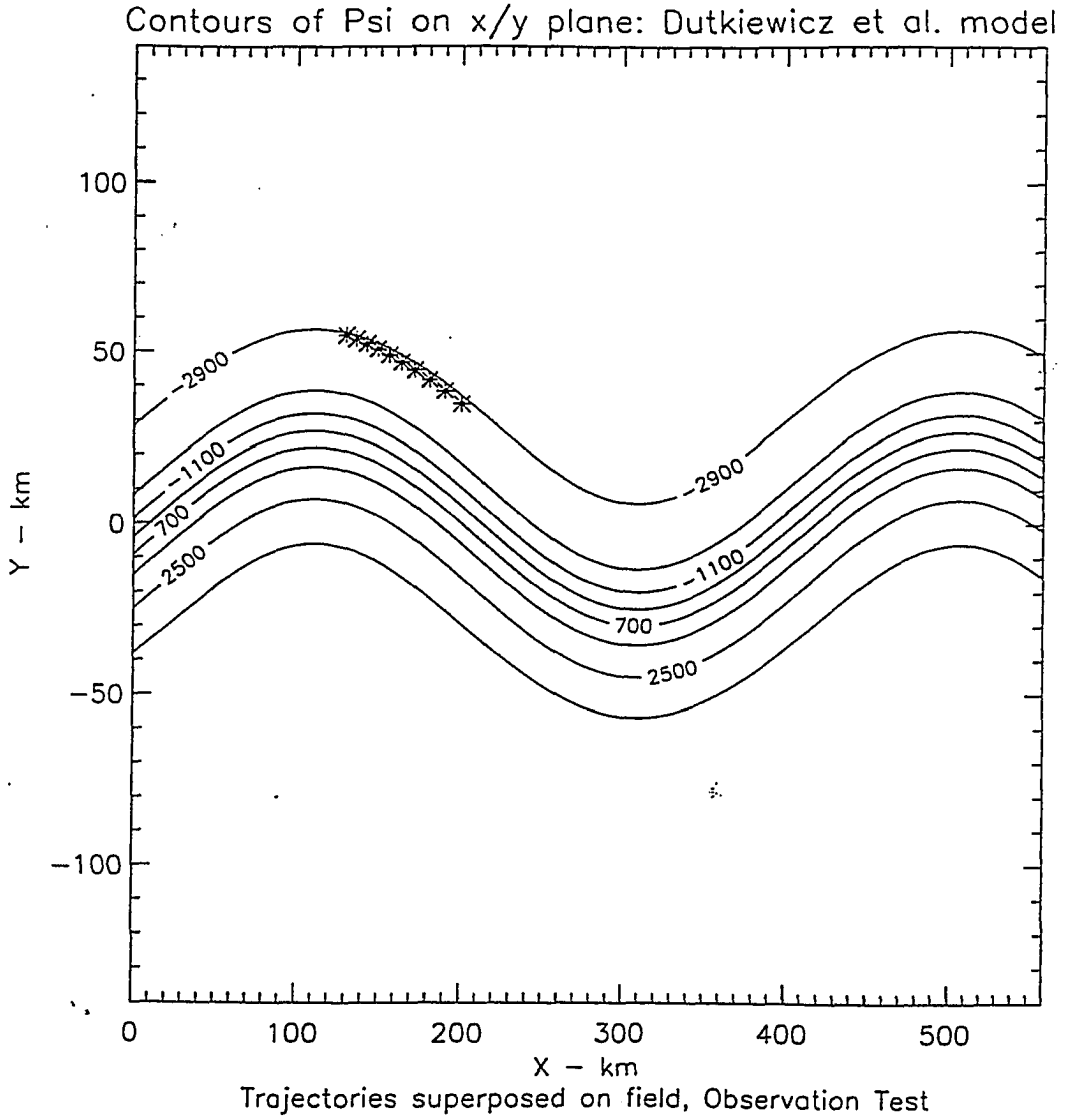

Trajectories superposed on field, Observation Test

Figure 68: Diagram showing a particle trajectory superposed on the five-day average streamfunction field for BM91. The "box" line represents the particle trajectory produced from case 1 of the observation experiments. See the text for further discussion.

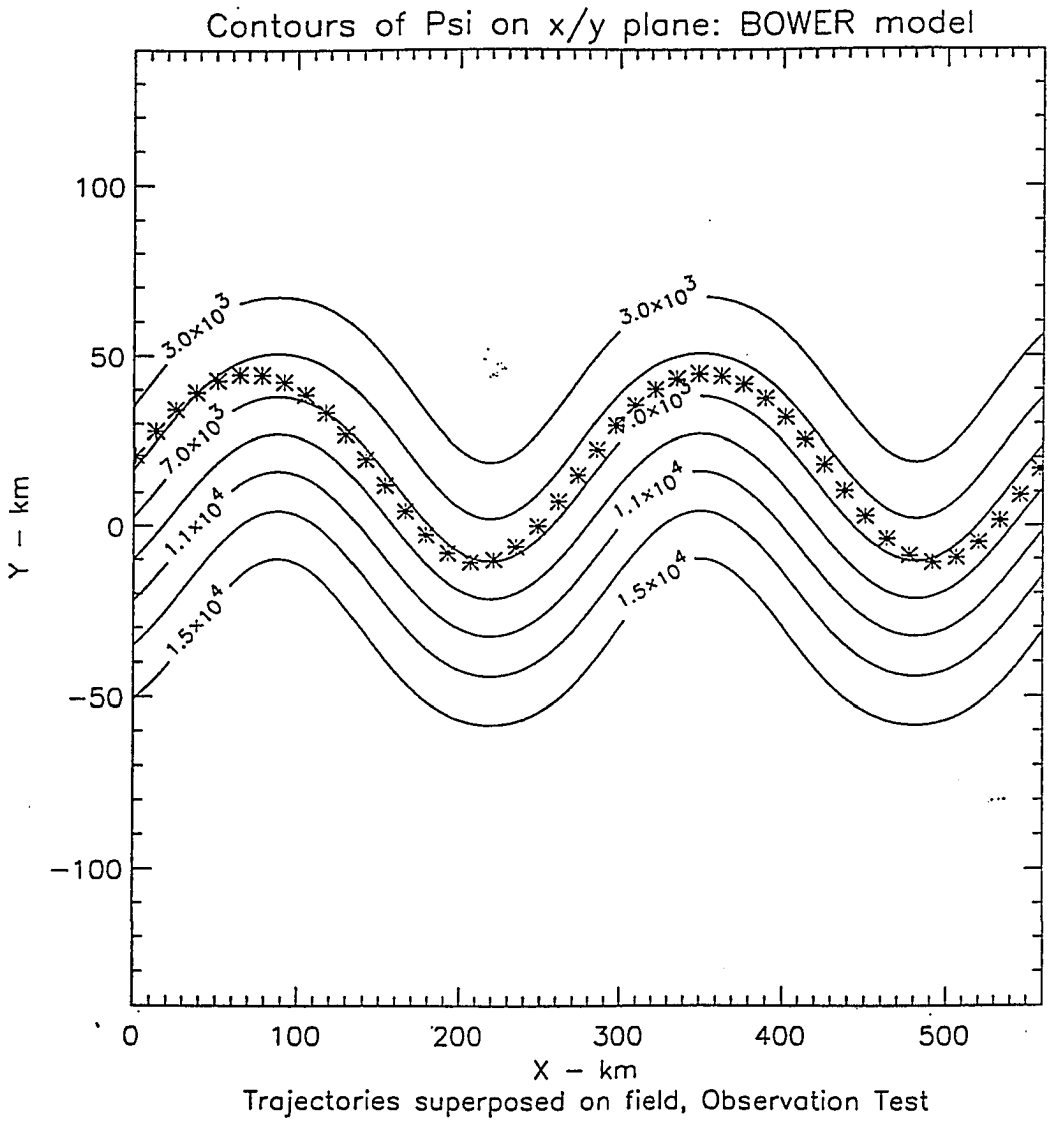

Trajectories superposed on field, Observation Test

Figure 69: Same as Figure 68, but this is for case 2.

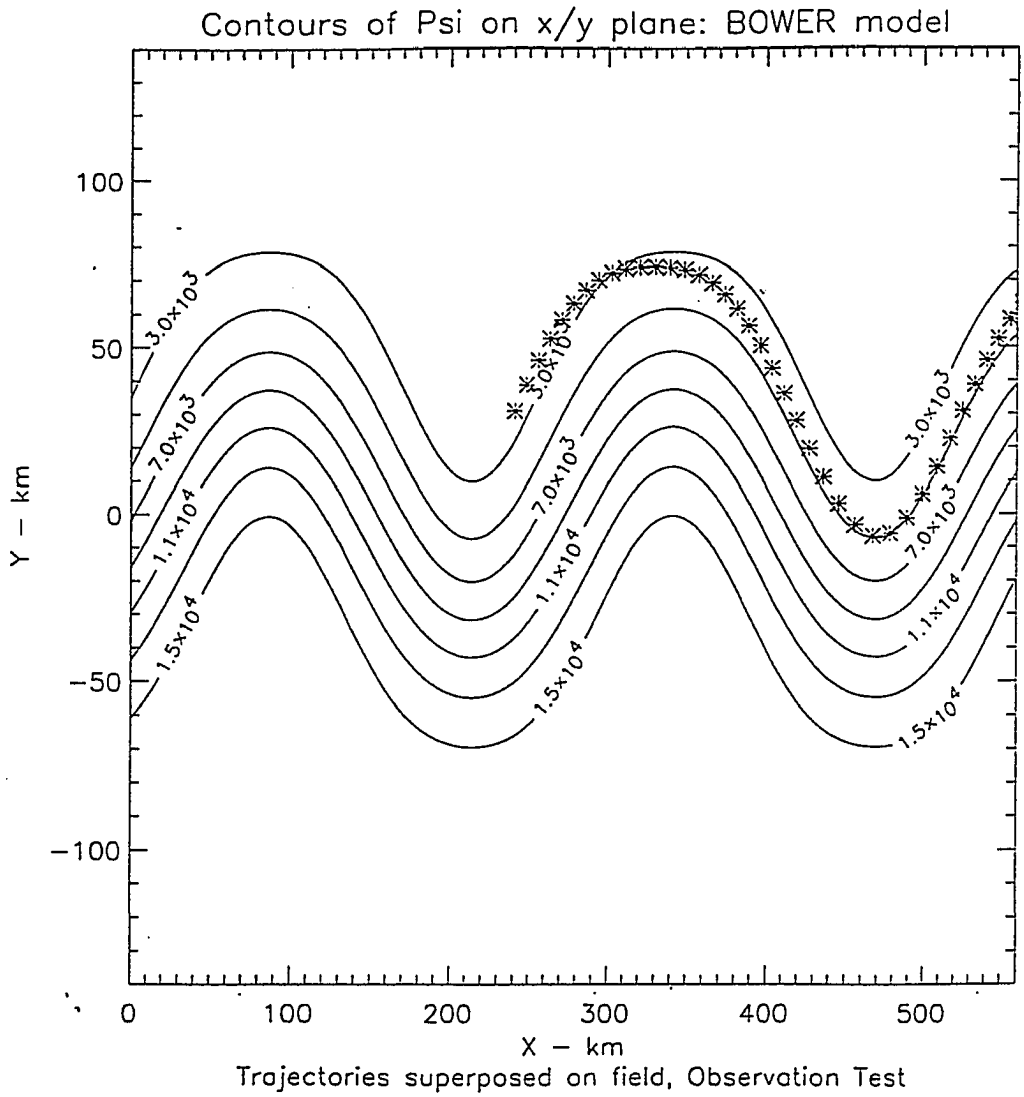

water. The model trajectory reveals a path quite similar to the drifter trajectory in image 96.

Case 3 is illustrated in Figure 70. Here, the particle is released at the crest of the meandering jet. The particle moves from warm water in the crest to cold water. At the trough it flows from cold to warm water. Referring to Figure 35, it is evident that the model particle corresponds well to the trajectory for 4480 in image 101.

The lack of a large data set means that conclusions concerning the observations experiments are tenuous. Overall, as illustrated by the figures, BM91 trajectories closely follow the pattern of the meandering jet and the trajectory of 4480. In contrast the trajectory obtained for DM93 in case 2 is significantly different from the drifter trajectory depicted in image 96. However, in case 3 both model trajectories are similar to drifter 4480 superposed on image 101. Comparing the two models it appears that the BM91 trajectories correlate more favorably with the observations than do those of DM93.

6.4 Inferring velocity from imagery

Both of these kinematic models were developed to look at mixing and exchange across a meandering jet. DM93 also looked at turbulence in the jet region. However, if the models are useful for this they should also be useful as "feature models" for inferring the surface velocity from imagery. To assess this utility, calculations of the u and v velocity components and speed at every location along all the particle trajectories which were discussed in Sections 6.2 and 6.3 are undertaken. Comparisons between the speeds calculated from the STD and observation data obtained from using both models also are examined in this section. Of particular interest is the determination of the speeds at the meander crests and troughs. This is of impor-

Figure 70: Same as Figure 68, but this is for case 3.

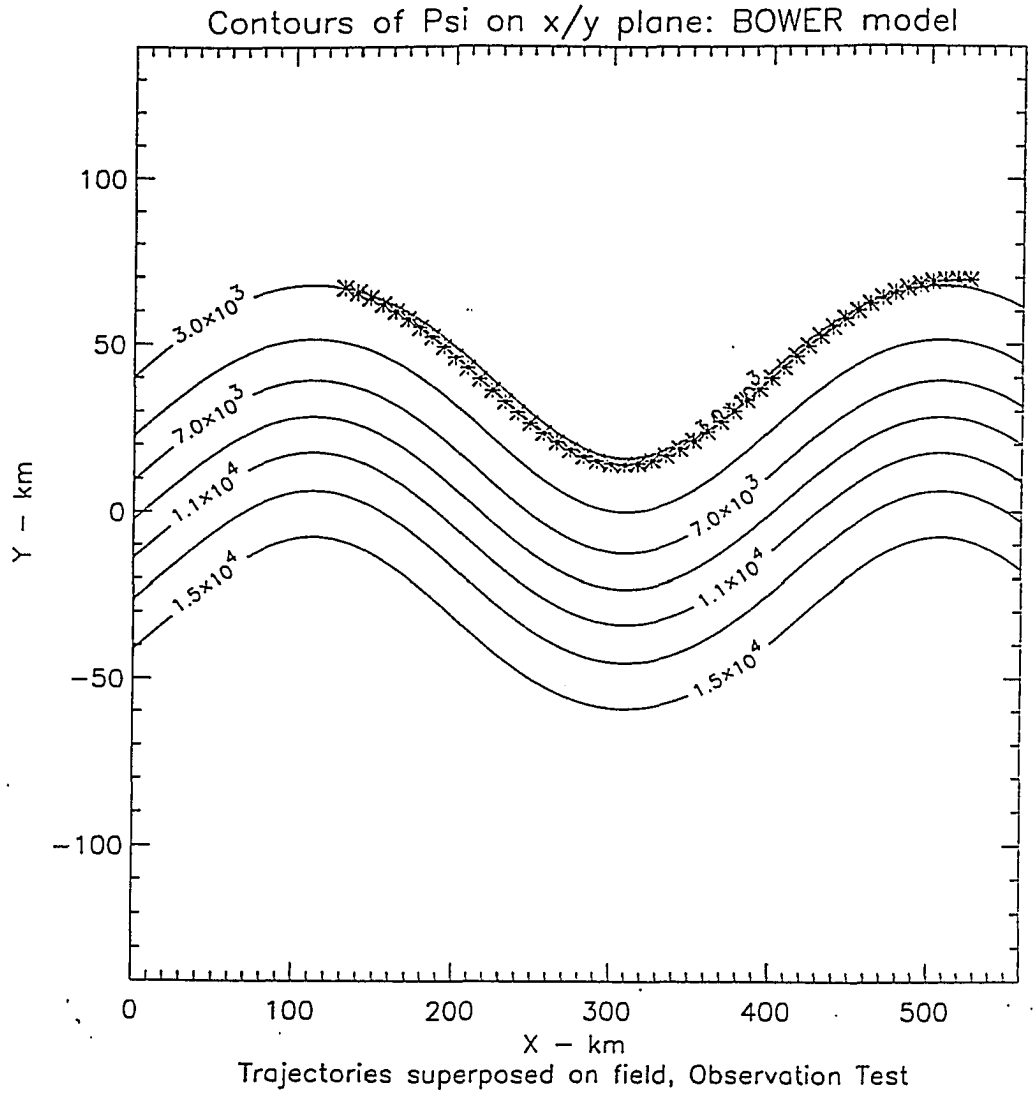

Trajectories superposed on field, Observation Test

tance because these are critical points of the flow field which can serve as tests of models and observations. They are also the locations that particles are most likely to escape from the meandering jet and enter the recirculation areas. Thus, determining speeds at these locations would aid in the understanding of the jet, as well as determining whether there is a strong correlation between the surface velocity and composite satellite imagery.

The three trajectories in case A for DM93 differ in length (see Figure 55). This is because of the starting positions for each of the particles. Two trajectories are started south of the centerline, while the third is started near the center. The speeds calculated for the "box" particle are much greater than those found for the other two particles. At the starting point of the "box" particle the speed is 190 $km\ dy^{-1}$. As this particle flows along its path, its speed fluctuates. At the crest it attains a speed of 158 $km\ dy^{-1}$. On the eastern flank of the first crest, its speed is 183 $km\ dy^{-1}$. The speed decreases as the particle flows into the trough. Here, the value is 156 $km\ dy^{-1}$. At the peak of the second crest, the value has remained at 156 $km\ dy^{-1}$. The "star" particle has speeds that range from 45 - 64 $km\ dy^{-1}$, with the maximum attained at the crest. The shortest of the three trajectories corresponds to the southernmost particle. It reaches a maximum speed of 33 $km\ dy^{-1}$ at the crest.

In case B (see Figure 56), the "box" and "plus" particle paths are much shorter than the "star" path. This is because the "star" path is confined to the region of the jet with the maximum speeds. The "star" trajectory reaches a speed of 158 $km\ dy^{-1}$ at its first crest, and then accelerates to 178 $km\ dy^{-1}$ along the eastern flank of the crest. A low of 136 $km\ dy^{-1}$ is calculated for the speed at the trough. Eventually, the "star" particle does gain more speed and acquires a speed of 156 $km\ dy^{-1}$ at the second crest. This value is consistent with that seen at the first

crest. At the peak of the first crest, the "box" particle has a speed of 52 $km\ dy^{-1}$. However, the "plus" trajectory, which is located south of the center streamline, only attains a speed of 28 $km\ dy^{-1}$ at the crest.

As shown in case C (see Figure 57), three particles are released from the first crest. The "star" particle reaches speeds much greater than the other two particles. This is expected because this trajectory is confined to the region of maximum speed. At the first crest, this particle has a speed of 156 $km\ dy^{-1}$. However, as it flows from the crest to the trough it reaches speeds of 183 $km\ dy^{-1}$ on the eastern flank of the crest. It is interesting to note that the speed along this eastern flank is much greater than that observed at the crest. At the trough the value is 159 $km\ dy^{-1}$. Eventually, the particle reaches the second crest where its speed is the lowest at only 152 $km\ dy^{-1}$. The northernmost particle starts off with a speed of 26 $km\ dy^{-1}$ and increases to 92 $km\ dy^{-1}$ at the trough. It decreases again to 70 $km\ dy^{-1}$ at the second crest. The "plus" parcel has a speed of 61 $km\ dy^{-1}$ at the crest.

Case D depicts particles being released on the eastern flank of the first crest (see Figure 58). The starting speeds vary greatly for the three particles. Here, the speeds are 92 $km\ dy^{-1}$, 39 $km\ dy^{-1}$ and 10 $km\ dy^{-1}$ for the "plus", "star" and "box" parcels, respectively. A speed of 32 $km\ dy^{-1}$ is attained at the trough for the "plus" particle. Also at the trough, the "box" parcel reaches a speed of 40 $km\ dy^{-1}$. The "star" particle (the middle trajectory) has a speed of 61 $km\ dy^{-1}$, which is substantially larger than the other two.

The final STD experiment was started at a meander trough (see Figure 59). There is a wide range in speeds for the three particles at this position. The speed for the southernmost particle is only 19 $km\ dy^{-1}$. The "star" particle has a maximum speed of 128 $km\ dy^{-1}$ at the trough location. The remaining particle starts off with a speed of 94 $km\ dy^{-1}$. There is also a significant range in the speeds calculated

for the second crest region. Here, the "plus" particle dramatically increases from its speed of 19 $km\ dy^{-1}$ to 88 $km\ dy^{-1}$. At the other extreme is the "box" particle which went from 94 $km\ dy^{-1}$ at its trough to 28 $km\ dy^{-1}$ at the second crest. The "star" particle speed increases relatively slightly to 152 $km\ dy^{-1}$.

In summary, analysis of the STD data using DM93 show that the speeds are usually greater in the crests than at the troughs. However, in some instances the speeds obtained at the troughs are larger than those at the crests. This is observed in case C and for the shorter trajectories in case E (see Figures 57 and 59). Another interesting factor is that the speeds recorded on the eastern flank of the first crest are always much greater than values calculated at either the crests or the troughs. In case D, however, the speeds at the troughs are slightly larger. Particles that are released closest to the center streamline always recorded the highest speeds. Therefore, this analysis suggests that the location of particles across the jet and along the jet affect the speeds obtained by these parcels when they are released and run through DM93.

As discussed earlier the same five STD cases are run through BM91. Figure 60 illustrates the results obtained for case A using BM91. The "box" particle maintains a fairly consistent speed along its trajectory of 158 $km\ dy^{-1}$. Recall that this is the value used to calculate the Ψ_o scale factor within the model. The "star" parcel also maintains a fairly constant speed. It starts off at 143 $km\ dy^{-1}$ at the first crest, decreases to 134 $km\ dy^{-1}$ in the trough and then increases again to 143 $km\ dy^{-1}$ in the second crest. Speeds around 105 $km\ dy^{-1}$ are attained at both crests for the "plus" particle. At the trough, the "plus" parcel decreases to 87 $km\ dy^{-1}$. The magnitude of the speeds for these three particles is different but, the trend showing an increase in speeds at the crests and a decrease in the troughs is consistent.

Case B for BM91 (see Figure 61) follows a similar trend as revealed in case

A, where the particle in the middle of the stream maintains the greatest speeds. The northernmost particle has the second largest speed and the "plus" particle the smallest. The "star" particle attains the greatest speeds of 158 $km\ dy^{-1}$. The "plus" parcel has speeds ranging from 122 $km\ dy^{-1}$ at the crests to 108 $km\ dy^{-1}$ at the trough. It is interesting to note that the speeds at the two crests for the "box" particle are lower than the speed at the trough. The speed at the crests is 138 $km\ dy^{-1}$, however at the trough it is 146 $km\ dy^{-1}$.

As shown earlier in Figure 62, the three trajectories are released from the first crest. The "box" particle has speeds which range from 124 $km\ dy^{-1}$ at its first crest to 135 $km\ dy^{-1}$ at the trough, then decreases again at the second crest to 124 $km\ dy^{-1}$. The particle ("star") which is confined to the center streamline region has maintained a speed of 158 $km\ dy^{-1}$ along its entire path. A speed of 144 $km\ dy^{-1}$ at both crests is calculated for the "plus" parcel. At the trough, its speed decreases to 134 $km\ dy^{-1}$.

The fourth case for BM91 starts the trajectories on the eastern flank of the first crest (see Figure 63). The speeds at the starting position and second crest are the same at 151 $km\ dy^{-1}$ for the "plus" particle. The speed is lower in the trough, where it only reaches a speed of 145 $km\ dy^{-1}$. The middle parcel maintains a speed of approximately 141 $km\ dy^{-1}$ throughout its path. However, at the second crest its speed decreases to 132 $km\ dy^{-1}$. The northernmost particle maintains a speed of about 120 $km\ dy^{-1}$ along its path. It too has speeds which decrease once the particle reaches the second crest. Here, the "plus" particle has a speed of 106 $km\ dy^{-1}$.

The final case for BM91 is illustrated in Figure 64. In this case, the particles are simultaneously released from the trough region. The "plus" particle has a value of 100 $km\ dy^{-1}$ for its speed at the trough. At the crest, this particle has a speed

of 116 $km\ dy^{-1}$. Speeds ranging from 150 $km\ dy^{-1}$ at the trough to 156 $km\ dy^{-1}$ at the second crest are seen by the middle particle. The trend is reversed with the "box" parcel. Here, the larger speed is recorded in the trough at 154 $km\ dy^{-1}$, while the crest only has a speed of 148 $km\ dy^{-1}$.

A brief summary of the analyses of BM91 shows that the speeds are usually higher in the crests or the crests and troughs have the same values. Some instances in cases C and D (see Figures 62 and 63), the speeds are greater at the troughs. The speeds recorded along the eastern flanks of the crest have the same values as those obtained at the crest. However, overall the speeds for a particular particle do not vary much along its trajectory. The length of all the trajectories are much longer than displayed in the figures.

Several differences are found in the comparison between the speeds obtained by running the STD values through the kinematic models. In case A) the speeds for the "box" particle are the same. The "star" and "plus" particles in BM91 have speeds significantly larger than in DM93. The length of the trajectories for the "star" and "plus" particles is also significantly larger in BM91. For case B, the speeds for the "box" particle are consistent in BM91 at 158 $km\ dy^{-1}$. However, in DM93 the values span over a larger range from 136 - 178 $km\ dy^{-1}$. Again, the speeds recorded for the "box" and "plus" particle are much larger in BM91 than they are in DM93. This is the reason that trajectory lengths for these two particles in DM93 are shorter than BM91. The third case reveals similar results for the "star" trajectory. In DM93 values vary a great deal, but in BM91 this particle maintains a constant speed of 158 $km\ dy^{-1}$. As observed in the other cases, the trajectory length and particle speeds are much lower for the two other particles. In case D, the speeds for the particles launched in BM91 range from 120 - 152 $km\ dy^{-1}$. These are at least twice as large as those revealed in running DM93. Also note, that the

trajectories of the DM93 particles are again much shorter than those observed in BM91. Finally, case E calculates speeds for all particles which are much larger in BM91 than they are in DM93.

The observation experiments reveal different results than those obtained in the STD analyses. As stated earlier, the parameters and starting positions of the particles used for this analyses are obtained directly from the contemporaneous set of GT37 composite imagery and drifter data. For case 1 using DM93 (see Figure 65), the speed at the starting position is 128 $km\ dy^{-1}$. At the crest the particles speed only increases slightly to 129 $km\ dy^{-1}$. The speed dramatically decreases to 90 $km\ dy^{-1}$ at the meander trough, and then increases again to 127 $km\ dy^{-1}$ at the second crest. The emphasis here should be placed on the first crest because this is the only position that corresponds to drifter 4480 on image 92. Figure 66 shows case 2 for DM93. Here, the trajectory is extremely short and not at all similar to the path observed on the imagery. The speed throughout the particle trajectory is approximately 9 $km\ dy^{-1}$. The final observed case for DM93 (see Figure 67) also shows low speeds. At the meander crest the particle has a speed of 12 $km\ dy^{-1}$ but, its final speed is 25 $km\ dy^{-1}$.

It is difficult to draw any substantial conclusions about DM93 in the observation experiments. The particle speeds generated do not follow a trend. In case 1, the speeds are greater in the crests than in the trough. However, in the third case, the speeds are twice as large on the eastern flank than at the crest. The trajectory in case 2 is too short to make a significant conclusion.

The speeds calculated for BM91 are much larger than those determined for DM93 during the observation experiments. In case 1 (see Figure 68), the particle speeds range from 136 $km\ dy^{-1}$ to 147 $km\ dy^{-1}$. At the starting position the particle has a speed of 141 $km\ dy^{-1}$. The speeds decrease as the parcel moves

towards the crest where it reaches a value of 136 $km\ dy^{-1}$. As it flows towards the trough, the speed along the eastern flank of the crest shows the maximum speed of 147 $km\ dy^{-1}$. The particle attains a speed of 138 $km\ dy^{-1}$ at the second crest, which is consistent with the value at the first crest. The speeds at both troughs are greater than those at the crests. Here, the value is 145 $km\ dy^{-1}$.

The speeds along the particle trajectory in case 2 (see Figure 69) are relatively constant. The starting speed for this particle is 114 $km\ dy^{-1}$. At the crest, its speed decreases to 93 $km\ dy^{-1}$. On the eastern flank of this crest the speeds reach a maximum of 116 $km\ dy^{-1}$, and then decrease slightly to 113 $km\ dy^{-1}$ at the meander trough. Figure 70 depicts the final case for the observed experiments run through BM91. Here, the particle is released at the crests and flows along the meandering jet. The speed at the first crest is 80 $km\ dy^{-1}$. At the eastern flank of the crest, the particle reaches a speed of 87 $km\ dy^{-1}$ and eventually increases to 88 $km\ dy^{-1}$ at the meander trough. The particle speed decreases again at the second crest recording a speed of only 80 $km\ dy^{-1}$.

Overall, the observation experiments utilizing BM91 produce the greatest particle speeds on the eastern flanks of the meander crests. A comparison between the values obtained at the crests and troughs shows that the speeds are greater in the troughs than at the crests. This is true for all three cases.

Comparisons between these model results and the drifter observations now can be pursued. Because the observation experiments uses parameters specifically related to drifter 4480 and its contemporaneous satellite imagery, a good correlation between the speeds is expected. However, this is not the case. In DM93, the particle speeds are drastically lower than the true speeds for drifter 4480 at the same locations along the meandering jet. Case 1 for DM93 reveals a speed of 129 $km\ dy^{-1}$ at the crest, while at the trough it is 90 $km\ dy^{-1}$. In contrast to this, the

drifter speeds for 4480 on image 92 are 158 $km\ dy^{-1}$ at the crest and 157 $km\ dy^{-1}$ at the trough. The values obtained when running BM91 are much closer to the above stated speeds for drifter 4480. At the crest, the particle for BM91 has a value of 136 $km\ dy^{-1}$. The speed attained in the trough is 145 $km\ dy^{-1}$.

The second observation experiment is related to drifter 4480 superposed on image 96. Here, the drifter has values ranging from 87 $km\ dy^{-1}$ in the trough to 164 $km\ dy^{-1}$ at the second crest. DM93 shows no correlation at all to this data. Its speeds are extremely low, only reaching a value of 10 $km\ dy^{-1}$. It is difficult to even make a comparison because of the length of the particle trajectory, which is very short. Once again, BM91 has speeds which are closer in value to those obtained by 4480, but are still 40 - 50 $km\ dy^{-1}$ less.

The final comparison between the drifter speeds and the particle speeds generated by the models is represented by case 3. Here, the case uses data from drifter 4480 superposed on image 101. Drifter 4480 has a speed of 120 $km\ dy^{-1}$ at the meander crest and one of 135 $km\ dy^{-1}$ at the trough. As in the two other scenarios, the particle speeds and trajectory length generated by DM93 are much lower than those of drifter 4480, by more than 100 $km\ dy^{-1}$. However, the speeds produced by BM91 are relatively closer to those calculated for drifter 4480 on image 101. Here, the speeds also show the same pattern of being greater in the troughs than at the crests.

In summary, it appears as if there is no correlation between the drifter speeds and the speeds generated from the observation experiments. Analysis also shows that of the two kinematic models, BM91 speeds correspond the best to the drifter data. Even though the speeds are much lower, the trend of values at the crests and troughs is similar. Despite the fact that two kinematic models are run using the same amplitudes, wavelengths and phase speeds determined for the composite

imagery and drifter data, no direct link was found with the contemporaneous data.

6.5 Summary

The following conclusions can be drawn from using the observed and standardized parameters in the kinematic models.

- Particle trajectories cross each other in DM93, but not in BM91.
- There is a significance difference between the particle trajectories generated by the two kinematic models. This is due to the scaling width in each model and the addition of the β term in DM93.
- Particles flow from warm water to cold water in the crests. They move from cold to warm water in the troughs. This is true for both models utilizing STD. However, there are some exceptions where the particles move from cold to warm water in the crests and warm to cold in the troughs.
- Particles released closest to the center of the Stream followed the meandering jet pattern the best.
- The STD trajectories for BM91 are much longer than those generated by DM93.
- The trajectories in BM91 also appear to remain evenly spaced during the standardized experiments.
- In the observation experiments, the BM91 trajectories closely follow the meandering jet pattern and drifter 4480.
- Trajectories generated from using observed values in DM93 are different from the drifter trajectories superposed on the corresponding images.

- STD data run through both models record speeds greater in the crests than in the troughs.
- Speeds calculated at the flanks of the meander crests are usually larger than values attained at the crests of troughs when using the STD data in DM93. However, when BM91 is utilized the maximum speed is either located at the troughs or on the flanks.
- Particles released closest to the center streamline recorded the highest speeds in both DM93 and BM91 in the STD experiments.
- For the observed experiments utilizing DM93, the particle speed is greatest at the crest in one case and on the eastern flank in the other case.
- In the observed experiments for BM91 the greatest speeds are attained at the trough or the eastern flank, rather than at the crests. The maximum speed is always located on the flank.
- No direct link between the drifter speeds and those generated from the observations experiments can be established.
- Of the two kinematic models, speeds generated by BM91 are most closely related to the drifter speeds.
- As a feature model, BM91 is better than DM93.

7 Potential Vorticity Model Results

The world is what it is
and I am what I am....
This out there and this in me,
all this, everything, the resultant
of inexplicable forces. A chaos
whose order is beyond comprehension.
Henry Miller

In this chapter, the focus is on the results attained from the equivalent barotropic potential vorticity model, PVM94. A similar format to Chapter 6 is followed, whereby three experiments are discussed. The first experiment, which is analyzed in Section 7.1, examines the results obtained from PVM94 using the original DM93 parameters. In Section 7.2, the standardization experiments are addressed. The results of the observation experiments are examined in the following section, and in Section 7.4, the speed and velocity components are calculated. A brief statement about the similarities and differences between the potential vorticity and two kinematic models for each experiment is made at the end of each section. Lastly, a detailed summary of this chapter is provided in Section 7.5.

7.1 Comparison of PVM94 with DM93 and BM91

A comparison between the results obtained from PVM94 and those of the kinematic models utilizing the original DM93 parameters is pursued. Recall, that the original DM93 parameters are wavelength = 450 km, phase speed = 14 $km\ dy^{-1}$,

width = 70 km and amplitude = 70 km. Within the two kinematic models these parameters can be substituted directly into the models and their effects on the streamfunction field can be easily recognized. However, in PVM94 the substitution is not as straightforward. Therefore, a brief discussion concerning these parameters in PVM94 is necessary before the results of the experiments are discussed.

Section 3.2 gives a detailed description of the potential vorticity model. Of particular importance to recall from that section are (3.2.8) - (3.2.12) and the corresponding G(y) and Y(y) solutions for all three regions; upper, lower and inner. Meander wavelength and phase speed are incorporated in the $sin(k(x-ct)$ component of the solution. The jet width and meander amplitude, however, are not specifically identified in PVM94. Rather, they are parameterized in A, λ and γ. Moreover, there is a non-linear coupled relationship between these parameters. This makes it difficult to make a direct comparison between PVM94 and the kinematic models. Thus, a parametric study is undertaken to "tune" PVM94 by systematically varying A, λ and γ so that good visual agreement with the kinematic model streamfunction fields is achieved.

To be more specific, values for the parameters, χ, Q_u, and Q_l in PVM94 are affected every time the value of A is altered. This is shown in Section 3.2. The only way to attain the desired meandering jet with a certain width and amplitude is to systematically change the values of A, γ and λ in the solutions of PVM94. The values for γ and λ directly affect the solutions to the G part of Ψ, while A affects both the G and Y parts. By examining, the equations in Section 3.2, it can be seen that the relationship between all the variables is not as directly linked as those in the kinematic models. Analysis of numerous experiments with variations of the parameter values in PVM94 shows that the parameters A and λ are responsible for the meander jet width and amplitude, respectively. Of course, these are not the only

values that affect the jet shape, but they do play a dominant role. Examination of the tests shows that as A increases the meander width also increases. Similarly, as the value of λ increases, the meander amplitude also increases.

It is a little more difficult to assess the affects of γ on the meandering jet shape. Analysis suggests that as the value of γ increases the amplitude decreases. This increase also appears to make the meander crest flat instead of peaked. The variation in γ slightly affects the meandering jet width, where a decrease in γ leads to a decrease in the width. However, the reader must keep in mind that these parameters are non-linearly coupled and that other factors also affect the meandering jet shape. Overall, it is clear that the determination of the correct parameter values to substitute into PVM94 is not as straightforward as the direct substitution of parameters into the kinematic models.

Figure 71 displays the streamfunction field for PVM94 with three particle trajectories overlaid. The trajectories are generated in the same manner as those in DM93 and BM91, where the starting positions are relative to the "box" particle and are lined normal to the meandering jet. Examination of the results from the three models utilizing the original DM93 data set (see Figures 53, 54 and 71) shows that there are notable differences. The streamfunction fields are quite different, however the PVM94 model does meet the requirements of having amplitude and width equal to 70 *km*. Within Figure 71 the "box" particle is started at the initial position of (0,0). At the crest, it moves from warm to cold water. The particle converges towards the center streamline as it travels to the trough. Here, the "box" particle goes from warm to cold water. The "star" particle follows a similar pattern. It moves from warm to cold water in the crest, as well as in the trough. This particle diverges from the center as it flows to the trough. The remaining particle, "plus", flows into the crest moving from warm to cold water. As it continues to move near

Figure 71: Diagram illustrating the five-day average streamfunction field for PVM94 utilizing the original DM93 parameters. The "box", "star" and "plus" lines represent particle trajectories. The time interval elapsed between each symbol along the trajectory is 0.1 days. Water north of the Gulf Stream meandering jet region represents the cold water of the North Atlantic. South of the meandering jet region is the warm water of the Sargasso Sea.

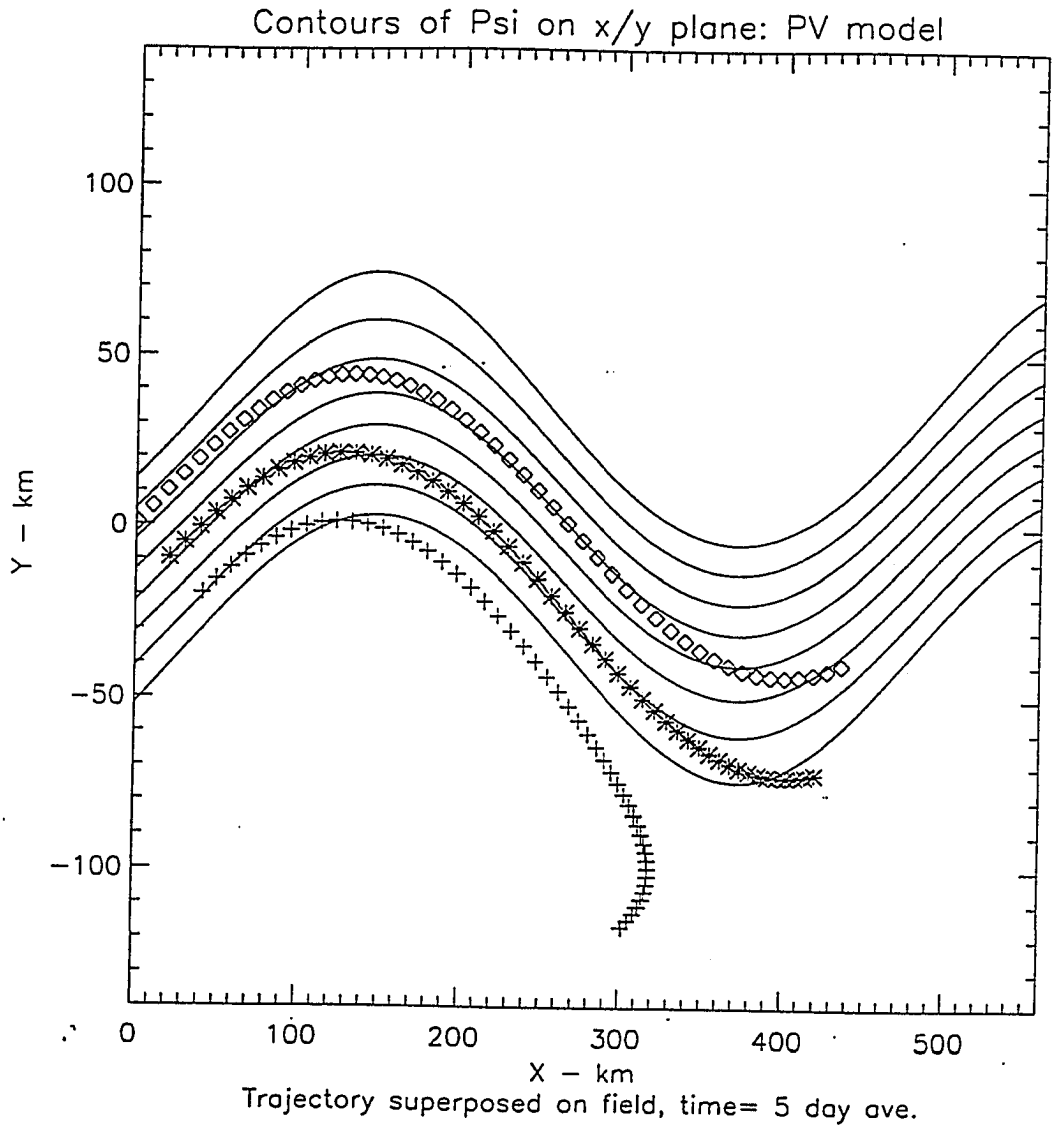

the crest, the "plus" particle gets trapped in the recirculation region outside the meandering jet. Here, it continues to flow southward and eventually reaches a point where it begins to move back to the west.

The comparison between the three models shows that PVM94 (see Figure 71) is most similar to BM91 (see Figure 54). The similarities lie in the length of the three trajectories, the movement of the particles and the path of the "plus" particle. PVM94 and BM91 have much longer trajectories than DM93. The particles have the same movement from warm to cold water at both the crest and trough. The interesting item to note is that the "plus" particle diverges from the center and becomes entrained in the recirculation region in both PVM94 and BM91. However, in BM91 the "plus" particle flows southward but, does not turn and travel westward. In DM93, this particle converges towards the center of the meandering jet and crosses the other trajectories. The particle trajectories in PVM94, as in BM91, do not cross each other.

In summary, PVM94 results are similar to those obtained from BM91. All three particles move from warm to cold water at the crest and trough. An exception to this is the "plus" parcel which does not enter into the trough region. Instead it becomes entrained in the recirculation region and begins to flow westward. A major difference between this model and DM93 is the fact that the separate trajectories do not cross each other as they do in DM93.

7.2 Standardization Experiments

The standardization experiments were explained in detail in Section 5.7 and 6.2. The geographic locations for the five cases are the same except for case A. Here, the initial position is (0,20) instead of (0,0). This position was chosen so that three

particle trajectories could be aligned across the entire width of the jet, instead of only being concentrated in the lower half of the jet. Note that the time interval elapsed between symbols for the particle trajectories is 0.1 days, which is consistent with BM91.

In case A for PVM94 (Figure 72), the "box" particle closely follows the meandering pattern of the jet. It moves from warm to cold water in the crest. In the trough, it appears to maintain a fairly constant temperature or increases only slightly. As it flows into the second crest, the "box" parcel moves from cold to warm water. The entire trajectory length spans a total of 708 *km* over the five day composite period. The "star" particle starts near the middle of the stream. As it flows into crest, it moves from warm to cold water. On the downswing side of the first crest, the particle diverges from the center streamline. In the trough, it also appears to maintain a constant temperature or increases slightly. Flowing from the trough towards the second crest, the "star" particle moves back towards the center of the jet. At the crest, it maintains a constant temperature. The length of this trajectory is also longer than the x axis. Its length reaches a total of 772 *km*. The remaining particle is positioned south of the jet center. It flows from warm to cold water in the crest. As it moves towards the trough, it briefly leaves the meandering jet pattern of the model. However, at the trough the "plus" particle is entrained back into the meandering jet and flows from cold to warm water. At the following crest, this parcel also appears to maintain a relatively constant temperature. Its length is 718 *km*. All three trajectories closely follow the meander jet pattern and do not cross each other.

The next case, case B (Figure 73), the particles are released from the western flank of the meandering jet. The "box" particle spans a total length of 756 *km*. This parcel flows from warm to cold water in the crest. As it flows to the trough, it con-

Figure 72: Plot depicting three trajectories superposed on the five-day average streamfunction field for PVM94. The "box", "star" and "plus" lines represent particle trajectories produced from STD parameters. The symbols are equally spaced in time with an interval of 0.1 days.

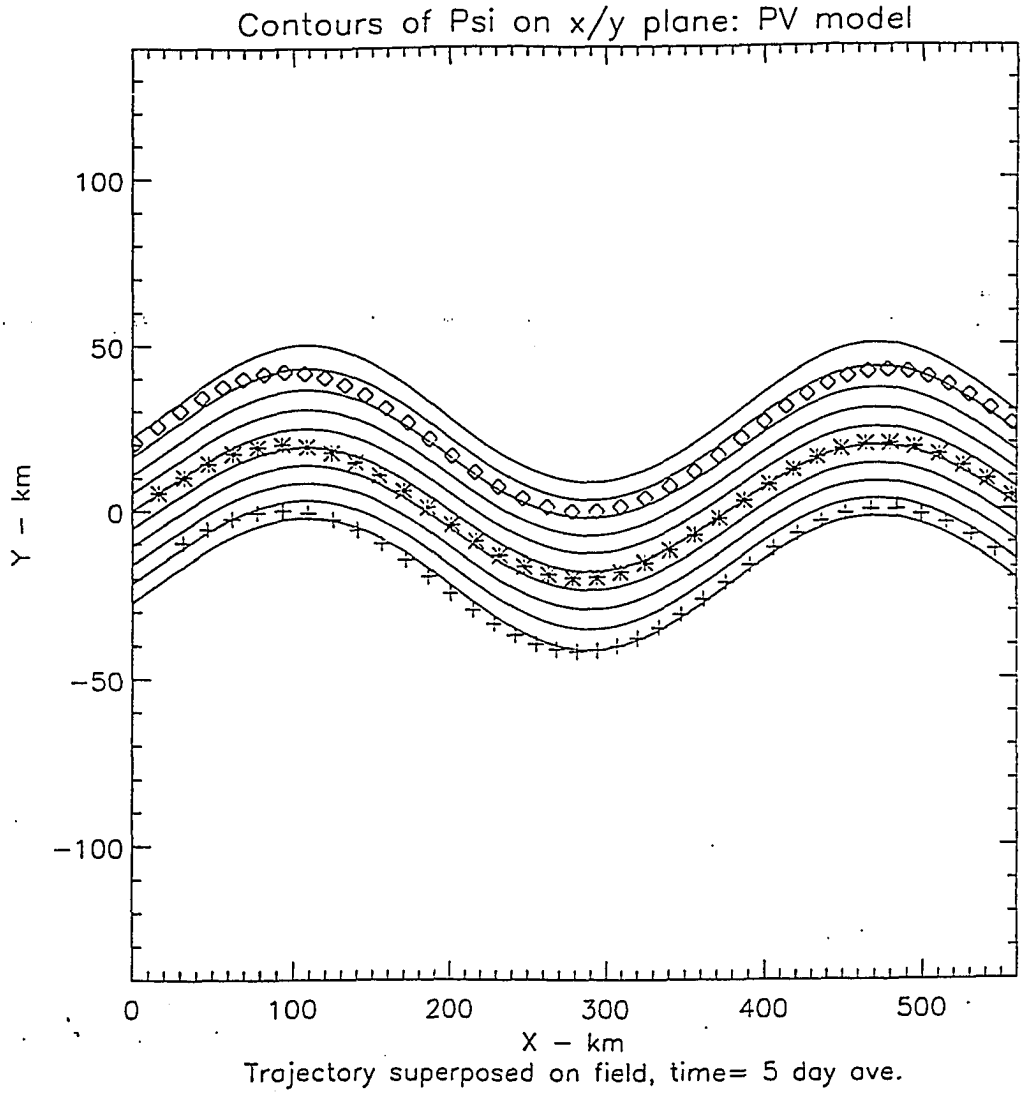

Figure 73: Same as Figure 72, but the starting position is different.

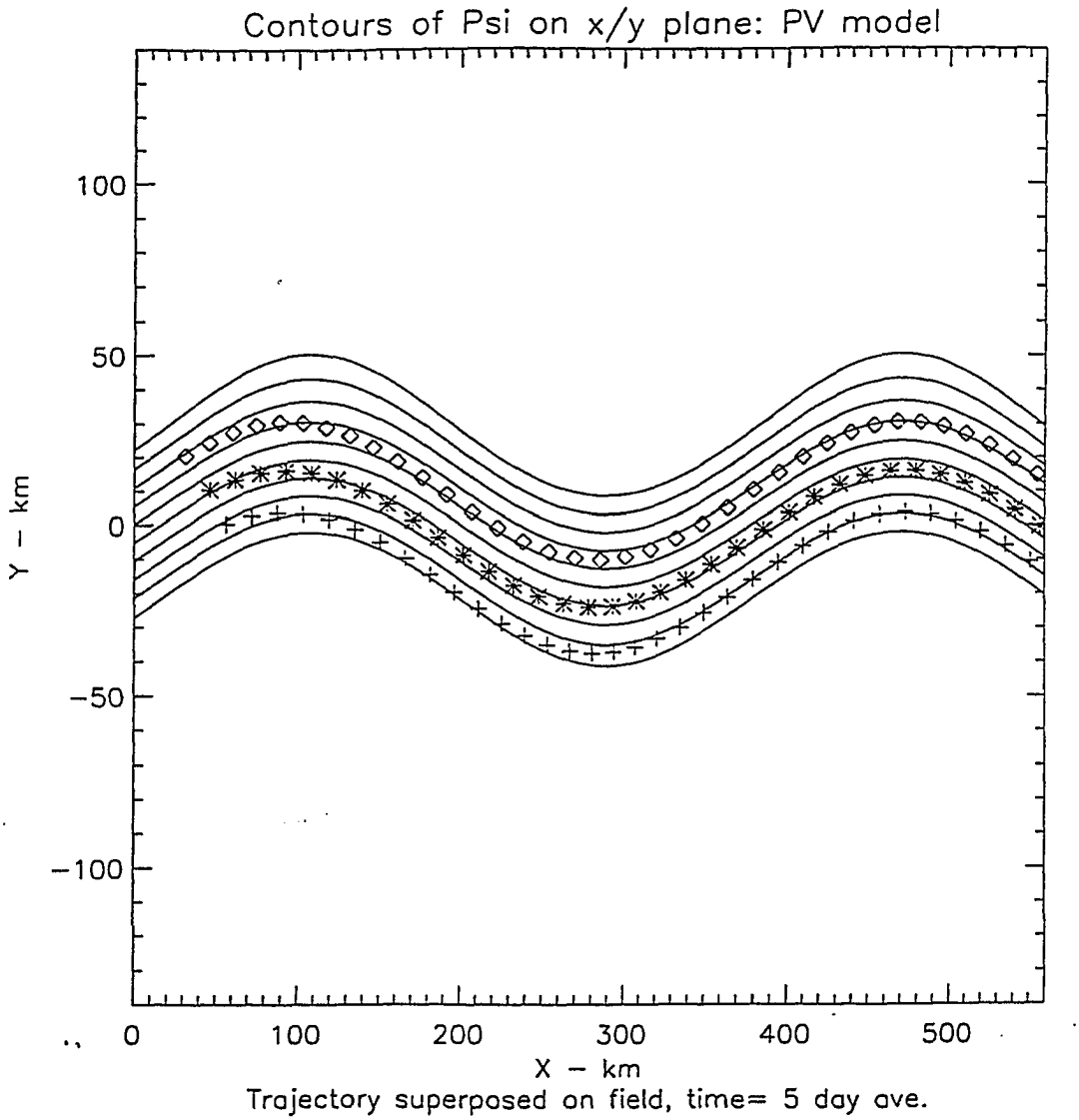

verges towards the center streamline. Within the trough, the "box" particle keeps a relatively constant temperature or increases slightly. Moving along the western flank of the second crest, the particle diverges from the center of the meandering jet and moves into warm water. At this crest, the "box" particle maintains a constant temperature. The "star" particle follows a trend similar to the "box" particle. It moves from warm to cold water in the crest, maintains a constant temperature or increases slightly at the trough and maintains a constant temperature at the second crest. It diverges from the center as it moves along the eastern flank of the first crest, but converges back towards the center as it flows up the western flank of the second crest. Its total length is also much longer than the x axis. It reaches a length of 770 km over the five day period. The "plus" parcel also closely follows the meandering jet shape. At the crest, it moves from warm to cold water. However, in the trough it moves from cold to warm water. The "plus" particle at the second crest maintains a constant temperature. The length of the "plus" particle trajectory is 737 km.

Case C is depicted in Figure 74. Here, the three particles are released from the meander crest. All three particles start in warm water and move to cold water as they flow away from the crest. They also follow the same pattern in the trough, whereby they each move from cold to warm water. At the second crest, the three parcels also maintain a constant temperature. Again, the total lengths of the trajectories are all much greater than the 560 km distance in x.

Figure 75 shows the three particles which were simultaneously released from the eastern flank of the first crest. At the trough, all three particles move from cold to warm water. The "box" particle flows outside the meandering jet; however, at the downswing side of the second crest it appears as if it has been reentrained. Even though this particle has moved only slightly outside the jet, it continues to follow closely the meandering jet pattern. At the second crest, both the "star" and "plus"

Figure 74: Same as Figure 72, but the starting position is different.

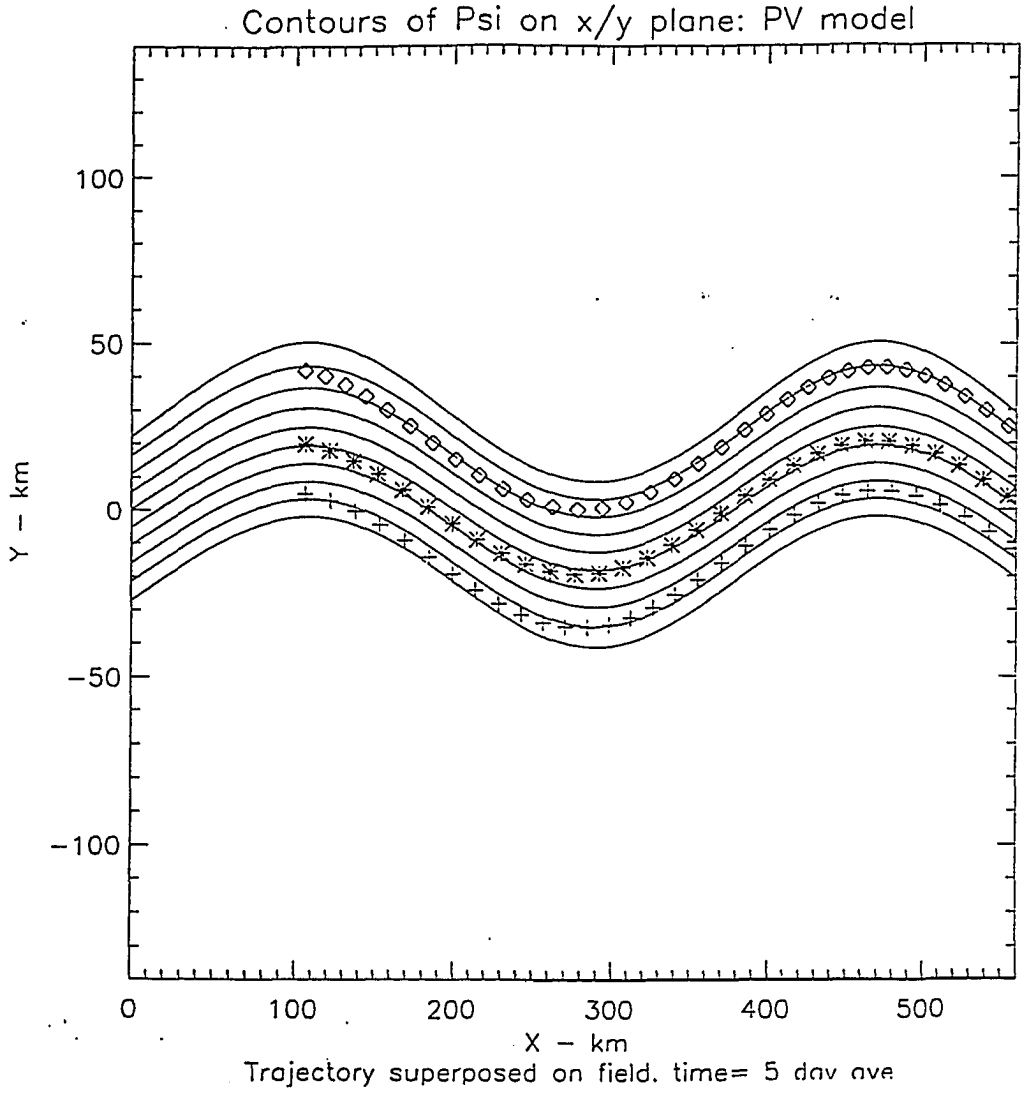

Figure 75: Same as Figure 72, but the starting position is different.

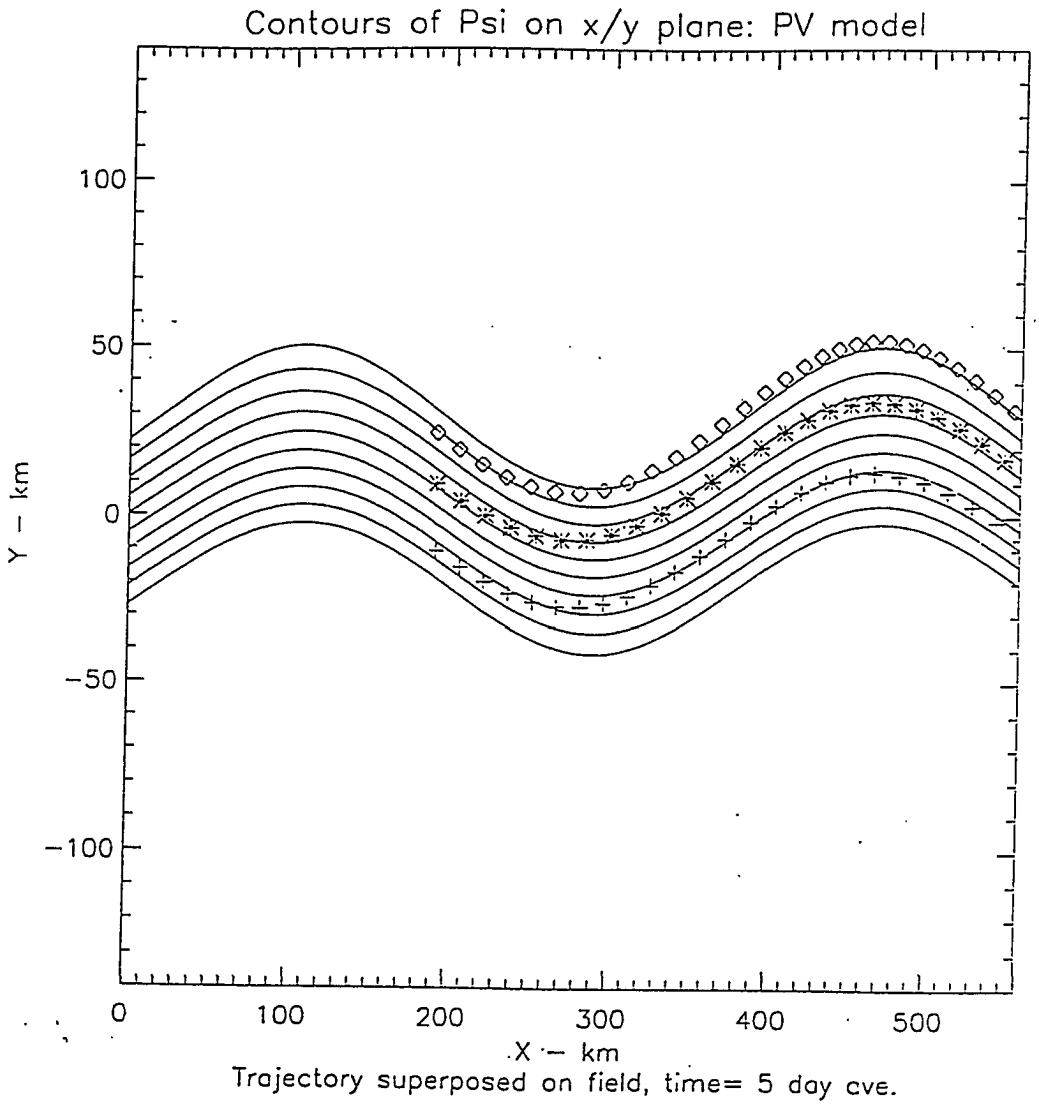

parcels maintain a constant temperature or appear to move only slightly to a colder temperature. The total lengths for the three trajectories for this time period are 660 *km*, 744 *km* and 767 *km* for the "box", "star" and "plus" particle trajectories, respectively.

The final case for the standardization experiments is case E, which is depicted in Figure 76. Here, the particles are started at the meander trough. All the particles flow from cold to warm water at the trough. While at the crest, they move from warm to cold water. All three trajectories follow the meandering jet pattern and do not cross each other. The total lengths for these three trajectories also span a distance greater than shown on this plot.

There are two conclusions which can be drawn from the standardization experiments. The particles released closest to the center streamline are always the longest in length for the five day composite period. In all these cases, this is the "star" particle. Unlike DM93, the three particles do not cross each other. At the first crest, the particles always move from warm to cold water. However, at the second crest they maintain a fairly constant temperature. In the troughs, the three particles move from cold to warm water. Note, that in cases A and B the "box" and "star" particles maintain a fairly constant temperature or increase slightly within the meander trough region. Finally, it should be noted that these results are not inconsistent with the observations reported by McClain et al. (1984).

7.3 Observation Experiments

The observation experiments for PVM94 are carried out in the same manner as those for DM93 and BM91. A detailed explanation of the observation experiments is given in Section 6.3. However, the maximum speed of 158 $km\ dy^{-1}$ is slightly

Figure 76: Same as Figure 72, but the starting position is different.

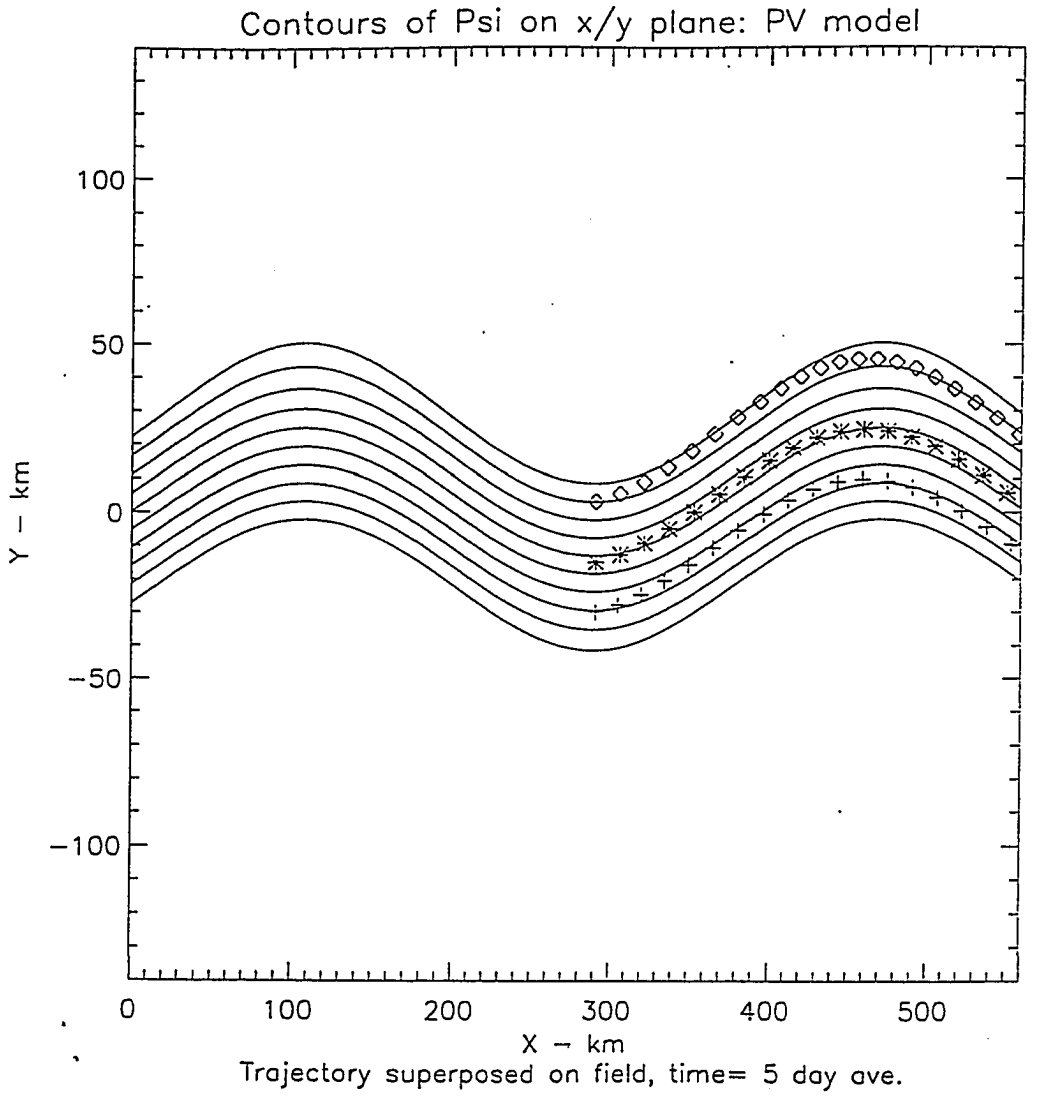

higher in PVM94, only because the non-linearity of the model makes it difficult to obtain the required maximum speed. The maximum value is closer to 162 $km\ dy^{-1}$. The amplitude and width of the meandering jet are also difficult to determine. Note for the observation experiments the time interval between particle symbols along the trajectories is 0.1 days.

Case 1 is depicted in Figure 77. Recall, that the desired parameters for this case are that amplitude = 26 km, wavelength = 262 km, phase speed = 9 $km\ dy^{-1}$ and width = 50 km. In image 92 (see Figure 33), only a portion of drifter trajectory 4480 is in GT37. Drifter 4480 is located near the middle of the stream. The "box" particle is released at a similar position on the meandering jet as the location of drifter 4480 on image 92. The model particle flows within the meandering jet, closely following its pattern. At the crest, the "box" particle moves from warm to cold water. It converges towards the center streamline as it moves down the eastern flank of the first crest. The particle flows from cold to warm water in the trough. Moving from the trough to the second crest, the particle diverges from the center of the meandering jet. As seen in the standardization experiments, the "box" particle maintains a fairly constant temperature at the second crest.

Results for case 2 are illustrated in Figure 78. Here, the amplitude = 37 km, wavelength = 255 km, phase speed = 9 $km\ dy^{-1}$ and width = 50 km. Figure 78 shows that the particle is released within the recirculation region of the streamfunction field. This position is at the same location as drifter 4480 on image 96 (see Figure 34). The "box" particle flows along the outside of the meandering jet pattern. At the meander crest, the particle is reentrained into the meandering jet and moves from warm to cold water. The particle moves from cold to warm water in the trough. This particle reaches a total distance of 676 km.

Figure 77: Diagram showing a particle trajectory superposed on the five-day average streamfunction field for PVM94. The "box" line represents the particle trajectory produced from case 1 of the observation experiments. The spacing between symbols is 0.1 days. See the text for further discussion.

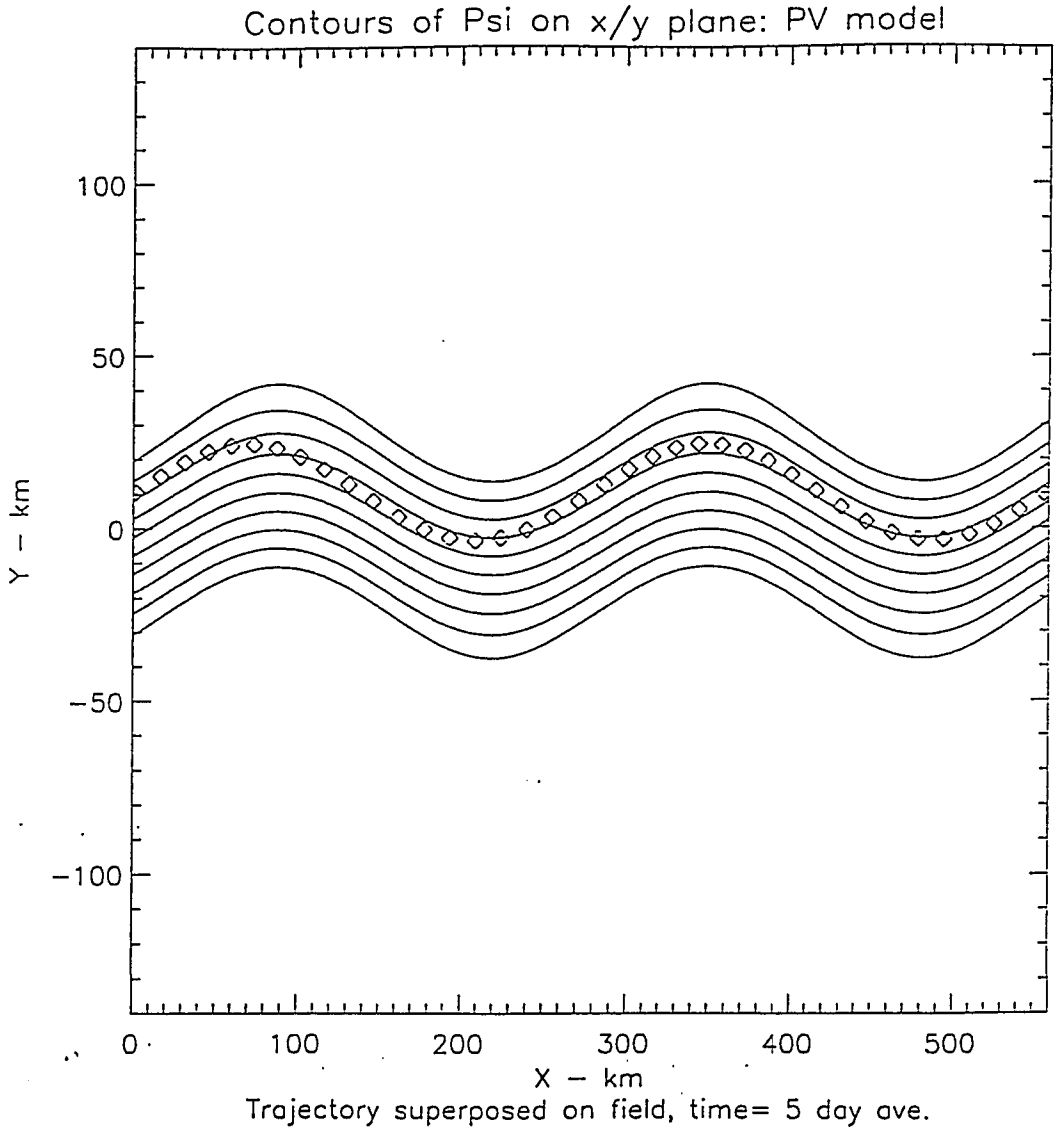

Figure 78: Same as Figure 77, but this is for case 2 of the observation experiments. The time interval is 0.1 days.

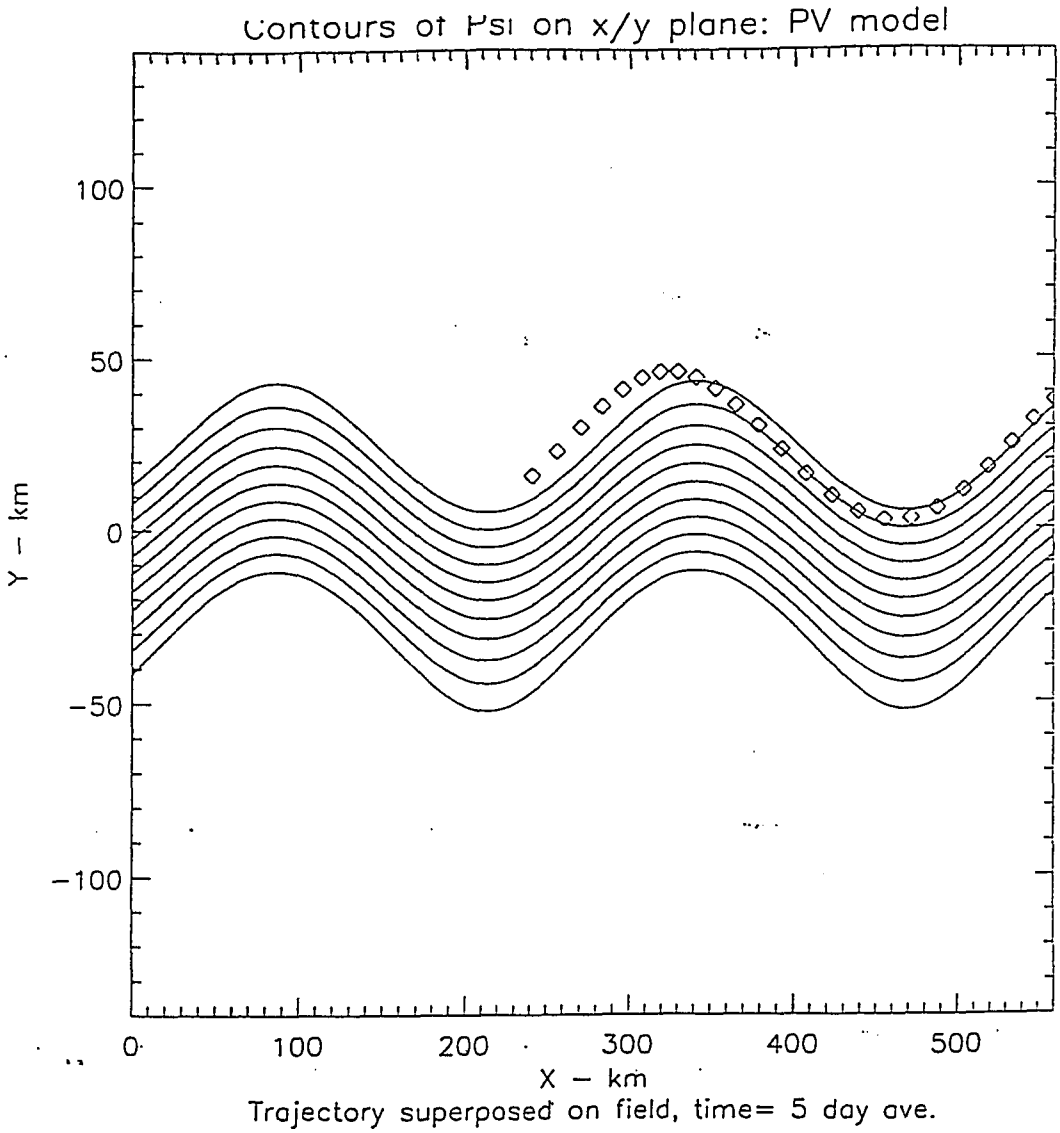

Figure 79 shows a particle which is released at the crest of the jet. A total length of 716 *km* is recorded for this particle trajectory. This case models drifter 4480 superposed on image 101 (see Figure 35). The "box" parcel clearly follows the northernmost streamline of the meandering jet streamfunction field. At the crest, it looks as if the particle moves only slightly from warm to cold water. Then, at the trough, it again moves only slightly from cold to warm water. At the second crest, the particle appears to maintain a constant temperature.

The main conclusion to draw from these experiments is that the PVM94 particle closely corresponds to the drifter trajectory depicted on all three images. An exception to this is case 2 (see Figure 78), where the "box" particle is started outside the meandering jet and closely follows the meandering jet shape. In comparison to this case, drifter 4480 on image 96 (see Figure 34) also is located outside the meandering jet, but its path cuts through the meander crest and then, follows the jet pattern. Thus, it is evident in case 2 that the model particle does not closely correspond to the drifter trajectory as it does in the other two cases. Another conclusion to draw from this analysis is that the PVM94 particles have the same temperature trend along their trajectories as evidenced in the previous experiments. At the crest, the "box" particle moves from warm to cold water; meanwhile in the trough it travels from cold to warm water. At the second crest, the particle maintains a constant temperature.

7.4 Inferring Velocity from Imagery

This section is similar to Section 6.4, whereby calculations of the u and v velocity components and the speed at every location along the particle trajectories are discussed. A comparison between the particle speeds from the standardization and observation experiments are undertaken. As noted earlier, the determination of

Figure 79: Same as Figure 77, but this is for case 3 of the observation experiments. The time interval is 0.1 days.

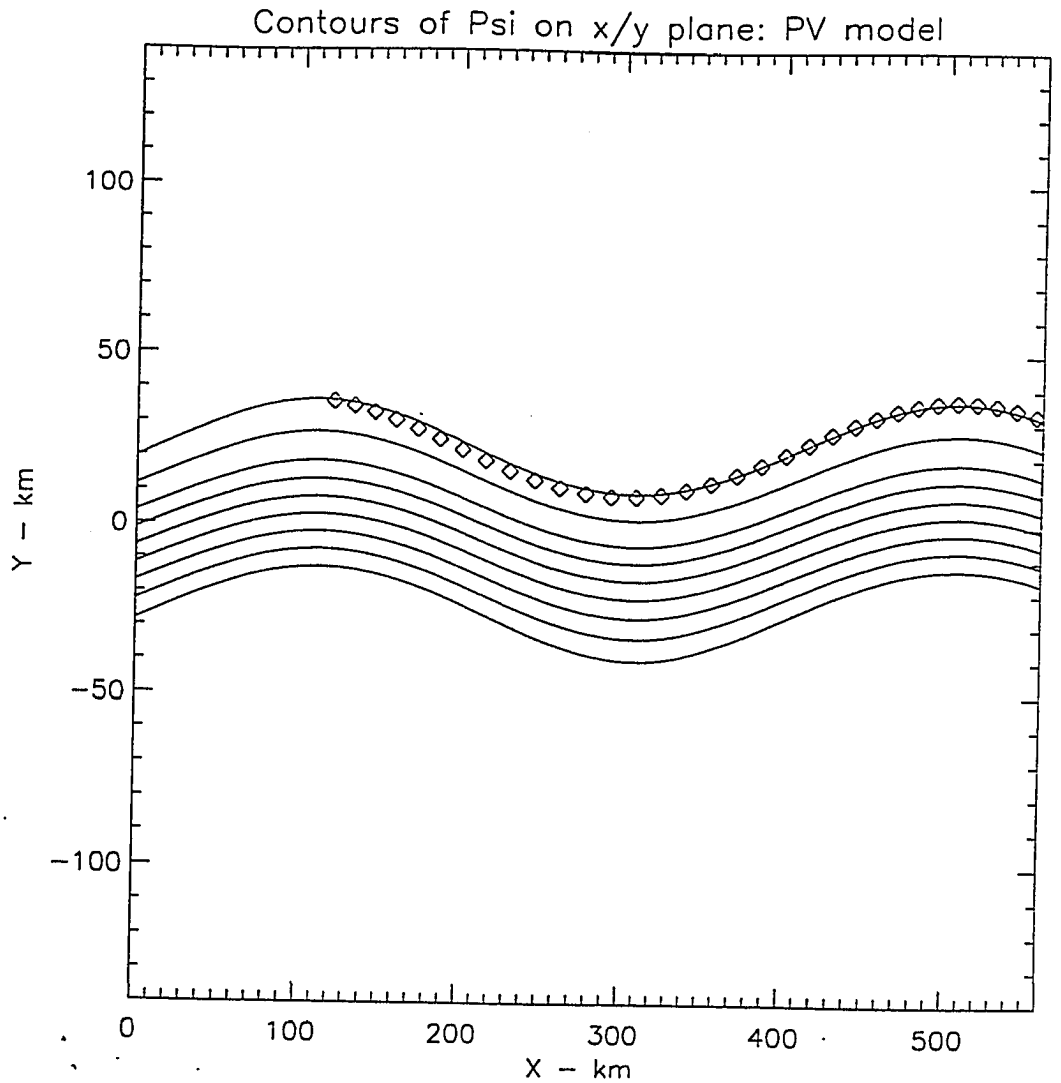

the speeds at the crests and troughs will be of particular importance in this study. See Section 6.4 for a more detailed discussion concerning this. Also, the maximum velocity is slightly larger than 158 $km\ dy^{-1}$.

First, the speeds obtained from the standardization experiments utilizing PVM94 are discussed. In case A, (see Figure 72), the speed at the staring position for the "box" particle is 154 $km\ dy^{-1}$. At the crest, decelerates to a value of only 125 $km\ dy^{-1}$. Along the the eastern flank of the first crest, the "box" particle reaches a speed of 154 $km\ dy^{-1}$. The particle continues to gain speeds of up to 157 $km\ dy^{-1}$ at the meander trough. It maintains this speed along the western flank of the second crest. The "box" parcel decreases greatly to a speed of 125 $km\ dy^{-1}$ at the second crest. The middle particle, "star", is located near the center of the meandering jet. Here, it reaches values close to the maximum speed. The "star" particle has a speed of 164 $km\ dy^{-1}$ at its starting point, but then decreases to 152 $km\ dy^{-1}$ at the first crest. Along the downswing side of this crest, the particle has attained a speed of 165 $km\ dy^{-1}$. This value is also obtained at the western flank of the second crest. At the trough, the speed is only 154 $km\ dy^{-1}$. Finally, at the second crest the particle speed decreases to 152 $km\ dy^{-1}$. The southernmost particle has speeds which range from 160 $km\ dy^{-1}$ at its starting position to 124 $km\ dy^{-1}$ at the meander trough. The values at the other designated points average about 156 $km\ dy^{-1}$.

As discussed earlier, Figure 73 shows three particles released from the upswing side of the meander crest. The "box" particle has an initial speed of 155 $km\ dy^{-1}$ and decreases to 142 $km\ dy^{-1}$ at the crest. As expected the speed increases substantially at the eastern flank of this crest, where it obtains a speed of 162 $km\ dy^{-1}$. The value at the trough is 158 $km\ dy^{-1}$. Again, the speed increases to 163 $km\ dy^{-1}$ on the flank. At the second crest, the "box" particle obtains the same speed as at

the first crest, which is 142 $km\ dy^{-1}$. The "star" parcel starts with a speed of 160 $km\ dy^{-1}$. At the crest, it decreases to 155 $km\ dy^{-1}$ and then increases again along the eastern flank. Here, it reaches a value of 165 $km\ dy^{-1}$. A low of 151 $km\ dy^{-1}$ is attained at the meander trough. This is followed by a dramatic increase to 165 $km\ dy^{-1}$ on the upswing side of the crest. Again, a similar speed as that found on the first crest is achieved on the second. The "plus" particle maintains a relatively constant speed of 157 $km\ dy^{-1}$, where it only varies by 1 - 2 $km\ dy^{-1}$. However, within the trough, the "plus" particle has a speed of only 135 $km\ dy^{-1}$.

The third case is illustrated in Figure 74. The northernmost particle has a starting speed of 125 $km\ dy^{-1}$, which is at the crest. Along the eastern flank the "box" particle has a speed of 155 $km\ dy^{-1}$. The particle speed in the trough increases slightly to 157 $km\ dy^{-1}$. It then decreases again to 155 $km\ dy^{-1}$ on the following flank. On the second crest, the "box" parcel decreases substantially to 123 $km\ dy^{-1}$. Because the "star" particle is closer to the center of the jet its speeds are higher. A value of 162 $km\ dy^{-1}$ is attained at both flanks. Meanwhile, at the crests its speed is only 152 $km\ dy^{-1}$. The speed in the trough is a little higher than that at the crest, which is 154 $km\ dy^{-1}$. The last particle for this case is the "plus" parcel. The speeds at the crests and flanks are basically the same; around 158 $km\ dy^{-1}$, with the flanks being higher by 1 $km\ dy^{-1}$. A low of 138 $km\ dy^{-1}$ is attained at the meander trough.

Case D for PVM94 has three trajectories released from the eastern flank of the first crest (see Figure 75). Here, the speeds for the three trajectories are 148 $km\ dy^{-1}$, 161 $km\ dy^{-1}$ and 163 $km\ dy^{-1}$ for the "box", "star" and "plus" trajectory, respectively. The speed for the "box" particle increases to 153 $km\ dy^{-1}$ at the trough and then decreases to 145 $km\ dy^{-1}$ on the western flank of the second crest. At the second crest, the speed decreases substantially to 105 $km\ dy^{-1}$. These two values

are due to the fact the "box" particle has entered the region outside the meandering jet. The "star" parcel decreases to 158 $km\ dy^{-1}$ at the trough. However, it increases again to 161 $km\ dy^{-1}$ along the western flank. Following the previous trend, the speed decreases at the second crest to 137 $km\ dy^{-1}$. The southernmost particle, "plus", also decrease at the trough. It reaches a value of 148 $km\ dy^{-1}$. As expected, the speed for the "plus" particle increases to 164 $km\ dy^{-1}$ along the upswing side of the second crest. At the crest it decreases to 156 $km\ dy^{-1}$.

The final case for PVM94 is illustrated in Figure 76. These three particles are released from the trough of the meandering jet. The "box" particle has a speed of 156 $km\ dy^{-1}$ at its trough and then decreases to 150 $km\ dy^{-1}$ along the upswing flank. At the crest its speed is only 119 $km\ dy^{-1}$. The middle parcel, "star", also has a value of 156 $km\ dy^{-1}$ at the trough. However, for this particle the speeds increase to 164 $km\ dy^{-1}$ along the western flank of the second crest. This particle also has speeds much lower at the crest measuring 148 $km\ dy^{-1}$. The southernmost particle has speeds of 145 $km\ dy^{-1}$, 163 $km\ dy^{-1}$ and 157 $km\ dy^{-1}$ at its trough, western flank and crest, respectively.

Analysis of the speeds obtained from the observation experiments reveals similar results to those of the STD experiments. Observation experiment case 1 (see Figure 77) shows an initial speed of 160 $km\ dy^{-1}$ at the western flank. At the crest, the particle's speed decreases to 142 $km\ dy^{-1}$. It eventually accelerates back to 162 $km\ dy^{-1}$ on the downswing side of the crest. The parcel obtains a speed of 157 $km\ dy^{-1}$ in the trough and increases to 161 $km\ dy^{-1}$ on the western flank of the second crest. At the second crest the speeds decrease to 138 $km\ dy^{-1}$.

The second observation case is shown in Figure 78. The initial position for the particle is outside the meandering jet boundaries. At this location the "box" particle has a speed of 168 $km\ dy^{-1}$. As the particle moves to the crest, its speeds

decrease substantially to 116 $km\ dy^{-1}$. Here, the particle is just starting to enter into the meandering jet region. Along the eastern flank of the crest the parcel again obtains a speed of 168 $km\ dy^{-1}$ and only decreases slightly at the trough to 163 $km\ dy^{-1}$.

Case 3 for the observation experiments of PVM94 is shown in Figure 79. The particle is started at a crest of the meandering jet. At this position the parcel has a speed of 124 $km\ dy^{-1}$. As the particle flows along the downswing side of the crest and into the trough its speed progressively increases from 153 $km\ dy^{-1}$ on the flank to 159 $km\ dy^{-1}$ in the trough. However, at the western flank of the second crest the "box" particle decrease in speed to 150 $km\ dy^{-1}$. Finally, at the second crest, the particle continues to decreases in speed where it reaches a value of 121 $km\ dy^{-1}$.

The standard experiments utilizing PVM94 usually generate the greatest particle speeds at the western flanks of the meander crests. However, in three instances the greatest speed is observed at the meander trough. As stated earlier two important regions of the stream to analyze are the meander crests and troughs. Analysis shows that for all cases the speeds are greater in the troughs than in the meander crests. Similar results are revealed in the observation experiments, where the greatest speeds are located along the flanks of the meander crests. Again, in one instance the trough has the greatest speed. A comparison between the values at just the crests and troughs for these experiments show that the greatest value is always obtained at the meander troughs.

A comparison between the actual drifter data and the observation experiments now can be undertaken to see how closely PVM94 corresponds to the true observations. The drifter speeds have already been detailed in section 6.4, but also are examined here in relation to the PVM94 results. In case 1 (see Figure 77) the observation experiment is related to drifter 4480 overlaid on image 92 (see Figure 33).

Drifter 4480 has a speed of 158 $km\ dy^{-1}$ on the meander crest and decreases to 157 $km\ dy^{-1}$ at the trough. In comparison to the drifter and image data, PVM94 results show that the particle has a speed of 142 $km\ dy^{-1}$ at the crest and 157 $km\ dy^{-1}$ at the trough. Clearly, for this case the comparison shows that the PVM94 does closely correspond to the drifter speeds.

The second observation experiment corresponds to drifter 4480 overlaid on image 96 (see Figures 34 and 78). The model results show values of 167 $km\ dy^{-1}$ at the meander trough and 115 $km\ dy^{-1}$ at the crest. The particle reaches a speed of 162 $km\ dy^{-1}$ within the second trough. The speeds for the drifter are quite different from those seen in the model. Drifter 4480 has speeds of 87 $km\ dy^{-1}$, 146 $km\ dy^{-1}$ and 152 $km\ dy^{-1}$ at the trough, crest and second trough, respectively. It is evident that the values differ by at least 15 $km\ dy^{-1}$.

Observation case 3 is depicted in Figures 35 and 79. Here, the PVM94 model results are compared to drifter 4480 superposed on image 101. For this image only a small portion of the drifter trajectory is shown. Drifter 4480 has a value of 119 $km\ dy^{-1}$ at the crest. It reaches a speed of 135 $km\ dy^{-1}$ once it enters the trough region of the jet. In comparison to this, PVM94 results show that the "box" particle has a speed of 123 $km\ dy^{-1}$ at its crest and dramatically increases to 159 $km\ dy^{-1}$ at the trough. Again, these speeds are different from drifter 4480. However, they only vary by as much as 20 $km\ dy^{-1}$, unlike the two kinematic models which show a much greater variance.

In summary, it appears as if there is a good correlation between the speeds of the drifter and those generated by PVM94. The speeds from the model may be slightly higher because of the difficulty in generating the desired maximum speed for the meandering jet. This was discussed earlier in the chapter. Making a comparison between the two kinematic models, potential vorticity model and the drifter data,

it is quite clear that the speeds obtained by PVM94 correspond much better with the drifter data than either kinematic model.

7.5 Summary

The following conclusions can be drawn from using the observed and standardized parameters in the barotropic potential vorticity model.

First, the conclusions from the experiment utilizing the DM93 original parameters are detailed. The model particles move from warm to cold water in the crest and trough. However, the "plus" particle enters the recirculation region of the jet model and begins to flow westward. The particles do not cross each other, as was evident in DM93. The trajectories obtained from PVM94 are most like those produced in BM91.

The standardization experiments also show that the particles move from warm to cold water at the crest and from cold to warm water in the troughs. However, in cases A and B the "box" and "star" particles maintain a constant temperature or increase only slightly within the trough. At the second crest, all three particles maintain a constant temperature.

Cases 1, 2 and 3 of the observation experiments also follow the same temperature trend as seen in the STD experiments. The particles move from warm to cold water in the crest and from cold to warm water in the trough. They also appear to maintain a constant temperature at the second crest. The first and third cases depict model trajectories which closely correspond to the path of drifter 4480.

For both the standardization and observation experiments, the greatest speeds were produced at the flanks of the meander crests. In three instances, however,

the trough revealed the greatest particle speeds. The comparison between just the meander crests and troughs showed that the greatest speeds were always obtained at the meander troughs.

After the observation experiments were completed, a comparison between the drifter data and the model trajectories from cases 1, 2 and 3 could be undertaken. Case 1 shows that there is a good correlation between the drifter and particle trajectories, as well as the speeds obtained. In case 2, the correlation is not as good. This is most likely due to the fact that the model particle does not follow the same path as drifter 4480 does on image 96. Within the model, the "box" particle moves outside the meandering jet for part of its path. In contrast, the drifter cuts directly through the meander crest of the jet. Finally, in case 3 the speeds calculated are larger in PVM94. But, it is important to note that the speeds obtained from the potential vorticity model for all three cases correspond much better to the true drifter data than do the kinematic model results.

8 Summary

Patience-Faith-Openness,
is what the sea has to teach.
Simplicity-Solitude-Intermittency...
but there are other beaches to explore.
There are more shells to find.
This is only the beginning-
Anne Morrow Lindbergh

8.1 Answers to research questions

Return now to the three research questions posed in Chapter 1.

- Is it possible to relate quantifiable features of composite images to oceanic processes?

Chapter 6 and 7 address the possibility of relating quantifiable features of composite imagery to oceanic processes. This can be observed by taking characteristic parameters of large-scale features observed from imagery and utilizing them in both kinematic and dynamic models. The model output can be compared to *in situ* data portraying the oceanic processes and flow of the meandering Gulf Stream. Results from the kinematic models reveal that the particle motion calculated from BM91 correlate much better with the drifter trajectories than those from DM93. The BM91 trajectories closely follow the meandering jet and the trajectory of 4480. Section 6.4 details the particle speeds obtained when the observation data is run through each

kinematic model. The particle speeds for both kinematic models are substantially lower than those for drifter 4480. Despite some similarities between the observations and model data, there appears to be no direct link between the particles produced from these models and the observations.

In contrast to Chapter 6, Chapter 7 shows that it is possible to relate quantifiable features of composite imagery to oceanic processes. Section 7.3 discusses the results obtained by running the observation experiments through PVM94. Results show that the PVM94 particles do correspond closely to the drifter trajectories depicted on the composite satellite imagery. The PVM94 particle speeds, also, show a good correlation to the drifter data. As noted earlier, PVM94 models the meandering jet of the Gulf Stream much better than the two kinematic models. Thus, the utilization of PVM94 shows that relating large-scale features of the composite imagery with the oceanic processes of the Gulf Stream is possible. This suggests that the gradients of the temperature field can be used in conjunction with a dynamically based feature model to infer surface velocity.

- Can the spectral and geometric properties of the contemporaneous data set be used to quantify the variability of the Gulf Stream?

Chapter 4 shows that there is not a strong link between the set of drifter trajectories and composite temperature fronts. This is evidenced by the large difference between the two data sets concerning the scaling ranges, fractal dimension and spectral slope values. Fractal analysis gives a fractal dimension of 1.21 ± 0.2 for the drifter data with a scaling range of 83-343 *km*. The fractal dimension for the temperature fronts of the composite imagery is 1.12 ± 0.01 over a average scaling range of 4-36 *km*. Spectral analysis reveals a spectral slope value of 2.67 ± 0.01 over a range of 616-1915 *km* for the drifter data and an average value of 2.81 ± 0.01 over a range

of 137-434 *km* for the composite imagery. Also, the calculated spectral slopes and fractal dimensions obtained in the different geographic regions for the imagery are consistent between the two regions. Results from these analyses methods show that the temperature fronts are not fractal and the drifter trajectories are fractal; that there is no geographic variability and that there is no strong link between the drifter trajectories and composite temperature fronts. Spectral and geometric properties of the contemporaneous data set of drifter trajectories and composite temperature fronts can not be used to quantify the variability of the Gulf Stream.

- Are the calculated geometric (fractal) properties of large-scale composite features and corresponding time and space scales sufficient enough to infer near-surface flow?

The third question posed in this research deals with the feasibility of just using the geometric properties of the composite satellite imagery to infer the surface flow structure of the Gulf Stream. As shown in Chapter 4, the composite temperature fronts are not fractal, while the total drifter data set is fractal. There is also no dependence on the location of the temperature front and its value of the fractal dimension. Results show that there is not a good correlation between the drifter and temperature front geometric properties and their corresponding time and space scales. Thus, Chapter 4 shows that the calculated geometric properties of the large-scale composite features are not sufficient enough information to infer near-surface flow.

8.2 Implications of Research

There are some broader implications of this research regarding fractal and spectral analysis, image composites and surface temperature profiles across the Gulf

Stream using remote sensing.

Fractal analysis of the contemporaneous data set gives different results for the satellite-tracked drifter data and the five-day composite imagery. The temperature fronts of the composite imagery for both geographic regions show a fractal dimension of 1.12 $\pm$0.01 over an average scaling range of 4-37 *km*. This value shows the internal consistency of the fractal dimension for the composite temperature fronts. A fractal dimension of 1.21$\pm$0.02 for the drifter data with a scaling range of 83-343 *km* was calculated. This suggests that the drifter data is fractal and that the temperature front data is not fractal. However, if only the drifter paths which correspond to the satellite imagery are analyzed, the fractal dimension and scaling range for the drifter data decreases dramatically. A value of $D = 1.17 \pm 0.02$ over a scaling range of 65-182 *km* is obtained. This reveals a fractal dimension which corresponds well with the composite temperature fronts, suggesting now that the drifter trajectories are not fractal. The inconsistency in the values of the fractal dimension, here and in comparison with past studies, suggests that a more judicious utilization of the fractal dimension than has been used by other investigators is required.

This study and past studies have suggested that the determination of the spectral slope is not always a straight forward matter. Slope characteristics are usually dependent on the selected scaling range and the amount of spectral smoothing undertaken. Therefore, it has been shown that ample care must be exercised in calculating the spectral slope values of a space curve. As stated in Chapter 4 a new method was employed in determining the power spectral slope to help alleviate these problems. Previous studies fitted the spectra to power-laws by using the least squares fit method. However, here the calculated spectral slope was used to determine the scaling range of the data sets. Results of this procedure gave values of 2.79$\pm$0.01 over a scaling range of 139-434 *km* for LT37 and 2.82 $\pm$0.01 with a range of 134-

434 *km* for GT37. This shows the internal consistency between the two geographic regions. The calculated slope is much lower and the scaling range is higher for the drifter trajectories than they are for the temperature fronts. However, again it is interesting to note that if only the drifters which correspond to composite satellite imagery are analyzed, then the spectral slope value is much closer to that of the composite temperature fronts, producing a value of 2.72 ± 0.01. Spectral analysis also shows that a more judicious approach in its utilization and calculation of the power spectral slopes was needed.

A principal objective of this study was to determine whether there was any utility in analyzing composite satellite imagery instead of sequential imagery. Previous studies used sequential images to track small-scale features in order to infer the flow kinematics of oceanographic phenomena. Because of the many problems which are encountered with such a method, the approach taken in this study was to attempt to infer the near-surface flow kinematics and dynamics of the Gulf Stream by using composite imagery in conjunction with feature models. As discussed earlier in this section and in Chapter 7, the use of PVM94 showed that there is a direct relationship between composite image features and oceanic processes. Comparison between drifter trajectories and the PVM94 observation experiment particle paths shows a good correlation between the two. Analyses of the drifter speeds and model particle speeds reveals that the two data sets are similar in value. In some instances, the particle speeds are larger by as much as 20 $km\ dy^{-1}$. However, this may be due solely on the fact that it was difficult to accurately assign a maximum speed when utilizing PVM94. Thus, results show that the correlation between observational data and features of the composite imagery is good. It seems then that there is great potential in analyzing composite satellite imagery to delineate large-scale oceanic features and processes. Overall, analyses has shown that composite images and the potential vorticity model can be used to infer the surface velocity along a front.

There is great importance in this finding because other analyses methods, such as feature tracking and MCC, can not be used to determine the velocity along a front. Thus, composite imagery and dynamic feature models can be used to recover surface flow around warm core rings and other frontal features, such as the coastal/open ocean exchange.

Another important issue deals with the transects across the Gulf Stream constructed from imagery. Temperature values were recorded along the transects which crossed the Gulf Stream and the drifter trajectories. Speeds were calculated at this drifter/transect intersection. Within GT37, the speeds reached values up to 200 $km\ dy^{-1}$. However, in LT37, the speeds were substantially lower at a maximum of only 60 $km\ dy^{-1}$.

These transects were used to obtain temperature profiles across the Gulf Stream. The majority of these profiles displays a sharp temperature gradient on the coastal side of the Gulf Stream. Just past the peak of the profile, the temperature values remain relatively constant, then slowly taper off. An interesting fact that is illustrated in these figures is that the drifters usually are trapped within the sharp gradient region of the temperature profile. The positioning of the drifter and the similarity of this profile with the velocity profile across the Gulf Stream shows that there is a direct relationship between the velocity and temperature fields of the Gulf Stream. However, recall that in some cases the temperature profile across the Gulf Stream is not similar to the velocity profile. Thus, there is great importance in analyzing and understanding the temperature profile and velocity profile across the Gulf Stream.

8.3 Future Research

There are several logical extensions and additional questions worth pursing that have arisen from this study.

The most obvious would be to repeat the analysis for a larger contemporaneous data set. Particularly useful would be more imagery from 1984 which could be combined with the FACTS drifter data. Perhaps with the additional satellite imagery, a more stringent test could be undertaken regarding the relationship between the five-day composite satellite imagery temperature fronts and the Lagrangian drifter trajectories. It would be interesting to determine whether the time scale of the composite imagery affects the correlation between the imagery and the satellite-tracked drifters. Also it would be appropriate to reanalyze data from other older experiments, such as SYNOPS.

With the advent of the SeaWiFS launch in the near future, a tremendous amount of new, cutting edge satellite imagery will be available. It would be important to see if the same conclusions which were obtained here can be drawn from compositing the imagery from this new data set.

Osborne et al. (1989) analyzed the Kuroshio Extension and obtained an average fractal dimension of $1.27 \pm .06$. Apparently, little is known about fractal scaling properties of other major currents, such as the East Austrailian Current or Agulhas Current. It would be interesting to determine whether the fractal dimension of these currents would be consistent with those obtained here, around $1.12 \pm .01$, or with those of Osborne et al. (1989). The analysis of other areas of the world oceans would help solidify or nullify the conclusions drawn from this study.

A fourth question to pursue is to determine whether there is a substantial

difference in the spectral and geometric properties of the Gulf Stream temperature fronts on the eastern side of the Gulf Stream in comparison to the coastal side. By visually inspecting the composite images, one would expect that the properties would be significantly different. Two reasons which would cause one to come to that conclusion are: 1) the amount of data analyzed for each temperature set would be much greater and 2) the amount of "wiggles" in the curve have greatly increased.

Another possibility would be to apply these analyses methods to the coastal/ open ocean interface. Here, the analyses would be used to quantify submesoscale surface features within this region of the oceans. It could be used to examine the cross-shelf exchange which occurs in this slope region.

The comparison of the image data and drifter data through the use of an algorithm established by Kirwan et al. (1974) to analyze and calculate the differential kinematic parameters (dkps) of the data set would be beneficial to implement. This would determine normal and shear deformation, vorticity, divergence, as well as the total, swirl and translation velocities. This analysis would provide insight into the evolution of a region. It would be intriguing to determine whether the values obtained for the drifter trajectories would be the same as the temperature fronts. If this is the case, then the analysis of only the composite image temperature fronts in a region where drifter data was unavailable, the temperature fronts could provide this information concerning the evolution of a certain phenomenon within a particular area.

References

Bower, A. S., Notes and Correspondence: A simple kinematic mechanism for mixing fluid parcels across a meandering jet, *J. Phys. Oceanogr.*, *21*, 173-180, 1991.

Brown, O. B. and G. P. Podesta, Satellite sea surface temperature (SST) climatology development for fisheries, Final Report, Contract NA 85-WC-77-06134, submitted to US National Oceanic and Atmospheric Administration. Univ. of Miami, 1989.

Chatfield, C., *The analysis of time series: an introduction*, Chapman and Hall, Ltd., New York, 1984.

Cushman-Rosin, B., Trajectories in Gulf Stream meanders, *J. Geophys. Res.*, *98*, *C2*, 2543-2554, 1993.

Dutkiewicz, S., A. Griffa, and D. B. Olson, Particle diffusion in a meandering jet, *J. Geophys. Res.*, *98*, 16487-16500, 1993.

Emery, W. J., A. C. Thomas and M. J. Collins, An objective method for computing advective surface velocities from sequential infrared satellite images, *J. Geophys. Res.*, *91*, 12865-12878, 1986.

FACTS: Physical Oceanographic Study of Florida's Atlantic Coast Region - Florida Atlantic Coast Transport Study, 2-Tech Report, Florida Institute of Technology, 1986.

Gillman, C. S., A study of the Gulf Stream downstream of Cape Hatteras 1975-1986, MS. thesis, University of Rhode Island, Graduate School of Oceanography, Narragansett, RI, 1988.

Grassberger, P. and I. Procaccia, Measuring the strangeness of strange attractors, *Physica*, *9D*, 189-208, 1983.

Halkin, D. and T. Rossby, The structure and transport of the Gulf Stream at 73°W, *J. Phys. Oceanogr.*, *15*, 1439-1452, 1985.

Halliwell, G. R. and C. N. K. Mooers, Meanders of the Gulf Stream downstream from Cape Hatteras 1975-1978, *J. Phys. Oceanogr.*, *13*, 1275-1292, 1983.

Hansen, D. V., Gulf Stream meanders between Cape Hatteras and the Grand Banks. *Deep-Sea Res.*, *17*, 495-511, 1970.

Ingmanson, D. E., *Oceanography: an introduction*, Wadsworth Publishing Co., Belmont, CA, 1989.

Iselin, C. O., A study of the circulation of the western North Atlantic. *Pap. Phys. Oceanogr. Meteorol.*, *4*, 1-101, 1936.

Kamachi, M., Advective surface velocities derived from sequential images for rotational flow field: limitations and applications of maximum cross-correlation method with rotational registration, *J. Geophys. Res.*, *94*, 18227-18233, 1989.

Kirwan, A. D., Jr., W. J. Merrell, Jr., J. K. Lewis, R. E. Whitaker, and R. Legeckis, A model for the analysis of drifter data with an application to a warm core ring in the Gulf of Mexico, *J. Geophys. Res.*, *89*, (C3), 3417-3424, 1974.

Kirwan, A. D., Jr., and G. R. Cresswell, Observations of large and mesoscale motion in the near-surface layer, in *Topics in Ocean Physics*, Society Italiana de Fisica, Bologna, Italy, 79-125, 1982.

La Violette, P. E., Advection of submesoscale thermal features in the Alboran Sea gyre, *J. Geophys. Res.*, *14*, 550-565, 1984.

Mandelbrot, B. B., How long is the coast of Britain? Statistical self-similarity and fractional dimension, *Science*, *155*, 636-638, 1967.

Mandelbrot, B. B., *Fractals: form, chance and dimension*, W. H. Freeman, San Francisco, 1977.

Mandelbrot, B. B., *The fractal geometry of nature*, W. H. Freeman, New York, 1982.

Maul, G. A., FACTS: The Florida Atlantic Coastal Transport Study, *Eos Trans.* AGU, *66*, (19), 434-435, 1985.

McClain, C. R., L. J. Pietrasfesa, and J. A. Yoder, Observations of Gulf Stream-induced and wind-driven upwelling in the Georgia Bight using ocean color and infrared imagery, *J. Geophys. Res.*, *89*, 3705-3723, 1984.

McClain, C. R., G. Fu, M. Darzi and J. K. Firestone, PC-SEAPAK user's guide, version 4.0, NASA Tech. Memo. 104557, Nat'l Aero. and Space Admin., Goddard Space Flight Center, Greenbelt, MD, 1992.

McNally, G. J., W. C. Patzert, A. D. Kirwan, Jr., and A. C. Vastano, The near-surface circulation of the North Pacific using satellite tracked drifting buoys, *J. Geophys. Res.*, *88*, 7507-7518, 1983.

Moon, F. C., *Chaotic Vibrations: an introduction for applied scientists and engineers*, John Wiley & Sons, New York, 1987.

Mullen, C. P., and A. D. Kirwan, Jr., Surface flow structure of the Gulf Stream from composite imagery and satellite-tracked drifters. *Nonlin. Proc. Geophys.*, 1, 64-71, 1994.

Osborne, A. R., A. D. Kirwan, Jr., A. Provenzale and L. Bergamasco, Fractal drifter trajectories in the Kuroshio Extension, *Tellus*, *41A*, 416-435, 1989.

Osborne, A. R. and Caponio, R., Fractal trajectories and anomalous diffusion for chaotic particle motion in 2D turbulence. *Phys. Rev. Lett.*, *64*, 1733-1736, 1990.

Paladin, G. and A. Vulpiani, Anomalous scaling laws in mutlifractal objects, *Phys. Rep.*, *156*, 147-225, 1987.

Panchev, S. *Random functions and turbulence*, Pergamon, Oxford, 1971.

Pond, S. and G. L. Pickard, *Introductory dynamical oceanography*, Pergamon, New York, 1983.

Pratt, L. J., Meandering and eddy detachment according to a simple (looking) path equation, *J. Phys. Oceanogr.*, *18*, 1627-1640, 1988.

Provenzale, A., A. R. Osborne, A. D. Kirwan, Jr., and L. Bergamasco, The study of fluid parcel trajectories in large scale ocean flows, in *Nonlinear Topics in Ocean Physics*, edited by A. R. Osborne and L. Bergamasco, 367-401, Elsevier, New York, 1989.

Rapaport, D. C., The fractal nature of molecular trajectories in fluids, *J. Stat. Phys.*, *40*, 751-758, 1985.

Richardson, P. L., Gulf Stream trajectories measured with free-drifting buoys, *J. Phys. Oceanogr.*, *11*, 999-1010, 1981.

Richardson, P. L., Eddy kinematic energy in the North Atlantic from surface drifters, *J. Geophys. Res.*, *88*, 4355-4367, 1983a.

Richardson, P. L., Gulf Stream rings, in *Eddies in Marine Science*, edited by A. R. Robinson, Springer-Verlag, New York, 1983b.

Robinson, A. R., J. R. Luyten and F. C. Fuglister, Transient Gulf Stream meandering I, an observational experiment, *J. Phys. Oceanogr.*, *4*, 237-255, 1974.

Samelson, R. M., Fluid exchange across a meandering jet, *J. Phys. Oceanogr.*, *22*, 431-440, 1992.

Sanderson, B. G. and A. Goulding, The fractal dimension of relative lagrangian motion, *Tellus*, *42A*, 550-556, 1990.

Sanderson, B. G., and D. A. Booth, The fractal dimension of drifter trajectories and estimates of horizontal eddy-diffusivity, *Tellus*, *43A*, 334-349, 1991.

Schertzer, D. and S. Lovejoy, Physical modeling and analysis of rain and clouds by anisotropic scaling multiplicative processes, *J. Geophys. Res.*, *92*, 9693-9714, 1987.

Shaw, P. and H. T. Rossby, Towards a lagrangian description of the Gulf Stream, *J. Phys. Oceanogr.*, *14*, 528-540, 1984.

Sturges, W., Sea level slope along continental boundaries, *J. Geophys. Res.*, *79*, 825-830, 1974.

Svejkovsky, J., Sea surface flow estimation from advanced very high resolution radiometer and coastal zone color scanner satellite imagery: a verification study, *J. Geophys. Res.*, *93*, 6735-6743, 1988.

Tokmakian, R., P. T. Strub, and J. McClean-Padman, Evaluation of the maximum cross-correlation method of estimating sea surface velocities from sequential satellite images, *J. Atmos. Oceanic. Technol.*, *7*, 852-865, 1990.

Tracey, K. L., and D. R. Watts, On Gulf Stream meander characteristics near Cape Hatteras, *J. Geophys. Res.*, *91*, 7587-7602, 1986.

Vastano, A. C., and S. E. Borders, Short communication: sea surface motion over an anticyclonic eddy on the Oyashio Front, *Remote Sens. Environ.*, *16*, 87-90, 1984.

Vazquez, J. and D. R. Watts, Observations on the propagation growth and predictability of Gulf Stream meanders, *J. Geophys. Res.*, *90*, 7143-7152, 1985.

von Arx, W. S., *An introduction to physical oceanography*, Addison-Wesley, Reading, MA, 1974.

Watts, D. R., Gulf Stream variability, in *Eddies in Marine Science*, edited by A. R. Robinson, 114-144, Springer-Verlag, New York, 1983.

Appendix

This appendix contains the portion of the contemporaneous set of composite images and satellite-tracked drifter trajectories not described in this text. Most of the images correspond to drifter path 4478 and 4481. Within all these images the drifters are extremely short and do not appear to follow any particular temperature front. Some have become trapped in a circulation pattern and have not entered the Gulf Stream meander region. Other drifter trajectories have meandered out into the Sargasso Sea where they remained for the five day period, moving only slightly over that duration. Because of the geographic location of these drifters and the length of their trajectories, it was decided that these images and their corresponding drifter trajectories would not be necessary for this research and would only be included in the appendix as a record of this contemporaneous data set.

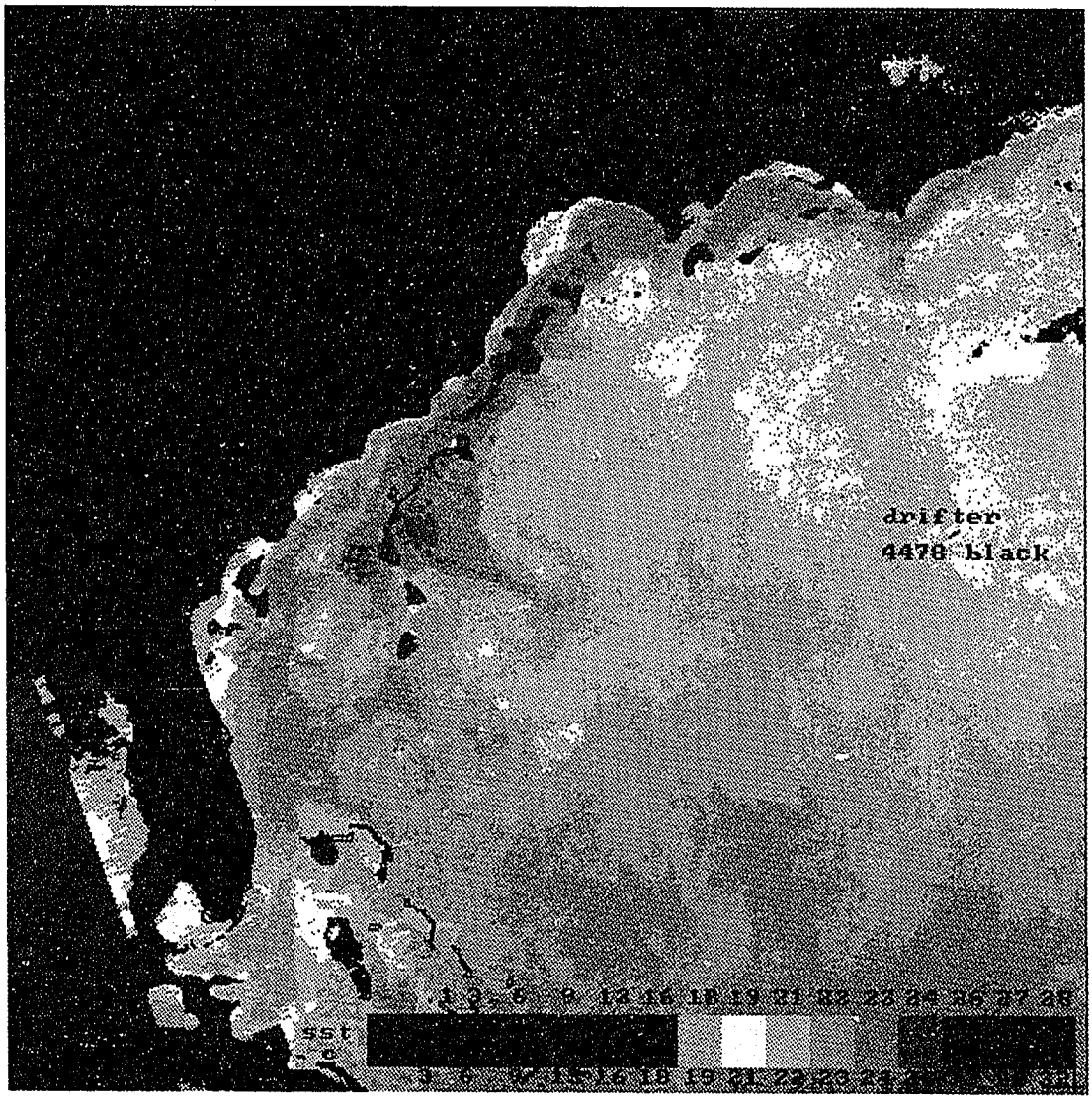

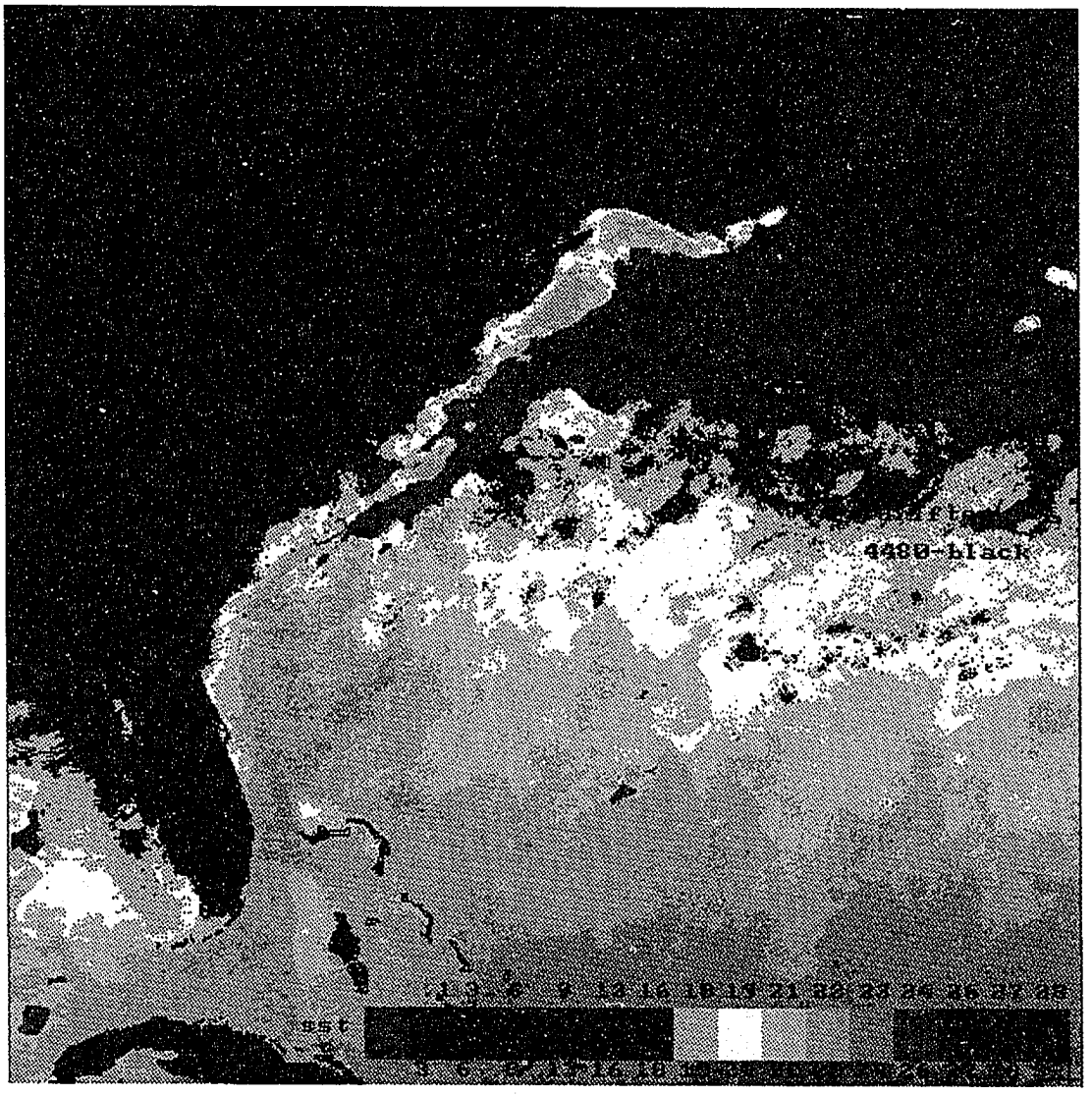

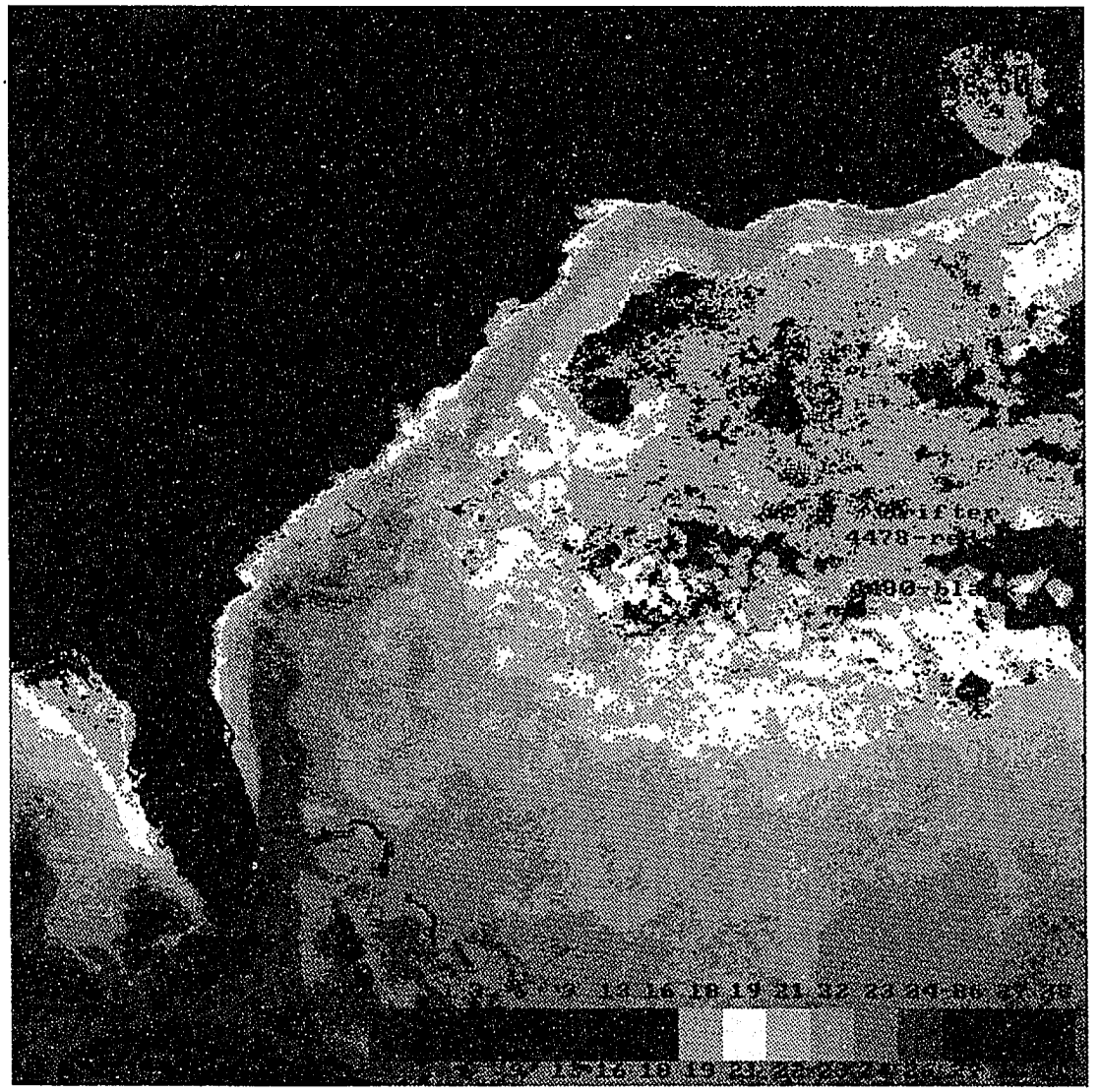

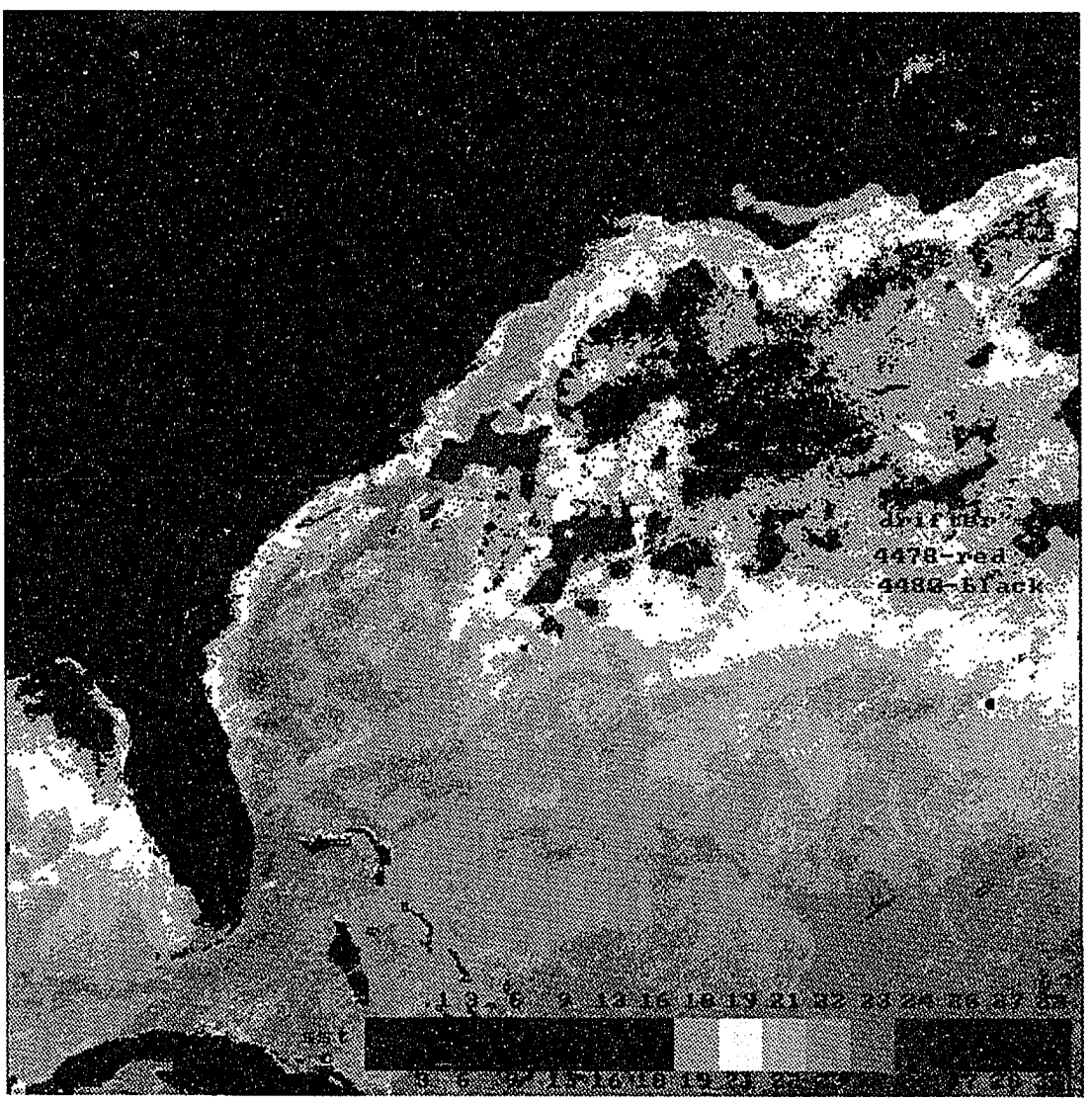

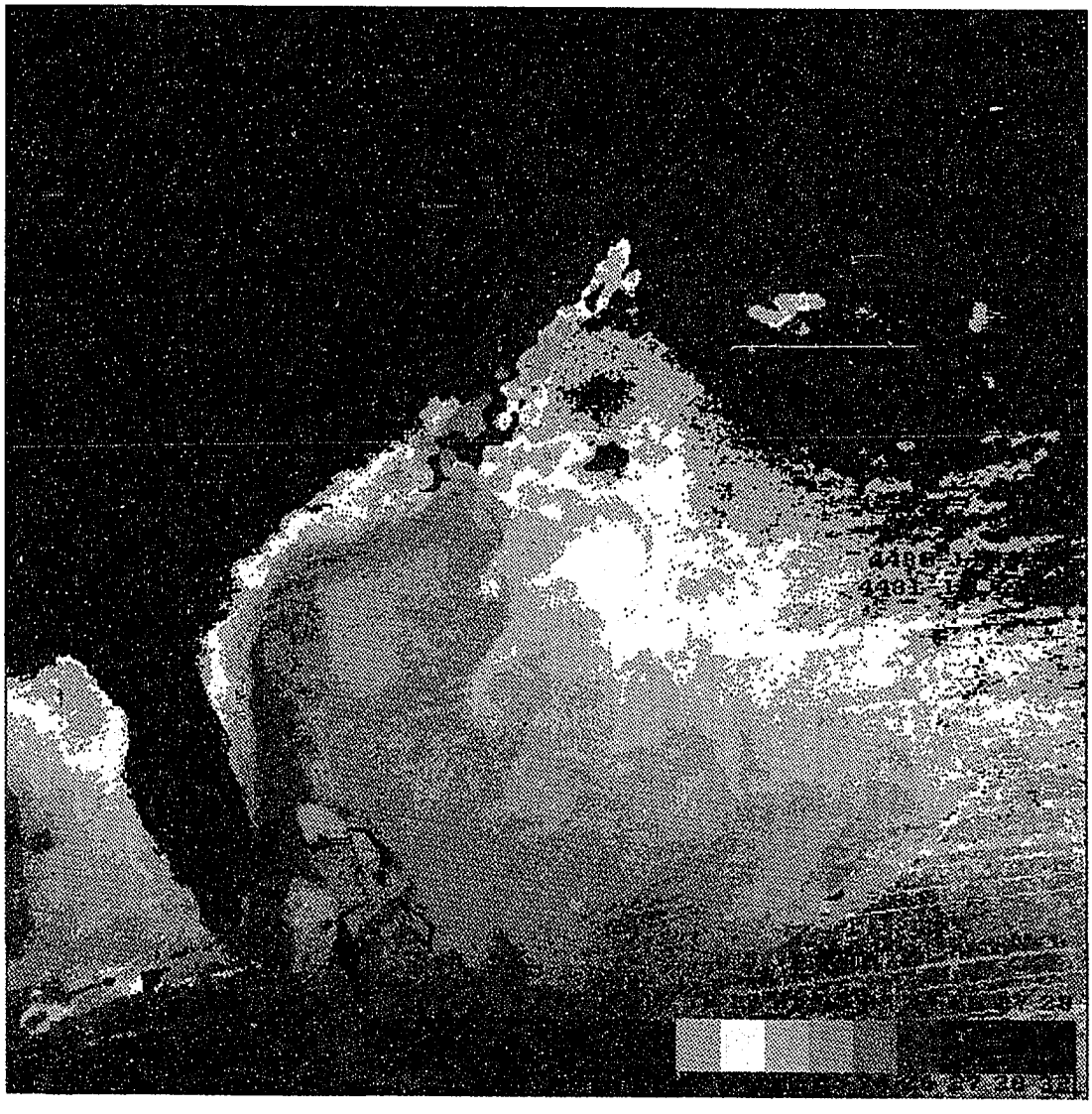

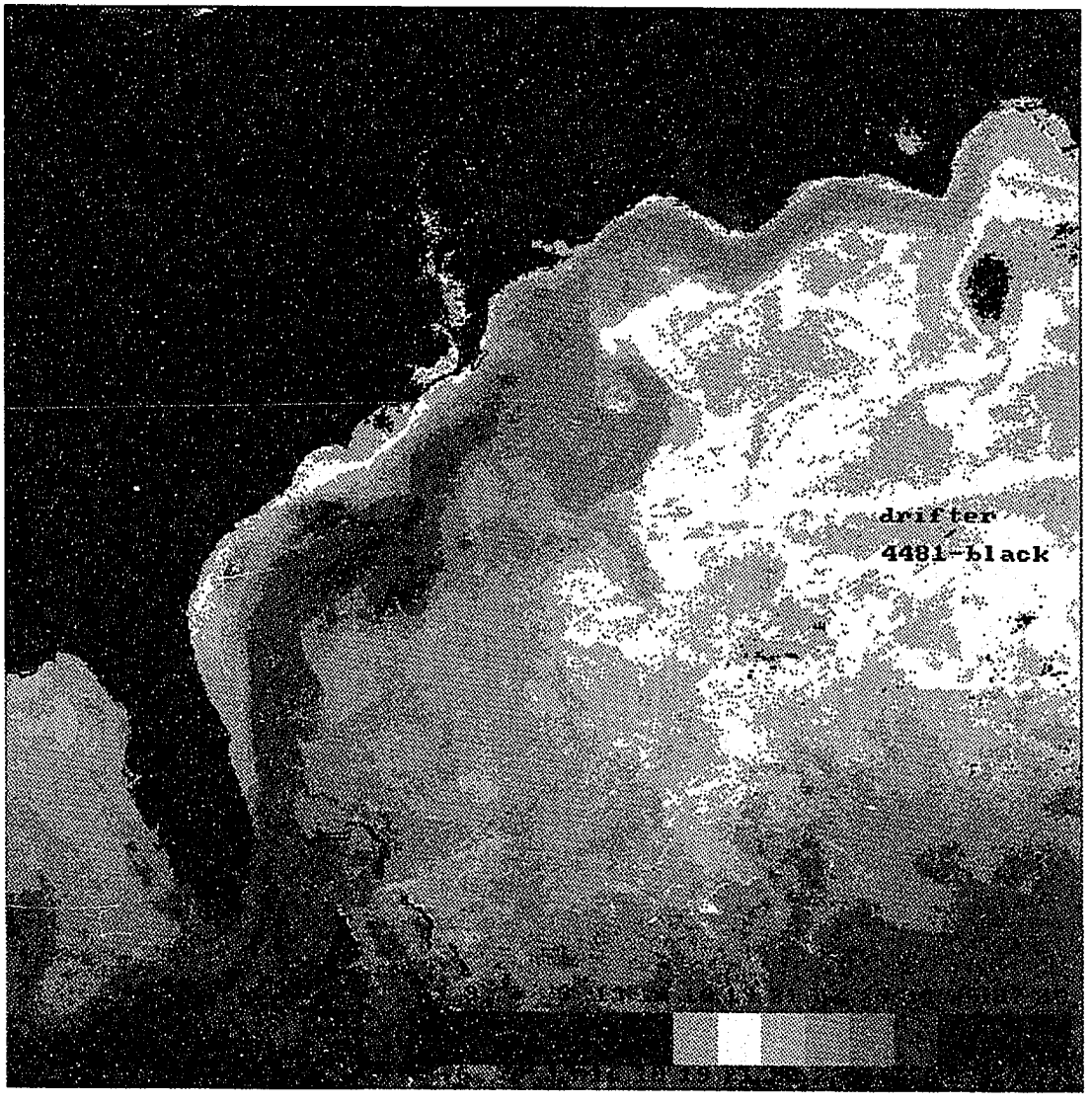

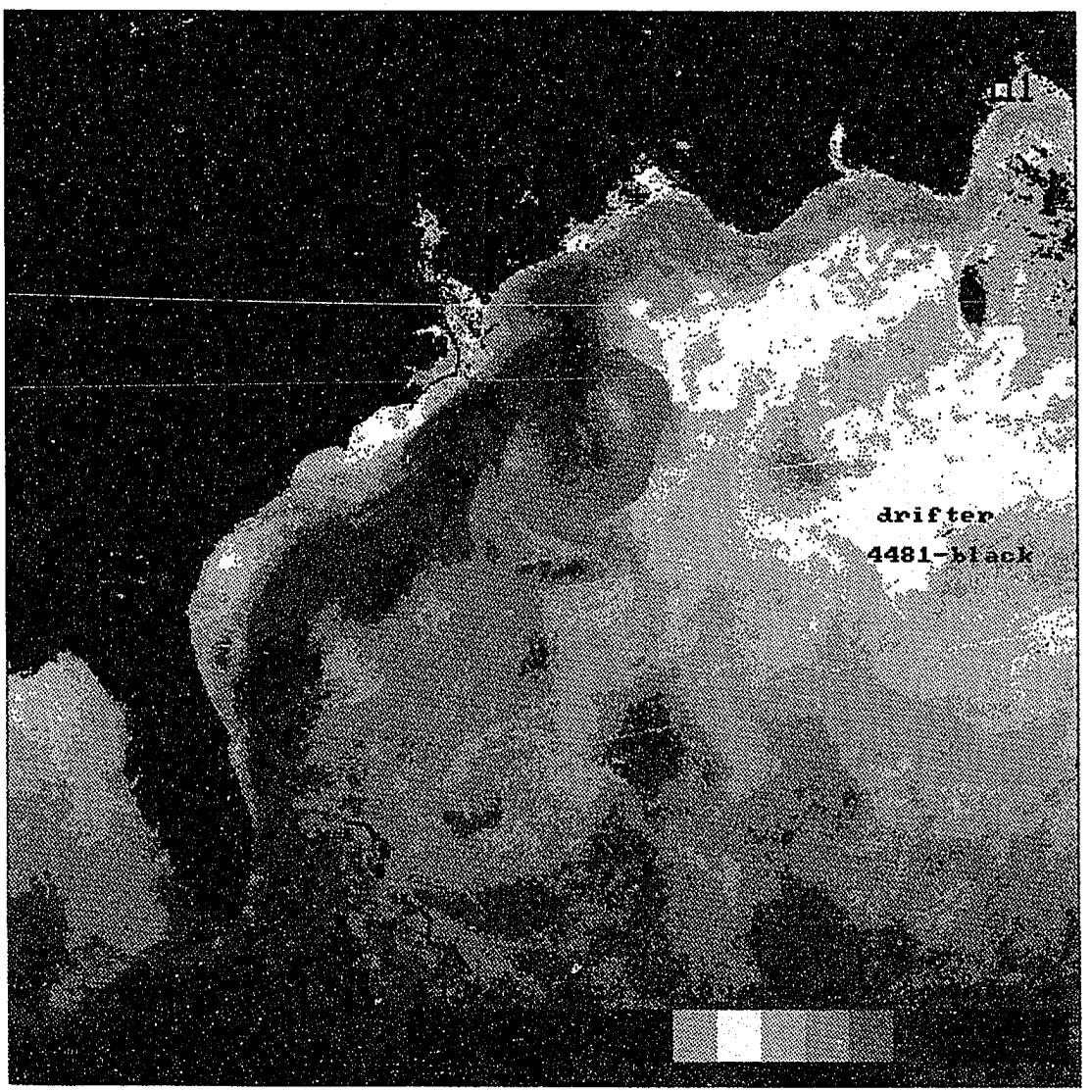

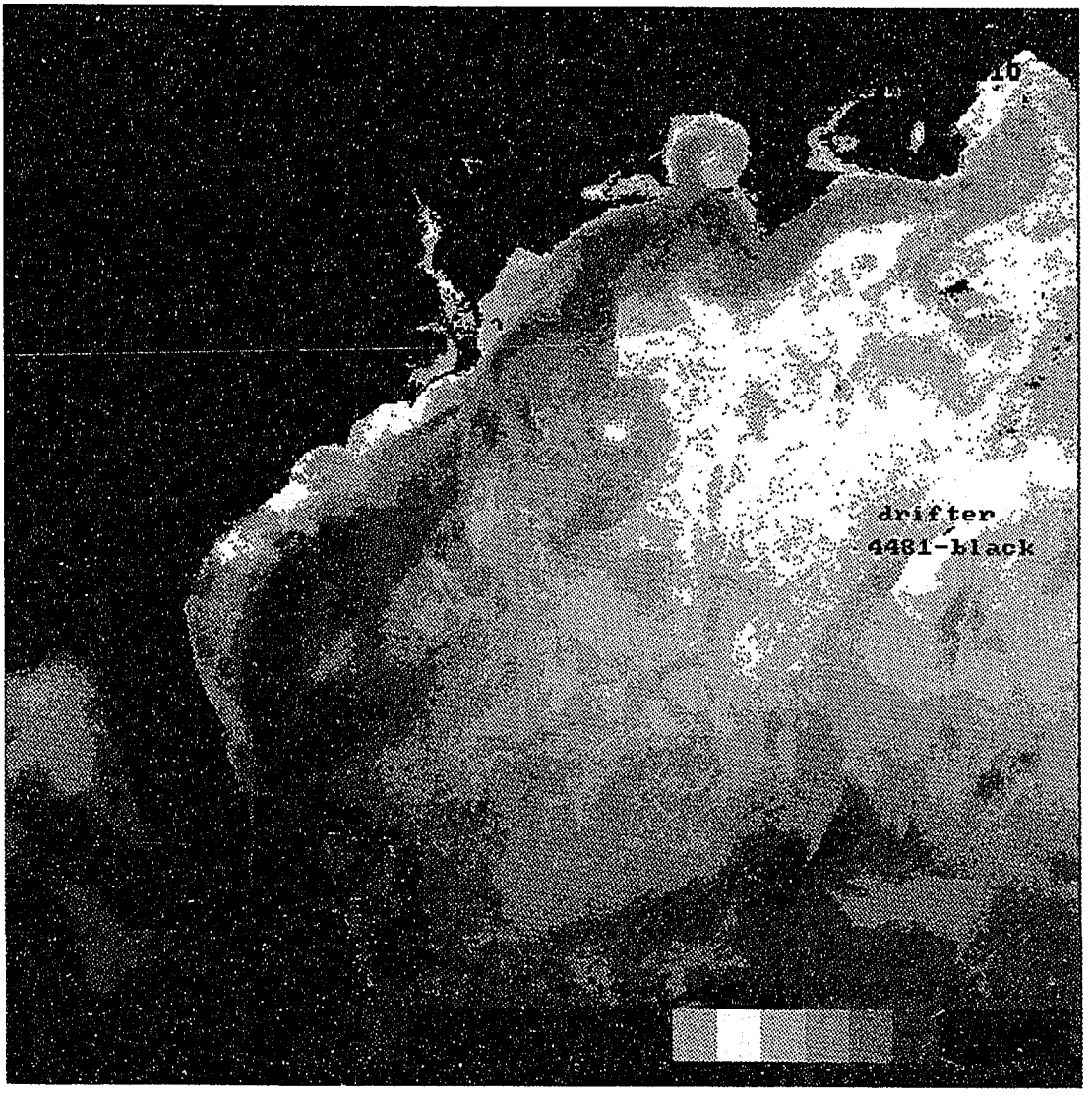

Autobiographical Statement

Caitlin Patrice Mullen was born February 27, 1965 in Portsmouth, New Hampshire to George Henry and Virginia Oshier Mullen.

Ms. Mullen received her B.S. in geology from Dickinson College, Carlisle, Pennsylvania in 1987. She matriculated to Old Dominion University in that year to pursue a Ph.D in geological oceanography. After two and a half years of coursework and research towards the Ph.D, she was given the opportunity to pursue her true interest in physical oceanography. In 1990, she switched her major to the Ph.D program in physical oceanography.

Ms. Mullen has accepted employment at the United States Naval Academy as a Visiting Assistant Professor in the Chair of Oceanographic Remote Sensing, Oceanography Department, Division of Mathematics and Science. She will be teaching courses in dynamical oceanography and meteorology and developing a new course in remote sensing of the oceans.

Caitlin is a member of The Oceanography Society, American Geophysical Union, American Meteorological Society and American Assocation for the Advancement of Science.

She hopes to become an astronaut and pursue a life-long dream of exploring the universe for new phenomena and discovering the answers to many challenging questions.

Her publications and abstracts include the following:

Mullen, C. P. and A. D. Kirwan, Jr. Flow kinematics of the Gulf Stream from composite imagery. *EOS*, 73(43), 1992.

Mullen, C. P. and A. D. Kirwan, Jr. Surface flow structure of the Gulf Stream from composite imagery and satellite-tracked drifters. Chapman/IAPSO Conference on Fractals, Chaos and Predictability in Oceanography and Meteorology, Galway, Ireland, Fall 1993.

Mullen, C. P. and A. D. Kirwan, Jr. Dynamics of the Gulf Stream from composite imagery and satellite-tracked drifters. *Eos* Trans., 75(3), 1994.

Mullen, C. P. and A. D. Kirwan, Jr. Surface flow structure of the Gulf Stream from composite imagery and satellite-tracked drifters. *Nonlin. Proc. Geophys.*, 1, 64-71, 1994.